

CRANFIELD UNIVERSITY

School of Engineering

Space Research Centre

PhD THESIS

Academic Year 2007

GIUSEPPE OTTAVIANELLI

**SYNTHETIC APERTURE RADAR REMOTE SENSING
FOR LANDFILL MONITORING**

Supervisors:
Dr Stephen Hobbs
Dr Richard Smith

Presented: May 2007

Abstract

Despite today's intensive efforts directed at the recycling and recovery of solid wastes, the controlled disposal of refuse into land remains an important and necessary means of effective waste management. The work presented in this thesis investigates the use of Synthetic Aperture Radar (SAR) data to monitor solid waste landfills. The end-users' interests vary from detecting the presence of a landfill to more specifically monitoring on-site operations and environmental conditions. Following a general literature review on the application of Earth Observation data for landfill monitoring, the identified research objectives are to: 1) assess whether SAR data can support the identification of landfill sites by distinguishing them from other disturbed areas which present similar optical spectral signatures, and 2) assess the possibility of correlating SAR data with on-site operational procedures.

Data acquired for the research are: ground observations and measurements examining the spatial, temporal and biophysical characteristics of a landfill that can influence SAR data; historical and new programmed SAR scenes obtained from the ESA ERS-1 and -2 satellites and from Envisat ASAR instrument; ground based SAR (GB-SAR) acquisitions; simulations based on the RT2 backscatter model; additional space-based and airborne optical data to support the analysis and discussion.

The examination of both the SAR amplitude spatial structure and the temporal decorrelation of these sites shows that there are three key characteristics that can distinguish them from other disturbed areas with similar optical spectral signatures: the presence of anisotropic features that strongly affect the SAR backscatter; the fact that the coherence magnitude images of these sites are characterised by large decorrelated areas with transient attributes; and their distinctive positive topography.

The analysis highlights that one single-polarisation acquisition can hardly provide correct land-cover information, and consequently knowledge on land-use. The research demonstrates the key value of merging together complementary information derived from both the space and time dimensions, achieving fairly accurate land-use classification results.

The research also provides an appreciation of the applicability of the developed techniques in an operational framework. These can suffer a number of limitations if a landfill site is located in a particular environment, and/or if meteorological conditions can significantly affect the radar signal, and/or unusual landfilling procedures are applied by the operators. Concluding remarks on the end-users needs point out that there are a number of aspects, ranging from practical and managerial matters to legal and technical issues, that often discourage the utilisation of EO data by new potential users.

Acknowledgements

First of all, I wish to thank my parents, Afra and Franco, for their constant encouragement. It wouldn't have been possible without their support.

I should like to express my sincerest gratitude to my Ph.D. supervisor, Steve Hobbs, Director of the Space Research Centre at Cranfield University. He guided me throughout the various stages of the research with his precious advices and constructive suggestions. My appreciation also goes to Richard Smith, from the Cranfield University Centre for Resource Management and Efficiency, for his interest in my research and his kind assistance.

I would also like to thank all those people that contributed with their expertise and know how to the realization of this research:

- Les Oswald from the Cranfield University Computer Centre,
- Keith Morrison from the Cranfield University Shrivenham Campus,
- Andy Race, John Bennett and Tony Whitaker from Sheffield University,
- Jo Kirkland, Julie Skinner, Martin Lowe, Ricky Haycock, Robin Tucker and Stewart Lethbridge from Waste Recycling Group Ltd,
- all the Cranfield University Library staff,
- Chris Thompson, Head of the Cranfield University Applied Mathematics and Computing Group and internal examiner during my PhD reviews,
- Gabriela Lovelace, Graham Thomas, Dick Thomson, Gavin Wood, Christophe Sannier from the former Cranfield University Silsoe Campus,
- Derek Brown from the Cranfield University Design and Manufacturing Office,
- Ted Milton from the University of Southampton and Crispin Hambidge from the UK Environment Agency,
- Ian Poll from Cranfield University and Sir Peter Norris, Chairman of the RAeS Centennial Scholarship Fund,
- Jim Gautrey and Richard Rogers from the Cranfield National Flying Laboratory Centre,
- Nthabi and Jarrod Ball from Jbawaste in South Africa, and Stephen Opoku-Duah from Durham University,
- many experts from: the European Space Agency, the National Aeronautics and Space Administration, Delft University, the UN Office for Outer Space Affairs, the International Space University, the Global Land Cover Network programme hosted by UN Food and Agricultural Organisation, the Alpbach Summer School 2006 and

the PROBA CHRIS and PolInSAR scientific community. In particular I would like to thank: Alessandro Donati, Francesco Sarti, Gordon Campbell, Chung-Chi Lin, Sergio Camacho, David Stevens, Vern Singhroy, Dan Glover, Siamak Khorram, John Latham, Reuben Sessa, Bert Kampes, Petar Marinkovich, Helmut Rott, Yngvar Larsen, Pierre Briole, Ramon Hanssen, Peter Schrotter, Peter Fletcher, Bianca Hoersch, Eric Pottier.

I would like to acknowledge the Royal Aeronautical Society and the Remote Sensing and Photogrammetry Society for partially sponsoring this research. Their contribution funded both field work activities and the acquisition of remote sensing data.

An exceptional thought goes to all the good friends I have met in Cranfield and around the globe during these long years of work and with who I shared both fun and hard times. To the next step!!!

Last but certainly not least, I would like to express my deep appreciation to B er enice for her love and support.

“The exploration and use of outer space, including the Moon and other celestial bodies, shall be carried out for the benefit and in the interests of all countries, irrespective of their degree of economic or scientific development, and shall be the province of all mankind.”

Article 1 of the United Nations Office for Outer Space Affairs “Treaty on Principles Governing the Activities of States in the Exploration and Use of Outer Space, including the Moon and Other Celestial Bodies”, 1967.

“The challenge of finding sustainable development paths ought to provide the impetus – indeed the imperative – for a renewed search for multilateral solutions and a restructured international economic system of co-operation. These challenges cut across the divides of national sovereignty, of limited strategies for economic gain, and for separated disciplines of science.”

Gro Harlem Brundtland, Our Common Future, 1987.

“The costs of stabilising the climate are significant but manageable; delay would be dangerous and much more costly.”

Sir Nicholas Stern, The Economics of Climate Change, 2007

“A picture is worth a thousand words.”

(Anon.)

Contents

Abstract	i
Acknowledgements.....	iii
Contents.....	vii
Nomenclature	xi
List of Figures and Tables.....	xv
1. Introduction.....	1
1.1 Background and Rationale.....	1
1.1.1 Earth Observation	1
1.1.2 Waste Management.....	3
1.1.3 Landfill Design.....	5
1.1.3.1 Landfill Operations	6
1.1.3.2 Post Closure Management.....	7
1.1.4 Research Aim	8
1.1.5 Literature Review on Remote Sensing for Landfill Monitoring	9
1.2 Problem Formulation and Research Objectives.....	11
1.3 Overall Research Methodology.....	12
1.4 Report Outline.....	14
2. Literature Review.....	17
2.1 Introduction to SAR Principles	17
2.1.1 SAR Geometry and Image Formation	17
2.1.1.1 Resolution in Range	19
2.1.1.2 Resolution in Azimuth: the Synthetic Aperture	19
2.1.2 SAR Backscatter and Factors Affecting Reflectivity	20
2.1.3 SAR Image Structure and Speckle	24
2.1.4 Principles of Polarimetry.....	25
2.1.5 Repeat-pass Interferometry	27
2.1.6 Complex Degree of Coherence	31
2.1.6.1 Decorrelation	35
2.1.7 Surface Displacement Monitoring.....	38
2.2 Optical Remote Sensing	39
2.2.1 Digital Image Processing	40
2.3 Multi-Sensor Data Fusion.....	42
2.4 Summary of Literature Review	42
3. Preliminary Ground Observations	43
3.1 Preliminary Observations	43
3.1.1 Artificial Lagoons.....	45
3.1.2 Infrastructure	46
3.1.3 Open Cells and Capped Areas.....	47
3.1.4 Fully Restored Areas	51

3.1.5	Conclusions of Preliminary Observations.....	53
4.	Data Acquisition and Analysis Techniques.....	55
4.1	Satellite Remote Sensing Data Acquisition.....	55
4.1.1	SAR Data.....	55
4.1.2	Optical Data.....	58
4.2	Overall Methodology for Software Development and Validation.....	58
4.3	Tools Used in the Preliminary Ground Observations.....	59
4.3.1	Geometrical Properties of Bare Surfaces.....	59
4.3.2	Volumetric Soil Moisture and Soil Temperature.....	65
4.4	SAR Amplitude Spatial Structure.....	66
4.4.1	Power Spectrum.....	66
4.4.2	The Application of Power Spectrum.....	67
4.4.3	Radon Transform.....	68
4.5	Interferometric Processing.....	69
4.5.1	Reading SLC Data and Cropping a Sub-scene.....	70
4.5.2	Precise Orbit Determination.....	72
4.5.3	Coregistration.....	72
4.5.4	Azimuth and Range Filtering.....	73
4.5.5	Resampling.....	73
4.5.6	Interferogram Generation.....	73
4.5.7	Phase Filtering and Unwrapping.....	74
4.5.8	Slant-to-Height Conversion.....	74
4.5.9	SAR SLC Image Terrain Correction.....	77
4.5.10	DORIS Interferometric Coherence Calculation Testing.....	78
4.5.11	Coherence Bias Correction.....	79
4.6	Ground-Based SAR.....	81
4.6.1	GB-SAR System Modifications.....	82
4.6.2	Initial Testing and Validation.....	84
4.6.3	GB-SAR Data Processing.....	86
4.7	RT2 Software.....	87
4.8	Ascending and Descending Scenes Coregistration.....	90
4.9	Land-Use Classification.....	92
4.9.1	Fundamentals of Fuzzy Logic.....	94
4.9.2	Overall Classification Procedure.....	98
4.9.3	Definition of the Land-Use Classes.....	99
4.9.4	Rule-Based Fuzzy Logic Classifier.....	101
4.9.5	Featured-Based Classification.....	104
4.9.6	Class Selection.....	106
4.9.7	Land-use Classification Accuracy Assessment.....	106
5.	Landfill Site Identification.....	107
5.1	Optical Data Spectral Analysis.....	107
5.2	Analysis of SAR Amplitude Spatial Structure.....	115
5.2.1	Spatial Analysis Results.....	118
5.2.2	Validation.....	121

5.2.3	Discussion	124
5.3	Analysis of Temporal Change Characteristics.....	128
5.3.1	Analysis of Historical Weather and Ground Reference Data	129
5.3.2	Coherence Magnitude Results.....	140
5.3.3	Discussion	145
5.3.4	Analysis and Discussion of Interferometric DEM	148
5.4	Conclusions of Landfill Site Identification Analysis	150
6.	On-site Conditions Monitoring.....	153
6.1	GB-SAR Acquisitions	153
6.1.1	Acquisitions on Tipping and Capped Area.....	153
6.1.2	Comparative Analysis and Discussion.....	157
6.2	Sensitivity Analysis: RT2 Simulations.....	161
6.2.1	Conclusion of Sensitivity Analysis.....	166
6.3	Detection of Subsidence: Results and Discussion.....	168
6.4	Land-use Classification Results	170
6.4.1	Discussion	173
6.5	Conclusion of On-site Conditions Monitoring.....	177
7.	Overall Discussion	179
7.1	Summary of Previous Analysis and Discussion.....	179
7.2	Analysis of SAR System Parameters	180
7.2.1	Ground Resolution.....	180
7.2.2	Temporal Resolution and Interferometry.....	182
7.2.3	Wavelength.....	183
7.2.4	Polarisation.....	184
7.2.5	Ascending and Descending Orbits and SAR Incidence Angle	184
7.2.6	Conclusion of the Key SAR System Parameters Analysis	184
7.3	Review of Future SAR Space-borne Missions	185
7.3.1	COSMO-SkyMed	185
7.3.2	TerraSAR-X and TanDEM-X	185
7.3.3	Radarsat-2.....	186
7.3.4	TecSAR.....	186
7.3.5	GMES Sentinel-1.....	187
7.3.6	Conclusion of the Review of Future SAR Space-borne Missions	187
7.3.7	Results of the L-band SAR Mission Analysis and Design	188
7.4	Extrapolation of the Analysis Techniques Beyond the United Kingdom	188
7.4.1	Analysis of Optical High Spatial and Spectral Resolution Data	191
7.4.1.1	CASI.....	191
7.4.1.2	PROBA CHRIS	195
7.4.2	Conclusion of the Analysis on the Extrapolation Potentials.....	198
7.5	Analysis of End-Users Needs for the Utilisation of EO Data in an Operational Context	198
7.5.1	Example for Landfill Regulators	199
7.5.2	Conclusion of the Analysis of the End-User Needs	200
7.6	Concluding Remarks of the Overall Discussion	201

8.	Conclusions and Further Work	203
8.1	Summary of the Research	203
8.2	Objective 1: Landfill Site Identification	204
8.3	Objective 2: On-site Conditions Monitoring	205
8.4	Conclusions of the Overall Discussion.....	206
8.5	Further Work.....	206
9.	References	209
9.1	References.....	209
Appendix A	- Matlab and IDL Routines.....	231
A.1	soil_profile.m	233
A.2	PowerSpectrum.m and rotagv.m	234
A.3	SAR_2or4B_read.pro	235
A.4	SARcrop.pro	236
A.5	SARmodify.pro	249
A.6	terrain_correction.m	251
A.7	coherence_correction.m.....	253
A.8	coherence_sd.m.....	264
A.9	GBSAR_min_RCS.m	265
A.10	GBSAR_read.pro.....	266
A.11	GBSAR_proportional.pro	267
A.12	GBSAR_sigma0.pro	268
A.13	land_use_classification.m	269
Appendix B	- Access to DORIS and DORIS Card Examples.....	271
B.1	How to access and use DORIS from Windows	271
B.2	DORIS Card Examples.....	275
Appendix C	- Fuzzy Logic Classifier Rules.....	293
C.1	Fuzzy Rules.....	293
Appendix D	- L-band SAR Mission Analysis and Design.....	294
D.1	Mission Analysis and Design.....	294
D.2	Orbit Selection	296
D.3	SAR Scene Dimensions	298

Nomenclature

2D	Two-Dimension
3D	Three-Dimension
AC	Autocorrelation
AOI	Area(s) of Interest
ARA	Airborne Research Australia
ASAR	Advanced SAR
ASPRS	American Society for Photogrammetry and Remote Sensing
AVHRR	Advanced Very High Resolution Radiometer
CASI	Compact Airborne Spectrographic Imager
CAT	Compact Active Transponder
CCT	Computer-Compatible Tapes
CHRIS	Compact High Resolution Imaging Spectrometer
CNES	Centre National d'Etudes Spatiales
COSMO-SkyMed	Constellation of Small Satellites for Mediterranean basin Observation
CRInSAR	Corner-Reflector SAR Interferometry
DEFRA	Department for Environment, Food and Rural Affairs
DEM	Digital Elevation Model
Descw	Display Earth remote sensing Swath Coverage for Windows
DInSAR	Differential InSAR
DMC	Disaster Monitoring Constellation
DORIS	Delft object-oriented radar interferometric software
EC	European Commission
EEA	European Environment Agency
ENL	Effective Number of Looks
Envisat	Environmental Satellite

EO	Earth observation
EoliSA	Earthnet On-Line Interactive Stand Alone
ERS	European Remote Sensing Satellite
ESA	European Space Agency
ETM+	Enhanced Thematic Mapper Plus
FL	Fuzzy Logic
GB-SAR	Ground Based SAR
GDP	Gross Domestic Product
GH	Ghana
GIS	Geographical Information Systems
GMES	Global Monitoring of Environment and Security
GNSS	Global Navigation Satellite System
GPS	Global Positioning System
GSD	Ground Sample Distance, also called Ground-projected Instantaneous Field Of View (GIFOV)
IDL	Interactive Data Language
InSAR	SAR Interferometry
IPR	Intellectual Property Rights
Jaxa	Japanese Aerospace Exploration Agency
jpeg	Joint Photographic Experts Group
LIDAR	Light Detection and Ranging
MNF	Minimum Noise Fraction
MODIS	Moderate-resolution Imaging Spectroradiometer
NASA	National Aeronautics and Space Administration
NDVI	Normalised Difference Vegetation Index
NIR	Near Infra-Red
NOAA	National Oceanic and Atmospheric Administration
NSRI	National Soil Resources Institute
PALSAR	Phased Array type L-band Synthetic Aperture Radar

PCA	Principal-component analysis
Pixels	Picture Elements
PRF	Pulse Repetition Frequency
PROBA	Project for On-board Autonomy
PSInSAR	Permanent Scatterer SAR Interferometry
PVI	Perpendicular Vegetation Index
Radar	Radio Detection and Ranging
RAeS	Royal Aeronautical Society
RAR	Real Aperture Radars
RGB	red-green-blue
rms	root mean square
RS	Remote Sensing
SA	South Africa
SAR	Synthetic Aperture Radar
SAVI	Soil-Adjusted Vegetation Index
SBAS	Small Baseline Subset
SLC	Single Look Complex
SMOS	Soil Moisture and Ocean Salinity Mission
SPOT	Système Probatoire d’Observation de la Terre
SRC	Space Research Centre
SRTM	Shuttle Radar Topography Mission
SST	Sea Surface Temperature
SSTL	Surrey Satellite Technology Limited
TM	Thematic Mapper
USA	United States of America
VTU	Void Take-Up
VV	Vertical-Vertical
WWW	World Wide Web

List of Figures and Tables

Figure 1-1. Engineered containment landfill configurations: (a) trench type, cross section A-A from (b); (b) trench type top view; (c) canyon type; (d) at grade, or landraising, type. (Modified by Bagchi, 2004).....	5
Figure 1-2. Overall research procedure.....	13
Figure 2-1. SAR geometry and system parameters.	18
Figure 2-2. ESA ERS-1 SAR backscattered amplitude values. The scene was acquired on 25 th June 1995 (descending orbit: 20623; track: 94; frame: 2547). The SAR look angle is from right to left. The image shows a 30 by 30 km area centred on Cranfield University. It is possible to identify the University runways as three crossing dark lines. These are also pointed out by the external arrows. The cities of Milton Keynes and Bedford are identifiable by the brighter backscatter return. They are located respectively in the bottom left and the top right of the image. The original scene has been flipped horizontally and spatially averaged by 5 pixels in the azimuth direction to eliminate the ground resolution distortion.	21
Figure 2-3. SAR signal effects and distortion due to topographic heights (ESA, 2005).23	
Figure 2-4. Geometry for SAR repeat-pass interferometry (Hanssen, 2001).	27
Figure 2-5. Example of flat-Earth removal ((a) to (b)) and phase unwrapping ((b) to (c)) steps to obtain the final relative height values (right).	29
Figure 2-6. Probability density function for three coherence magnitude levels (i.e. 0.1, 0.5 and 0.9). Left with no multilooking (L=1) and right with a multilook factor of 20.....	32
Figure 2-7. Standard deviation of the interferometric phase as a function of coherence, for four different multilook levels.....	33
Figure 2-8. Left: the expectation value of the estimated coherence magnitude as a function of the true coherence and for various multilook factors. Right: the standard deviation of the estimated coherence magnitude as a function of the true coherence and for various multilook factors.	35
Figure 2-9. Coherence magnitude image obtained using the SAR interferometric pair of 25 th and 26 th June 1995 (descending orbit: 20623 and 950 respectively; track: 94; frame: 2547). The multilook factor is 2 pixels in range and 10 in azimuth. The original SAR image of 25 th June can be seen in Figure 2-2. The original scene has been flipped horizontally.	36
Figure 2-10. Model for the ERS C-band system indicating dependence of the temporal correlation (vertical axis) on random motion of scattering centres within a resolution element. The model takes into account horizontal and vertical variations, and shows that decorrelation is more dependent on the vertical displacements.....	38
Figure 3-1. Case study area: Brogborough landfill. Printed by permission of Harper Collins and Multimap. The black cross in the centre marks the landfill location,	

midway between Milton Keynes and Bedford (i.e. 52.05° North and 0.595° West).	44
Figure 3-2. Aerial view of the entire Brogborough landfill acquired by the author on 11 th July 2005 in collaboration with the Cranfield National Flying Laboratory Centre.....	44
Figure 3-3. A survey map of the Brogborough landfill developed in November 2004. The grid is spaced at 100 m. The pink contour represents the operational void where open cells are located. Stage 1 is the selected area for ground observations of a fully restored cell. (Courtesy: Waste Recycling Group Ltd.).....	45
Figure 3-4. Brogborough landfill. A lagoon dug to contain surface water run off. The water is monitored quarterly for presence of leachate and other harmful chemicals (23 rd February 2005).....	46
Figure 3-5. Brogborough landfill. Left: a variety of trucks continuously operate in the open cells (i.e. tipping areas) to deposit and compress the waste. Right: site buildings might include offices, power stations, storage buildings, and truck maintenance buildings (11 th July 2005).	47
Figure 3-6. Brogborough landfill. Left: waste deposited and immediately compressed in the open cell. A one-meter length is shown in the image. Right: temporary layer of clay deposited on top of the tipping area to cover the waste (09 th May 2005).....	48
Figure 3-7. Brogborough landfill. A capped area. In this particular picture, the engineered Oxford clay presents visible cracks due to shrinkage of the soil. A one- meter length is shown in the image. (13 th June 2006).....	48
Figure 3-8. Brogborough landfill. Left: batter of an open cell. Right: high vertical step in an area where the daily clay is piled and managed. A two-meter length is shown in the image. (09 th May 2005).....	49
Figure 3-9. Variation of air temperature on 10th May 2005 from 9.50am to 4.50pm measured with a thermometer provided by the Space Research Centre.	50
Figure 3-10. Brogborough landfill. Fully restored area. (05 th November 2004).....	52
Figure 3-11. Location of the samples with respect to the local topography of the area, which was obtained from the accurate surveying data. The interpolation between the points is computed with the Sandwell (1987) method.	53
Figure 4-1. Design and implementation phases for the data processing routines.	58
Figure 4-2. Profilometer picture distortion correction: (a) original picture, (b) distortion correction (c) validation that mesh grids are exactly squared.	60
Figure 4-3. Modification of the brightness and contrast of the profile images to obtain a black and white image only.	61
Figure 4-4. The black and white profile is used to mask the original image to verify the consistency of the developed technique.	61
Figure 4-5. Digitized height profile computed with soil_profile.m. The vertical axis does not shows the complete height of the profilometer, therefore the height appears distorted by around 5 times. Each interval on the horizontal axis represents 3 mm.	62
Figure 4-6. Unwanted shadows effects created by the mesh attached to the board and by other object projected on the board.	62

Figure 4-7. Systematic unaligned pattern sampling method with 5 samples applied to the two surfaces under examination.....	64
Figure 4-8. Power spectrum example. Left: original SAR amplitude data with 5 pixel averaging in the azimuth direction (i.e. each pixel represents a 25 m ² area). Right: power spectrum computed with the Matlab routine PowerSpectrum.m. The numbers on the axis of the left and right images respectively represent the pixel number and the wavenumber.....	67
Figure 4-9. Log-log plot of the rotationally averaged power spectrum shown in Figure 4-8. The red dotted lines represent the trend of the data.	68
Figure 4-10. Example of Radon transform.....	69
Figure 4-11. Interferometric processing chain using DORIS and other additional routines.	70
Figure 4-12. Detail of a ERS SAR sub-scene: amplitude data averaged by 5 in azimuth. The circled black cross identifies the selected feature with constant scattering characteristics used as centre when cropping the SLC scenes. Being a descending orbit scene, the image should be flipped horizontally to have a realistic view.	71
Figure 4-13. Aerial view of Cranfield University. The arrow identifies the selected feature with constant scattering characteristics used as centre when cropping the SLC.....	71
Figure 4-14. Left: oblique aerial view of the two Cardington hangars, just south of Bedford (UK), built in the early 1920s for the construction of airships. They measure 247 m in length, 84 m in width and 55 m in height. Right: height computed with the first ERS interferometric tandem pair (i.e. 25 th and 26 th June 1995). The average computed height of the two hangars is 54 m. The two images have a different scale and orientation, and are presented for illustration purposes only.....	75
Figure 4-15. Left: aerial view of the Bedford-Luton (UK) train line tunnel between Milbrook and Amphill (Google Earth, 2007; with the education setting reproduction agreements). The height step change before the train enters the tunnel is roughly equal to 12 m. Right: height computed with the first ERS interferometric tandem pair (i.e. 25 th and 26 th June 1995). The average computed height at the two exits is 11.5 m. The two images have a different scale and orientation, and are presented for illustration purposes only.....	75
Figure 4-16. Left: aerial view of disused grain silos located on Station road, Turvey, Bedfordshire (UK) (Google Earth, 2007; with the education setting reproduction agreements). These buildings are 30 m high Bedford Borough Council (2007). Right: height computed with the first ERS interferometric tandem pair (i.e. 25 th and 26 th June 1995). The phase unwrapping algorithm is not able to successfully compute an accurate height of these structures. The two images have a different scale and orientation, and are presented for illustration purposes only.	76
Figure 4-17. Left: aerial view of industrial units located in the south-east area of Milton Keynes (UK). (Google Earth, 2007; with the education setting reproduction agreements). Right: height computed with the first ERS interferometric tandem pair (i.e. 25 th and 26 th June 1995). The phase unwrapping algorithm is not able to	

successfully compute an accurate height of these buildings. The two images have a different scale and orientation, and are presented for illustration purposes only. ...	76
Figure 4-18. Slant range – ground range conversion (Hein, 2004).	77
Figure 4-19. Slant-ground range conversion for the sub-scene of 25 th June 1995. Even if not apparent, the corrected image (right) presents some black pixels on its right edge due to the shift linked to topography.	77
Figure 4-20. This image shows the amplitude of a modified ERS 1 sub-scene acquired on 25 June 1995 and averaged by 5 in azimuth. Complex Gaussian noise is added in a rectangle in the right half.	78
Figure 4-21. Magnitude of interferometric coherence between original and modified ERS 1 sub scenes.	78
Figure 4-22. Zoom into the top right corner of the magnitude of interferometric coherence between original and modified ERS 1 sub scenes.	79
Figure 4-23. Flow chart of coherence magnitude bias correction routine. This is repeated for each pixel of the area of interest selected by the user.	80
Figure 4-24. Example of coherence bias correction applied on the Brogborough landfill, which is identified by the turquoise contour. The image on the left is the original biased coherence computed with a 10 by 2 pixels (in azimuth and range respectively) processing window. The middle image shows the result of the algorithm implemented in the research. It is possible to notice without losing spatial resolution, the procedure obtains better contrast and more defined boundaries between high- and low-coherence areas. The image on the right shows the ENL for each pixel. Dark pixels correspond to a low ENL, whilst white pixels correspond to a high ENL.	80
Figure 4-25. Left: GB-SAR stowed configuration. The 4-wheel-drive vehicle is used to transport it and house the majority of the instrumentation. Right: GB-SAR set-up, with the hydraulic lift not deployed and the C-band antennas pointing horizontally	81
Figure 4-26. GB-SAR system deployed at a height of 10 m. The antenna incidence angle θ is set a 45°. The weather station has not been installed.	82
Figure 4-27. New GB-SAR system configuration.	83
Figure 4-28. Inverse FFT of a single scan with the Gore cables connected together. The amplitude is in dB and normalised to the maximum value. The abscissa represents range in pixels, with every pixel corresponding to 0.0586 m. The peak corresponds to the distance of the cables (i.e. 15 m).	85
Figure 4-29. Levelled trihedral position at nadir at a height of 1.3m.	85
Figure 4-30. Inverse FFT of a single scan of three acquisitions. The y-axis represents the amplitude in dB normalised to the maximum value (i.e. the return signal with the Gore cables connected together), and plotted from 0 to -5dB. The abscissa represents range in pixels, with every pixel corresponding to 0.0586 m. Range increases towards the left. The abscissa values are not absolute, but represent only a value of the distance between two points. Refer to main text for detailed explanation.	86

Figure 4-31. RT2 backscatter modelling software. The rtsetup modules allows the user to define the surface parameters.	88
Figure 4-32. Soil texture. Classification of separates (USDA, 2007).....	89
Figure 4-33. Flow chart of ascending and descending SAR sub-scenes coregistration.	91
Figure 4-34. RGB colour composite with three coherence magnitude images derived from three different 1-day ERS tandem pairs. The black contour identifies the Brogborough site boundary.	94
Figure 4-35. Fuzzy sets for the degree of coherence (left) and the backscatter amplitude (right). Note the different functions used to model the membership grades and the overlapping difference between them which is left at the discretion of the developer.	95
Figure 4-36. Fuzzy set for the Water Body class.	96
Figure 4-37. Fuzzy membership of Rule 1 for the degree of coherence (left) and backscatter amplitude (right). The results are approximate and for explanation purposes only.	97
Figure 4-38. Fuzzy membership of Rule 2 for the degree of coherence (left) and backscatter amplitude (right). The results are approximate and for explanation purposes only.	97
Figure 4-39. Application of the consequent fuzzy rules. Rule 1 on the left and Rule 2 on the right. The results are approximate and for explanation purposes only.....	97
Figure 4-40. Aggregation of the consequent fuzzy rules and defuzzification through the centroid calculation. The results are approximate and for explanation purposes only.....	98
Figure 4-41. Land-use classification algorithm.....	100
Figure 4-42. Fuzzy logic classifier structure. It uses a Mamdani defuzzification algorithm. It has 13 input variables and 8 output variables and it uses 27 fuzzy rules.	101
Figure 4-43. Example of a fuzzy set and membership functions developed for the FL classifier. This examples shows the 9-day coherence difference fuzzy set. The transition from a low to medium value is smoother than from a medium to high value. This is used to make a more defined separation between the latter two levels.	102
Figure 4-44. Example of a fuzzy set and membership functions for the land-use classes. All classes are modelled by the same linear membership functions.....	102
Figure 4-45. Example of a fuzzy set and membership functions for the land-use classes. All classes are modelled by the same linear membership functions.....	102
Figure 4-46. Relationship between $O(P)$ and $S(P)$ for different values of the second highest degree of membership as specified in the legend.	104
Figure 5-1. As pointed by the label, the Buckden landfill (located at 52° 18' 31.39'' North and 0° 13' 28.32'' West) is identified by the red area in the bottom left corner of the map. (Environment Agency, 2005).	108
Figure 5-2. An aerial photo of the Buckden landfill at a 2 m resolution taken in the second half of 1999 (GetMapping, 2004).....	108

Figure 5-3. The wide image is the original UK_Cambridge_Agriculture.jpg available from the DMCII DVD. Two enlargements highlight the Buckden landfill.	109
Figure 5-4. Top: the aerial photo of the Buckden landfill at a 32 m resolution, obtained by simple averaging of the original image. Bottom: image of the Brampton landfill available from the DMCII DVD.	110
Figure 5-5. SPOT 2 sub-scene of Bedfordshire with 20 m ground resolution acquired on 16 th May 1992. The image is obtained with a standard false colour composite with Band 1 (wavelength from 0.50 to 0.59 μm – green) as Blue, Band 2 (0.61 - 0.68 μm – red) as Green, and Band 3 (0.78 - 0.89 μm – NIR) as Red. The image is centred at 52° 2' 12'' N and 0° 31' 53'' W. The image was provided by the Cranfield University Centre for Geographical Information Management. Copyright CNES 1992.	111
Figure 5-6. Landsat 5 TM sub-scene of Bedfordshire with 30 m ground resolution acquired 12 th June 1992. The image is obtained with a standard false colour composite with Band 2 (wavelength from 0.525 to 0.605 μm – green) as Blue, Band 3 (0.630 - 0.690 μm – red) as Green, and Band 4 (0.75 - 0.90 μm – NIR) as Red. The image is centred at 52° 2' 12'' N and 0° 31' 53'' W as Figure 5-5. Its printed size appears smaller than Figure 5-5 due to the coarser spatial ground resolution. Copyright University of Manchester/University College London Year 2001 (Landmap, 2005). Original Landsat 5 distributed by Infoterra International.	112
Figure 5-7. Landsat 7 ETM+ sub-scene of Bedfordshire with 30 m ground resolution acquired 12 th May 2001. The image is obtained with a standard false colour composite as for Figure 5-6. The image is centred at 52° 2' 12'' N and 0° 31' 53'' W as Figure 5-5. Its printed size appears smaller than Figure 5-5 due to the coarser spatial ground resolution. Copyright University of Manchester/University College London Year 2001 (Landmap, 2005). Original Landsat 7 distributed by Infoterra International.	113
Figure 5-8. Spectral signatures for the three selected AOI in the three sub-scenes. The Landsat band number 6 in the graphs actually represents the official band number 7 (2.08 - 2.35 μm – reflected IR).	114
Figure 5-9. Landsat 7 ETM+ image (12 th May 2001) and ERS-2 scene (11 th June 2001).	116
Figure 5-10. Mean value and standard deviation of the AOI size.	118
Figure 5-11. Mean value and standard deviation of SAR backscatter.	118
Figure 5-12. Power spectra for landfill sites (above) and disturbed areas (below). The red dotted line represents the average power-law exponent of the two groups.	120
Figure 5-13. Mean value and standard deviation of spectrum power-law exponents. .	121
Figure 5-14. Power spectra for Brogborough and Stewartby landfills used as validation sites. The red dotted lines represent the average power-law exponent.	123
Figure 5-15. Radon transform for two AOI.	125
Figure 5-16. Particular of a survey map with a 100 m spacing grid of Brogborough landfill provided by Waste Recycling Group Ltd. (Void Take Up Survey 24 th January 1996). It highlights a 35 m high step occurring in about 180 m across. .	125

Figure 5-17. 1995 – 1996 acquisition dates of the ERS 1-2 tandem pairs.....	129
Figure 5-18. Daily soil temperature and rainfall during the 1995 ERS tandem pairs acquisitions.	131
Figure 5-19. Soil temperature and rainfall data at 15-min intervals during the 1996 ERS tandem pairs acquisitions. The vertical and dotted lines respectively identify the time of the ERS 1 and ERS 2 passes. Cont.	132
Figure 5-20. Daily soil temperature and rainfall during the 1999 and 2000 ERS tandem pairs acquisitions.....	133
Figure 5-21. Survey map with a 125 m spacing grid of Brogborough landfill provided by Waste Recycling Group Ltd. The two solid lines indicate the areas in which waste was filled during 1994/1995.	134
Figure 5-22. Survey map with a 125 m spacing grid of Brogborough landfill provided by Waste Recycling Group Ltd. The solid line in the northern part of the landfill indicates the area in which waste was filled during 1995/1996.	135
Figure 5-23. Topographic survey with a 100 m spacing grid of Brogborough landfill provided by Waste Recycling Group Ltd. 15 th February 1996. These surveys specify the exact location of the tipping areas and the presence of any lagoon used to monitor run of water or the presence of leachate.....	136
Figure 5-24. Topographic survey of Brogborough landfill provided by Waste Recycling Group Ltd. June 2004. The black dashed line indicates the site extension permitted towards the end of 1998. The red dotted line refers to an area leased at the end of 2006 used for a provisional clay stock pile. The grid has a 500 m spacing.	137
Figure 5-25. Topographic survey with a 100 m spacing grid of Stewartby landfill provided by Waste Recycling Group Ltd. 28 th January 2004. The red line refers to the area covered in Figure 5-26.	138
Figure 5-26. Topographic survey with a 200 m spacing grid of Stewartby landfill provided by Waste Recycling Group Ltd. 6 th March 2004.	139
Figure 5-27. Quest pit of the Stewartby clay extraction site. Particular of the activities during a site visit on 22 nd November 2006.	139
Figure 5-28. Coherence magnitude images of the three selected sites.	140
Figure 5-29. Difference map between the coherence magnitude images of (a) 16-17 February 1996 and 25-26 February 1996 and (b) 26-27 April 1996 and 05-06 May 1996. Red pixels represent areas in which change is detected in the first coherence image but not in the second, while blue pixels identify areas in which change occurred in the second coherence image but not in the first. Zones that have not changed their coherence magnitude characteristics between the 9 days of the two tandem pairs have a grey colour. The approximate site boundary is shown by the black contour.....	146
Figure 5-30. DEM of the three sites of interest for the ERS tandem scenes of 31 March - 1 April 1996. From top to bottom: Brogborough landfill, Stewartby landfill, Quest pit. The three DEM have a different scale from each other. The right column shows the topography values with a vertical exaggeration of 10 times. In the left column the coherence magnitude values are added on the topography. The red contours	

identify the approximate sites boundaries. The three axes in the middle show the approximate direction of the North (N), West (W) and the elevation.	149
Figure 5-31. Subtraction of two DEMs over Brogborough landfill derived from two different ERS tandem pairs (i.e. acquired on 25 th and 26 th June 1995 and on 3 rd and 4 th September 1995). The white colour represents areas that have increased in height. The white zones south east of the waste disposal site correspond to vegetation areas next to the Broughborough lake over which the DEM might not be accurate due to the decorrelation effects. The turquoise contours identify the approximate sites boundaries.....	150
Figure 6-1. GB-SAR deployed configuration at the Brogborough landfill.	154
Figure 6-2. Acquisitions surfaces: capped (left) and tipping areas (right).....	155
Figure 6-3. Angular response of σ_0 for all polarisations acquired over the capped area.	155
Figure 6-4. Angular response of σ_0 for all polarisations acquired over the tipping area.	156
Figure 6-5. Amplitude values of the HH polarisation acquisitions of the capped cell (left) and of the tipping area (right). The images' histograms have been optimised independently of each other to improve the visualisation. The SAR system point of view is in the middle top of each image. Light pixels represent a stronger backscatter signal.	156
Figure 6-6. Normalised histograms of the HH backscattering coefficients of the two acquisitions.	157
Figure 6-7. HH backscattering coefficient values for the capped surface (top) and for the tipping surface (bottom).	157
Figure 6-8. Mean and standard deviation of the correlation coefficients computed between the various backscattering coefficients for each acquisitions.	159
Figure 6-9. Angular response of the co- and cross-polarised ratios for both surfaces.	160
Figure 6-10. Variation of the cross and co-polar ratios as a function of a dipole orientation.	161
Figure 6-11. Variation of the cross and co-polar ratios as a function of a dipole orientation.	162
Figure 6-12. Backscatter variation with soil moisture at different radar wavelengths and polarisations for a 100 % clay soil texture. Fixed incidence angle at 23°.	163
Figure 6-13. Backscatter variation with soil roughness at different radar wavelengths. Fixed incidence angle at 23°.	164
Figure 6-14. Backscatter variation with soil moisture at different radar wavelengths for a 100 % sand soil texture. Fixed incidence angle at 23°.	164
Figure 6-15. Backscatter variation with soil moisture at different radar wavelengths for a 100 % silt soil texture. Fixed incidence angle at 23°.	165
Figure 6-16. Backscatter variation with soil texture at L band. Fixed incidence angle at 23°.	165
Figure 6-17. Backscatter variation with incidence angle at L band.	166

Figure 6-18. Backscatter amplitude of (a) ERS-1 acquisition of 30 th July 1995 (i.e. orbit 21124, track 94, frame, 2547, VV pol) and (b) ERS-2 acquisition of 31 st July 1995 (i.e. orbit 1451, track 94, frame 2547, VV pol). These sub scenes, which also include Cranfield University with its airfield, confirm the difficulty of extracting land-cover information with one single-polarisation SAR image. The red lines identify the Brogborough landfill boundary.....	167
Figure 6-19. Left: red-green-blue composite using respectively the coherence magnitude, backscattered amplitude and coherence magnitude for each colour band. Data of the SAR interferometric pair of 25 th and 26 th June 1995. The radar view direction is from right to left. The black contour identified the boundaries of the Brogborough landfill in 1995. Right: Same colour composite superimposed on the interferometric DEM. The black circle highlights the spike in the DEM.	169
Figure 6-20. Left: topographic survey over the Brogborough landfill (22 nd February 2005). Right: surveying data download and processing.....	170
Figure 6-21. Left: topographic survey with a 100 m spacing grid of Brogborough landfill provided by Waste Recycling Group Ltd. 15 th February 1996. Right: example of land-use class selection based on the topographic survey and additional reference data provided by the operators. Areas of no specific use are grouped into the capped area with no vegetation class.....	172
Figure 6-22. Land-use classification results. The map is obtained by setting the degree of ownership $O(P)$ higher that 0.6 and the degree of classification success $S(P)$ higher than 0.18. The turquoise contour identifies the site boundary.....	172
Figure 6-23. Ordnance Survey map. The red arrow identifies the centre of the Brogborough landfill (copyright Ordnance Survey).....	174
Figure 6-24. Land-use classification results obtained by increasing the degree of classification success $S(P)$ threshold to 0.25. The turquoise contour identifies the site boundary.....	175
Figure 6-25. Ground validation of the road and building class pixels observed in the results. (Google Earth, 2007; with the education setting reproduction agreements).	176
Figure 7-1. Size of landfills in England and Wales (left) and normalised modelled cumulative distribution using a gamma distribution (right). The gamma parameters a and b are respectively equal to 2.5 and 2.....	181
Figure 7-2. Relation between landfill size and its topography features. The polynomial used to model this relationship is: $y = -0.0007 x^3 + 0.0549 x^2 - 1.1354 x + 11.2672$	182
Figure 7-3. Examples of how temporal resolution can support the development of change dynamics models of land-use characteristics.....	183
Figure 7-4. Aerial view of the planned Eagle Mountain landfill (SDLA, 2007).	189
Figure 7-5. Aerial view of the Bissasar Road landfill (Google Earth, 2007; with the education setting reproduction agreements).....	190
Figure 7-6. Aerial view of the Oblogo landfill (Google Earth, 2007; with the education setting reproduction agreements).....	191

Figure 7-7. Colour composites of a CASI image with 1 m ground resolution of the Bletchley landfill site near Milton Keynes. Top: original data, true colour composite with bands 4 3 2 as RGB. Top: landfill site, false colour composite with bands 1 4 7 as RGB. Copyright 2005 Environment Agency.....	193
Figure 7-8. True colour composites of a CASI image with 1 m ground resolution of the Bletchley landfill site near Milton Keynes, UK. true colour composite with bands 4 3 2 as RGB. Copyright 2007 Environment Agency.....	194
Figure 7-9. Bletchley landfill. Normalized Difference Vegetation Index (Schowengerdt, 1997). Bright areas corresponds to vegetation, whilst dark areas correspond to bare zones. Copyright 2007 Environment Agency.....	194
Figure 7-10. CHRIS Proba spectral windows (ESA, 2007e). The instruments in Mode 3 acquires 18 bands (in red). A spectrum of healthy vegetation is shown in green. The blue spectrum depicts the atmospheric absorption.	195
Figure 7-11. CHRIS Proba acquisition centred on the Brogborough landfill. Partial cloud cover and relative shadows limit the utilisation of the image.	196
Figure 7-12. Proba CHRIS red-green-blue composite using the first three components after the image dimensionality reduction. Image acquired on 30th August 2005. The blue areas indicated by the arrows refer to the open cells. Red areas correspond to water, while blue marine corresponds to clouds. The black line identifies the perimeter of the northern part of the landfill.	197
Figure 7-13. Aerial view of the tipping areas of the Brogborough landfill acquired by the author on 5 th September 2005 in collaboration with the Cranfield National Flying Laboratory Centre. The three axes show the approximate direction of the North (N), West (W) and the elevation. Point A north of the landfill facilitates the comparison of this picture with the Proba CHRIS colour composite in Figure 7-12 as a ground truthing tool.....	197
Table 3-1. Surfaces roughness characteristics.....	50
Table 4-1. SAR data (all Envisat scenes have VV polarisation with a mean incidence angle of 23°).....	57
Table 4-2. Perpendicular baseline and centre pixel location of the 1200 by 6000 pixels sub-scenes cropped from the ERS SAR tandem data.	72
Table 4-3. Variation of σ_{\min} with range at C-band.....	83
Table 5-1. Number of representative pixels per AOI in each sub-scene.	112
Table 5-2. List of the twenty AOI selected in the SAR scene. The columns specify the name of the AOI, the coordinates of its centre location, the number of pixels and the actual SAR backscatter amplitude image.	116
Table 5-3. Power-law exponents, β , of the model fitted on the rotationally averaged power spectrum of each AOI.	119
Table 5-4. AOI used as validation sites. The columns specify the name of the SAR platform, the orbit specifications, the acquisition date and time, the number of pixels and the actual SAR backscatter amplitude image.....	122
Table 5-5. Power-law exponents β of each AOI.	123

Table 5-6. Concluding remarks on landfill site identification.....	151
Table 6-1. SAR scene used in the land-use classification.....	170
Table 6-2. Qualitative analysis of land-use classes.	171
Table 6-3. Error matrix for the land-use map obtained setting $O(P)$ higher than 0.6 and $S(P)$ higher than 0.18. It is assumed that the southern half of the site is covered by bare soil and is not a restored area with low or high vegetation.....	173
Table 7-1. Spectral bands acquired by the CASI instrument.	192

1. Introduction

This report presents research undertaken at the Cranfield University Space Research Centre (SRC) from January 2004 to May 2007. The work focuses on the development and assessment of new remote sensing applications and data processing techniques specifically for solid waste landfill monitoring. The origins of this study are in line with current European efforts (ESA, 2006a; European Commission, 2006) to bridge the gap between satellite remote sensing data providers and end-users. In recent years, in fact, many Earth observation (EO) organisations have shifted their attention from technology driven to application driven developments.

This first chapter describes the background and rationale of the research. It then presents a literature review on the application of remote sensing for solid waste landfill monitoring, which leads to the problem formulation and the definition of the research objectives. The chapter then describes the overall research methodology and outlines the content of the report.

1.1 Background and Rationale

Before presenting the specific objectives of the research, it is important to introduce its background and rationale, covering aspects related to both Earth observation and waste management. This section also provides the reader with an overview of landfill design and operations. It explains the need for certain practices and also describes post-closure monitoring requirements.

1.1.1 Earth Observation

Remotely-sensed images of the Earth provide information on geophysical variables that can be translated into significant and often unique knowledge of both environmental parameters and anthropological features. They can be used for a great variety of purposes ranging from weather forecast and natural resource monitoring to disaster management and law enforcement activities.

Surface imaging space-borne sensors operate in specific regions of the electromagnetic spectrum where constituents of the atmosphere (e.g. water vapour and carbon dioxide) do not absorb radiation. Such sensors can be primarily divided into passive and active types. The former group measures radiation naturally reflected or emitted from the ground, atmosphere and clouds (e.g. optical sensors in the visible or thermal infrared spectrum). The latter instead employs an artificial source of radiation as a probe and

measures the resulting signal that is scattered back (e.g. Synthetic Aperture Radar (SAR) platforms operating in the microwave spectral region).

Other parameters that characterise EO sensors and platforms are the spatial, spectral, radiometric and temporal resolutions. In general terms, spatial resolution identifies the minimum separation between two objects at which the resulting images of the objects appear distinct and separate. Spectral resolution can be defined in terms of both the number of spectral channels being imaged over a given spectral region and by the range of wavelengths (or frequencies) incorporated into each single channel. Radiometric resolution determines how finely the sensor can distinguish between objects of similar reflection. The higher the radiometric resolution, the more sensitive it is to detect small differences in reflected or emitted energy. Finally, the temporal resolution is the frequency at which images of the same location on Earth can be captured.

The existing EO platforms offer a wide range of solutions in order to meet the needs of the different applications. Depending on the final purpose, some satellite systems provide frequent, repetitive coverage with relatively low spatial resolution and a broad ground swath (e.g. meteorology applications), others provide exceptionally high spatial resolution with a more sporadic coverage (e.g. precision mapping purposes), whilst a third group has to satisfy both high spatial resolution and frequent coverage with rapid image processing and final product delivery (e.g. military intelligence utilisation).

As reported by the Committee on Earth Observation (2006), there are approximately 70 EO satellite missions currently operating, and around 100 more, carrying over 300 instruments, are planned for the next 15 years or so by the world's civil space agencies. This proliferation of EO missions and the growing involvement of commercial companies reflects the unique abilities and benefits that satellites offer. They allow a non-intrusive worldwide collection of data, reaching remote or hostile areas and without compromising national sovereignty. They provide a synoptic view of large-scale phenomena and place in situ measurements into the global context required for the observation of many environmental events. Finally, they can offer a relatively rapid measurement capability and long-term continuity, satisfying disaster management scenarios and climate studies.

Among the many developed remote sensing applications, one that has hitherto been largely undervalued, but which may have great significance in the coming decades, is the management and monitoring of solid waste landfills. Indeed, increasing waste quantities around the globe are becoming extremely complex to deal with and waste management is one of the most critical environmental concerns that modern society is facing (Tammenagi, 1999).

1.1.2 Waste Management

As highlighted by the United Nations in the far-reaching Agenda 21 document (United Nations, 1992), “unsustainable patterns of production and consumption are increasing the quantities and variety of environmentally persistent wastes at unprecedented rates”. It is becoming extremely problematic to manage and dispose with environmentally sound solutions the growing amount of waste generated by household, industrial, commercial and other human activities. Waste is therefore considered as key sustainable development indicator linked to the economical development of our society (DEFRA, 2004).

Waste management is closely intertwined with many interdependent and trans-boundary issues such as industrial policies, international and national economic strategies, environmental protection agreements and local community development plans. Many international and national agreements and regulations also try to establish sustainable systems that prevent or reduce the adverse effects of waste processing and disposal on the environment (e.g. United Nations Environment Programme, 2004 and 2001; UK Legislation, 2000; European Union, 1999; United Nations, 1989; International Maritime Organization, 1972).

Emerging from this complex framework, modern practices concurrently tackle strategic issues related to resource efficiency, waste logistics, economic benefits and resource mass balance (Bagchi, 2004; McDougal et al., 2001). These practices also aim at reducing the amount of waste sent to landfill by encouraging its overall reduction, incineration, re-use and recycling. Nonetheless, the controlled disposal of waste into land is still an important and necessary means of effective waste management and, as stated in Waste Strategy 2000 for England and Wales (DEFRA, 2000), it remains “the Best Practicable Environmental Option for certain types of waste in the foreseeable future”. Current European figures (European Environment Agency, 2006) also confirm that in recent years the generation of municipal waste in western European countries continues to grow slightly above Gross Domestic Product and has reached almost 600 kg per capita per year. Clearly, the European Union (EU) target to reduce municipal waste generation to 300 kg/capita by the year 2000 was not achieved, and no new targets have been set since. In the United States of America (USA), the amount of refuse generated per person per year has reached 750 kg, 30% of which is recovered and recycled or composted, 14% is burned at combustion facilities, and the remainder is disposed in landfills (US EPA, 2003).

Evidently, as currently operational sites reach their capacity, new ones will have to be approved by planners, permitted by the regulator and consequently monitored. In England and Wales, there are around 2200 operational landfills (Environment Agency, 2006) and since 1999 more than 100 licences have been issued for new or already existing municipal waste sites (Butcher, 2005). Under the Pollution Prevention and Control regulatory regime (UK Legislation, 2000), landfills are currently permitted by

the Environment Agency and periodic inspections are required to ensure that all site activities comply with permit conditions. Due to the potentially harmful effects associated with methane and carbon dioxide emissions and leachate land contamination, the monitoring of a landfill is an activity which is inherent in all phases of the site life cycle, from the initial appraisal to the operational and post-closure phases (UK Legislation, 2000).

In the UK, the broad current policy on landfills is to optimise their design promoting operational practices that will reach the site stabilisation within one generation. This would achieve the overall objectives of environmental protection and beneficial after-use compatible with the aims of sustainable development. Nonetheless, even if modern landfills are highly-engineered risk-assessed facilities, there is considerable uncertainty regarding their long-term efficacy and post-closure monitoring requirements until the permit surrender can be accepted by the regulator (Environment Agency, 1996). Insufficient monitoring points, poor sampling methods, inappropriately positioned monitoring facilities, insensitive analytical methods and monitoring timescales, all increase the likelihood of inadequate site characterisation and management.

Significant costs are associated with these waste disposal and landfill management practices and therefore the business aspects of waste management are not to be underestimated. In the USA, for instance, the private waste management industry (primarily involved in the collection, transfer and landfill disposal of non-hazardous solid waste) includes over 10,000 companies with combined annual revenue of \$50 billion. Three national companies, Waste Management, Allied Waste, and Republic Services together handle more than half the solid waste generated in the USA. Beyond the top three companies, the industry is highly fragmented. A moderate-sized company has \$10 million in annual revenue (First Research, 2005).

Exporting and importing waste at a regional, national or international level is also an integral part of waste management solutions needed to overcome unmanageable quantities and increase the profitability of available disposal resources. Linked to these financial aspects is the problem of illegal dumping. For instance, a recent paper by the Northern Ireland Audit Office (2005) reports that the Environment and Heritage Service (an Agency within the Department of the Environment) has undertaken 31 successful prosecutions related to the illegal carrying and dumping of waste and an additional 150 are still pending. If this is the current state of affairs in countries with established environmental policies, the situation in states with developing economies is much more critical. Recent surveys (Smith Korfmacher, 1997; Ogawa, 1996; Yhdego, 1995; Nair, 1993) and a World Bank study (Johannessen and Boyer, 1999) provide evidence that in low- and middle-income countries the open dump approach remains the predominant waste disposal option, especially as there is often limited legislation, regulation and guidance. Future establishment of uncontrolled and illegal landfilling activities of both hazardous (e.g. clinical and chemical wastes) and non-hazardous wastes is therefore an urgent problem.

1.1.3 Landfill Design

The controlled disposal of waste into land is no longer a simple practice. A municipal solid waste landfill is a sophisticated facility and its technology requires application of principles from disciplines such as hydrology, civil engineering, chemistry and material sciences. With the exception of certain cases for developing countries, landfills are no longer simple natural attenuation sites that allow leachate to percolate into ground water aquifers and do not control gas emissions. They have evolved into containment-type sites that have one or more low permeability liners at the base and are provided with engineered pipe systems to collect the harmful decomposition products. As shown in Figure 1-1, there exist three main configurations: the trench, canyon and at grade types.

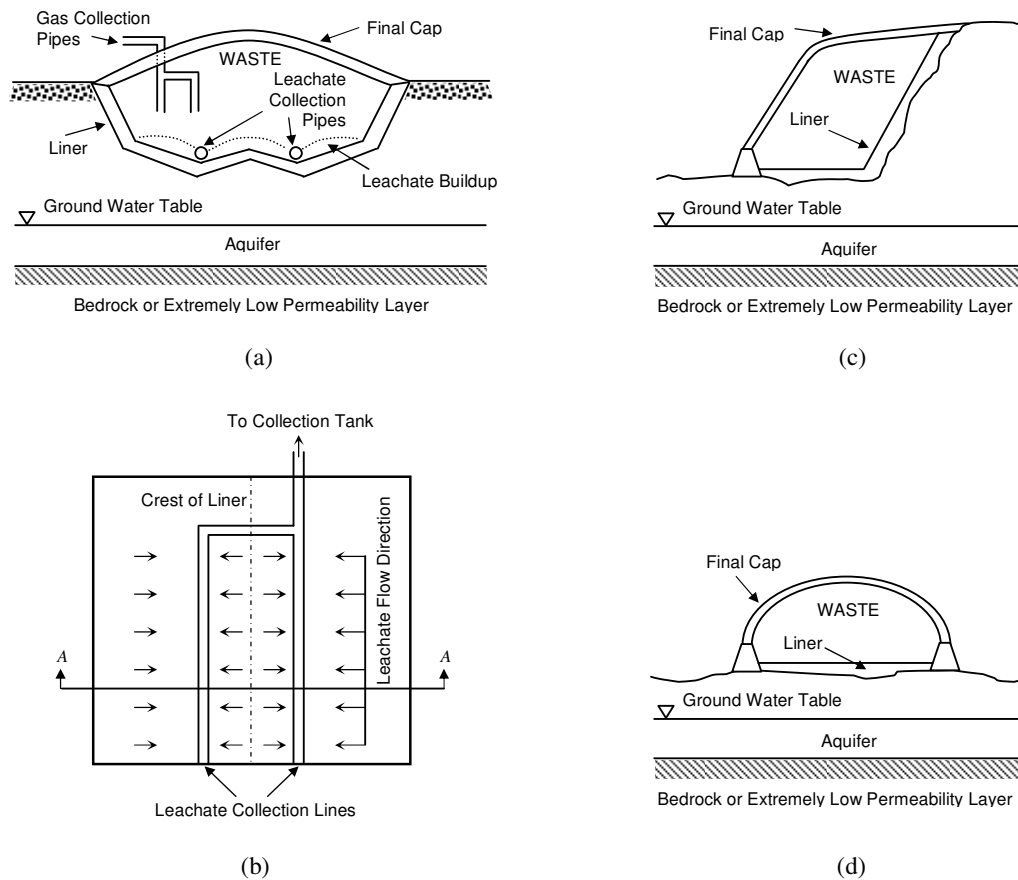


Figure 1-1. Engineered containment landfill configurations: (a) trench type, cross section A-A from (b); (b) trench type top view; (c) canyon type; (d) at grade, or landraising, type. (Modified by Bagchi, 2004).

Due to strict national and international regulations, it can take up to a few years and the investment of millions of pounds to prepare a landfill to accept waste. They are designed to take account of the geology of an area, the flow and direction of local watercourses, the level of the water table and the appearance of the existing physical environment. This ensures that all waste deposited in a landfill will be safely contained and that when it is restored, the landfill will blend naturally into the surrounding landscape (Bagchi, 2004). The planning permission granted for a landfill determines from the very beginning the total amount of waste which can be deposited, as well as the height of the landfill (final contours) and how the site will be restored. The way a landfill site will be developed and managed is laid out in a public document known in the UK as a Working Plan which is produced by the developer and, in England and Wales, held by the Environment Agency (Baldock, 2005).

1.1.3.1 Landfill Operations

Essentially, a landfill is operated in a series of steps, each involving the filling of a cell, while the next is prepared to receive waste. The part in an open cell where waste is deposited is called the tipping area. After being accumulated, waste is spread out and compressed into layers. At the end of each day the top layer is covered with soil. This daily cover prevents odours, avoids both rubbish being blown away and the presence of birds and vermin, and improves the site's visual appearance. It is also advocated as a means of shedding surface water during the filling sequence, thereby assisting in leachate management. This temporary clay cover is then removed in the morning when work starts again. When the cell reaches its capacity, it is capped with engineered soil and possibly restored with vegetation. The particular method employed by the site operator to discharge and emplace waste depends on different factors. The most important ones are the physical condition of waste, weather conditions at the time of emplacement, special requirements to avoid hazards inherent in the waste and the overall site design objectives.

Once the biodegradable waste, such as paper, card and waste food, is disposed of in the anaerobic conditions of a landfill, breakdown by bacteria produces gas and soluble chemicals. The soluble chemicals combine with liquids in the waste (e.g. rainwater) to form landfill leachate. Landfill gas consists of 50-60% methane and 35-40% carbon dioxide. It also contains trace levels of other gases such as hydrogen sulphide and organic substances. Landfill gas poses a threat to the local environment and site workers (Gregory et al. 2000): it can cause fires, explosions and asphyxiations if allowed to migrate and escape in the surroundings. The gas can also kill vegetation on restored landfills by displacing air from around plant roots. In addition to these local impacts, landfills are now recognised as the UK's biggest human-made source of environmentally harmful methane releases to the atmosphere (Environment Agency, 1999). For these reasons, landfill gas control is mandatory at all sites taking waste that will lead to gas production. The properties of landfill gas and the routes and

mechanisms by which it migrates from a landfill are now sufficiently understood to be controlled through the use of combinations of physical barriers and gas abstraction systems (Parsons, 2000; Moody et al., 1992; Moody et al., 1991). Gas collection systems may also burn the gas and use it as a fuel. Using landfill gas in this way is consistent with the objectives of controlling emissions for environmental reasons, which remains the priority, and helps to displace fossil fuels.

Landfill leachate can be hazardous by virtue of the chemicals within it, including dissolved organic chemicals, ammonia and metals, which may contaminate land and water. Leachate is produced from liquid in the waste being compressed out, from rain falling on the site permeating the cap and running through the waste and also from water entering the site from sub-surface streams. One of the major means of control of leachate migration is the use of combinations of mineral (e.g. clay) and synthetic liners (e.g. High Density Polyethylene - HDPE), which create a seal against the escape of liquid (Parsons, 2000), and pump systems. Landfill liners can also collect leachate to ensure that it is treated before being discharged to sewer or surface water. If leachate does escape to the environment, then it is often difficult and expensive to rectify and can have effects that will remain for many tens and possibly hundreds of years. Recognition of this has resulted in more stringent requirements for the initial landfill site identification, design, construction and monitoring (Environment Agency, 1996). Leachate could also be re-circulated and moved from a wet volume of the landfill into a drier one. This would speed up the decomposition processes of the dry areas.

Operation of the site using small cells with rapid cover of the waste ensures that large areas are not open to rain and it also minimises the potential for litter, dust and smell to be carried away by rain or wind. The detailed description of the day-to-day waste disposal operations and control practices is not presented here as it is beyond the scope of this report. It is documented in many books, such as DoE (1997). Some of the control procedures become even more crucial when new strategies, such as those to accelerate degradation processes (i.e. aerobic landfilling) are utilised. The waste industry is also facing a growing need to implement and standardise electronic databases to facilitate and enhance the monitoring and inspection procedures (Beaven, 2001).

1.1.3.2 Post Closure Management

Upon completion of the filling phase of a landfill, the land must be restored in accordance with the requirements of the local planning authority and in a way that controls environmental emissions. Traditionally a clay cap with soil and vegetation is used to cover the landfill, although an additional membrane liner is increasingly included. Site licence conditions, as issued by the Environment Agency, may require that the site contours agree with specified levels, that the restored land is put to an agreed use (e.g. cereal farming, pasture, civic open space, golf course, forestry), and that landfill leachate and gas are managed until such time as they no longer constitute an

environmental risk. The analysis of groundwater and surface run-off water is required and gas emission levels have to be monitored as well.

With time, waste tends to settle and the topographic characteristics of the site may change significantly. The amount of settlement of landfills will depend firstly on the waste constituents, and secondly on how waste was deposited. For instance, traditional loose tipping of material will result in much higher settlements than modern highly compacted or baled waste landfills. Bagchi (2004) reports that total settlements of 10 to 40% of the overall depth may occur, including compression under the self weight during placement. Settlement rates vary according to waste depth and type, density (influenced by compaction), moisture content, presence/absence of landfill gas extraction and leachate recirculation. Typically, operators plan for a 20% settlement (Smith, 2006).

As a result of settlement, cracks in the final cap may appear and the surface may become unstable or even collapse, potentially causing environmental damage. At the same time though, the void that is generated by the settling allows the operator to strip off the final cap and re-fill the volume with additional waste. This is why surveys are usually carried out to monitor the settlement. These void take-up (VTU) surveys are accomplished using accurate differential Global Positioning System (GPS) measurements by a surveyor. Nonetheless, due to the lack of resources and the high costs they are often performed only on a yearly basis. This post-closure management period may extend for tens of years and now requires landfill operators to make financial provision against the potential costs incurred. The costs associated with site closure and aftercare have increased considerably in recent years and are one of the factors that have led to increased charges for landfill disposal.

1.1.4 Research Aim

The foundation of this research builds on the background of this introductory overview, understanding that data from the broad array of satellite platforms could provide key support to a number of landfill management and monitoring practices. This could potentially reduce operational costs and hazards, and meet the challenges of the future waste management agenda. It is therefore possible to state the overall aim of the research:

The research aim is to make an innovative contribution to the analysis of space-borne remote sensing data for solid waste landfill monitoring.

The potential user community is acknowledged to be heterogeneous across several dimensions, leading to a variety of classification methods. Users for solid waste landfill management issues can be segmented according to criteria on:

- geography by country/region (European, developing country, etc.) or by scale (global, national, local),

- organisation type (industry, science, government, non-governmental organisation etc.),
- working practice,
- familiarity with EO technology,
- policy objectives and
- motivation (profit, efficiency, new applications, research, public image etc.).

Based on the motivation criteria, seven different parties have been identified. It is important to appreciate that they are closely interlinked, often with overlapping programmes and objectives:

- waste industry managers,
- landfill regulators,
- landfill operators,
- independent environment protection agencies,
- research institutions,
- property land owners and real estate companies and
- private individuals.

Their interest may vary from the broad site detection to the more specific on-site monitoring of operations and conditions. They have diverse characteristics across several dimensions, leading to a variety of needs, both technical and managerial. These should be extensively addressed when formulating and implementing a sustainable operational use of EO data.

1.1.5 Literature Review on Remote Sensing for Landfill Monitoring

The first study on the application of remote sensing for waste management was published by Garofalo in 1974. His analysis discusses the utilisation of aerial photographs to support estimation techniques of solid waste distribution and production. The methodology is based on the visual interpretation of land use (i.e. low and high residential areas, commercial and industrial areas, agricultural fields and open public areas) and the incorporation of these data into solid waste production models. This preliminary study also suggests that small-scale aerial remote sensing records could support the location selection of new waste disposal sites, the implementation of new waste collection and transportation systems, and a preliminary assessment of potential environmental impacts.

Due to increasing concerns for the environment in the late 1970s and the full awareness of the harmful effects caused by both hazardous and municipal landfills, most of the research that followed focused primarily only on landfill detection and the monitoring of gas and leachate migration, without exploring or further developing any of the additional applications proposed by Garofalo. The only exception is a general review published by Breton and Chorowicz (1996).

At the simplest level, a number of studies (Irvine et al., 1997; Warner, 1994; Rugge and Ahlert, 1992; Marsh et al., 1991; Lyon, 1987; Stohr et al., 1987; Evans and Mata, 1984; Titus, 1984; Lyon, 1982; Erb et al., 1981) demonstrates the significant value of visual interpretation techniques of airborne data (e.g. historical black and white, colour and infrared photographs and photogrammetry data) to identify land cover changes on and around the sites and describe the structure of the sites themselves. The principal aim of these projects is to carry out a basic environmental examination by studying the soil textural and hydrological characteristics, and using this information as a guide for subsequent remediation efforts. Visual interpretation is also used by Philipson et al. (1988) to test the suitability of satellite images (i.e. panchromatic and multispectral SPOT images acquired in 1986) for regional scale monitoring of land cover changes. The main aspect emphasized by Philipson et al. is the interpretation ambiguity between landfills and areas undergoing some type of development, or simply derelict areas. This level of uncertainty intrinsic in a visual interpretation approach has been tackled by Brivio et al. (1993) by investigating aspects of spatial autocorrelation of data acquired from the National Aeronautics and Space Administration (NASA) Landsat Thematic Mapper (TM) instrument.

On the next level of examination, other studies investigate spectral characteristics and band mathematical procedures using air and space-borne multispectral data. Again, the main aims are to detect landfills based on their spectral signatures (Stohr et al., 1994; Johnson, 1993) and to observe signs of gas emissions or leachate release by detecting vegetation stress on closed reclaimed sites (Hopper, 1996; Jones and Elgy, 1994; Vincent, 1994; Brivio et al., 1991; Jones, 1991). Jones and Elgy (1994) conclude that the relationship between landfill gas dynamics, plant health and soil characteristics is extremely difficult to establish and demonstrate, and that poor vegetation growth also strongly depends on soil reinstatement during site restoration, waste settlement and waterlogging in certain areas. They further stress that remote sensing is not envisaged in this respect as a substitute for in situ borehole sampling methods. Rather, the approach to adopt is to integrate both techniques to optimise their individual advantages. More recent studies by Jago and Curran (1997), Folkard and Cummins (1998) and Jensen (2005) demonstrate that the use of airborne hyperspectral data can improve the contaminant-monitoring capabilities of remote sensing over that provided by multispectral data.

With regards to direct gas detection, and without taking into consideration the available ground based sensors described by Bryce et al. (2003), airborne sensors have the technological edge over proposed satellite systems. As Long (1999) explains, the shorter atmospheric columns that airborne sensors have to see through allows them to experience less deleterious effects on the detector performance. Due to the better spectral resolution and signal-to-noise ratio, it is argued that methane remote detection technology designed for airborne platforms will always provide better quality information than satellite systems.

Another critical argument presented in many of the above publications is that the 30 m ground resolution of many satellite images is insufficient for studying the often small scale variations in contamination that may occur in a landfill site. Indeed, recent work based on space-borne data (Kwarteng and Al-Enezi, 2004; Perakis et al., 2004; Dewidar, 2002) has only highlighted that the clear advantage of satellite remote sensing is its capability of providing a synoptic and holistic view of vast areas for change detection at relatively low costs.

The review of these studies shows that depending on the sensor parameters (i.e. spectral, spatial and temporal resolution) EO images can be successfully used for a variety of applications related to waste management. It also highlights three other key points. Firstly, as regards to leachate and gas monitoring, space-borne remote sensing has not proved to be a valid tool for an accurate quantitative analysis. However, it can support ground remediation efforts based on the expertise of the visual interpreter and the knowledge of the landfill operator. Secondly, the additional research that focuses on landfill detection by investigating both the images' spatial and spectral dimensions shows some ambiguity in the results. Thirdly, none of the studies explores the potentials of SAR remote sensing and SAR interferometric (InSAR) processing (e.g. coherence analysis, digital elevation model formation, subsidence studies) to achieve a more robust detection algorithm and extract additional information and knowledge for landfill management and monitoring.

1.2 Problem Formulation and Research Objectives

The previous literature review has established the achievements and limitations of optical remote sensing for landfill monitoring and has highlighted the fact that SAR data have never been explored for such application. In addition, as explained in more details in the next chapter, a SAR system measures the physical structure and electrical properties of the ground targets and it is not affected by cloud cover. It is therefore of great interest to investigate the opportunities of SAR for landfill monitoring. The general problem statement addressed in this study is:

How can the qualitative and quantitative interpretation and analysis of SAR data contribute to the monitoring of solid waste landfills?

As such, this research presents a high degree of novelty as it uses SAR data for a completely new application. The research investigates what SAR data can offer towards landfill site monitoring and does not intend to compare optical and SAR data. In order to identify specific research objectives, it is vital to appreciate that the various entities with an interest in landfill monitoring are very heterogeneous, ranging from operators and regulators to environment protection agencies and private individuals.

Subsequently, they have different needs and concerns. With respect to the aim of this research, this factor translates into different parameters to be observed and information to be derived from SAR data. As a result, two specific research objectives are derived that give further direction to this study:

1. *The first objective is to assess whether SAR data can support the identification of landfill sites by distinguishing them from other disturbed areas that present similar optical spectral signatures.*
2. *The second objective is to assess the possibility of monitoring on-site operational procedures with SAR data.*

In this context, the research methodically addresses the variables related to SAR systems (e.g. wavelength, polarisation, incidence angle, temporal and ground resolution) and it explores different analysis techniques in both the space and time dimensions. Overall, the research presents novel aspects in both the specific application under investigation and some analysis procedures. A brief introduction of the analysis methodology used in the research is presented in the following section. A more thorough explanation of the data acquisition and processing is instead provided in Chapter 4.

1.3 Overall Research Methodology

The block diagram in Figure 1-2 shows the overall high-level research methodology starting with the problem formulation and objectives definition previously presented. The subsequent phase is to define and obtain the necessary space-borne datasets. These are obtained by various sources and with the financial support of the Royal Aeronautical Society Centennial Scholarship awarded to the author and the Remote Sensing and Photogrammetry Society.

In parallel, preliminary ground observations are carried out in order to appreciate those spatial, temporal and biophysical characteristics of a landfill that can influence SAR data. They examine general features and characteristics that can subsequently support the data analysis.

The data analysis and discussion phase then follows. In terms of methodology, different approaches are used to address the two main research questions listed above. The first objective is tackled by means of a spatial analysis of SAR backscatter amplitude data and by qualitatively investigating the temporal decorrelation of the interferometric coherence magnitude. The significance of the digital elevation models derived from the InSAR processing is also assessed.

With regards to the second objective, the analysis of the backscatter signal is instead used to correlate SAR images with on-site conditions and operational procedures. Empirical acquisitions with a ground based SAR (GB-SAR) system and simulations based on the RT2 radiative transfer model software are used support the analysis of the radar wave interaction with different surfaces common to waste disposal sites. Subsequently, the fusion of SAR data is then applied to develop a novel land-use classification algorithm.

The fourth phase is the overall discussion of the results. The research provides an appreciation of the applicability of such techniques in an operational context and of the possibility to extrapolate the developed SAR data analysis methodologies beyond the UK. Concluding remarks also cover issues related to the needs of the potential end-users related to the operational application of such remote sensing products.

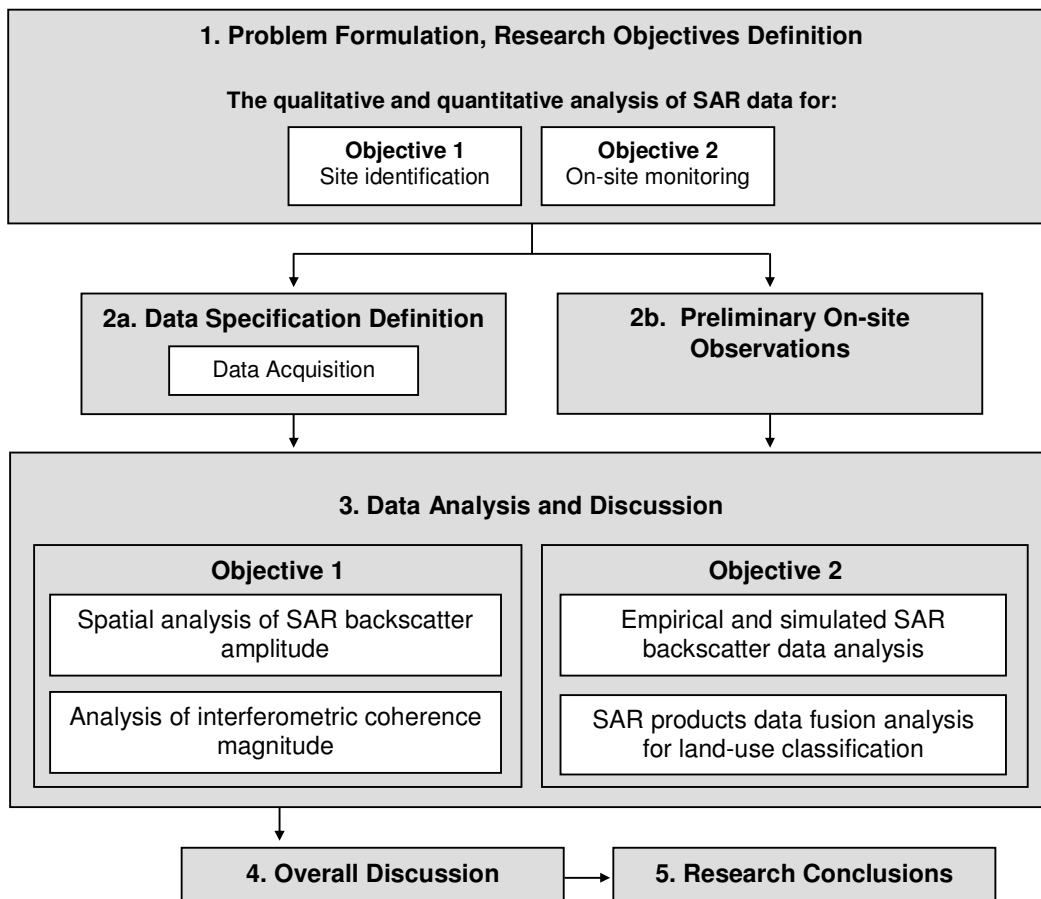


Figure 1-2. Overall research procedure.

1.4 Report Outline

Chapter 1, *Introduction*, outlines the background of the research and provides the reader with an overview on landfill design and operations. It presents a literature review on applications of remote sensing for waste management leading to the rationale of the research. This is followed by the definition of the research objectives. The chapter then clarifies the overall research procedure.

Chapter 2, *Literature Review*, is mainly dedicated to space-borne SAR remote sensing. It first presents the imaging principles and then focuses on the backscatter signal properties and interferometry processing techniques. The chapter also presents introductory concepts on optical remote sensing and data fusion techniques.

Following the overall methodology, Chapter 3, *Preliminary Observations and Data Acquisition*, describes the preliminary ground observations carried out in order to appreciate the spatial, temporal and biophysical characteristics of a landfill that can influence SAR data. The results of these observations have supported the selection of the analysis techniques and are used in the discussion presented in the following chapters.

Chapter 4, presents the *Data Acquisition and Analysis Techniques* used in the research. The study explores a variety of approaches and uses several data acquisition and processing methods. Although they be related to different subject matters, these procedures are described in this single chapter to allow the reader to appreciate aspects of the overall research methodology presented in Section 1.3. This also avoids the next chapters including detailed methodological explanations that would otherwise disrupt the presentation and discussion of results.

The rest of the thesis is structured around the two objectives of the research. Chapter 5, *Landfill Site Identification*, systematically presents the SAR data analysis methodologies used for the specific goal of distinguishing landfill sites from areas that present a similar signature in multispectral optical data. The chapter initially presents a brief analysis of optical data to corroborate what is presented in Section 1.1.5. It then tackles the research objective by investigating the spatial characteristics of SAR backscatter amplitude data of landfills and disturbed areas (Section 5.2) and by observing their temporal variability (Section 5.3). The analysis discusses the obtained results and draws conclusions on potentials and limitations of the applied techniques.

Chapter 6, *On-site Conditions Monitoring*, explores other processing techniques to assess the possibility of correlating SAR data with on-site conditions and operational procedures. Apart from the general survey maps, no exact ground reference information relative to the historical SAR data is available to relate SAR backscatter values with on-site conditions. Additional measurements are therefore required in order to obtain the

SAR backscatter coefficient values for areas common to waste disposal sites and whose surface characteristics are investigated in Section 3.1.3. These data are obtained with the use of a ground based SAR (GB-SAR) system. Simulations based on the RT2 backscatter model are subsequently used to carry out a sensitivity analysis on the variables affecting the radar backscatter. The objective of this analysis is not to provide a detailed discussion of the modelling of the interaction of the radar signal with bare soils, but to more quantitatively assess the parameters which have an effect on it.

Following this analysis, historical ERS SAR scenes are used to develop a novel classification methodology to identify different land-use areas on the Brogborough landfill. This method is based on a Fuzzy Logic classifier and on featured-based pixel-by-pixel classification procedures. The discussion of the results also identifies limitations of this methodology.

These two main analysis chapters are followed by the *Overall Discussion*, Chapter 7. This investigates the applicability of the developed techniques in an operational context. The discussion focuses on three different aspects: the impact of the main SAR system parameters, the extrapolation potential in other regions of the UK and beyond the UK and finally the end-user needs.

Chapter 8, *Conclusions and Further Work*, summarises the key points of the data analysis and discussion and presents areas of further development of the research.

2. Literature Review

Having introduced the research background and defined its objectives, this chapter presents a literature review on the different subject matters related to the research. As such, it is mainly dedicated to space-borne SAR remote sensing. Section 2.1 presents the SAR imaging principles and then focuses on the backscatter signal properties, interferometry processing techniques and the analysis of the complex degree of coherence. Section 2.2 briefly presents concepts of optical and infrared remote sensing. This is followed by a short introduction, Section 2.3, on data fusion techniques. These are all key topics for the understanding of the research, however a reader who already has a strong background in any of the areas might want to skip relative sections accordingly.

It is important to clarify that specialist reviews of literature on topics related to data acquisition and analysis procedures are considered in other sections of the following chapters.

2.1 Introduction to SAR Principles

The purpose of this section is to briefly present fundamentals of SAR related to both image formation and processing techniques. They determine the principles needed to accurately interpret radar imagery.

2.1.1 SAR Geometry and Image Formation

Radar is an acronym for RAdio Detection And Ranging. As mentioned in the introductory chapter, a radar imaging system generates its own source of illumination. A radar antenna emits a series of electromagnetic pulses in the microwave portion of the spectrum and it subsequently records the energy scattered back by any physical object illuminated and the time it takes for the pulse to return to it. Being an active system, radar images can be acquired day and night, independently of solar illumination. Additionally, as the radio waves remain nearly unaffected by clouds, a radar system has an all-weather imaging capability. The three main electromagnetic bands used for SAR systems are the L band (i.e. frequency: 1 - 2 GHz; wavelength: 30 - 15 cm), the C band (i.e. frequency: 4 - 8 GHz; wavelength: 7.5 - 3.75 cm), and X band (i.e. frequency: 8 - 12 GHz; wavelength: 3.75 - 2.50 cm). Examples are the Japanese Advanced Land Observing Satellite (ALOS) with its Phased Array type L-band Synthetic Aperture Radar (PALSAR) instrument (Jaxa, 2004), the European Space Agency (ESA) Environmental Satellite (Envisat) (ESA, 2006b) and the Canadian Radarsat platforms (CSA, 2007) with C band sensors and the German TerraSAR-X satellite that carries a high frequency X-band SAR instrument (Infoterra GmbH, 2006).

The radar transmits a coherent signal with a definite phase against which the phase of the received signal is detected. Space-borne platforms are mostly monostatic ones, meaning that there is only one antenna that transmits and receives the signal. Coherent monostatic radars therefore detect the backscattered component of the radiation (i.e. both the magnitude and phase of the signal). SAR systems use the phase and magnitude information to overcome the azimuth ground resolution limitation of real aperture radars (RAR) by using sophisticated signal-processing and creating the synthetic aperture. Introductory references are provided in Section 2.1.1.2. As illustrated in Figure 2-1, the direction of the emitted radiation is side-looking with respect to the satellite's direction of travel, also known as along-track or azimuth. The antenna is looking at an incidence angle θ , and repeatedly radiates radio pulses of duration τ_p at a rate defined by the Pulse Repetition Frequency (PRF). The antenna is of length L and height D and mounted on a platform at an altitude H_{sat} .

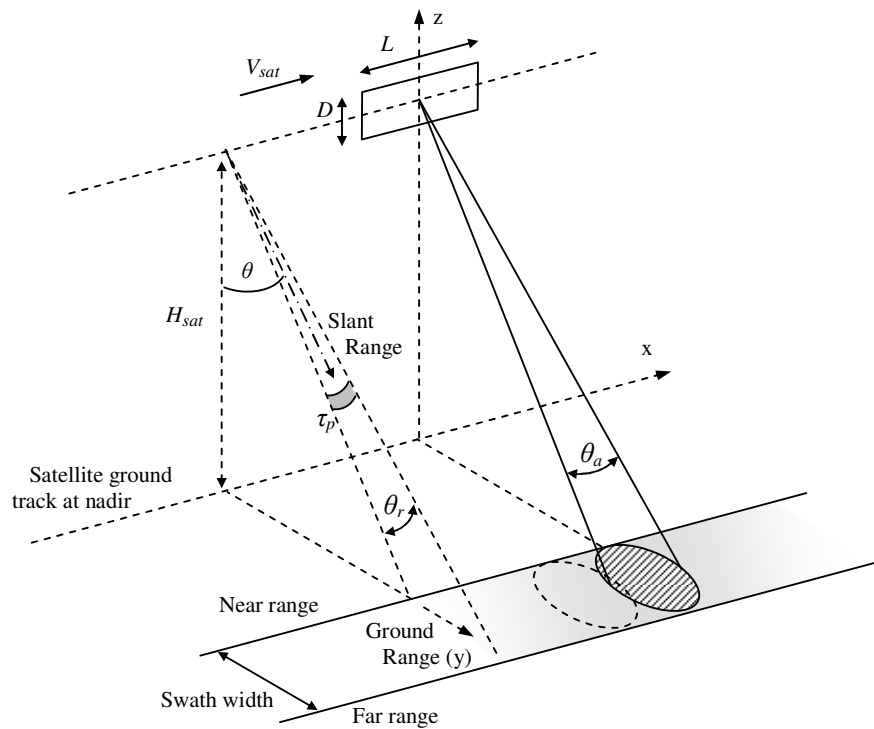


Figure 2-1. SAR geometry and system parameters.

2.1.1.1 Resolution in Range

In all radar systems, range resolution is directly related to the pulse duration and is independent of the satellite height. The range resolution, R_r , is defined as the minimum range separation of two points that can be distinguished as separate by the system. If the arrival time of the leading edge of the pulse echo from the more distant point follows the arrival time of the trailing edge of the echo from the nearer point, each point can be distinguished in the time history of the radar echo (Curlander and McDonough, 1991). Therefore, the minimum separation of two resolvable points is:

$$R_r = \frac{c \tau_p}{2 \sin \theta} \quad \text{Equation 2-1 (Rees, 2003)}$$

where c is the speed of light. A shorter pulse therefore results in a higher resolution in range direction. However, to achieve a satisfactory signal-to-noise ratio, the pulse length is limited by high output power requirements and the fact that an antenna can only emit a finite amount of energy in a certain time span. This backdrop is overcome by the introduction of the chirp compression technique (Soumekh, 1999), which linearly modulates the frequency of the pulse to increase the bandwidth of the signal. With appropriate processing of the received pulse, matched filtering (Soumekh, 1999), the ground range resolution obtainable is:

$$r_r = \frac{c}{2B_R \sin \theta} \quad \text{Equation 2-2 (Curlander and McDonough, 1999)}$$

where B_R is the frequency bandwidth of the transmitted pulse. For a radar system such as the European Remote Sensing (ERS) 1 and 2 satellites, with a pulse length of $37.1 \mu\text{s}$, a range bandwidth of 15.55 MHz , and at a mean incidence angle of 23° , the achieved ground range resolution is approximately 24.7 m . Equation 2-2 also explains why a variation in pixel resolution occurs as the distance across-track from the projection of the satellite orbit on the ground increases (i.e. because the incidence angle increases).

2.1.1.2 Resolution in Azimuth: the Synthetic Aperture

Resolution in azimuth for RAR systems is determined by the physical length of the antenna. The angular width of the emitted beam is normally set by the diffraction limit (Rees, 2003) and at half maximum (-3dB) it can be approximated by $\theta_a \approx \lambda / L$, which for ERS-1/2 equals to 0.287° . Neglecting the Earth's curvature, the distance from the antenna to the target, the slant range R_s , can also be defined in terms of the height H_{sat} and the incidence angle θ by:

$$R_s = \frac{H_{sat}}{\cos \theta} \quad \text{Equation 2-3 (Rees, 2003)}$$

The azimuth ground resolution r_a can be then approximated by $R_s \cdot \theta_a$. Hence:

$$r_a = R_s \theta_a = \frac{H_{sat}}{\cos \theta} \cdot \frac{\lambda}{L} \quad \text{Equation 2-4 (Rees, 2003)}$$

For the ERS-1/2 C-band instrument with a wavelength 5.66 cm, at an average distance of 850 km from its target and with an antenna length of 10 m, Equation 2-4 gives an azimuth ground resolution of a single transmitted pulse on the order of 5 km. This is clearly an unacceptable value and therefore space-borne systems use a “synthetic aperture” to obtain more reasonable results.

The SAR technique takes advantage of the Doppler history of the radar echoes generated by the motion of the spacecraft to synthesise a large antenna, enabling high azimuthal resolution in the resulting image despite a physically small antenna. As the satellite moves at velocity V_{sat} , a scatterer on the ground is illuminated by the antenna’s main lobe for a period Δt . During this time, the point target is hit by a vast number of pulses depending on the PRF, whose echoes are recorded (amplitude and phase). Due to the satellite relative velocity with respect to the ground target, the echoed pulses are affected by a systematic phase shift. By processing the return signals according to their phase shifts, it is then possible to reconstruct the signal that would have been collected from an antenna of length $V_{sat} \Delta t$. As derived by Hanssen (2001), the azimuth ground resolution is then:

$$r_a = \frac{L}{2} \quad \text{Equation 2-5 (Hanssen, 2001)}$$

The above result shows that the azimuth resolution does not depend on the wavelength or the distance to the target. The ERS satellite is therefore able to achieve a 5 m azimuth ground resolution. However, the resolution can not be increased by simply shortening the antenna length L , as with decreasing dimensions the sensitivity of the radar diminishes due to a low signal to noise ratio.

2.1.2 SAR Backscatter and Factors Affecting Reflectivity

The basic quantity measured by a single-frequency single-polarisation SAR system is a pair of voltages in the in-phase and quadrature channels which can be subsequently used to compute the amplitude and phase of the backscatter signal. Figure 2-2 shows an example of a SAR amplitude image. These measured values represent the effects of the target on the transmitted wave, and through an absolute radiometric calibration they can be translated into the geophysical properties of the scene. The calibration procedure also allows data from different SAR sensors to be compared.

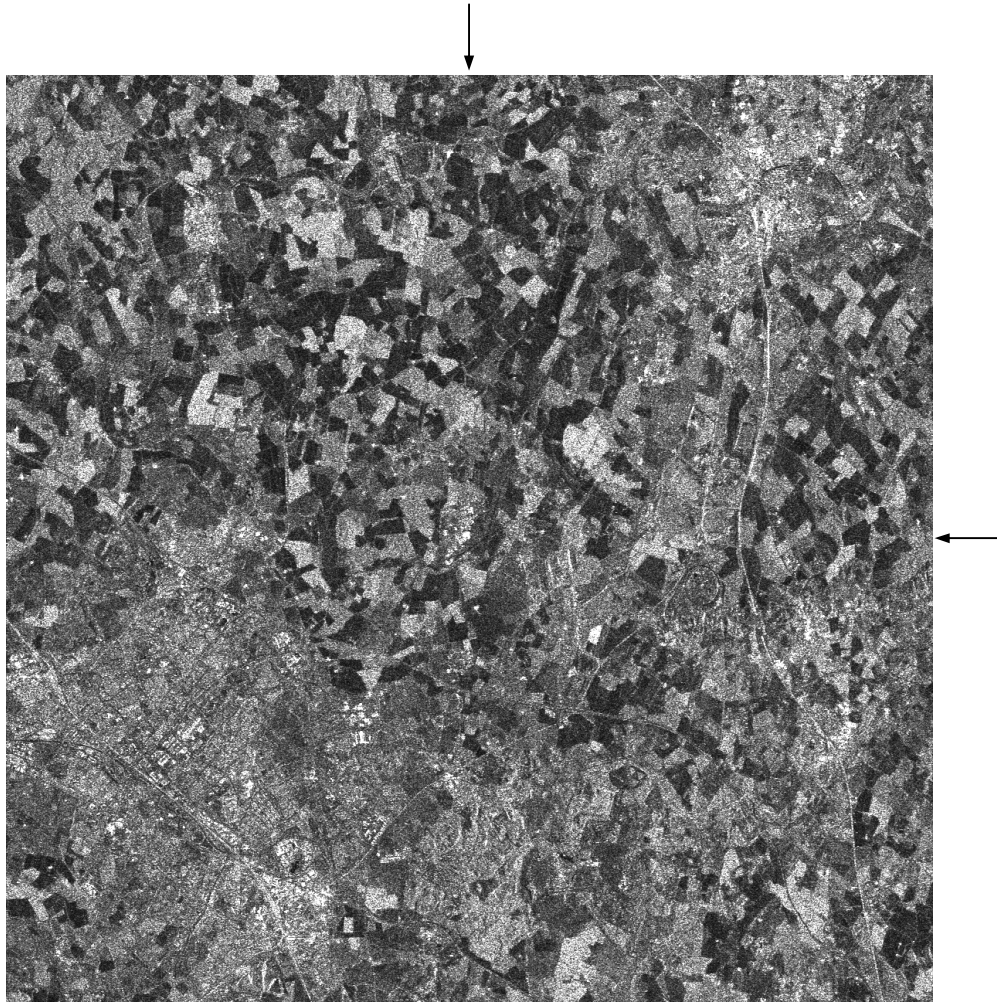


Figure 2-2. ESA ERS-1 SAR backscattered amplitude values. The scene was acquired on 25th June 1995 (descending orbit: 20623; track: 94; frame: 2547). The SAR look angle is from right to left. The image shows a 30 by 30 km area centred on Cranfield University. It is possible to identify the University runways as three crossing dark lines. These are also pointed out by the external arrows. The cities of Milton Keynes and Bedford are identifiable by the brighter backscatter return. They are located respectively in the bottom left and the top right of the image. The original scene has been flipped horizontally and spatially averaged by 5 pixels in the azimuth direction to eliminate the ground resolution distortion.

As systematically explained by Ulaby et al. (1982) and Skolnik (2001), the power P_r received back at a monostatic antenna can be written as:

$$P_r = \frac{P_t S^2 \sigma}{4\pi\lambda^2 R^4} \quad \text{Equation 2-6 (Ulaby et al., 1982)}$$

where P_t is the total power transmitted by an antenna of effective area S , at a wavelength λ , R is the distance from the scatterer and the monostatic radar, and σ is the backscattering cross-section parameter that combines the effective area of the scatterer and its absorbing and directivity characteristics. The backscattering cross-section is therefore a function of the direction of the incidence wave as well as of the scatterer shape and dielectric properties. As such, it can provide a link between observations and measurable quantities on the ground.

The monostatic radar Equation 2-6 is a general equation for both point and distributed targets. The basic scattering model for a distributed target is based on the assumption that the observed area consists of many discrete scatterers and that in each resolution cell no single one dominates. As the wave interacts with the target, each scatterer contributes a backscattered wave with a phase and amplitude change. It is therefore possible to define the differential backscattering coefficient as the average value of the scattering cross-section per unit area:

$$\sigma^0 = E \left\{ \frac{\sigma_i}{\Delta S_i} \right\} \quad \text{Equation 2-7 (Ulaby et al., 1982)}$$

where $E\{ \}$ is the statistical expectation operator and ΔS_i represents an area on the ground containing enough scattering centres over which the parameters of Equation 2-6 (i.e. P_t , R) remain nearly constant. Generally, in remote sensing applications the differential backscattering coefficient, σ^0 , is shortened to backscattering coefficient and it is expressed in Decibels (dB) which is given by:

$$\sigma_{dB}^0 = 10 \log \sigma^0 \quad \text{Equation 2-8 (Elachi, 1988)}$$

There are a number of different variables that affect the target reflectivity. The main ones are the incidence angle, the terrain topography, the surface roughness and the dielectric constant of the target. Additionally, the frequency of the incidence wave also plays a major role as it is a key factor in the penetration depth and other scattering mechanisms (Elachi, 1988).

The radar backscatter is strongly dependent on the incidence angle of the incoming wave. Consequently, the topographic characteristics of the terrain are also of foremost importance. In general, the backscatter from a target area can be described as the superposition of the facet model and the Bragg (or point scatterers) model (Ulaby et al., 1982; Elachi, 1988). The first predominates at near vertical incidence and the second at larger angles of incidence. Generally, surfaces perpendicular to the transmitted radiation appear brighter than surfaces parallel to it. As illustrated in Figure 2-3, topography causes effects such as foreshortening, layover and shadows. Foreshortening results in a compression of the slopes nearly normal to the emitted signal. In the case of features on the ground with a very steep slope, the signal emitted by the satellite may first reach the top of the feature and later the bottom of it. This effect is called layover and in the

resulting radar image, it causes the vertical feature to appear as if it was leaning toward the nadir. Shadowing is the phenomenon in which one part of the surface is hidden from the radar's view by another. Shadows increase proportionally with increasing look angles.

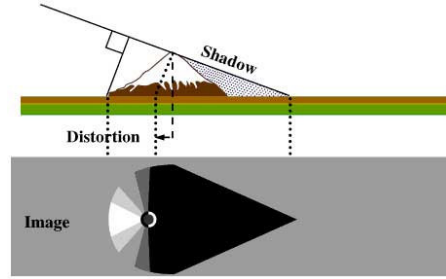


Figure 2-3. SAR signal effects and distortion due to topographic heights (ESA, 2005).

The backscattered signal is also affected by the ground surface roughness. The most important parameters are the standard deviation of the surface height variation, s , and the surface autocorrelation length (AC), l . This latter value is defined as the value of the displacement for which the normalised AC is equal to $1/e$ (i.e. 0.3679). For the discrete case, the normalised AC for a spatial displacement $x' = (j-1)\Delta x$, where j is an integer ≥ 1 , is defined as:

$$\rho(x') = \frac{\sum_{i=1}^{N+1-j} z_i z_{j+i-1}}{\sum_{i=1}^N z_i^2} \quad \text{Equation 2-9 (Ulaby et al., 1982)}$$

where z corresponds to the height values. The longer the radar wavelength and the lower the ground surface roughness, the weaker the backscattered signal. Additionally, as the surface becomes rougher, the backscattered signal approaches polarisation independence. Ulaby et al. (1982) also present the Fraunhofer criterion for smoothness (i.e. $s < \lambda / (32 * \cos \theta)$) for a surface to be considered smooth in backscattering models.

Volume scattering and the electrical properties of the scatterers also have an effect on the backscattered signal. For instance, the vegetation causes the propagating wave to lose part of its energy by scattering in all directions (Elachi, 1988). Also, moisture in either soil or vegetation results in significantly greater reflectivity (Elachi, 1988). Linked to soil moisture is the soil texture. As explained in more detail in Section 4.7, this term designates the size of mineral particles in a soil, without considering any organic matter. Particles are grouped according to their size into what are called soil separates (clay, silt, and sand).

2.1.3 SAR Image Structure and Speckle

Together with other numerous texts, the references presented throughout the previous two Sections comprehensively describe empirical and theoretical models in which the properties of the scattering medium and the incoming wave are specified and used to predict the scattered electromagnetic field. These models may also be used, in the opposite situation, to infer the properties of an unknown scene from the backscatter signal. Currently, full wave solutions are in most cases unavailable or achieved only by imposing considerable restrictions on the scattering medium. More recently, increasingly sophisticated solution techniques have been presented (Fung, 1994; Fung and Chen, 2004), but as explained by Oliver and Quegan (1998) there is still a considerable gap between the scattering medium as it is described in most models and the actuality of what is contained in the scattering cell. This is due to the fact that some parameters may be difficult to measure reliably and others might exhibit rapid spatial variation especially within a ground resolution area such as the one of Envisat and ERS (i.e. 5 by 25 m).

Oliver and Quegan (1998) clarify that even if current models provide us with a description of the physical processes of the wave-target interaction, they remain “semiquantitative explanatory tools” that identify the dominant scattering mechanisms and highlight failures in our representation of the scattering medium. Due to this reason, they explore another layer of information, which is that of the image structure. A primary difficulty in exploiting this approach is that all measurements or inferences from the data must take into account the coherent speckle characteristic of SAR images.

As explained in Section 2.1.2, each pixel can be viewed as containing a high number of discrete scatterers, each of them contributing to the overall backscatter signal of that pixel with a phase and amplitude change. The result is highly unpredictable and therefore SAR images appear with a characteristic type of granularity termed speckle. It is important to underline that speckle is a real electromagnetic measurement and not noise. Although the scattering component is unpredictable, it is a deterministic quantity. This means that if the phase measurement were to be repeated under exactly the same conditions, it would yield the same result. According to this model, the total backscatter signal A can be expressed as

$$A = |A| e^{i\phi} = \sum_{k=1}^N |A_k| e^{i\phi_k} \quad \text{Equation 2-10 (Oliver and Quegan, 1998)}$$

where $|A_k|$ and ϕ_k are respectively the individual amplitude and phase contributions from each scatterer in the ground resolution cell. This summation is therefore comparable to an interference phenomenon between the individual contributions. As Oliver and Quegan (1998) explain, the slant range resolution is typically many wavelengths across. Hence scatterers at different parts of the resolution cell will contribute very different phases to the return even if the scattering behaviour is

identical. As a result, the phase is uniformly distributed over $[-\pi, \pi]$ and independent from the amplitude. In each ground resolution cell, it can be assumed that there is a large number of individual scatterers and it is not physically possible to account for all their individual contributions. Therefore speckle must be modelled statistically. This leads to a data model of a SAR image in which the information content per pixel is very low within a distributed target. Therefore, averaging pixels improves the accuracy of the parameter estimates at the expense of spatial resolution. As a result, when the useful scale of variation of the target is larger than the SAR ground resolution, it becomes advantageous to pre-average the supplied data. This process is known as multilooking.

Analysis (Oliver and Quegan, 1998) shows that if the individual scatterers are considered to be uniformly spatially distributed in the ground resolution cell, the summation of equation Equation 2-10 is equivalent to a random walk in 2 dimensions. Hence, the real and imagery components follow a Gaussian distribution. The amplitude has a Rayleigh distribution and the corresponding intensity, defined as $I = |A|^2$, can be described by a negative exponential distribution. These distributions are of fundamental importance in the analysis of SAR data as they provide quantitative information about the targets. Also, it is important to notice they are completely characterised by a single parameter, the average intensity, which corresponds to the backscattering coefficient for distributed targets.

A detailed investigation of statistical properties of uniform and nonuniform targets and their textural properties is presented in Oliver and Quegan (1998). With regards to the phase, as it is uniformly distributed over $[-\pi, \pi]$, it carries no information if the data handling involves only one single image. However, phase becomes important when we turn to polarimetric and interferometric data.

2.1.4 Principles of Polarimetry

The polarisation of a plane wave describes, in a plane orthogonal to the direction of propagation, the shape drawn out by the tip of the electric field vector as a function of time. In a general case, this locus is an ellipse and the wave is called elliptical polarised. As explained by Ulaby and Elachi (1990), the polarization state of a plane wave can be described by its orientation Ψ , ellipticity Ω and a parameter S_0 that is proportional to the total intensity of the wave.

The orientation is defined as the angle of the ellipse semi-major axis measured counter-clockwise from the positive horizontal axis, while the ellipticity is defined as the arctan of the ratio between the semi-minor and semi-major axis. Writing the horizontal and vertical components of the electric field vector as E_h and E_v , the British physicist, Gabriel Stokes, described the polarization state of the wave by a 4-element vector known as the Stokes vector:

$$\begin{bmatrix} S_0 \\ Q \\ U \\ V \end{bmatrix} = \begin{bmatrix} |E_v|^2 + |E_h|^2 \\ |E_v|^2 - |E_h|^2 \\ 2 \operatorname{Re}\{E_v E_h^*\} \\ 2 \operatorname{Im}\{E_v E_h^*\} \end{bmatrix} = \begin{bmatrix} S_0 \\ S_0 \cos 2\Psi \cos 2\Omega \\ S_0 \sin 2\Psi \cos 2\Omega \\ S_0 \sin 2\Omega \end{bmatrix} \quad \text{Equation 2-11 (Ulaby and Elachi, 1990)}$$

where $|\cdot|$ is the absolute value and $*$ is the complex conjugate. In a completely polarized case, only 3 of the Stokes parameters are independent, because of the total power relation:

$$S_0^2 = Q^2 + U^2 + V^2 \quad \text{Equation 2-12 (Ulaby and Elachi, 1990)}$$

Most radar remote sensing applications deal with vertically and horizontally polarised waves, so that it is common to define four different backscattering coefficients σ_{VV} , σ_{HH} , σ_{HV} , σ_{VH} , where the first letter represents the polarisation of the transmitted wave and the second letter that of the returning wave. As the horizontal and vertical components form a complete basis set to describe the electromagnetic wave, the backscattering properties of the target can be completely described by a scattering matrix, S , called the Sinclair matrix:

$$\begin{bmatrix} E_h^s \\ E_v^s \end{bmatrix} = \begin{bmatrix} S_{hh} & S_{hv} \\ S_{vh} & S_{vv} \end{bmatrix} \begin{bmatrix} E_h^i \\ E_v^i \end{bmatrix} \quad \text{Equation 2-13 (Boerner et al., 1998)}$$

Equation 2-13 describes the transformation of the electric field of the incident wave to the electric field of the scattered wave. Polarisation is currently a subject of great interest with regards to land characterisation and classification. A great number of papers have been recently presented during the three ESA International Workshops on Science and Applications of SAR Polarimetry and Polarimetric Interferometry. Pottier (2005) gives an exhaustive overview on theoretical and application aspects. Touzi et al. (1992) present a number of parameters that have a useful physical interpretation. They can be computed for every pixel in a polarimetric radar image, but are often averaged over groups of samples to reduce the effect of SAR speckle. Averaging is performed in the “power domain”, because the energy is not preserved when averaging in the “voltage domain” (Touzi and Lopes, 1994; Lee et al., 1999). Advanced speckle filtering techniques are presented by Lee et al. (2003).

Two variables are used to portray the polarization signatures: the ellipticity and orientation angle of the incident wave. This gives rise to two signatures, the co-polarised and cross-polarised signatures. In the co-pol case, the polarization of the scattered wave is the same as the polarization of the incident wave, while in the cross-pol case, the polarization of the scattered wave is orthogonal to the polarization of the incident wave.

2.1.5 Repeat-pass Interferometry

A comprehensive description of InSAR processing is given by Hein (2004), Hanssen (2001), Armour et al. (1999) and Bamler and Hartl (1998). SAR interferometry exploits the phase measurements to infer differential range and range change in two or more SAR images of the same target area. From space there are two ways to achieve this. The first option is to have two SAR antennas orbiting at the same time. This can be achieved by having them on the same platform, as implemented in the Shuttle Radar Topography Mission (SRTM), or by having a satellite constellation as suggested by Massonnet (2001). The second option is to acquire the same scene with the same SAR antenna at two different times. This latter solution is mostly used with space-borne SAR systems and it is called repeat-pass interferometry. The first pass is usually called the master and the second pass the slave. For this interferometric technique to be applicable, data sets must be obtained when the scene is viewed from almost the same look angle for each of the passes. Figure 2-4 illustrates a simplified interferometric imaging geometry, showing the two passes with range vectors R_1 and R_2 to the target elements.

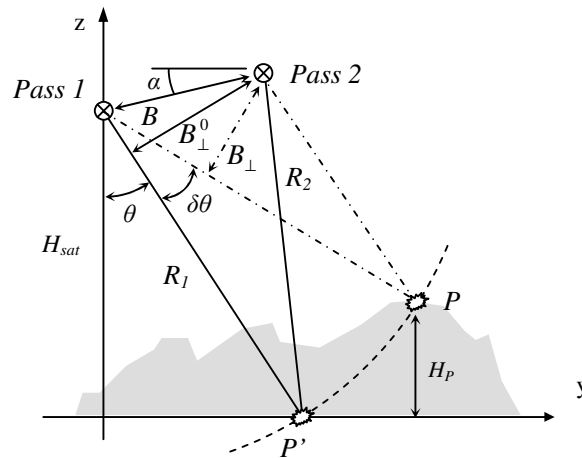


Figure 2-4. Geometry for SAR repeat-pass interferometry (Hanssen, 2001).

The look angle of the radar is θ , and the distance B between the satellites is called baseline. B_{\perp} is the baseline normal to the direction of the radar look angle, named perpendicular or effective baseline. After aligning (i.e. image coregistration) the two SAR images and resampling the pixels of the slave image on the master reference frame, complex multiplication yields the complex interferogram whose phase is proportional to the range difference to the point on the ground:

$$v = |A_1| |A_2| e^{j(\phi_1 - \phi_2)} = |A| e^{j\phi} \quad \text{Equation 2-14 (Hanssen, 2001)}$$

where $|A|$ and ϕ are respectively the magnitude and phase of each pixel. Assuming that the scattering characteristic are equal during both acquisitions, the difference between the phases in Equation 2-14 corresponds to the interferometric phase and can be written:

$$\phi = -\frac{4\pi \Delta R}{\lambda} - n \cdot 2\pi \quad \text{Equation 2-15 (Bamler, 2006)}$$

The negative sign originates from the Doppler notation. In Equation 2-15, the interferometric phase is evidently a relative computation and not an absolute one. Also, ΔR is much bigger than λ , leading to an ambiguity of many wavelength cycles. However, by knowing the variation of interferometric phase between adjacent pixels, using a recursive scheme it is possible to extract relative surface topography values.

Absolute topography values can be thought as the difference between the measured interferometric phase ϕ and the expected phase for the reference frame ϑ (e.g. a sphere or ellipsoid) derived from the orbit geometry:

$$\partial\phi = \phi - \vartheta \quad \text{Equation 2-16 (Hanssen, 2001)}$$

Applying the parallel-ray approximation to estimate the baseline B (Zebker and Goldstein, 1986), the relation between an interferometric phase change and the change in the look angle θ is found to be:

$$\partial\phi = -\frac{4\pi}{\lambda} B \cos(\theta^0 - \alpha) \partial\theta \quad \text{Equation 2-17 (Hanssen, 2001)}$$

where the initial value of θ^0 is obtained for the arbitrary reference surface.

The interferometric phase has inherently a 2π phase ambiguity, which must be removed through a process called phase unwrapping (Ghiglia and Pritt, 1998). After removing the flat-Earth effect that causes the high frequency phase variation (e.g Figure 2-5 (a) to (b)), the phase unwrapping procedure eliminated the remaining 2π fringes (e.g Figure 2-5 (b) to (c)), therefore obtaining a Digital Elevation Model (DEM) of the surface. The 2π height ambiguity (i.e. the height difference corresponding to a 2π phase shift) is derived as:

$$h_{2\pi} = \left| \frac{\lambda R_1 \sin \theta^0}{2B_{\perp}^0} \right| \quad \text{Equation 2-18 (Hanssen, 2001)}$$

Substituting values of $R_1 = 870$ km, a look angle $\theta = 23^\circ$ and the C-band wavelength of 5.6 cm in Equation 2-18, with a baseline of 50 m the computed height ambiguity is roughly 200 m. As the baseline increases the height ambiguity decreases, until at the critical baseline it is equal to the slant-range resolution and the view from the two satellites is not comparable anymore and consequently interferometry is not applicable (Zebker and Villasenor, 1992).

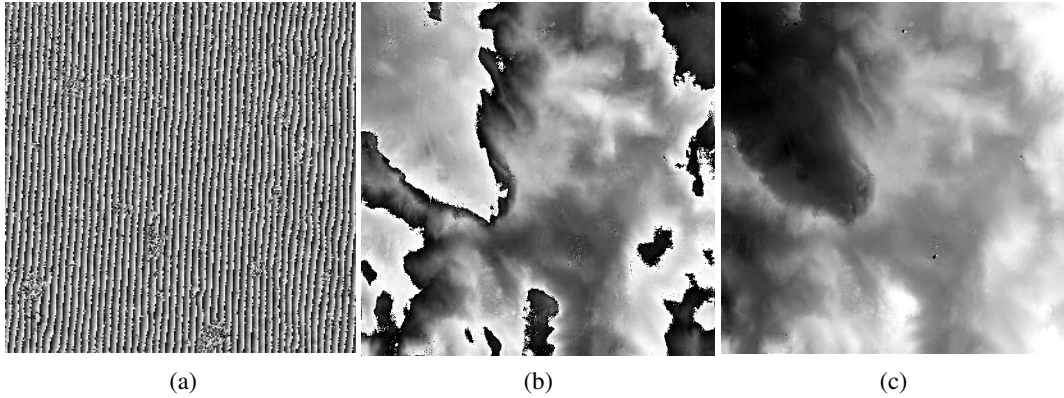


Figure 2-5. Example of flat-Earth removal ((a) to (b)) and phase unwrapping ((b) to (c)) steps to obtain the final relative height values (right).

Until now the scattering characteristic of the master and slave acquisitions have been assumed to be equal. In repeat-pass interferometry this is clearly not a realistic assumption as the two scenes are acquired in two separate instances. This time lag is known as temporal baseline. As a result, the phase of the interferogram, displayed as an image, contains fringes that directly measure the topographic height as well as possible surface deformation mechanisms, $\phi_{displacement}$, and atmospheric propagation delays, $\phi_{propagation}$. Furthermore, orbit errors introduced during the repeat-pass InSAR processing propagate directly into the computed interferometric phase, ϕ_{orbit} . Finally, changes in the target scattering conditions (e.g. target shape, orientation towards the incidence wave and dielectric properties) over the temporal baseline also affect the interferogram phase, $\phi_{scattering}$. Therefore, a repeat-pass interferogram contains the following terms:

$$\phi = \phi_{topo}(H_p; B) + \phi_{displacement} + \phi_{propagation} + \phi_{orbit} + \phi_{scattering} \quad \text{Equation 2-19 (Bamler, 2006)}$$

The $\phi_{propagation}$ term is due to ionospheric and atmospheric propagation conditions. Often these perturbations exhibit a turbulence-like structure (Ferretti et al. 1997 and Goldstein 1995). This phase delay due to turbulent mixing and vertical stratification in the atmosphere has been more recently statistically analysed by Hanssen (2001). He modelled it as a stochastic signal that generates a spatially correlated phase variation. He concluded that the influence of the atmospheric refractivity distribution can significantly affect the repeat-pass radar interferograms when looking at scales that go from 1 to 100-200 km. At larger scales, residual fringes are caused by orbit errors, ϕ_{orbit} . At smaller scales instead, phase variations cannot have an atmospheric origin since there is no physical explanation for delay variations. Also, the effect of stratification

does not have an influence for relatively flat areas. Therefore at scales smaller than one kilometre, phase perturbations must be described by other sources linked to changes of the target scattering conditions, $\phi_{scattering}$. This term is discussed in Section 2.1.6. It may contain both deterministic phase offsets (e.g. due to a change of the target dielectric properties or movements of the scatterers within a resolution cell) and phase noise due to changes that are more complex to model analytically. Also, accurate ground truth data used to quantify and validate the $\phi_{scattering}$ contribution are not always available. As explained by Bamler and Just (1993), the $\phi_{scattering}$ term can be considered a noise affecting the standard deviation of the computed interferometric phase. Therefore, for small scale applications (i.e. < 1 km) it is possible to disregard atmospheric and orbit phase delays and consider the scattering contribution as noise. Hence:

$$\phi = \phi_{topo}(H_p; B) + \phi_{displacement} \quad \text{Equation 2-20 (Bamler, 2006)}$$

Combining the influence of topography and surface displacement, D_p , on the interferometric phase differences relative to the reference body, the interferometric phase change is derived as:

$$\partial\phi = -\frac{4\pi}{\lambda} \left(D_p - \frac{B_{\perp}^0}{R_1 \sin \theta^0} H_p \right) \quad \text{Equation 2-21 (Hanssen, 2001)}$$

Again, using ERS parameter, this implies that for an effective baseline B_{\perp} of 100 m, a height difference H_p of 1 m yields a $\partial\phi$ of approximately 4.2° , which is well below the noise level of about 40° and it is therefore practically undetectable (Hanssen, 2001). On the other hand, a displacement D_p , of only 1 cm in the range direction yields to a phase difference of 128° , which is easily detectable. Due to this reason, many studies have focused on deformation monitoring linked to subsidence or seismic movements as discussed in Section 2.1.7.

Because of the SAR imaging geometry, displacements can only be measured in the slant direction and subsequently decomposed in the y and z components (refer to Figure 2-1 and Figure 2-4) according to developed ground models. The integration of information coming from ascending and descending satellite passes can lead to models describing the presence of any displacement in the along-track direction.

As mentioned before, changes of the target scattering conditions between the two acquisitions lead to additional phase errors, therefore limiting the interferometric capability for topography mapping. The similarity of the scattering mechanisms in the two images is indicated by a correlation coefficient, known as complex degree of coherence.

2.1.6 Complex Degree of Coherence

The complex degree of coherence is a direct measure for the similarity between the two observations. Any dissimilarity of the scattering mechanism between the two images, indicated by a low coherence, results in phase noise. The signals A_1 and A_2 received from the same area at the two different passes can be written as:

$$\begin{aligned} A_1 &= |A_1| e^{j\phi_1} = |A_1| e^{-\frac{4\pi}{\lambda}R_1} e^{j\xi_1} \\ A_2 &= |A_2| e^{j\phi_2} = |A_2| e^{-\frac{4\pi}{\lambda}R_2} e^{j\xi_2} \end{aligned} \quad \text{Equation 2-22 (Hanssen, 2001)}$$

The phase $\phi_{1,2}$ is decomposed into a “travel” phase $4\pi R_{1,2} / \lambda$ corresponding to the path of the radar wave travelling a distance equal to the range, and a “random” phase $\xi_{1,2}$ that with the speckle model introduced above, is uniformly distributed in the interval $[0, 2\pi]$. If the phases ξ_1 and ξ_2 are very different from each other, they corrupt the useful phase signal $4\pi (R_2 - R_1) / \lambda$ as defined in Equation 2-14. Consequently, a measure of the correlation between the two SAR images is an important quality factor. The complex correlation coefficient (or complex coherence) γ of the complex backscatter signals A_1 and A_2 is defined by:

$$\gamma = \frac{E\{A_1 A_2^*\}}{\sqrt{E\{|A_1|^2\} E\{|A_2|^2\}}} = |\gamma| e^{j\phi_0} \quad \text{Equation 2-23 (Hanssen, 2001)}$$

where $E\{ \}$ is the statistical expectation operator. The numerator of the fraction in Equation 2-23 is equal to $E\{v\}$ where v is defined in Equation 2-10. Also, since the denominator has a real value, the phase of the complex correlation corresponds to the phase of the interferogram. The magnitude of the complex coherence, or degree of coherence $|\gamma|$, has a value in the range between 0 and 1, and can be considered as a measure of the phase noise (i.e. null coherence corresponds to a total loss of correlation between the two images).

Following the speckle model introduced in Section 2.1.3 and applying a multilook process (i.e. $L > 2$), Goodman (1963), Barber et al. (1993), Lee et al. (1994) and Tough et al. (1995) show that the marginal probability density function for the interferometric phase, ϕ , for different coherence levels is:

$$pdf(\phi; \gamma, L, \phi_0) = \frac{\Gamma(L+1/2)(1-\gamma^2)^L |\gamma| \cos(\phi - \phi_0)}{2\sqrt{\pi}\Gamma(L)(1-\gamma^2 \cos^2(\phi - \phi_0))^{L+1/2}} + \frac{(1-\gamma^2)^L}{2\pi} {}_2F_1(L, 1; 1/2; \gamma^2 \cos^2(\phi - \phi_0))$$

Equation 2-24 (Hanssen, 2001)

The gamma function, $\Gamma(\cdot)$, is defined as:

$$\Gamma(L) = \int_0^{\infty} t^{L-1} e^{-t} dt, \quad \text{for } L \in \Re$$

Equation 2-25

And the hypergeometric function can be computed with:

$${}_2F_1(L, 1; 1/2; \gamma^2 \cos^2 \phi) = \frac{\Gamma(1/2)}{\Gamma(L)\Gamma(1)} \sum_{i=0}^{\infty} \frac{\Gamma(L+i)\Gamma(1+i)}{\Gamma(1/2+i)} \frac{(\gamma^2 \cos^2 \phi)^i}{i!}$$

Equation 2-26 (Hanssen, 2001)

The interferometric phase variance resulting from $|\gamma| < 1$ can be derived using its definition:

$$\sigma_{\phi}^2 = \int_{-\pi}^{\pi} [\phi - E\{\phi\}]^2 pdf(\phi) d\phi$$

Equation 2-27

Equation 2-24 and Equation 2-27 are plotted in Figure 2-6 and Figure 2-7 respectively. Clearly, as the coherence and the multilook factor increase the phase variance decreases.

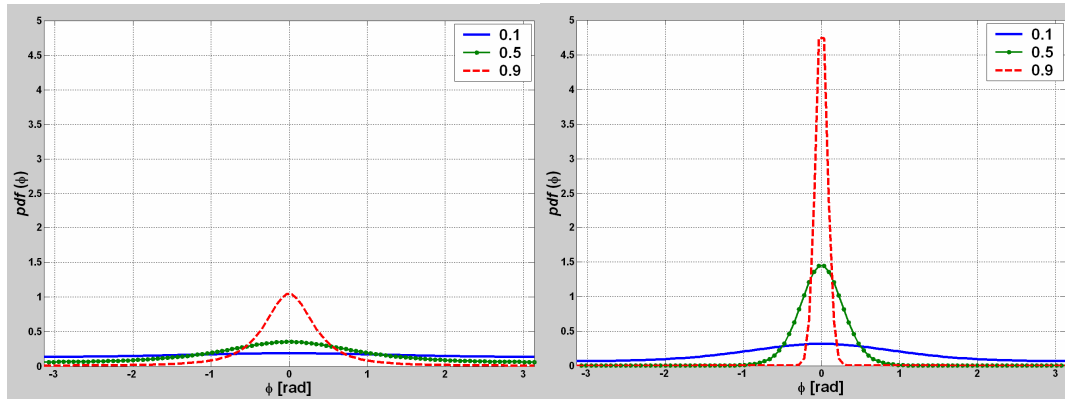


Figure 2-6. Probability density function for three coherence magnitude levels (i.e. 0.1, 0.5 and 0.9). Left with no multilooking ($L=1$) and right with a multilook factor of 20.

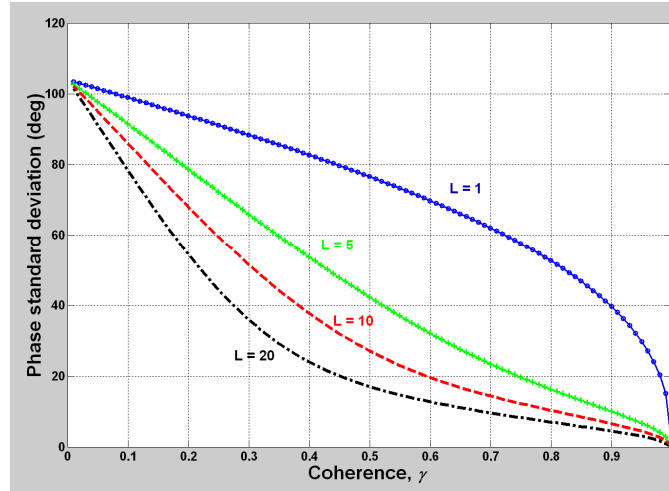


Figure 2-7. Standard deviation of the interferometric phase as a function of coherence, for four different multilook levels.

It must be clarified that the multilook factor, L , does not exactly correspond to the $M \times N$ as pixels in a SAR cannot be exactly considered as statistically independent samples (Rignot and van Zyl, 1993). In fact, the SAR signal processing algorithms introduce oversampling, in other words correlation between adjacent pixel values. Oliver and Quegan (1998) provide the equation to estimate the number of independent looks, also called effective number of looks (ENL), in an $M \times N$ processing window:

$$L = \frac{\bar{I}^2}{\sigma_I^2} \cdot \frac{MN}{\sum_{|k|<M} \sum_{|l|<N} \left(1 - \frac{|k|}{M}\right) \left(1 - \frac{|l|}{N}\right) \rho_{I,a}[k] \rho_{I,r}[l]} \quad \text{Equation 2-28}$$

where \bar{I} and σ_I^2 are the mean and variance of the intensity, $\rho_{I,a}[k]$ and $\rho_{I,r}[l]$ are the azimuth and range intensity correlation coefficients as defined in Equation 2-9 and k and l are the pixel separation in each dimension respectively. Therefore a lower mean value and higher variance of the intensity the $M \times N$ window, reduce the effective number of looks. Also, if the pixels are independent the correlation coefficients are zero at all lags except at 0, so the denominator of the second term in Equation 2-28 would be equal to one and it would not affect the multilook number.

Under the assumption of ergodicity and taking into account the systematic phase variation due to topography and the flat-Earth effect, the “phase-corrected” coherence magnitude in a SAR scene is estimated using the following equation (Hagberg et al., 1995; Monti Guarnieri and Prati, 1997; Zebker and Chen, 2005):

$$|\gamma_{PC-estim}| = \frac{\left| \sum_{m=1}^M \sum_{n=1}^N A_1(m,n) A_2^*(m,n) e^{-j\phi(m,n)} \right|}{\sqrt{\left(\sum_{m=1}^M \sum_{n=1}^N |A_1(m,n)|^2 \right) \left(\sum_{m=1}^M \sum_{n=1}^N |A_2(m,n)|^2 \right)}} \quad \text{Equation 2-29}$$

where $A_1(m,n)$ is defined as the complex pixel values of the first image in a $M \times N$ pixel calculation window, and $A_2(m,n)$ is the corresponding values in the second image.

Section 2.1.3 explained that for distributed scatterers speckle can be described as a statistical quantity. Since the coherence is a function of the same complex pixels on a given area, the estimator in Equation 2-29 can also be modelled statistically. Full derivation of these models is presented in Touzi and Lopes (1996). The expectation of the “phase-corrected” coherence magnitude $|\gamma_{PC-estim}|$, can be expressed as a function of the true value of the coherence magnitude γ and of the number L of independent samples (with $L > 2$) used in the coherence calculation window (Hanssen, 2001):

$$E\{|\gamma_{PC-estim}|\} = \frac{\Gamma(L)\Gamma(3/2)}{\Gamma(L+1/2)} {}_3F_2(3/2, L, L; L+1/2, 1; |\gamma|^2) (1-|\gamma|^2)^L \quad \text{Equation 2-30}$$

The variance of the estimated coherence magnitude is (Hanssen, 2001):

$$D\{|\gamma_{PC-estim}|\} = \frac{\Gamma(L)\Gamma(2)}{\Gamma(L+1)} {}_3F_2(2, L, L; L+1, 1; |\gamma|^2) (1-|\gamma|^2)^L - E\{|\gamma_{PC-estim}|\}^2 \quad \text{Equation 2-31}$$

As shown in Figure 2-8, the expectation of the estimated coherence magnitude is biased towards higher values, especially for low coherence and small estimation windows. Furthermore, removal of the bias in $|\gamma_{PC-estim}|$ by inverting Equation 2-30 is only possible when the coherence magnitude is high or when L is sufficiently large (Touzi et al., 1999). The multilook factor could be therefore increased. However, this is done at the expense of spatial resolution on the coherence image and it also requires that the calculation window covers a homogeneous area on the ground. A compromise is made between spatial resolution and reliable estimation of coherence. As explained by Touzi et al. (1999), the coherence magnitude from an L -look coherence magnitude map may be better estimated by spatially averaging the sample coherence values over an area of interest, therefore increasing the effective number of looks, under the assumption that the coherence signal is stationary and ergodic (in mean). The loss of similarity between the SAR interferometric pair is called decorrelation. This can be more accurately defined as the noise caused by error sources that have an AC smaller or equal to the used coherence estimation window. As explained in Section 2.1.5, this implies that orbit and atmospheric phase errors are not included.

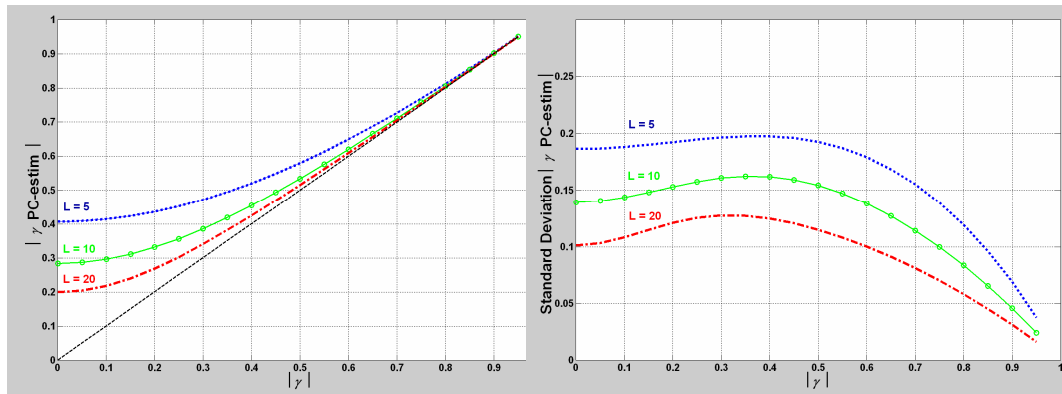


Figure 2-8. Left: the expectation value of the estimated coherence magnitude as a function of the true coherence and for various multilook factors. Right: the standard deviation of the estimated coherence magnitude as a function of the true coherence and for various multilook factors.

2.1.6.1 Decorrelation

Figure 2-9 shows an example of a coherence magnitude image with $M \times N = 20$ obtained with an ERS 1-2 interferometric tandem pair. The dark pixels, each of 50 m ground resolution, represent areas in which change has occurred between the master and slave acquisitions, whilst the bright ones identify targets that have not modified their scattering conditions. As a result, the coherence magnitude can be associated with different types of land cover and land use. As previously explained, low coherence could be considered as an unwanted effect which causes information loss on an interferogram. Although this is true if interferometry is used for topography and deformation mapping, the loss of coherence could be conversely used to extract additional information about the properties and characteristics of the surface. Indeed, the amount of surface change over time describes processes occurring on time scales of the orbit repeat time and size scales on the order of the SAR ground resolution and wavelength (Ichoku et al., 1998).

Extensive literature has demonstrated the value of the degree of coherence for a variety of applications such as the monitoring of forests, floods, lava streams, glaciers, land slides, fires, soil moisture changes and vegetation growth. Some recent examples are Drezet and Quegan (2006), Preiss et al. (2006), Terenuma et al. (2005), Lefort et al. (2004), Vincent et al. (2004), Blaes and Defourny (2003), Grey et al. (2003), Okhimamhe (2003) and Weydall (2001).

Due to the different geometric views and the time lag between the two acquisitions, repeat-pass interferograms are subject to some loss of coherence, or decorrelation. Assuming the processing stages from the SAR raw data to the single-look complex (SLC) SAR scene, decorrelation can be written as the product of three dominant

contributions, namely the thermal, spatial and temporal decorrelations (Zebker and Villasenor, 1992):

$$\gamma = \gamma_{thermal} \cdot \gamma_{spatial} \cdot \gamma_{temporal} \quad \text{Equation 2-32 (Zebker and Villasenor, 1992)}$$

The thermal decorrelation factor is associated with the system noise and can be derived theoretically by determining the signal-to-noise ratio of a specific system. For target radar cross section of -14dB , Hanssen (2001) computes the thermal decorrelation for the ERS 1-2 systems equal to 0.92. For high signal-to-noise ratios, the $\gamma_{thermal}$ factor can be considered as negligible (Zebker and Villasenor, 1992).

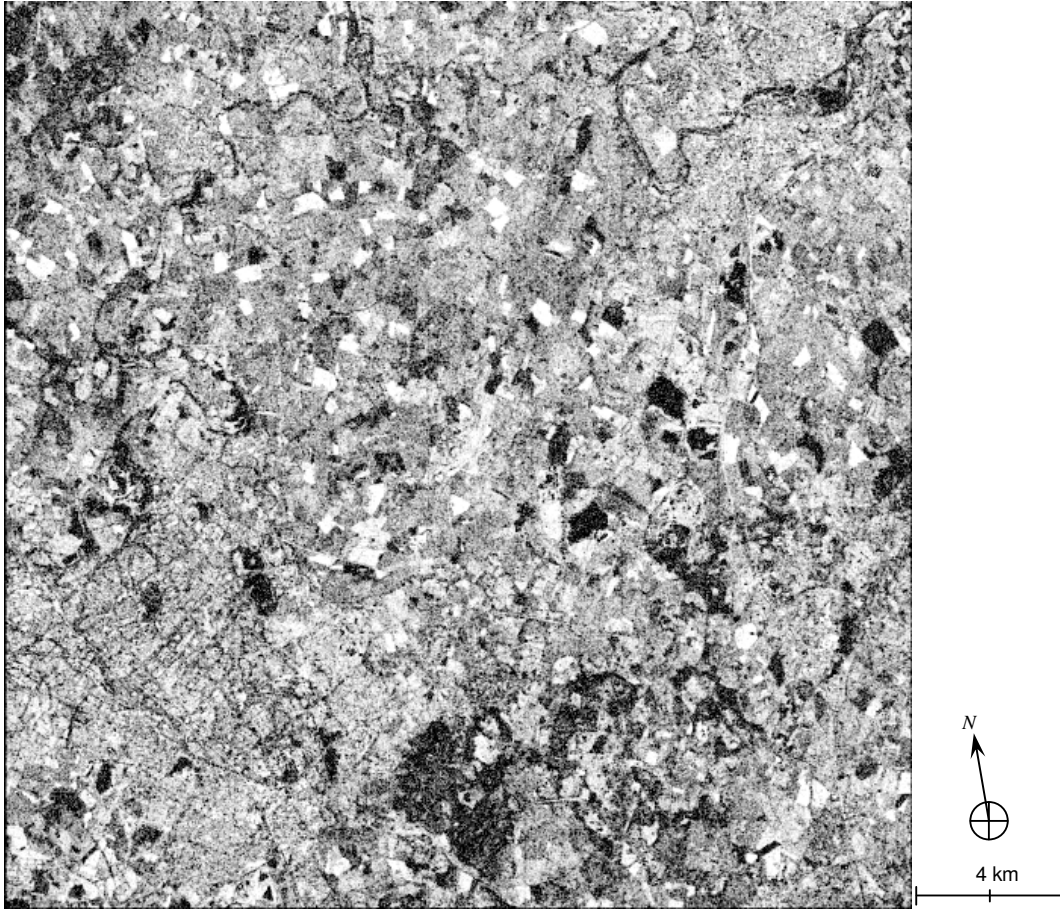


Figure 2-9. Coherence magnitude image obtained using the SAR interferometric pair of 25th and 26th June 1995 (descending orbit: 20623 and 950 respectively; track: 94; frame: 2547). The multilook factor is 2 pixels in range and 10 in azimuth. The original SAR image of 25th June can be seen in Figure 2-2. The original scene has been flipped horizontally.

The spatial decorrelation contribution is caused by in variations of the target's reflectivity as a function of the incidence angle, the geometric view. The variation of $\gamma_{spatial}$ as a function of the baseline is defined by Hanssen (2001) as:

$$\gamma_{spatial} = \frac{B_{\perp,crit} - B_{\perp}}{B_{\perp,crit}} \quad \text{Equation 2-33}$$

where the critical baseline $B_{\perp,crit}$ is a function of the wavelength λ , the incidence angle θ , the topographic slope α , the frequency bandwidth of the transmitted pulse B_R , and the slant range R_S defined in Equation 2-3. $B_{\perp,crit}$ is given by:

$$B_{\perp,crit} = \left| \frac{\lambda B_R R_S \tan(\theta - \alpha)}{c} \right| \quad \text{Equation 2-34 (Bamler 2006)}$$

The critical baseline for ERS 1 and 2 and Envisat with an incidence angle of 23° and zero topography is approximately 1100 m.

The third contribution, the temporal decorrelation, is due to changes of the imaged surface between the two SAR acquisitions. Such changes may be due to geometrical changes such as moving parts of the vegetation, erosion of the land surface, agricultural activities or construction. Temporal decorrelation may also be due to variations in the scattering properties related to soil moisture or volume scattering. Presenting analytical models for temporal decorrelation has proven to be unsuccessful so far (Hanssen, 2001) since the range of possible temporal changes is too wide. Assuming that $\gamma_{temporal}$ is caused by the movement of scatterers only, Zebker and Villasenor (1992) have obtained an approximation based on the root-mean-square of the displacements:

$$\gamma_{temporal} = \exp \left\{ -\frac{1}{2} \left(\frac{4\pi}{\lambda} \right)^2 \left(\sigma_{hor}^2 \sin^2 \theta + \sigma_{vert}^2 \cos^2 \theta \right) \right\} \quad \text{Equation 2-35}$$

As shown in Figure 2-10, there is a greater sensitivity to vertical changes than to horizontal changes for incidence angles less than 45° .

A more complete decorrelation analysis is presented by Hanssen (2001). This includes additional error contributions due to the InSAR processing itself (e.g. coregistration and interpolation errors) and due to the different Doppler centroids of the acquisitions. They add decorrelation in the scene and may reach value of even 0.90.

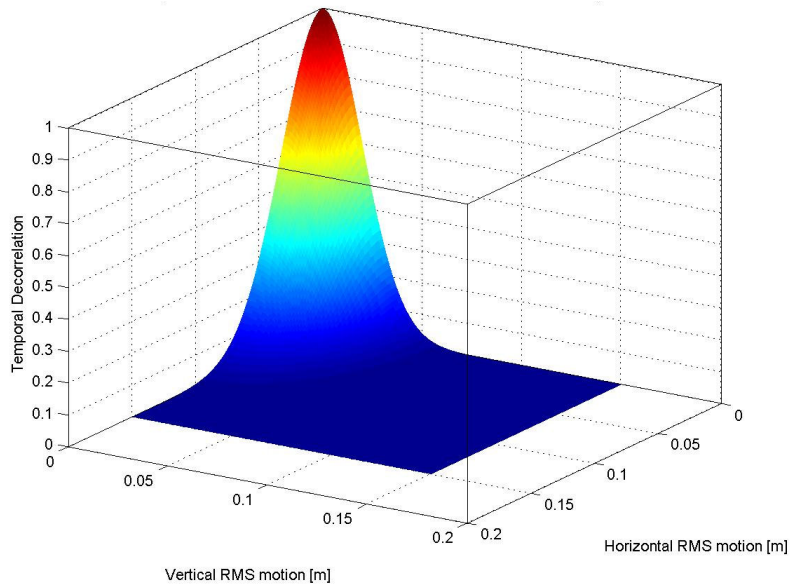


Figure 2-10. Model for the ERS C-band system indicating dependence of the temporal correlation (vertical axis) on random motion of scattering centres within a resolution element. The model takes into account horizontal and vertical variations, and shows that decorrelation is more dependent on the vertical displacements.

2.1.7 Surface Displacement Monitoring

As derived in Equation 2-21, SAR interferometry directly measures topography and surface displacement events in the radar line of sight such as those associated with earthquakes, landslip or subsidence. A technique called differential interferometry (DInSAR) is used to separate the topography from the deformation.

There are several ways to construct a differential interferogram. The two-pass method uses an external elevation model of the topography that is converted into radar coordinates, scaled using the baseline, and subtracted from the repeat-pass interferogram containing the displacement information (Massonet et al., 1993). The remaining fringes are therefore theoretically only related to deformation.

A second method is the three-pass method (Zebker et al. 1994). This approach uses three SAR scenes taken at different times in order to produce two interferograms. The first repeat-pass interferogram (called topographic pair) is assumed to have only topographic information. Conversely, the second interferogram, obtained with one SAR scene in common to the first, is affected by surface deformation. The topographic interferogram is unwrapped, scaled to the baseline characteristics of the deformation

pair and subtracted from it, yielding to the differential interferogram, the so called differential pair. As discussed by Hanssen (2001), generally this method requires:

- (i) $B_{\perp}^{topo} \geq B_{\perp}^{defo}$ to obtain at least the same height accuracy as the deformation pair,
- (ii) $B_{\perp}^{topo} < \sim 0.7B_{\perp,crit}$ to obtain coherent data,
- (iii) the deformation pair temporal baseline to be as small as possible to limit temporal decorrelation effect.

In the boundary situation, a zero baseline for the deformation pair would make the topographic pair unnecessary.

The above procedures are applied to analyse single deformation episodes only. Other methodologies are used to study the temporal evolution of the detected deformations. A relative new technique called Permanent/Persistent Scatterers Interferometry (PSInSAR) (Colesanti et al., 2003; Ferretti et al., 2001; Ferretti et al., 2000) can perform such temporal analysis. This technique first identifies ground features, such as buildings or geological outcrops, that exhibit sufficiently high coherence values over time and even at large spatial baselines (i.e. the persistent scatterers). It then processes 30 or more SAR scenes spanning many years to compute pointwise information of the scatterers displacement which is then extrapolated over the entire area achieving the monitoring of any slow long-term ground deformation.

Another recent technique is the Small Baseline Subset (SBAS) approach (Casu et al., 2006; Berardino et al., 2002). By considering sets of small perpendicular baseline interferograms, this DInSAR algorithm allows the generation of mean deformation velocity maps and displacement time series from a data set of subsequently acquired SAR images. The results have a standard deviation of 1 mm/year for a typical ERS data set including between 40 and 60 images.

2.2 Optical Remote Sensing

As the research explores the fusion of SAR and other remote sensing data, this section briefly introduces the basics of passive optical imaging. The presented material is introductory in scope as the subject is too large for it to be thoroughly considered here. A comprehensive overview is provided by Jensen (2005), Schowengerdt (1997) and Sabins (1996).

Passive remote sensing in the optical regime operates from the visible to the thermal infra-red spectral region and is based on the broad principles of radiation transfer, photo detection and image formation. As explained in Section 1.1.1, optical EO systems operate in specific regions of the electromagnetic spectrum within which constituents of the atmosphere (e.g. water vapour and carbon dioxide) do not absorb radiation. The various platforms are characterised by their spatial, spectral, radiometric and temporal resolutions.

The visible (V), near infrared (NIR) and short wave infrared (SWIR) regions (from $0.4\mu\text{m}$ to about $3\mu\text{m}$) are the solar-reflective spectral range because the energy supplied by the Sun at the Earth's surface exceeds that emitted by the Earth itself. The mid wave infrared (MWIR) is a transition zone from solar-reflective to thermal radiation up to about $5\mu\text{m}$. Afterwards, the Earth's natural black body self-emitting thermal radiation generally dominates and therefore thermal infrared (TIR) images (circa from 8 to $9.5\mu\text{m}$ and from 10 to $14\mu\text{m}$) can be acquired both in the daytime and at night, cloud cover permitting. Because energy decreases as the wavelength increases, thermal sensors generally have large instantaneous fields of view to ensure that enough energy reaches the detector in order to achieve a sufficient signal to noise ratio. As a result, MWIR and TIR images have a coarser resolution with respect to visible and reflected infrared images.

As in the case of a SAR imaging system, every material has different reflective, transmitting and absorbing characteristics depending on the incident wave frequency. Therefore, targets can be differentiated and subsequently studied on the basis of their observed spectral reflectance signatures. Depending on the number of spectral bands used in the imaging process, EO platforms can be classified into three main groups:

- Panchromatic: the sensor is a single channel detector sensitive to radiation within one broad wavelength range and thus achieving a higher spatial resolution. Usually, the frequency range coincides with the visible one and the acquired image corresponds to a "black-and-white" photograph. The physical quantity being measured is the apparent brightness of the targets, therefore any spectral information is lost.
- Multispectral and Superspectral: the sensor is a multi-channel detector with three to a dozen spectral bands. Each channel is sensitive to radiation within a narrow wavelength band and they can be combined in the Red-Green-Blue channels to obtain various image products.
- Hyperspectral: these imaging system, also known as an "imaging spectrometer", acquire a hundred or more spectral bands. The spectral information contained in a hyperspectral image enables better characterisation and identification of targets.

2.2.1 Digital Image Processing

In the past, data from the various satellite systems were supplied to the user in the form of computer-readable magnetic tapes, usually called computer-compatible tapes (CCT), as well as on miniature tapes such as Exabyte and DAT. The specification of the different data formats is usually well documented. ESA (2004), for instance, provides all the ERS SLC CCT and Exabyte format specifications. The situation has considerably improved over the past 10 years or so, and nowadays most remote sensing images are recorded and stored directly in digital form and are distributed in CD-ROMs, DVDs and via the Internet. In addition, commercial or freely available RS image processing

software provide procedures to automatically read and work with the most commonly used formats. This revolutionised image processing from an activity confined to dedicated facilities with expensive mainframe computers operated by specialists, to an inexpensive process performed on personal computers by users with average computer skills. Image processing procedures can be grouped into three functional categories: image restoration, image enhancement and information extraction.

Image restoration, or pre-processing, corrects the errors, noise and geometric distortion introduced into the data during the scanning, transmission and recording of images. Today some of these techniques are automated and defects are relatively rare. Some error sources examples with their respective restoration techniques are:

- Detector and receiver variations (e.g. restoring line dropouts, periodic line stripping and line offsets),
- Transmitter and receiver variations (e.g. filtering random noise),
- Atmospheric variations (e.g. correcting for atmospheric scattering, haze and solar illumination),
- Geometric distortion (e.g. correcting for systematic and non-systematic distortions),
- Radiometric errors.

Image enhancement, or processing, alters the visual impact that the image has on the interpreter in a fashion that improves the information content. These techniques generally modify the original digital value of the picture elements (pixels), therefore they are not applied until the restoration processes are completed. Some of these techniques are:

- Colour composites,
- Contrast enhancement and hue-saturation-intensity transformations,
- Density slicing,
- Edge enhancement,
- Digital mosaics,
- Filtering.

Information extraction, or post-processing, utilises the decision-making capabilities of the computer to recognise and classify pixels on the basis on their digital signatures. These techniques can be supervised or unsupervised by the operator, nevertheless, it is always critical to evaluate the significance and accuracy of the achieved product. Some of these techniques are:

- Principal-component Analysis (PCA),
- Computation of Indices,
- Classification techniques,
- Change detection procedures.

A more detailed explanation can be found in Jensen (2005) and Schowengerdt (1997).

2.3 Multi-Sensor Data Fusion

Recent research has explored the advantages of merging data obtained from more than one imaging sensor to exploit the complementary nature of the spectral and/or spatial resolution of different systems (e.g. polarised radar, visible, infrared or panchromatic). Henderson and Lewis (1998) present an extensive literature review on this topic and explain that “since a single system normally has both advantages and disadvantages, there is a potential synergy in data integration designed to capture the benefits of both systems without significantly distorting a desired characteristics of either.” Several methodologies have been developed for merging multi-sensor data. Waltz (2001) introduces the theory of pixel, feature and decision fusion. These techniques involve different disciplines including digital signal processing, statistical estimation, control theory, artificial intelligence and classic numerical methods. The choice of technique depends upon the purpose of the data integration and its intended application. Knowledge and experience for the final product interpretation is also extremely critical. All these techniques are not presented in this report due to length constraints. Nonetheless, any application of such procedures is duly referenced.

It is important to emphasise that geometric coregistration is a key challenge in multi-image data fusion. This problem requires the alignment of two or more images so that corresponding pixels on each image represent the same location on Earth. As previously explained, ground features in SAR remote sensing images can get distorted due to local topography and therefore the coregistration of scenes acquired from different point of views must be carefully carried out.

2.4 Summary of Literature Review

This chapter has presented to the reader key concepts of SAR remote sensing, image processing and landfill management. SAR data can be analysed using five types of information: spectral, spatial, temporal, angular and polarization. The radar backscattered signal is affected by topography (i.e. the incidence angle of the incoming wave), the target surface roughness and correlation length, the occurrence of volume scattering in the presence of vegetation and the target dielectric constant. All these radar system variables and ground characteristics must be taken into account when investigating SAR data. The chapter has also highlighted the value of interferometry and polarimetry for the computation of topography and ground displacements, and the classification of ground targets. Particular attention has been dedicated to the accurate evaluation of the degree of coherence. A bias correction is necessary if such information is used for land-use classification purposes. The chapter has also briefly introduced image processing techniques linked to the restoration and enhancement of remote sensing images and additional information extraction procedures.

3. Preliminary Ground Observations

This chapter describes the preliminary ground observations carried out in order to appreciate the spatial, temporal and biophysical characteristics of a landfill that can influence SAR data. The results of these observations have supported the selection of the analysis techniques and the physical interpretation of the results presented in the following chapters.

3.1 Preliminary Observations

After agreeing with Waste Recycling Group Ltd. on a research collaboration and specifically on the access to their Brogborough site, the author carried out a number of field trips to observe the ground characteristics that can influence the SAR backscatter return signal and SAR interferometric products.

This site, located midway between Milton Keynes and Bedford (i.e. 52.05° North and 0.595° West, see Figure 3-1) was originally worked as a clay pit extracting Oxford clay and it is currently operated by Waste Recycling Group Ltd. The site, pictured in Figure 3-2, currently has an area of circa 195 hectares. This aerial view was acquired by the author during the summer 2005 in collaboration with the Cranfield University National Flight Laboratory Centre. Filling activities at Brogborough commenced in 1982 and it currently receives approximately 2 million tonnes of wastes per annum. Receiving circa 400 vehicles per day from London and other regions of the UK, the planned closure date is 2009 (Kirkland, 2005). As illustrated in the aerial view, this site offers the possibility of assessing operational cells, recently capped areas, and older restored parts.

Figure 3-3 shows an example of an accurate plan developed quarterly by the site surveyors. These plans also contain accurate elevation data. As illustrated in Figure 3-2, the Brogborough site presents very different zones. This diversity is a distinctive characteristics of most landfills (Smith, 2005). The preliminary ground observations consider five different areas separately: artificial lagoons, infrastructures, open cells, capped areas and fully restored areas. The analysis deals with the spatial, temporal and biophysical characteristics of these five zones. Spatial observations are carried out at two different scales: the SAR ground spatial resolution dimension (i.e. from 5 to 25 m) and the radar wavelength dimension (i.e. from 3 to 25 cm).

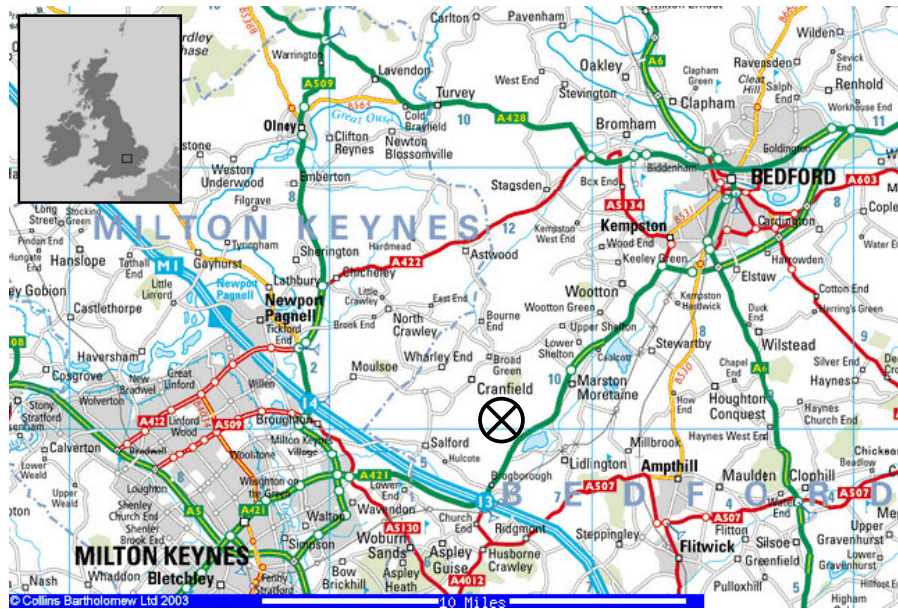


Figure 3-1. Case study area: Brogborough landfill. Printed by permission of Harper Collins and Multimap. The black cross in the centre marks the landfill location, midway between Milton Keynes and Bedford (i.e. 52.05° North and 0.595° West).

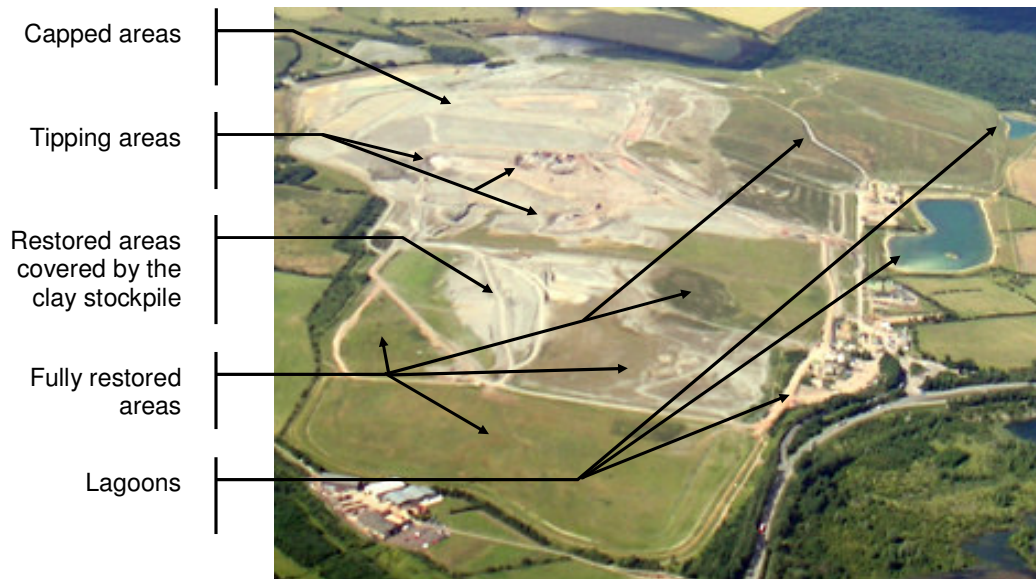


Figure 3-2. Aerial view of the entire Brogborough landfill acquired by the author on 11th July 2005 in collaboration with the Cranfield National Flying Laboratory Centre.



Figure 3-3. A survey map of the Brogborough landfill developed in November 2004. The grid is spaced at 100 m. The pink contour represents the operational void where open cells are located. Stage 1 is the selected area for ground observations of a fully restored cell. (Courtesy: Waste Recycling Group Ltd.)

3.1.1 Artificial Lagoons

Artificial lagoons within or around the landfill may extend approximately from 15 to 150 m² depending on their purpose (e.g. monitor run-off water, examine the presence of leachate). Figure 3-4 shows part of a relatively small lagoon in the Brogborough site.

The radar backscatter of water bodies has been extensively analysed by Long (2001) and Ulaby et al. (1982). Lakes can be considered as one single main horizontal facet on which waves are generated by the local wind speed and direction and bathymetry conditions. The return signal from such a surface can be modelled by the Bragg resonance. Its condition is:

$$\frac{2L}{\lambda} \sin \theta = n, \quad \text{for } n = 0, 1, 2, \dots \quad \text{Equation 3-1 (Ulaby et al., 1982)}$$

where L is the distance between wave crests. Without the presence of any wave, the signal would bounce off specularly. Conversely, in the presence of Bragg resonance and given the orientation of the waves is parallel to the SAR flight path, the backscatter signal can have very high values. This dependence on the wind conditions makes the return signal from water bodies extremely variable. As a result, this translates in very low values of the complex degree of coherence due to the temporal decorrelation that would occur at very short time scales such as fractions of seconds.



Figure 3-4. Brogborough landfill. A lagoon dug to contain surface water run off. The water is monitored quarterly for presence of leachate and other harmful chemicals (23rd February 2005).

3.1.2 Infrastructure

The term infrastructure includes both buildings and vehicles used on the site (Figure 3-5). In SAR images, these elements usually tend to appear as dominantly bright features (Lee, 2001; Dong et al., 1997; Dousset, 1997). This is because they often have a metal structure and with a suitable orientation to the incoming SAR wave they behave as corner reflectors. This specular reflected signal is generally much stronger than diffuse backscatter. The difference between buildings and vehicles would appear in the complex degree of coherence computation. In fact, with a temporal baseline of hours or days, the first group would be characterised by high coherence, while the second would have very low values.



Figure 3-5. Brogborough landfill. Left: a variety of trucks continuously operate in the open cells (i.e. tipping areas) to deposit and compress the waste. Right: site buildings might include offices, power stations, storage buildings, and truck maintenance buildings (11th July 2005).

3.1.3 Open Cells and Capped Areas

In England and Wales, stringent regulations restrain the tipping areas to a manageable size so that they can be covered by the daily temporary layer of clay as explained in the previous Chapter. Generally, a single open cell can vary approximately from 1 to 12 hectares. One landfill site might have more than one open cell in which activities are carried out (e.g. receiving waste, setting the capping, maintaining the gas extraction system, etc.). Additionally, there can be multiple tipping areas in the same open cell. These areas can vary from 300 to 2500 m². On the other hand, capped areas are usually larger and may even reach 30 to 50 hectares depending on the size of the overall landfill. These parts are covered with a layer of engineered highly compacted soil but not fully restored with vegetation. Examples of such areas are shown in Figure 3-6 and Figure 3-7.

An important characteristic of tipping areas is the ‘batter’. This is a vertical edge which may even reach heights of 6 m. Such vertical steps are present in most landfills and may also be found in areas where the daily clay is piled before it is transported and used on the open cell. Figure 3-8 illustrates such features. Given their geometry and depending on the incoming SAR look direction, they may have a strong backscatter signal as a combination of both specular and diffuse scattering effects.

Another key remark is that in order to minimise risks for the site operators, tipping areas are maintained flat. At the SAR ground resolution scale such zones usually only have an insignificant inclination and therefore they can be considered as horizontal surfaces. Additionally, as waste is immediately compressed and covered with a thin layer of rough soil at the end of each day, any volume scattering can be considered negligible. Plastics, metals and other solid materials tend to remain on the top surface, while organic products rapidly crumble, decompose and percolate through the waste.



Figure 3-6. Brogborough landfill. Left: waste deposited and immediately compressed in the open cell. A one-meter length is shown in the image. Right: temporary layer of clay deposited on top of the tipping area to cover the waste (09th May 2005).



Figure 3-7. Brogborough landfill. A capped area. In this particular picture, the engineered Oxford clay presents visible cracks due to shrinkage of the soil. A one-meter length is shown in the image. (13th June 2006).



Figure 3-8. Brogborough landfill. Left: batter of an open cell. Right: high vertical step in an area where the daily clay is piled and managed. A two-meter length is shown in the image. (09th May 2005).

With regards to the properties of tipping areas in open cells and capped areas at the radar wavelength scale, measurements were taken to calculate the surface roughness, the AC length and the spatial variation of volumetric soil moisture and soil temperature. The detailed methodology is presented in Section 4.1.2.

All data are averaged and results are summarised in Table 3-1, where s is the rms height, l is the AC length as defined in Equation 2-9. The estimated correlation does not severely differ from the initially assumed one, allowing the research to maintain the same error boundary of 18 %. The rms slope (m) is calculated from the ratio s / l , considering their mean values and estimating the effect of rounding errors. The wave number k (i.e. $2\pi/\lambda$) is then used to express s and l in terms of the wavelength. The quantities ks and kl are reported as reference because they are used in theoretical models (Ulaby et al., 1982) to describe the radar backscatter.

Considering a SAR look angle equal to 23° , these results show that tipping areas can always be considered as rough surfaces based on the Fraunhofer criterion for smoothness presented in Section 2.1.2. Capped areas can be considered smooth only with an L band SAR system. Therefore, the radar backscatter is not expected to decrease too rapidly with increasing angle of incidence. It must be said that if the less stringent Rayleigh criterion (Ulaby et al., 1982) is used (i.e. $s < \lambda / (8 * \cos \theta)$), then at L band both the tipping and capped areas can be considered as smooth surfaces. At C band instead the tipping area would still have to be modelled as a rough surface.

The volumetric soil moisture and soil temperature measurements for the top 5 cm of the soil were obtained using respectively the Theta probe HH2 manufactured by Delta-T Devices Ltd. (refer to Section 4.3.2) and a standard digital soil thermometer. These were provided by the Cranfield University National Soil Resources Institute.

Measurements were taken between 2pm and 6pm on 10th May 2005. As it is possible to see from Figure 3-9, over those hours, the air temperature remained stable enough not to considerably affect the soil temperature. Both the tipping and capped areas showed very homogeneous values within each of them. Considering the measured values and the effect of rounding errors, the computed standard deviations of the soil temperature and volumetric moisture are respectively 1 °C and 0.3 % for the tipping area and 1 °C and 0.2 % for the capped area.

Table 3-1. Surfaces roughness characteristics.

Surfaces		Parameters				
		s [mm]	l [cm]	m	ks	kl
1	Tipping area	Mean = 43.4 ±7.8 St. Dev = 11.2	Mean = 12.7 ±2.3 St. Dev = 3.2	0.38	λ = 3.10 cm ks = 8.80	λ = 3.10 cm kl = 25.74
					λ = 5.60 cm ks = 4.87	λ = 5.60 cm kl = 14.24
					λ = 23.60 cm ks = 1.15	λ = 23.60 cm kl = 3.38
2	Capped area	Mean = 7.77 ±1.4 St. Dev = 3.7	Mean = 13.45 ±2.41 St. Dev = 2.2	0.09	λ = 3.10 cm ks = 1.56	λ = 3.10 cm kl = 27.26
					λ = 5.60 cm ks = 0.86	λ = 5.60 cm kl = 15.09
					λ = 23.60 cm ks = 0.21	λ = 23.60 cm kl = 3.58

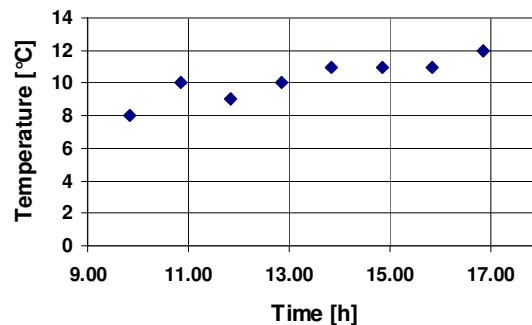


Figure 3-9. Variation of air temperature on 10th May 2005 from 9.50am to 4.50pm measured with a thermometer provided by the Space Research Centre.

With regards to the temporal characteristics, capped areas may not undergo any significant change for days, weeks and even months, apart from variations related to weather conditions. On the other hand, different time scales can be considered to account for the change of microwave scattering properties in an open cell:

- Short time scales (seconds, minutes). The geometrical (i.e. roughness and slope) and physics properties (i.e. material composition) of waste being accumulated in an open cell may vary in matters of seconds and minutes. The same applies for a clay stockpile used to manage the daily cover.
- Medium time scales (hours, days). At these scales, the signal temporal decorrelation may also be due to changes in the dielectric properties of the ground with relation to rain and temperature variations. These events would occur equally on the site and in areas around it. On the contrary, waste being deposited would considerably affect the topography only in open cells.
- Long time scales (weeks, months). With such long temporal baselines, operational practices and weather are equally a source of change, and subsequently of temporal decorrelation. For example, entire new cells might be opened or closed, new lagoons may be created, and significant topographic changes will occur. Ground observations showed that in about a week or two, an open cell is almost unrecognisable with new road paths and different levels of waste.

3.1.4 Fully Restored Areas

When a landfill is finally capped and closed, the site is typically restored to the former landscape (e.g. grassland). The site may also be restored with a variety of other plants, including trees, thereby maintaining its biodiversity and amenity value. Figure 3-10 shows the restored areas on the Brogborough site covered by grass and shrubs. Generally restored zones have a marked topography and they are larger than open cells or capped areas.

In the Brogborough site, grass and shrubs are not very dense, with a height varying from a few centimetres to about 0.9 m. Such conditions do not allow for an accurate measurement of ground roughness characteristics. Nonetheless, measurements of the soil temperature and volumetric soil moisture can be carried out in order to observe their variation within an area. The research focuses on Stage 1, the vast restored part visible at the bottom of Figure 3-2 and also indicated in Figure 3-3. This covers approximately 13 hectares.



Figure 3-10. Brogborough landfill. Fully restored area. (05th November 2004).

As for the open cell and the capped area, the measurements were made with a standard digital soil thermometer and the Theta probe HH2 manufactured by Delta-T Devices Ltd., both provided by the Cranfield University National Soil Resources Institute. The observations followed a random sampling method (McCoy, 2005) and were subsequently geo-located with a 12-channel GPS instrument manufactured by Garmin with an horizontal positioning accuracy of 7 m.

These measurements were taken between 11am and 1pm on 10th May 2005, during which air temperature did not have any significant variation. Figure 3-11 shows their location with respect to the local topography of the area, which was obtained from the accurate surveying data. The soil temperature is homogeneous around the whole area, with standard deviation of 0.4 °C. However, in contrast with open cells and capped areas, the volumetric soil moisture has a much higher standard deviation and equal to 6.9 %. A closer analysis shows that there is a strong correlation (i.e. -0.88) between the soil water content and the slope. Indeed, dump zones are often present in low areas of the site.

With regards to the temporal characteristics, fully restored areas may not undergo any significant change for months and years, apart from variations related to weather conditions and the occasional cutting of the grass and shrubs. Nonetheless, as explained in Section **Error! Reference source not found.**, waste usually settles between 10 and 40 % of the overall depth. This long term subsidence is a key characteristic of fully restored areas but it also occurs in open cells and capped areas.

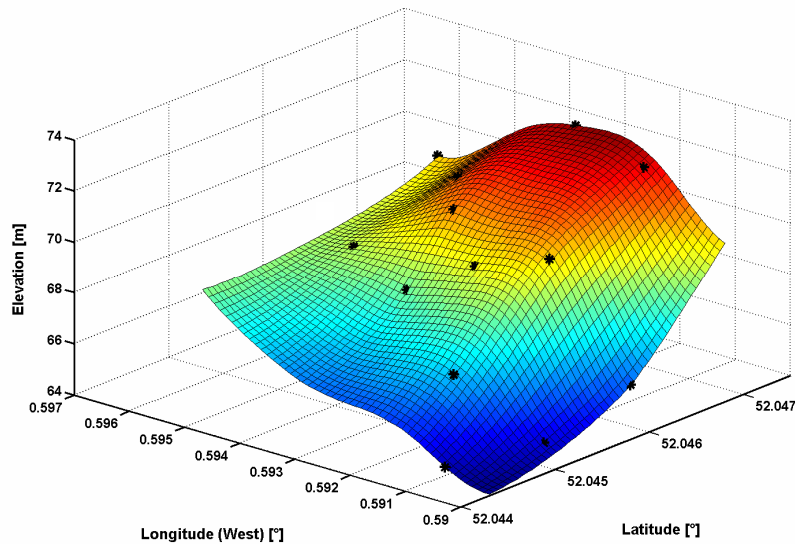


Figure 3-11. Location of the samples with respect to the local topography of the area, which was obtained from the accurate surveying data. The interpolation between the points is computed with the Sandwell (1987) method.

3.1.5 Conclusions of Preliminary Observations

Overall, the ground observations showed that a landfill has very variable characteristics in space and time.

The analysis allows the research to draw a number of conclusions and assumptions that can support the analysis of SAR data:

- a landfill presents complex topographic characteristics. Open cells tend to have steeper features, whilst capped areas and fully restored areas present a more gradual topography;
- a landfill contains distinctive features whose backscatter signal will likely depend on the SAR illumination direction (e.g. infrastructures, batter etc.);
- at the SAR ground resolution, tipping areas may be considered as horizontal surfaces with scattering centres moving randomly and independently of each others when waste is deposited. This is most evidently at medium temporal baselines (i.e. hours, days);
- due to the immediate compression of waste, the radar wave interaction with the ground in tipping areas should not involve any volume scattering;

- at SAR look angle of 23° , open cells can always be considered as rough surfaces whilst capped areas can be considered as smooth only with an L band SAR system;
- soil temperature in capped areas does not vary in space, but there is high negative correlation between elevation and soil moisture;
- waste settlement is most evident in fully restored areas but it also occurs in tipping and capped areas.

The temporal and spatial variability of landfill sites can be used as a source of information. When analysing SAR data it is possible to develop two different approaches in considering a landfill site. The first solution is to consider the site as a single entity, while the second solution is to divide it into zones depending on their characteristics. These two approaches lead to the development of a variety of SAR backscatter and interferometric analysis methodologies that address the various research objectives. Such methodologies and their outcome are presented in the following chapters.

4. Data Acquisition and Analysis Techniques

Having reviewed the theoretical background and the preliminary observations, this chapter presents the analysis techniques used in the research. The study explores a variety of approaches and uses several data acquisition and processing methods. Although they are related to different subject matters, these procedures are described in this single chapter to allow the reader to appreciate aspects of the overall research methodology presented in Section 1.3. This also avoids subsequent chapters including detailed methodological explanations that would otherwise disrupt the presentation and discussion of results.

In general, ground observation principles and guidance for the preparation of fieldwork protocols are obtained from Conklin (2004) and McCoy (2005).

The following sections describe:

- the acquisition of EO space-borne data used in the research,
- the methodology applied for the software development and validation,
- ground observations procedures,
- the SAR data spatial analysis,
- interferometric processing software and additional related routines,
- the ground-based SAR system,
- the RT2 backscatter modelling software,
- and the classification procedure developed in the research, including introductory concepts of fuzzy logic.

4.1 Satellite Remote Sensing Data Acquisition

The acquired EO space-borne images cover the region surrounding Cranfield University. This region includes waste disposal sites about which records of on-site operations can be more easily obtained. Additionally, historical weather data related to these areas are also available.

4.1.1 SAR Data

Space-based SAR data used in this research include both historical and new scenes from the ESA ERS-1 and -2 satellites and additional programmed acquisitions from the ESA Envisat Advanced SAR (ASAR) instrument.

The historical ERS scenes were ordered using the Descw (ESA, 2007b) software, and obtained within the framework of an existing agreement between ESA and the Cranfield University SRC (agreement identification number: AOT.UK317).

The author submitted a research proposal through the ESA Principal Investigator portal (ESA, 2007a). The project was accepted on 17th February 2005 (i.e. Category-1 proposal, identification number: 3138) and this allowed the research to obtain the SAR data at reproduction cost only. The Descw software was again used to select the scenes of interest. The proposal, titled "Assessment of Hyperspectral and SAR Remote Sensing for Waste Landfill Management" envisaged the simultaneous acquisition of the two data sets (i.e. hyperspectral and SAR) from early spring to autumn 2005. Unfortunately the Envisat ASAR acquisitions experienced significant delays due to a number of reasons. The plan kept clashing with calibration/validation activities of the satellite and other acquisitions had to be cancelled due to technical reasons or due to conflicts with commercial requests (EOHelpDesk, 2005). This caused the plan to be postponed by 1 year. In 2006 the plan was completely re-submitted using the newly developed software EoliSA (ESA, 2007c). However, there were further delays in the delivery of the correct scenes due to a bug in the EoliSA system which generated the wrong start time when a given frame retrieved by the software was ordered (EOHelpDesk, 2006).

Despite these difficulties, all necessary data were successfully acquired. These are listed in Table 4-1. The Envisat ASAR scenes are in VV polarisation and with Image Swath 2 (i.e. swath width of 105 km and incidence angle ranging from 19.2° to 26.7°). The information related to the practicalities of requesting and obtaining satellite remote sensing data might not seem relevant to the research technical objectives, nonetheless they become very important when analysing the operational aspects of such application.

The author also submitted two additional data requests which have both been successfully accepted: the first by the Canadian Science and Operational Applications Research programme (research project reference number: 1719) for high resolution C-band SAR data from Radarsat-2 (i.e. ultra-fine beam mode, 20 km swath, 3x3 m ground resolution), and the second by the Japanese Advanced Land Observing Satellite (ALOS) (research project reference number: 3568) for L-band fully polarimetric data through a cooperative agreement between ESA and the Japan Aerospace Exploration Agency (JAXA). Unfortunately, due to launch and bureaucratic delays, the data will only be delivered outside of the timeline of this research.

Table 4-1. SAR data (all Envisat scenes have VV polarisation with a mean incidence angle of 23°).

Satellite	Date	Orbit	Track	Frame	Asce/Desc
ERS-1	25/06/1995	20623	94	2547	D
ERS-2	26/06/1995	950	94	2547	D
ERS-1	30/07/1995	21124	94	2547	D
ERS-2	31/07/1995	1451	94	2547	D
ERS-1	03/09/1995	21625	94	2547	D
ERS-2	04/09/1995	1952	94	2547	D
ERS-1	08/12/1995	23006	473	1035	A
ERS-2	09/12/1995	3333	473	1035	A
ERS-1	16/02/1996	24008	473	1035	A
ERS-2	17/02/1996	4335	473	1035	A
ERS-1	25/02/1996	24130	94	2547	D
ERS-2	26/02/1996	4457	94	2547	D
ERS-1	31/03/1996	24631	94	2547	D
ERS-2	01/04/1996	4958	94	2547	D
ERS-1	26/04/1996	25010	473	1035	A
ERS-2	27/04/1996	5337	473	1035	A
ERS-1	05/05/1996	25132	94	2547	D
ERS-2	06/05/1996	5459	94	2547	D
ERS-1	12/11/1999	43547	473	1035	A
ERS-2	13/11/1999	23874	473	1035	A
ERS-1	30/01/2000	44671	94	2547	D
ERS-2	31/01/2000	24998	94	2547	D
ERS-2	11/06/2001	32119	201	1035	A
ERS-2	28/06/2004	48044	94	2547	D
ERS-2	02/08/2004	48545	94	2547	D
ERS-2	06/09/2004	49046	94	2547	D
ERS-2	04/04/2005	52052	94	2547	D
ERS-2	09/05/2005	52553	94	2547	D
ERS-2	13/06/2005	53054	94	2547	D
ERS-2	18/07/2005	53555	94	2547	D
ERS-2	22/08/2005	54056	94	2547	D
ERS-2	26/09/2005	54557	94	2547	D
ERS-2	31/10/2005	55058	94	2547	D
ERS-2	05/12/2005	55559	94	2547	D
ENVISAT	15/04/2006	21569	473	1035	A
ENVISAT	24/04/2006	21691	94	2547	D
ENVISAT	20/05/2006	22070	473	1035	A
ENVISAT	29/05/2006	21691	94	2547	D
ENVISAT	24/06/2006	22571	473	1035	A
ENVISAT	03/07/2006	22693	94	2547	D
ENVISAT	07/08/2006	23194	94	2547	D
ENVISAT	02/09/2006	23573	473	1035	A

4.1.2 Optical Data

The hyperspectral data were collected by the Compact High Resolution Imaging Spectrometer (CHRIS) instrument onboard of the ESA Project for On-Board Autonomy (PROBA) spacecraft. As presented in Chapter 7, cloud cover was a major obstacle for suitable acquisition.

Supplementary optical scene were obtained from the following platforms: the French Système Probatoire d’Observation de la Terre (SPOT) 2 satellite, the NASA Landsat 4 and 7 satellites, and finally the multispectral Compact Airborne Spectrographic Imager (CASI). Specific information on all data sets is given throughout the report.

4.2 Overall Methodology for Software Development and Validation

Most of the data processing routines implemented in the research are developed using Matlab[®], a popular numerical computing environment and programming language, and the Interactive Data Language (IDL) which is also used by ENVI[®], a remote sensing exploitation platform. Appendix A lists all the routines and it provides two complete examples of the programming script (i.e. Appendix A.4 SARcrop.pro and Appendix A.7 coherence_correction.m). These two examples show the software has been extensively commented and explicitly validated. As illustrated in the block diagram in Figure 4-1, following the design phase, the implementation divides a single routine into a number of subroutines which are developed, tested and validated one by one. The various tests are carried out by adding “checks” in the script that allow the author to progressively verify the correctness of the overall procedure and the accuracy of the algorithm.

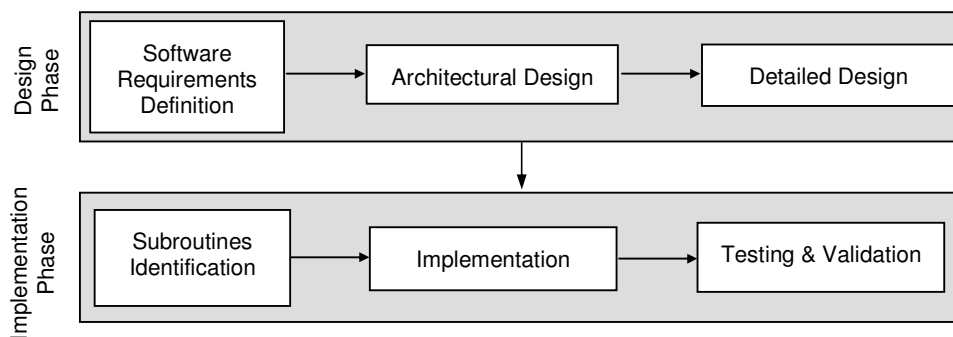


Figure 4-1. Design and implementation phases for the data processing routines.

4.3 Tools Used in the Preliminary Ground Observations

This section describes the tools and techniques used during the preliminary ground observations presented in the previous chapter.

4.3.1 Geometrical Properties of Bare Surfaces

As explained in Section 2.1.2, the SAR backscattered signal is also affected by the ground surface roughness, which can be characterised by the root mean square (rms) height, s , and the surface AC length, l , as explained in Equation 2-9. A soil meshboard profilometer, custom built by the author with the support of the Cranfield University Gas Turbine Workshop, is used to estimate these parameters over bare soil areas common to landfill sites.

The meshboard profilometer consists of a 1.227 m long rigid plate with a grid fixed on its surface. The apparatus is inserted in the soil and subsequently photographed. A spirit level glued to the profilometer is used to ensure the board top edge is horizontal. A digitization process is then required in order to transform the photographed profile into height coordinates. The main disadvantage of this technique lies in the disturbance of the soil surface, preventing an accurate repetition of the measurement. Nonetheless, this method is preferred to the initially used pin-profilometer provided by the Cranfield University National Soil Resources Institute as it achieves a higher sampling precision necessary for the X-band related measurements of the research. In fact, the horizontal spacing distance must satisfy the Ulaby et al. (1982) criteria such that $\Delta x \leq 0.1\lambda$. A short wavelength X-band systems therefore necessitates a 3 mm sampling distance which is not achievable by the pin-profilometer.

Figure 4-2 shows the first step of the digitization process: the geometric correction of the distorted 2048 by 1536 pixel photographs. The grid is only used as reference in order to correct such distortions and not to actually compute the height. Once the profilometer is geometrically corrected, the brightness and contrast of the meshboard area cropped out of the original picture are modified in order to increase the difference between the white profilometer surface and the darker soil. Then, the image is transformed into a black and white picture (Figure 4-3). Figure 4-4 shows that such a method achieves a nearly perfect match with the surface profile. The small discrepancies due to very thin items can be considered negligible due to their minute size (i.e. equal roughly to 1 mm). These two steps are carried out manually with Adobe® Photoshop, which is a powerful graphics editor. Clearly, this procedure would not be suitable for surfaces with a light colour (e.g. snow, white sand), but it satisfies the specific research measurements.

The black and white profile is then imported into Matlab[®] and processed by a routine called `soil_profile.m` (refer to Appendix A) that measures the height and computes s and l . The height is selected as the first black pixel encountered on each column starting from the top of the picture. An example of the height profile computed with `soil_profile.m` is presented in Figure 4-5.

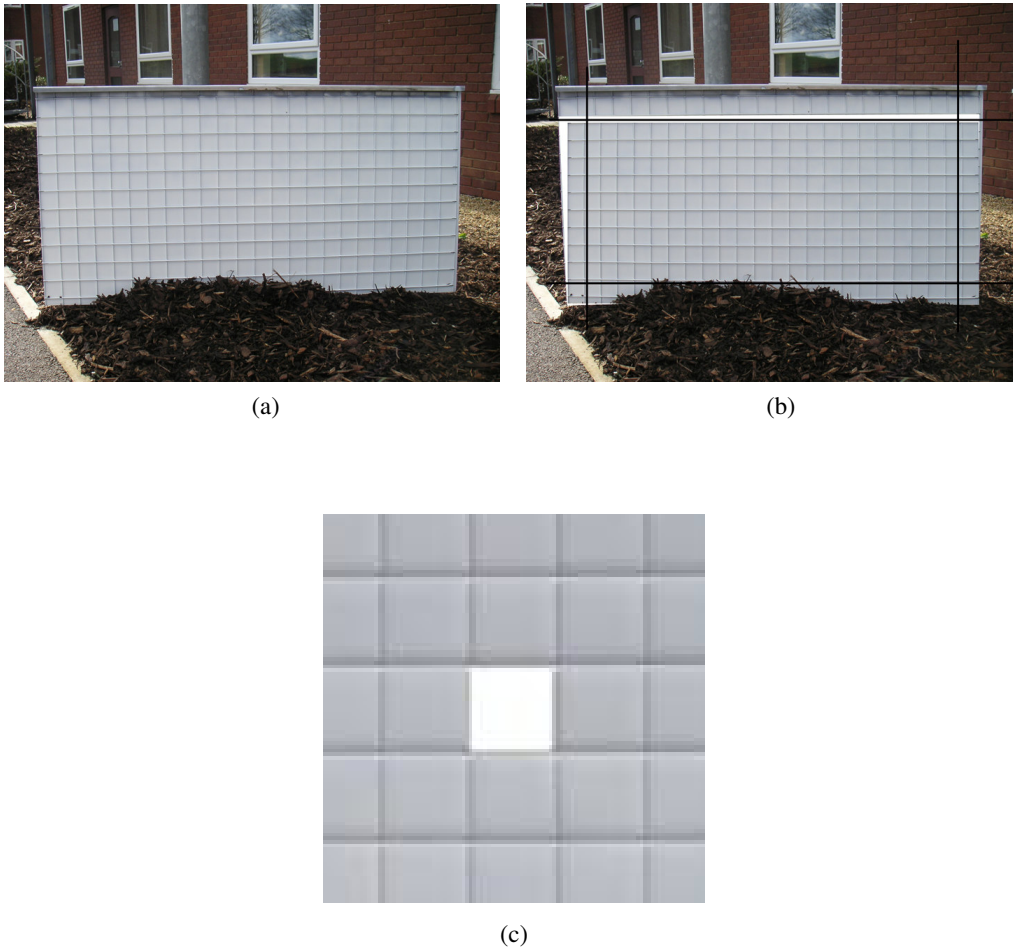


Figure 4-2. Profilometer picture distortion correction: (a) original picture, (b) distortion correction (c) validation that mesh grids are exactly squared.



Figure 4-3. Modification of the brightness and contrast of the profile images to obtain a black and white image only.

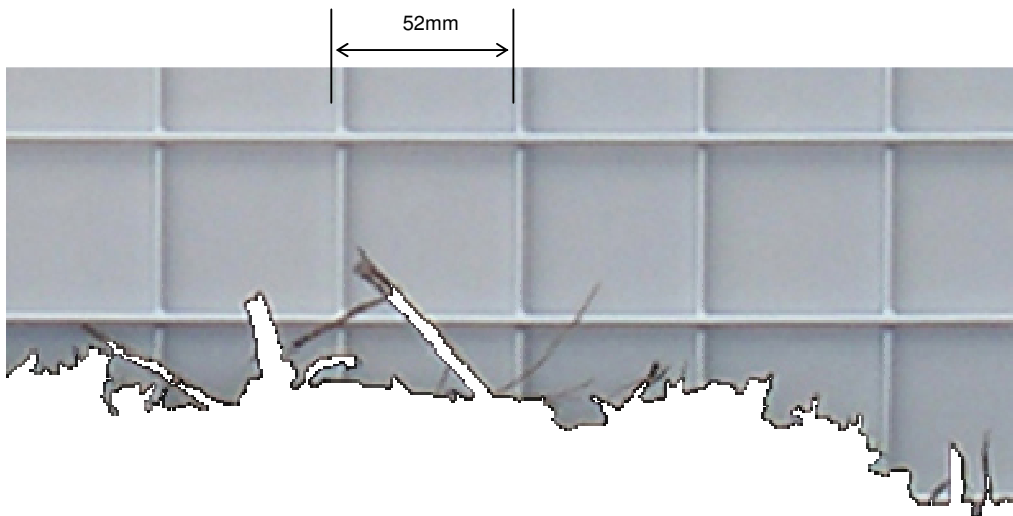


Figure 4-4. The black and white profile is used to mask the original image to verify the consistency of the developed technique.

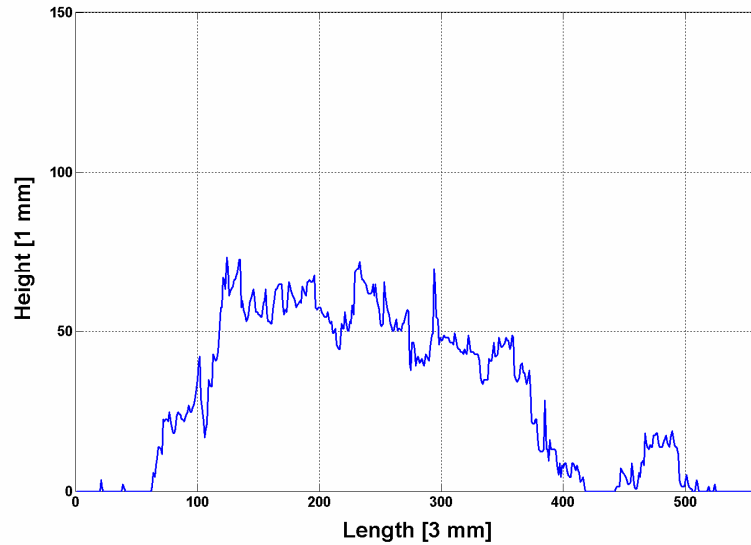


Figure 4-5. Digitized height profile computed with `soil_profile.m`. The vertical axis does not show the complete height of the profilometer, therefore the height appears distorted by around 5 times. Each interval on the horizontal axis represents 3 mm.

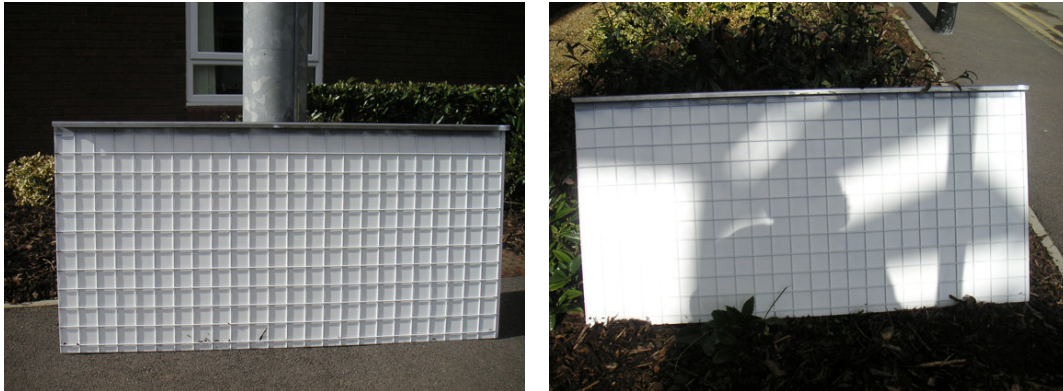


Figure 4-6. Unwanted shadows effects created by the mesh attached to the board and by other object projected on the board.

It is important to underline one drawback related to the specific meshboard profilometer built for the research. As visible in Figure 4-6 the grid can create dark unwanted shadows on the board itself. Other objects (e.g. trees, the person taking the picture) might also project shadows that can negatively impact the image processing steps based on the contrast between the white board and the bare soil. Careful consideration of such effects must therefore be taken into account when acquiring the pictures.

Justice and Townshend (1981) suggest a useful formula for determining the required area of a sample site that would achieve a representative and accurate estimation of these geometrical properties of bare surfaces present in landfill sites (i.e. tipping and capped areas):

$$A = P(1 + 2K) \quad \text{Equation 4-1}$$

where A is the minimum sample site dimension, P is the image pixel dimension, and K is the estimated location accuracy in number of pixels. Considering P as 25 m^2 (i.e. the range resolution for ERS SAR images) and K equal to 0.2 pixels due to azimuth resolution (i.e. 5 m), Equation 4-1 gives a sample area of 35 m^2 . This is selected for each of the two types of surfaces (i.e. tipping and capped areas).

As discussed by McCoy (2005), the number of samples per area can be calculated with the Fitzpatrick-Lins (1981) method:

$$N = Z^2 p q / E^2 \quad \text{Equation 4-2}$$

where N is the number of samples, Z is the standard normal deviate for a set confidence level, p is the expected accuracy of the measurements, q is $(100 - p)$, and E is the allowable error of the final results (i.e. $100 -$ the confidence level). It is therefore necessary to first establish what the accuracy of a single measurement is and then compute the number of samples that can satisfy a specific confidence level.

As presented in the next chapter, the preliminary observations also study the volumetric soil moisture and soil temperature of such areas. Nonetheless, because these readings are used to study the variances of such variables within each sample area and not to calculate their absolute value, which depends on weather conditions, the parameters in Equation 4-2 refer to the profilometer measurements.

Mattia et al. (2003) and Oh and Kay (1998) clarify that the precision associated with the rms height, s , and the AC length, l , depends on three factors: the sampling distance Δx on the profilometer, its overall length and the number of averaged segments, N , for the same surface. With the 3 mm sampling distance implemented in the measurements, Oh and Kay (1998) demonstrate that the measured accuracy reaches 99%, therefore not introducing any considerable error.

Still, Mattia et al. (2003) show that because the AC of a surface is a non-stationary process that is influenced by the length of the measurements, a short profilometer would introduce inaccuracies that can be partially diminished only by increasing the number of averaged segments. This is confirmed by Oh and Kay (1998), even though they argue that averaging multiple segments does not necessarily result in the same correlation

function. Generally, the shorter the segment length, the smaller the estimated values of s and l . The AC length is particularly affected by this limitation.

Setting a priori the AC length to 100 mm by making a reference to the work of Oh et al. (1992) and with 6 profilometer measurements next to each other on the same transect to achieve an overall profile of 7.326 m, results with a precision of about 82% of their mean values are obtained (Oh and Kay, 1998). From the simulations presented in their paper it is possible to extrapolate that in order to achieve a precision level of 90% suitable for the research, 5 such measurements are required. As presented in the next chapter, the final estimated AC length does not differ significantly from the one initially selected a priori, allowing the research to maintain the same error boundary of 18 %.

Hence, with such expected accuracy level and $N = 5$, Equation 4-2 gives an allowable error, E , of the estimated s and l over the whole surface equal to 18 % (i.e. $Z = 1.34$). This level of uncertainty is an acceptable result for the purpose of this study. Indeed, it allows the research to take into account the intrinsic level of variation of such areas by considering the error E not as an uncertainty but as the actual possible variation of these geometrical properties in other similar areas.

As highlighted by Mattia et al. (2003), all meshboard profilometer measurements must take into account that inaccuracies can arise because the picture of the intersection between the soil and the meshboard is not taken at ground level but at a height and distance which in the case of this research are respectively about 0.5 and 3 m. The height of any ground object that is actually physically separated from the meshboard surface is therefore projected at an angle onto it. The applied data collection procedure accounts for this factor by removing any significant material in front of the board that might generate such problems.

A systematic unaligned pattern (de Guijter, 1999), illustrated in Figure 4-7, was used as the sampling method for the 5 samples. The profile orientation for each sample was randomly chosen as long as no critical shadow effects were generated.

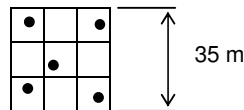


Figure 4-7. Systematic unaligned pattern sampling method with 5 samples applied to the two surfaces under examination.

4.3.2 Volumetric Soil Moisture and Soil Temperature

The volumetric soil moisture and soil temperature measurements, measured in the top 50 mm of the soil, are obtained using respectively a Theta probe HH2 manufactured by Delta-T Devices Ltd. and a standard digital soil thermometer. These were provided to the author by the Cranfield University National Soil Resources Institute.

Volumetric soil moisture content is the ratio between the volume of water present and the total volume of the sample. This is a dimensionless parameter, expressed either as a percentage (% vol), or a ratio ($\text{m}^3 \text{m}^{-3}$). Thus a value of 0 corresponds to a completely dry soil, and pure water gives a reading of 1. The Theta probe consists of a waterproof housing which contains the electronics, and, attached to it at one end, four sharpened stainless steel rods that are inserted into the soil. The probe generates a 100 MHz sinusoidal signal which is applied to a specially designed internal transmission line that extends into the soil by means of the four rods. The impedance of this array varies with the impedance of the soil, which has two components, the apparent dielectric constant and the ionic conductivity. The 100 MHz signal frequency is chosen to minimise the effect of ionic conductivity, so that changes in the transmission line impedance depend almost solely on the soil's apparent dielectric constant. Because the dielectric constant of water (circa 81) is very much higher than soil (typically 3 to 5) and air (1), the dielectric constant of soil is determined primarily by its water content (Delta-T Devices Ltd, 1999). Nonetheless, the soil water content measured by a Theta probe within one small locality can be affected by:

- the presence of air pockets around the rods, particularly around the central rod
- variations in soil density and composition
- stones and other material close to the rods
- roots (either nearby or pierced by the rods)
- subsoil drainage
- insertion angle
- small scale variability in transpiration and evaporation losses
- salinity variation

It is important to take the degree of variability of these various parameters into account when deciding on the number of probes to use at any particular location. If the soil is known to be very heterogeneous, it is necessary to take measurements from at least three closely-spaced locations. In addition to these sampling errors, there are others associated with the instrument itself and with the generalised calibration. As advised by Delta-T Devices Ltd. (1999), for each sample location, ten 0.5 m-spaced measurements are acquired and subsequently averaged. As discussed in the Theta probe manual (Delta-T Devices Ltd., 1999), the Theta probe percentage error is equal to 6 %.

No specifications for the digital soil thermometer accuracy are available. Although this does not have a significant impact on the overall research, for methodological completeness a value of $\pm 1^\circ \text{C}$ can be assumed.

4.4 SAR Amplitude Spatial Structure

In the field of geostatistics, or spatial statistics, many methods have been developed to describe different spatial textures. Numerous studies have shown that information on the image texture can be used to improve classification procedures. Many techniques, such as co-occurrence matrices (Haralick et al., 1973), local variance (Woodcock and Strahler, 1987), wavelets (Mallat, 1989) and spatial autocorrelation (Cliff and Ord, 1973; Woodcock et al., 1988a; Woodcock et al., 1988b) have been applied to extract information on the spatial variation of remotely sensed images. As discussed by Kandaswamy (2005) there is no general agreement on an overall best analysis method that outperforms all the others on various tasks such as classification or segmentation.

Based on the review presented by Schowengerdt (1997) and after investigating a number of techniques (Ottavianelli, 2004 and Ottavianelli et al., 2005), the author selected the power spectral density as the analysis procedure to study the spatial characteristics of landfill sites in SAR images as presented in Chapter 5. This method, also commonly known with the alternative term of power spectrum, is presented in the next sections.

It is essential to clarify that most of the previous studies on SAR data texture characteristics have focused on segmentation techniques that apply a sliding processing window over an entire image with specific attention to distributed targets. Some examples are Neeff et al., 2005; Dell'Acqua and Gamba, 2003; Oliver, 2000; Luckman et al., 1997. This research instead uses the spatial analysis to classify pre-selected areas of interest which present similar optical spectral signatures. This different approach is caused by the initial research objective derived from the optical data analysis.

4.4.1 Power Spectrum

The power spectrum is a processing technique that characterises spatial frequency and provides directional information for an image. In one dimension, the power spectrum can be defined as the Fourier transform of the autocorrelation function as defined in Equation 2-9. The computation can be extended to 2D images. By applying Parseval's theorem (James, 1999), the power spectrum can be computed in terms of the square of the complex Fourier coefficients of the 2D discrete Fourier transform $F(u,v)$, which for a spatial function $f(x,y)$ is defined mathematically as,

$$F(u,v) = \frac{1}{NM} \sum_{x=0}^{N-1} \sum_{y=0}^{M-1} f(x,y) e^{-2\pi i \left(\frac{ux}{N} + \frac{vy}{M} \right)} \quad \text{Equation 4-3}$$

where u , v are the spatial frequencies in the x and y dimensions, N is the number of pixels in the x dimension and M in the y dimension. These steps have been computed in Matlab with the routine PowerSpectrum.m (see Appendix A). An example is shown in

Figure 4-8. If the correlation length of the data is small, the power spectrum will be wide. Conversely, data with a high spatial correlation present a narrow spectrum, with little power at high frequencies. This method provides directional information about linear features such as edges and lines. The highest power components in the power spectrum image are orthogonal to the direction of such features present in the original image. This is noticeable also in Figure 4-8.

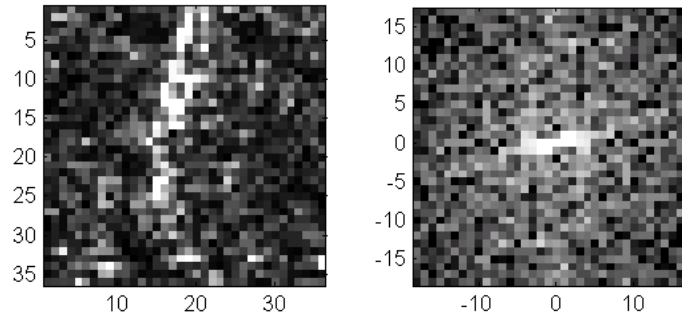


Figure 4-8. Power spectrum example. Left: original SAR amplitude data with 5 pixel averaging in the azimuth direction (i.e. each pixel represents a 25 m² area). Right: power spectrum computed with the Matlab routine PowerSpectrum.m. The numbers on the axis of the left and right images respectively represent the pixel number and the wavenumber.

4.4.2 The Application of Power Spectrum

Each radial distance from the centre of the image (i.e. all the points on a circle) corresponds to a wavenumber. Therefore, the power spectrum image can be rotationally averaged to compute the overall spatial frequency. Even if this step, developed in Matlab with `rotavg.m` (see Appendix A), partially smoothes evident linear features, as they are averaged with the rest of the image, it is still able to pick out anisotropic features which may not be strictly parallel or perpendicular to the image axis (Schowengerdt, 1997). The rotationally averaged power spectrum can be plotted on a log-log scale. This is illustrated in Figure 4-9. The linear trend obtained with an exponential regression indicates a power-law behaviour:

$$P(k) \propto k^{\beta} \quad , \quad \text{with } \beta < 0 \quad \text{Equation 4-4}$$

for all discrete wavenumbers k .

The analysis presented in Chapter 5 compares the power-law exponents, β , of a number of selected areas of interest to detect patterns in the spatial domain to support the identification of landfill sites by distinguishing them from other disturbed areas which present similar optical spectral signatures.

It is important to appreciate that the low frequency components might have a stronger influence than the low frequency ones when fitting the exponential regression. This can introduce errors in the methodology. Therefore, as presented in Chapter 5, results must be effectively validated.

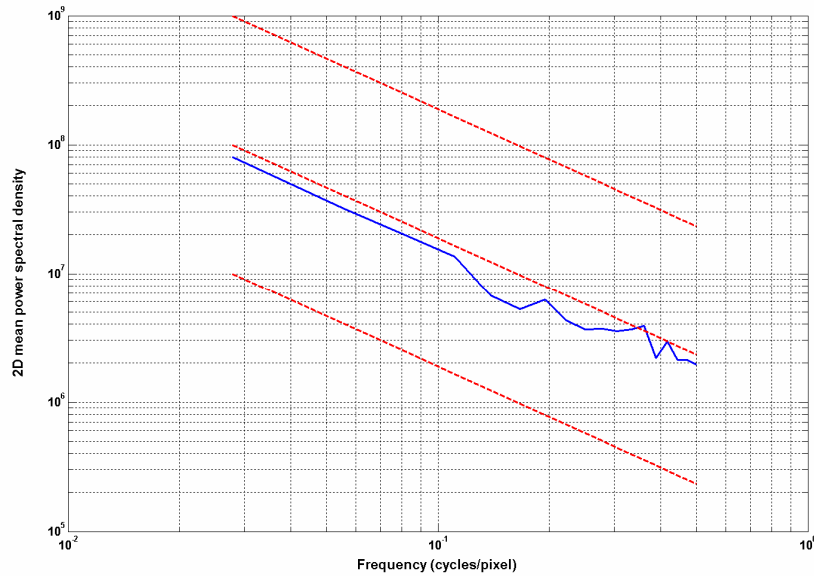


Figure 4-9. Log-log plot of the rotationally averaged power spectrum shown in Figure 4-8. The red dotted lines represent the trend of the data.

4.4.3 Radon Transform

As thoroughly explained by Toft (1996), the Radon transform computes projections of an image matrix along specified directions, θ . A projection of a two-dimensional function $f(x,y)$ corresponds to a set of line integrals. To represent an image, the radon function takes multiple, parallel-beam projections of the image from different angles by rotating the source around the centre of the image. As shown in Figure 4-10, the Radon transform can be used to detect specific features in an image. This highlights that in the 45° direction the pixels have higher values, and that they can be separable into two groups at θ equal to 135° .

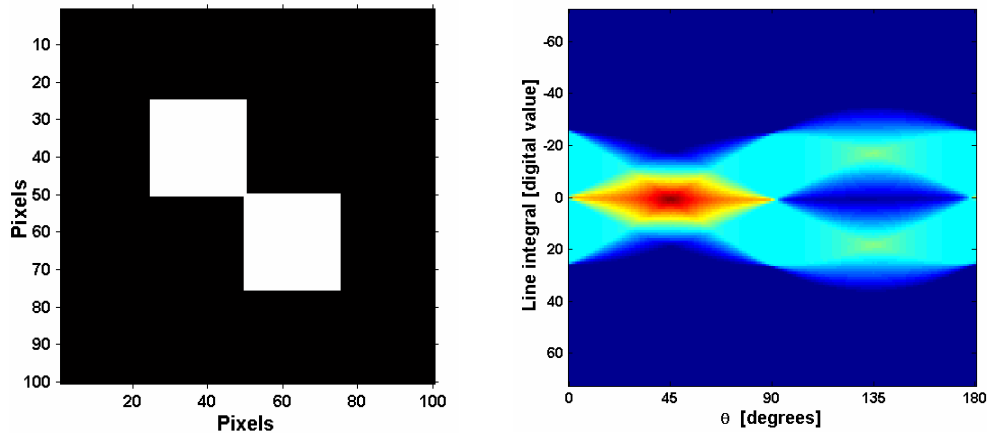


Figure 4-10. Example of Radon transform.

4.5 Interferometric Processing

The interferometric processing applied in the research is carried out with the Delft Object-oriented Radar Interferometric Software (DORIS), an open-source freely available modular software coded in C++ and developed by Delft University of Technology in the Netherlands. The author installed DORIS, together with the required support tools (i.e. the Getorb tool for precise orbit determination and the Snaphu software for phase unwrapping) on the Cranfield University Unix network. These programs are therefore accessible from any Linux machine or via a Linux emulator running on a Windows OS, providing an easy utilisation by any interested user (e.g. SRC Masters students or future research). A detailed explanation of how to access and use DORIS from Windows is provided in Appendix B.

Each DORIS module carries out a step of the interferometric processing and is independent from the others. Thus, as in this research, it can be substituted by another software that accomplishes the same function or additional processing steps can be added between any two modules. This software was selected because of such flexibility and its open-source characteristics. Extensive information on the software utilisation is provided by Kampes (2005). The program has also been extensively tested by Bruno (2003).

A complete overview of the processing chain applied in the research can be best achieved with a flow chart as in Figure 4-11. Some of these steps are briefly described in the following sections. Appendix B also includes all DORIS commands, or cards, used in the research with the specific settings for each processing step.

4.5.1 Reading SLC Data and Cropping a Sub-scene

IDL routines have been specifically developed by the author to read, visualise, crop and modify SLC data. These are presented in Appendix A and they are respectively named SAR_2or4B_read.pro, SARcrop.pro and SARmodify.pro.

The DORIS software is also able to perform these steps and it automatically creates the required files for subsequent interferometric processing. In fact, the relative geometry between the extracted sub-scene and the whole image is crucial to determine the correct satellite incidence angle during image acquisition.

All cropped sub-scenes are 1200 by 6000 pixels in range and azimuth respectively. As illustrated in Figure 4-12, they are centred on a specific image feature that presents constant scattering characteristics in time. This is the most southern of the three hangars next to the runway at Cranfield University (i.e. Building 83). The arrow in Figure 4-13 identifies the approximate location (i.e. $52^{\circ} 04' 12.9''$ North and $0^{\circ} 37' 36.00''$ West). Table 4-2 presents the exact selected pixel for each ERS tandem pair scene.

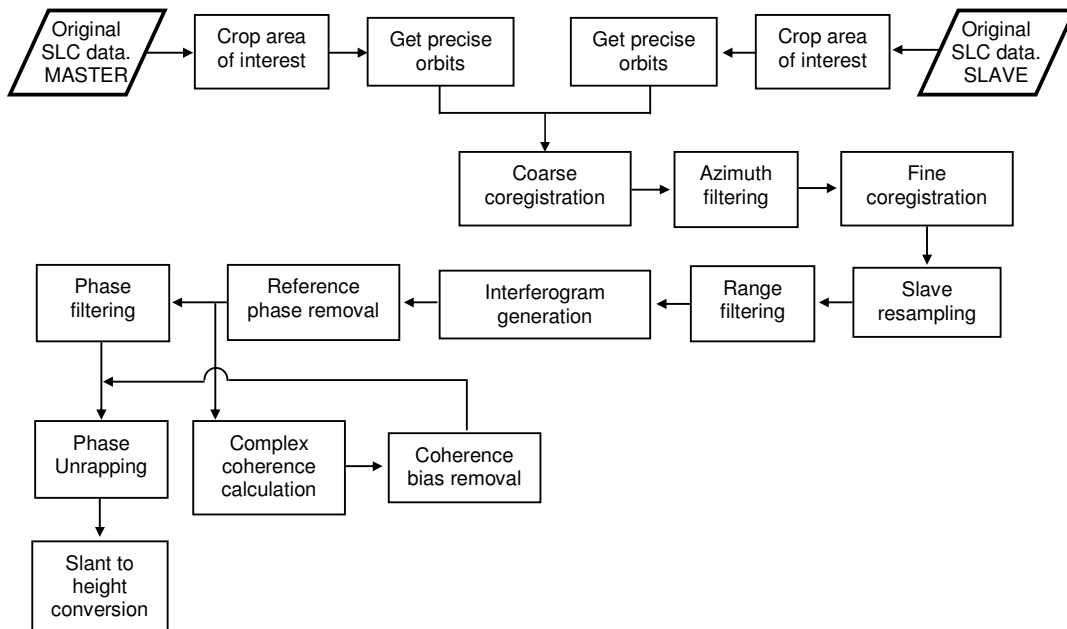


Figure 4-11. Interferometric processing chain using DORIS and other additional routines.

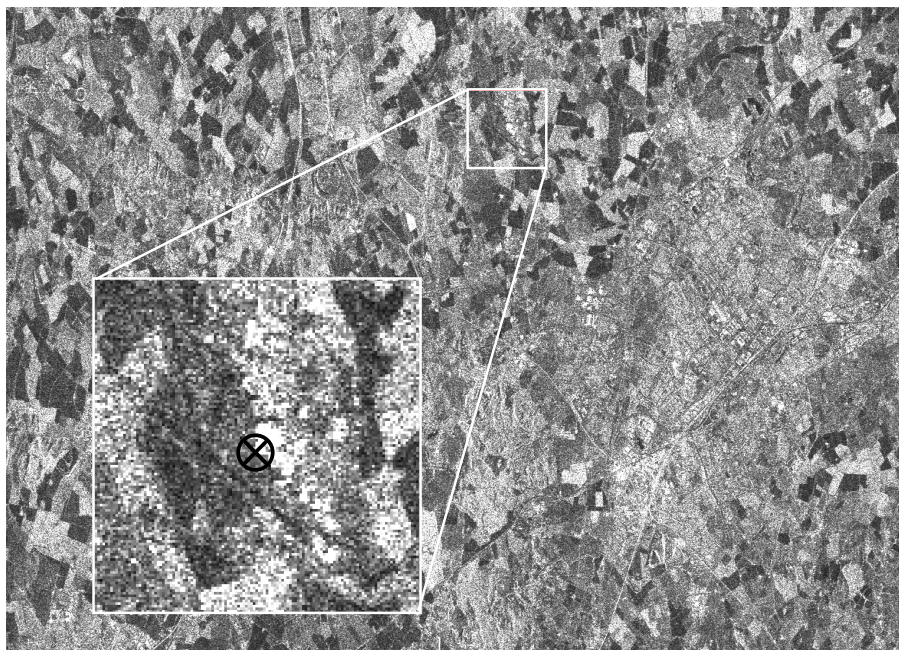


Figure 4-12. Detail of a ERS SAR sub-scene: amplitude data averaged by 5 in azimuth. The circled black cross identifies the selected feature with constant scattering characteristics used as centre when cropping the SLC scenes. Being a descending orbit scene, the image should be flipped horizontally to have a realistic view.



Figure 4-13. Aerial view of Cranfield University. The arrow identifies the selected feature with constant scattering characteristics used as centre when cropping the SLC.

Table 4-2. Perpendicular baseline and centre pixel location of the 1200 by 6000 pixels sub-scenes cropped from the ERS SAR tandem data.

Satellite	Orbit	Track	Frame	Asc/Desc.	Date	Perp. Baseline [m]	Centre Column	Centre Line
ERS-1	20623	94	2547	D	25/06/1995	-100.2	850	22294
ERS-2	950	94	2547	D	26/06/1995		856	22497
ERS-1	21124	94	2547	D	30/07/1995	16.3	814	22280
ERS-2	1451	94	2547	D	31/07/1995		640	22495
ERS-1	21625	94	2547	D	03/09/1995	-77.3	832	22193
ERS-2	1952	94	2547	D	04/09/1995		837	22524
ERS-1	23006	473	1035	A	08/12/1995	216.7	2860	17421
ERS-2	3333	473	1035	A	09/12/1995		2846	19233
ERS-1	24008	473	1035	A	16/02/1996	172.3	2860	18941
ERS-2	4335	473	1035	A	17/02/1996		2848	19094
ERS-1	24130	94	2547	D	25/02/1996	38.0	804	22390
ERS-2	4457	94	2547	D	26/02/1996		802	22514
ERS-1	24631	94	2547	D	31/03/1996	-92.1	846	22345
ERS-2	4958	94	2547	D	01/04/1996		854	22543
ERS-1	25010	473	1035	A	26/04/1996	29,7	2861	18931
ERS-2	5337	473	1035	A	27/04/1996		2852	19153
ERS-1	25132	94	2547	D	05/05/1996	-72,7	797	22295
ERS-2	5459	94	2547	D	06/05/1996		802	22495
ERS-1	43547	473	1035	A	12/11/1999	251.7	2846	18893
ERS-2	23874	473	1035	A	13/11/1999		2831	19189
ERS-1	44671	94	2547	D	30/01/2000	137.8	844	21598
ERS-2	24998	94	2547	D	31/01/2000		837	22550

4.5.2 Precise Orbit Determination

The precise orbit ephemerides, and the Getorb software used to extract them, are also provided by Delft. DORIS directly calls Getorb which computes the desired number of points interpolating the available ephemerides using cubic splines (Kampes, 2005). These data have an accuracy of 50 mm radially and 80 mm across-track (Kampes, 2005).

4.5.3 Coregistration

Once the orbit ephemerides have been determined, the master and slave images have to be coregistered exactly on the same grid. This is achieved in two steps, the coarse and fine coregistration. The first is based on the ephemerides data while the second is based on the spatial correlations computed in various areas of the master and slave images. A two-dimensional polynomial model for this offset is created for subsequent use by the resampling step. As documented by Kampes (2005), subpixel accuracy is achieved.

4.5.4 Azimuth and Range Filtering

Generating an interferogram includes a complex multiplication. This is equivalent to a convolution in the frequency domain. Therefore noise has to be removed before this process takes place to avoid it being smeared over the spectrum of the resulting interferogram (Hanssen, 2001).

The focusing of SAR images is based according to their Doppler centroid frequencies. They usually differ from one image to another, as a result the azimuth spectra of the two images being processed are not perfectly overlapping. Therefore, these non-overlapping parts of the spectra must be filtered out. This step is carried out following the coarse coregistration and before the fine coregistration. The DORIS filtering function performs a Fourier transform for every column and adjusts the spectra to the mean Doppler centroid frequency (Kampes, 2005).

The range filtering is instead applied to overcome the relative shift between the wavenumber spectra of the two images which is caused by the small difference in view incidence angles. This is also connected to the critical baseline concept presented in Section 2.1.5. Thus, the two non-overlapping parts of the spectra have to be filtered out with a bandpass filter in the frequency domain.

Kampes (2005) argues that azimuth filtering is very effective after the coarse coregistration step, while range filtering gives best results when used at the end of the coregistration process.

4.5.5 Resampling

This step resamples the slave image on the same grid of the master image by using the two-dimension polynomial computed during the coregistration step. The resampling process consists of two different parts: the reconstruction of a continuous signal from the slave image pixels by convolution with an interpolated kernel, and the sampling of this reconstructed signal at the new grid location with respect to the master reference frame.

4.5.6 Interferogram Generation

The interferogram generation theoretical background has been extensively discussed in the previous chapter. The processing window used in the research is 10 by 2 pixels respectively in azimuth and range. The outcome of this 20-look process is an image with 50 by 50 m spatial resolution.

4.5.7 Phase Filtering and Unwrapping

Following the interferogram generation and the subtraction of the reference ellipsoid, the phase is filtered to reduce the noise and improve its subsequent unwrapping. The research applies the Goldstein method presented in Goldstein and Werner (1998) with a processing window of 32 by 32 pixels and an alpha value of 0.8 (i.e. relative strong filtering). The phase unwrapping is achieved with the Statistical-cost Network-flow Algorithm for Phase Unwrapping (Snaphu) software developed at Stanford University. The software is directly called by a DORIS command. This program has been extensively tested by Bruno (2003) and Elder (2002). The description of the implemented algorithm is beyond the scope of this research. The reader can also refer to Chen and Zebker (2001) for a detailed analysis.

4.5.8 Slant-to-Height Conversion

The conversion from interferometric phase to terrain height is commonly known as phase to height conversion. The pixels remain in the range-azimuth radar coordinate system. Equation 2-21 is inverted to obtain the topographic height, considering null the surface displacement term. However, as illustrated in Figure 2-4, the perpendicular baseline as well as the look angle will change as soon as the initial height H_P has been derived. Hence, it is necessary to iteratively repeat this procedure until H_P satisfies some accuracy criterion (Hanssen, 2001).

The precision of the algorithm implemented in DORIS is tested on particular ground targets that are expected to present difficult height computation and phase unwrapping characteristics. In Figure 4-14 to Figure 4-17, the computed relative height of these targets is compared with ground data. Given the 50 by 50 m spatial resolution of the interferometric processing result, the achieved accuracy is very high. Generally, low coherence areas such as water bodies and forests are also correctly processed. Inaccuracies occur in the presence of structures with large vertical extent (i.e. around 15m) but small footprint (Figure 4-16) or areas where many large buildings with different orientations are present (Figure 4-17). It is also important to clarify that the absolute computation of topography is not very precise. This issue is discussed by Bruno (2003) but it is not critical to the objectives of this research.

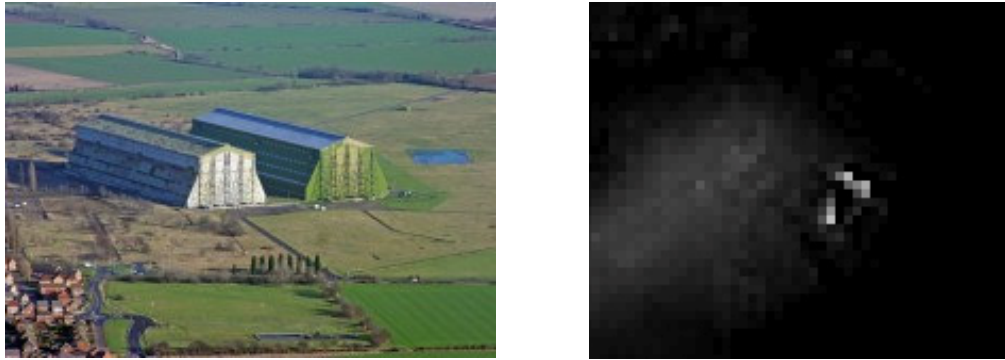


Figure 4-14. Left: oblique aerial view of the two Cardington hangars, just south of Bedford (UK), built in the early 1920s for the construction of airships. They measure 247 m in length, 84 m in width and 55 m in height. Right: height computed with the first ERS interferometric tandem pair (i.e. 25th and 26th June 1995). The average computed height of the two hangars is 54 m. The two images have a different scale and orientation, and are presented for illustration purposes only.



Figure 4-15. Left: aerial view of the Bedford-Luton (UK) train line tunnel between Milbrook and Amphill (Google Earth, 2007; with the education setting reproduction agreements). The height step change before the train enters the tunnel is roughly equal to 12 m. Right: height computed with the first ERS interferometric tandem pair (i.e. 25th and 26th June 1995). The average computed height at the two exits is 11.5 m. The two images have a different scale and orientation, and are presented for illustration purposes only.



Figure 4-16. Left: aerial view of disused grain silos located on Station road, Turvey, Bedfordshire (UK) (Google Earth, 2007; with the education setting reproduction agreements). These buildings are 30 m high Bedford Borough Council (2007). Right: height computed with the first ERS interferometric tandem pair (i.e. 25th and 26th June 1995). The phase unwrapping algorithm is not able to successfully compute an accurate height of these structures. The two images have a different scale and orientation, and are presented for illustration purposes only.

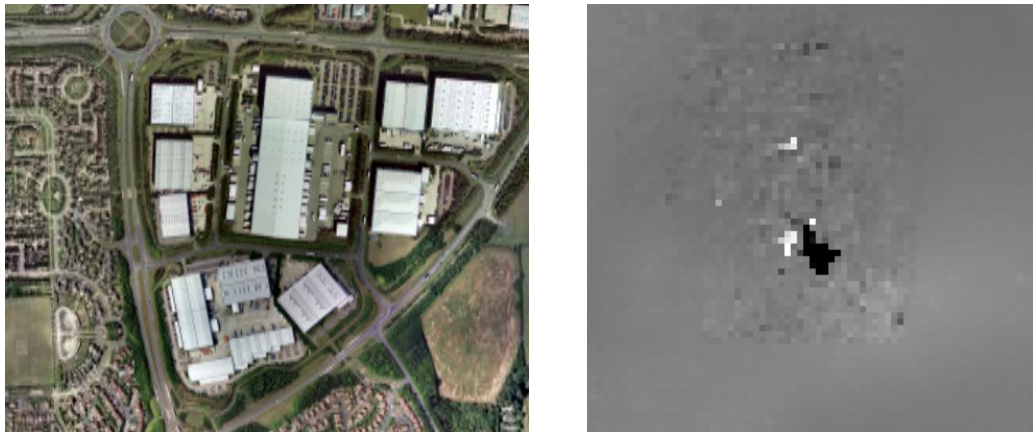


Figure 4-17. Left: aerial view of industrial units located in the south-east area of Milton Keynes (UK). (Google Earth, 2007; with the education setting reproduction agreements). Right: height computed with the first ERS interferometric tandem pair (i.e. 25th and 26th June 1995). The phase unwrapping algorithm is not able to successfully compute an accurate height of these buildings. The two images have a different scale and orientation, and are presented for illustration purposes only.

4.5.9 SAR SLC Image Terrain Correction

Once the topography of the sub-scene has been computed, it is possible to correct the original SLC images from the distortion generated by the local height. As the region under investigation presents a very gentle topography, it is possible to implement a simple algorithm that applies this correction. As explained in Section 2.1.1, the distance from the antenna to the target measured by the radar is defined as the slant range, sl_r (Figure 4-18). Ground range is its projection on the ground. Based on the topographic information computed through the interferometric process, ground range can be determined by Equation 4-5. The effectiveness and accuracy of this simplified algorithm has been validated by Rees and Steel (2001). This routine processes the data line by line in the range direction, starting from the closer range pixel, and it has been developed in Matlab (`terrain_correction.m`, refer to Appendix A). An example of the results is presented in Figure 4-19.

$$gr_r = \sqrt{sl_r^2 - (H_{sat} - z)^2} \quad \text{Equation 4-5 (Hein, 2004)}$$

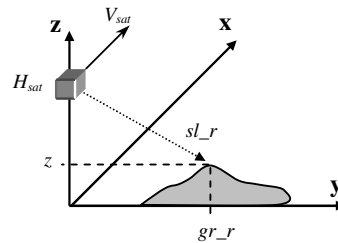


Figure 4-18. Slant range – ground range conversion (Hein, 2004).

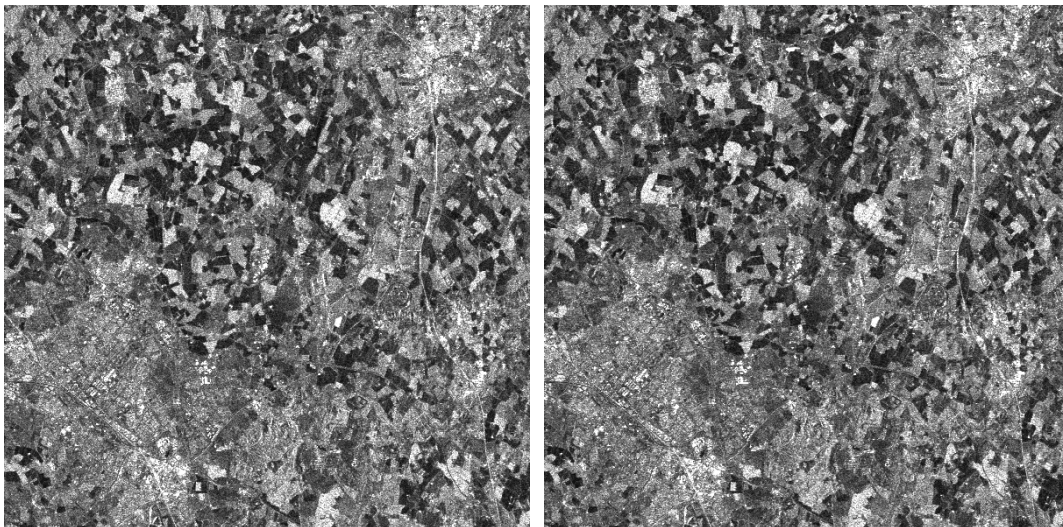


Figure 4-19. Slant-ground range conversion for the sub-scene of 25th June 1995. Even if not apparent, the corrected image (right) presents some black pixels on its right edge due to the shift linked to topography.

4.5.10 DORIS Interferometric Coherence Calculation Testing

Tests are carried out to assess the accuracy of the coherence calculation performed by the DORIS software. Figure 4-20 shows an ERS 1 sub-scene with modified values of magnitude and phase with Gaussian noise over a rectangular box. This image is then used to compute the interferometric coherence with the original sub-scene. The result is illustrated in Figure 4-21. This simple test confirms the expected outcome: absolute coherence over the whole sub-scene except for the modified patch. A closer look at the magnitude of the coherence (Figure 4-22) highlights the blurring due to the moving window of the computation algorithm, obtaining lower values of coherence over unchanged areas and higher values over noisy areas. This matter is addressed in the next section.

Discussion with Kampes (2006) pointed out that the estimated coherence by DORIS is not bias corrected. The next section also describes this step which is implemented with an external Matlab routine.

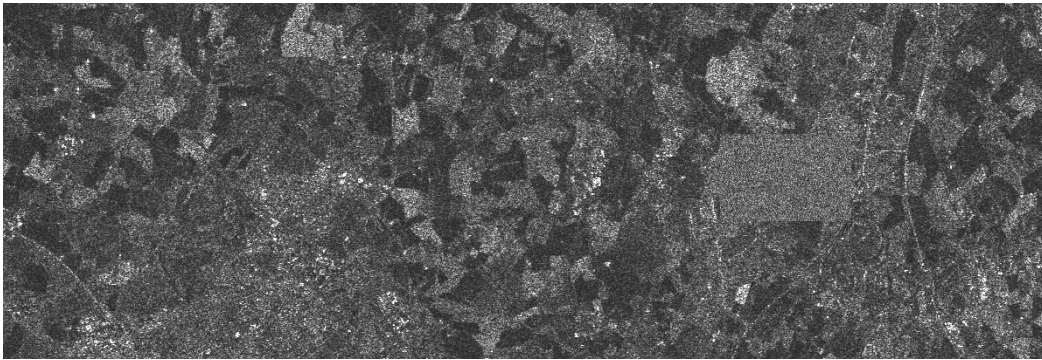


Figure 4-20. This image shows the amplitude of a modified ERS 1 sub-scene acquired on 25 June 1995 and averaged by 5 in azimuth. Complex Gaussian noise is added in a rectangle in the right half.

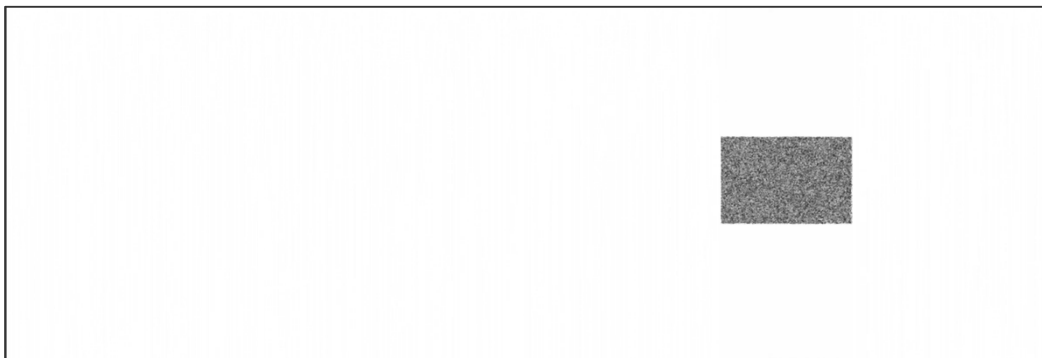


Figure 4-21. Magnitude of interferometric coherence between original and modified ERS 1 sub scenes.

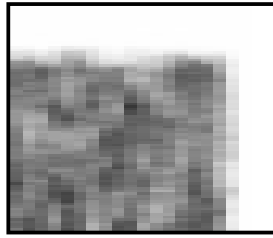


Figure 4-22. Zoom into the top right corner of the magnitude of interferometric coherence between original and modified ERS 1 sub scenes.

4.5.11 Coherence Bias Correction

The coherence bias correction, discussed in 2.1.6, is applied before the phase unwrapping step because it is then used to modify specific parameters in the unwrapping process (Kampes, 2005). In fact, as explained in Section 2.1.6, the magnitude of the complex coherence, or degree of coherence $|\gamma|$, can be considered as a measure of the interferometric phase noise.

The flow chart in Figure 4-23 illustrates the process implemented in this research. This is a spatially adaptive algorithm conceptually similar to the one presented in Weydahl (2001). However, instead of applying a Sobel operator to select a directional subset on a 3 by 3 pixel moving window, the developed routine selects the pixels to be processed if they fall within the standard deviation of the biased coherence of the central pixel. As explained by Weydahl (2001), this process increases the ENL without losing resolution. The example in Figure 4-24 shows that better contrast and more defined boundaries are obtained between high- and low-coherence areas, therefore partially correcting the blurring effect pointed out in the previous section.

The bias of the averaged value is ultimately corrected based on the new ENL. This routine therefore maintains low ENL in areas affected by a rapidly changing coherence which corresponds to a high level of uncertainty of the interferometric phase. This is shown as well in Figure 4-24.

The Matlab routine that applies this algorithm is `coherence_correction.m` and is presented in Appendix A. This function calls two additional routines to compute the coherence standard deviation (i.e. `coherence_sd.m`, refer to Appendix A) and the hypergeometric function (i.e. Equation 2-26) (`genHyper.m`).

Due to extensive computational requirements of this algorithm, the routine asks the user to select a specific area of interest on which to apply the routine. A Pentium III processor (i.e. 934 MHz 512 Mb of RAM) takes about 2.5 hours to process 100 pixels.

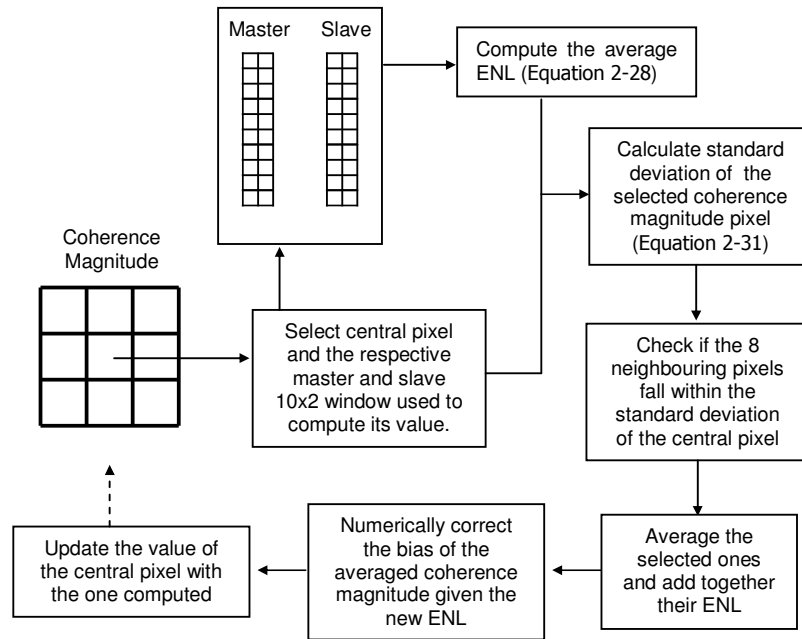


Figure 4-23. Flow chart of coherence magnitude bias correction routine. This is repeated for each pixel of the area of interest selected by the user.

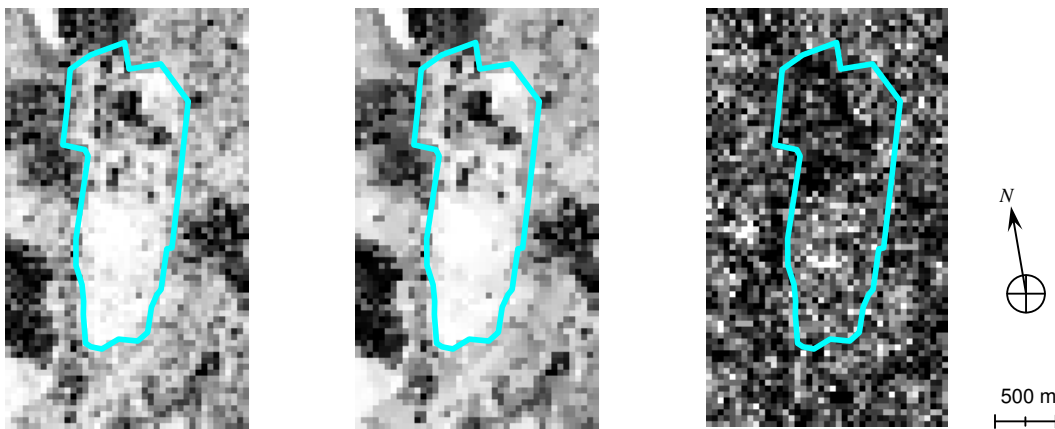


Figure 4-24. Example of coherence bias correction applied on the Brogborough landfill, which is identified by the turquoise contour. The image on the left is the original biased coherence computed with a 10 by 2 pixels (in azimuth and range respectively) processing window. The middle image shows the result of the algorithm implemented in the research. It is possible to notice without losing spatial resolution, the procedure obtains better contrast and more defined boundaries between high- and low-coherence areas. The image on the right shows the ENL for each pixel. Dark pixels correspond to a low ENL, whilst white pixels correspond to a high ENL.

4.6 Ground-Based SAR

Because no exact ground reference information relative to the historical SAR data is available to relate SAR backscatter values with on-site conditions, additional measurements are therefore required in order to obtain the SAR backscatter coefficient values for areas common to waste disposal sites.

The research therefore utilises a fully portable and polarimetric ground based SAR (GB-SAR) system. This apparatus (Figure 4-25 and Figure 4-26) was originally developed at the University of Sheffield (Bennett et al., 2000), but it is now managed by Cranfield University at the Shrivenham Royal Military College of Science.

The synthetic aperture is formed by using a 4 m long precision linear scanner to position the antenna at suitable sampling intervals along the scanner length. At each sample point, for each polarisation combination (VV, VH, HV, HH), the frequency response of the environment is measured by an HP 8720 DX vector network analyser (VNA) at a set of discrete frequencies over a bandwidth of interest. These data are then processed using SAR and pulse synthesis techniques to create multi-polarimetric images of the target surface over an area of typically 1,000 m². A Pentium PC is used to control the elements of the system, which include the scanning drives and the levelling motors, VNA and weather station.



Figure 4-25. Left: GB-SAR stowed configuration. The 4-wheel-drive vehicle is used to transport it and house the majority of the instrumentation. Right: GB-SAR set-up, with the hydraulic lift not deployed and the C-band antennas pointing horizontally



Figure 4-26. GB-SAR system deployed at a height of 10 m. The antenna incidence angle θ is set a 45° . The weather station has not been installed.

4.6.1 GB-SAR System Modifications

The GB-SAR system had not been used since 1998 and a new configuration is tested by Dr Morrison and the author in order to assist the signal to noise ratio of the system. The VNA initially housed in the rear of the vehicle is now set up on the hydraulic lift basket, close to the antennas. Two extenders are used to link the PC to the VNA. The antennas are then connected to the VNA by Gore low-loss cables. The system two-way path length is therefore reduced from 66 m to ~ 15 m. As the GB-SAR is usually deployed at a height of 10 m, there will be a large path difference between the VNA and reference channels. This is compensated for by inserting variable lengths of Andrew heliax cable, with a suitable amplifier, between the reference ports and the VNA. This modification is very important in order to maximise the frequency scan rate of the VNA during data acquisition. This new configuration is shown in Figure 4-27.

With regards to the system signal to noise ratio, the minimum detectable radar cross section, σ_{\min} , depends upon the sensitivity of the receiver in the VNA. The smaller σ_{\min} , the more sensitive the system. The following equation can be used to compute σ_{\min} at different distances:

$$\sigma_{\min} \equiv (4\pi)^3 \frac{P_r}{P_t} \frac{R^4}{G_t G_r \lambda^2} \frac{L_t L_r F}{N_f N_x} \quad \text{Equation 4-6}$$

where P_r = VNA receiver noise floor

P_t = VNA output power

G_t = transmit antenna gain

G_r = receive antenna gain

L_t = transmit cable attenuation losses

L_r = receive cable attenuation losses

R = range to target

λ = wavelength

N_f = number of frequencies

N_x = number of spatial samples

F = VNA Intermediate Frequency bandwidth figure

This formula implemented in GBSAR_min_RCS.m (refer to Appendix A), gives the following results:

Table 4-3. Variation of σ_{\min} with range at C-band.

Range [m]	σ_{\min} [dB]
5	-60
10	-49
15	-41
20	-36

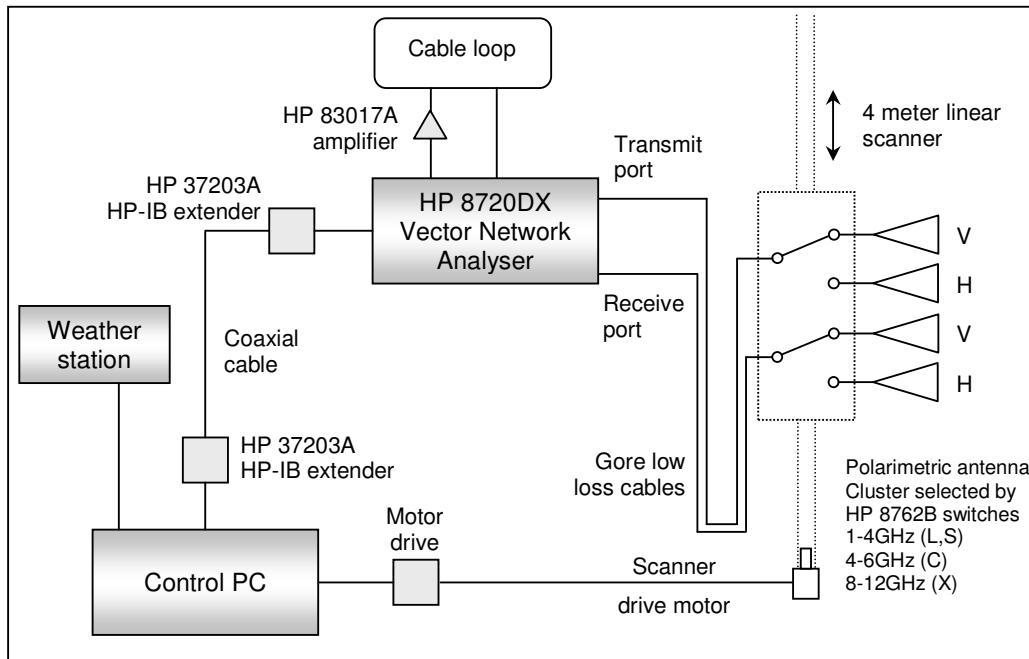


Figure 4-27. New GB-SAR system configuration.

4.6.2 Initial Testing and Validation

With a C-band antenna, the system data processing (Bennett and Morrison, 1996) achieves an average 100 by 200 mm resolution, with complex values of phase and magnitude. A new processing algorithm is developed to test the validity of the new GB-SAR system configuration. This algorithm applies an inverse fast Fourier transform (FFT) on the frequency response at each sample point and derives the backscatter amplitude against the distance in ground range.

An initial test involved the exclusion of the antenna in the system by directly connecting the two Gore cables together. The inverse FFT of a single sample is shown in Figure 4-28. This is then compared with the results obtained with the antenna connected and positioned at a height of 4 m, pointing nadir to the ground. A third acquisition is carried out with a corner reflector on a 1.3 m high stand looking directly to the antenna, as pictured in Figure 4-29. The results, presented in Figure 4-30, show that the new GB-SAR system configuration is operating correctly. In fact, the green line represents the scan with the Gore cables connected together as in Figure 4-28. The blue line represents the scan with the antenna pointing nadir to the ground from a height of 4 m. The red line illustrates the backscattered signal of a single scan with the antenna pointing nadir to the ground from a height of 4 m and with a corner reflector on a 1.3 m high stand looking directly to the antenna. It is possible to notice that the signal from the connected cables is still present even when the antenna is connected. The only difference is due to a shift in distance by about 60 cm. This is due to the antenna horns coupling, with the transmitted signal immediately entering the receiver. The two other peaks at circa 1295 and 1275 (pixel number) correspond respectively to the corner reflector and the ground. The red line is in fact also visible (i.e. reaching only - 4.5dB) at the ground distance. Two test acquisitions in an open field with a tree and in a car park validated the system.

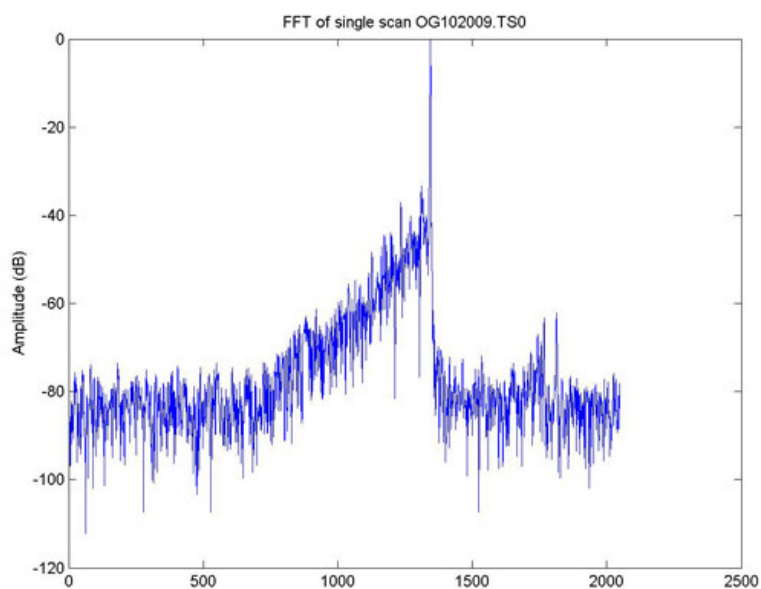


Figure 4-28. Inverse FFT of a single scan with the Gore cables connected together. The amplitude is in dB and normalised to the maximum value. The abscissa represents range in pixels, with every pixel corresponding to 0.0586 m. The peak corresponds to the distance of the cables (i.e. 15 m).



Figure 4-29. Levelled trihedral position at nadir at a height of 1.3m.

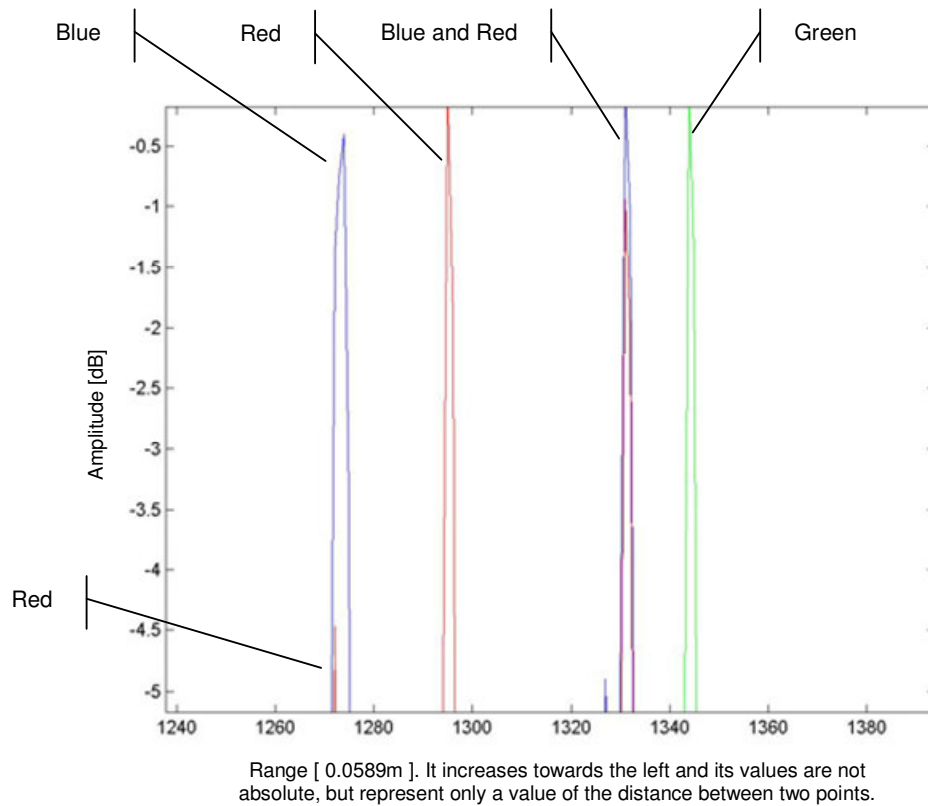


Figure 4-30. Inverse FFT of a single scan of three acquisitions. The y-axis represents the amplitude in dB normalised to the maximum value (i.e. the return signal with the Gore cables connected together), and plotted from 0 to -5dB. The abscissa represents range in pixels, with every pixel corresponding to 0.0586 m. Range increases towards the left. The abscissa values are not absolute, but represent only a value of the distance between two points. Refer to main text for detailed explanation.

4.6.3 GB-SAR Data Processing

For each acquisition the GB-SAR system is polarimetrically calibrated against a known reference target (i.e. levelled trihedral). The error margin is better than ± 0.8 dB.

The raw binary data saved in the PC are processed with a software tool called GBSARCVT.EXE to transform them into ASCII (American Standard Code for Information Interchange) format and compute the backscatter amplitude. Unfortunately, even if not critical to the research objectives, this process does not compute the phase information from the complex data.

The fully polarisation calibrated data are then imported into ENVI using an IDL routine named GBSAR_read.pro (refer to Appendix A). As explained by Bennett (2005), the mean system resolution is 100 mm in azimuth and 200 mm in range, but it slightly

varies depending on the incidence angle and the pixel position in azimuth. Additionally, the GBSARCVT.EXE software creates a 40 by 40 mm image interpolating the coarser system spatial resolution and not taking into account its variation in the image. Therefore, in order to obtain a 40x40 mm pixel image that contains the correct proportional values of backscatter amplitude which depend on the system ground resolution at a given position in range and azimuth, a new data processing routine is implemented by the author in IDL (GBSAR_proportional.pro listed in Appendix A). Finally the amplitude data are transformed into backscatter coefficient values using GBSAR_sigma0.pro (refer to Appendix A).

4.7 RT2 Software

As will be presented in Chapter 6, simulations based on the RT2 backscatter modelling software are used to carry out a quantitative sensitivity analysis on the variables affecting the radar backscatter from bare soils. This section introduces the RT2 program to the reader.

RT2 is a radiative transfer model simulator developed by ESA under task 4, contract 10644/93/NL/NB (Knight, 1997), with the scientific goal of assisting the study of radar signatures from the interaction with soil and canopy. The program is run from a Sun Operating System and consists of three modules: rtsetup, RT2, and read_and_write.

The first module, rtsetup, is used to create a model input file (extension .rtm) to be used by the RT2 module. The graphical user interface of rtsetup is shown in Figure 4-31. This allows the user to define the radar, soil and surface scattering model parameters. As the study concentrates on bare soils, the canopy layers parameters are not used. In addition to the ground roughness and correlation length, it is possible to define the volumetric soil moisture and the soil morphological structure, or soil texture, defined by percentage values of three soil components: clay, silt and sand. This parameter designates the proportionate distribution of the different sizes of mineral particles in a soil, excluding any organic matter. According to their size, these mineral particles are grouped into separates which can be classified following the US Department of Agriculture system of nomenclature as shown in Figure 4-32. Since various sizes of particle have quite different physical characteristics, the nature of mineral soils is determined to a remarkable degree by the particular separate that is present in larger amounts (USDA, 2007). Together with the volumetric soil moisture, soil texture is in fact used to compute the susceptibility characteristics of the soil which affect both radar backscatter amplitude and phase.

Once the model file has been created, the RT2 module calculates the backscatter coefficients for the four polarisation combinations and the vertical penetration depths for each vegetation layer. When the program is run for bare soil, as in this study, the

output for the layer depth is given as 0.1 E+007 m, simply meaning that they have not been computed.

In the program control section of rtsetup, a choice can be made between the two modes in which the software can run: single- or multi-variable mode. In the single mode the RT2 output is given for one specific setting. In multi-variable instead, one of the input parameters (e.g. radar incidence angle, soil moisture, ground roughness) can be varied over a user defined range for which RT2 simulates the radar signature. When run in the multi-variable mode, the RT2 module has to be operated by the Sun OS command window.

Finally, the read_and_write module, not actually used in this research, uses the output of the RT2 module to calculate the contribution of the total backscatter from the different layers of vegetation.

This software has been extensively tested and used by the Cranfield University SRC by Bobolina (2005) and Seynat (2000).

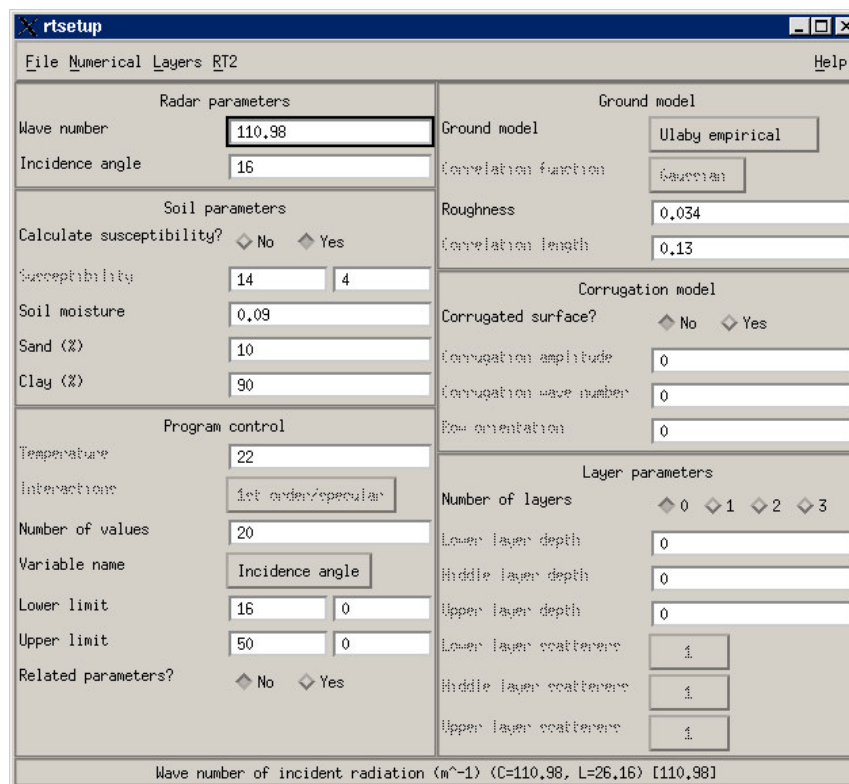
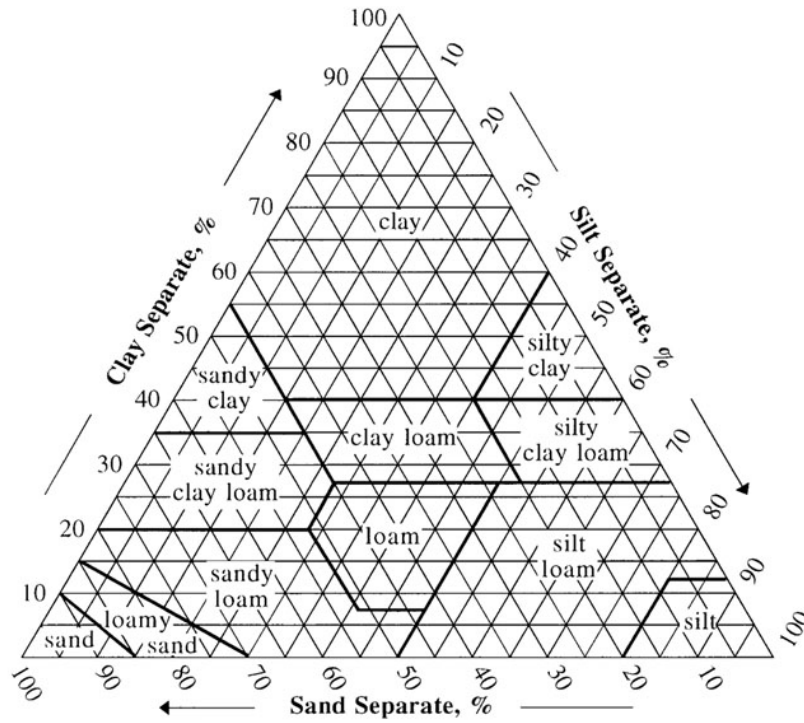


Figure 4-31. RT2 backscatter modelling software. The rtsetup modules allows the user to define the surface parameters.



COMPARISON OF PARTICLE SIZE SCALES

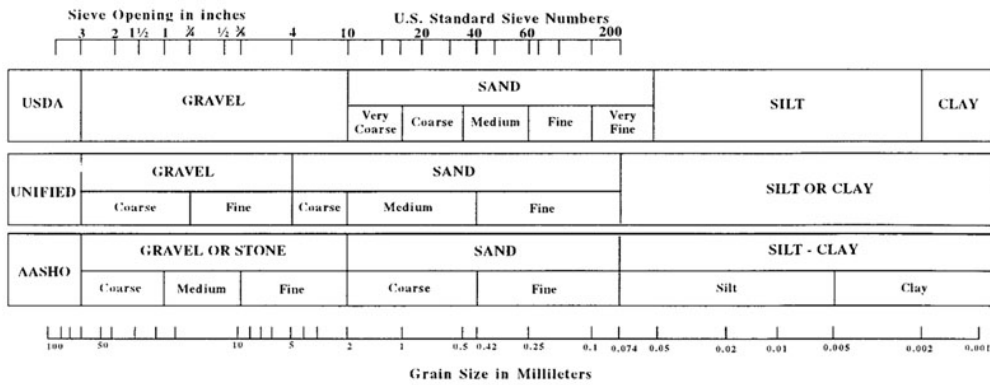


Figure 4-32. Soil texture. Classification of separates (USDA, 2007).

4.8 Ascending and Descending Scenes Coregistration

The research explores SAR data acquired from both ascending and descending orbits. In some instances, these scenes, or products derived from them, are merged together into a single image. As briefly explained in Section 2.1.2, foreshortening, layover and shadow effects in the radar slant direction can have a drastic impact on an image especially in the presence of steep topography. Due to the different points of view of the ascending and descending scenes, these distortion effects are produced in different directions and consequently the combination of such data sets must be carried out with particular attention. This matter has not been significantly investigated in the literature. The fusion of multi-angle ERS-1 and 2 tandem data has been applied in previous research (Sansosti et al., 1999; Coltelli et al., 1998 and Carrasco et al., 1997) to improve the accuracy of digital elevation models and to detect ground displacements in three dimensions as opposed to a single-orbit-direction tandem pair which can instead only detect displacements in the SAR slant direction. More specifically, Werner et al. (2002) discuss issues related to SAR geocoding and multi-sensor image registration. They use the satellite orbit and local terrain information to reduce coregistration errors. They also select recognisable image features as ground control points as an additional aid. Their analysis highlights the problem of selecting certain persistent scatterers which might not have the same position in the ascending and descending images due to their height (e.g. high buildings). The utilisation of SAR images with different acquisition geometries has also been applied by Dell'Acqua et al. (2003). They manually coregister three simulated SAR images with 3 m ground resolution and generated each with a different viewing geometry. Dell'Acqua et al. (2003) try to extract an accurate map of the road system of the city of Pavia in northern Italy and do not use the images for a direct multi-band classification because the same buildings have a difference appearance in the two images.

Taking in consideration such constraints, the research implements a novel algorithm which is illustrated in Figure 4-33. This method first coregisters the two coherence magnitude images obtained respectively from the ascending and descending tandem pairs and then applies the same coregistration settings to the SAR data (e.g. amplitude images). As such, the algorithm is specifically developed for the SAR images that are part of a tandem pair.

In more details, the terrain correction, as described in Section 4.5.9, is first applied on the two coherence magnitude sub-scenes by using the topography information obtained from the interferometric processing. Subsequently, ground features for which no SAR induced distortion is expected are selected as control points for the coregistration spatial transformation. Areas such as boundaries between agricultural fields, road intersections, edges of water bodies and other low-height man-made features are very suitable for such methodology. The coherence image is used instead of the original SLC data because it allows the user to identify these areas more accurately.

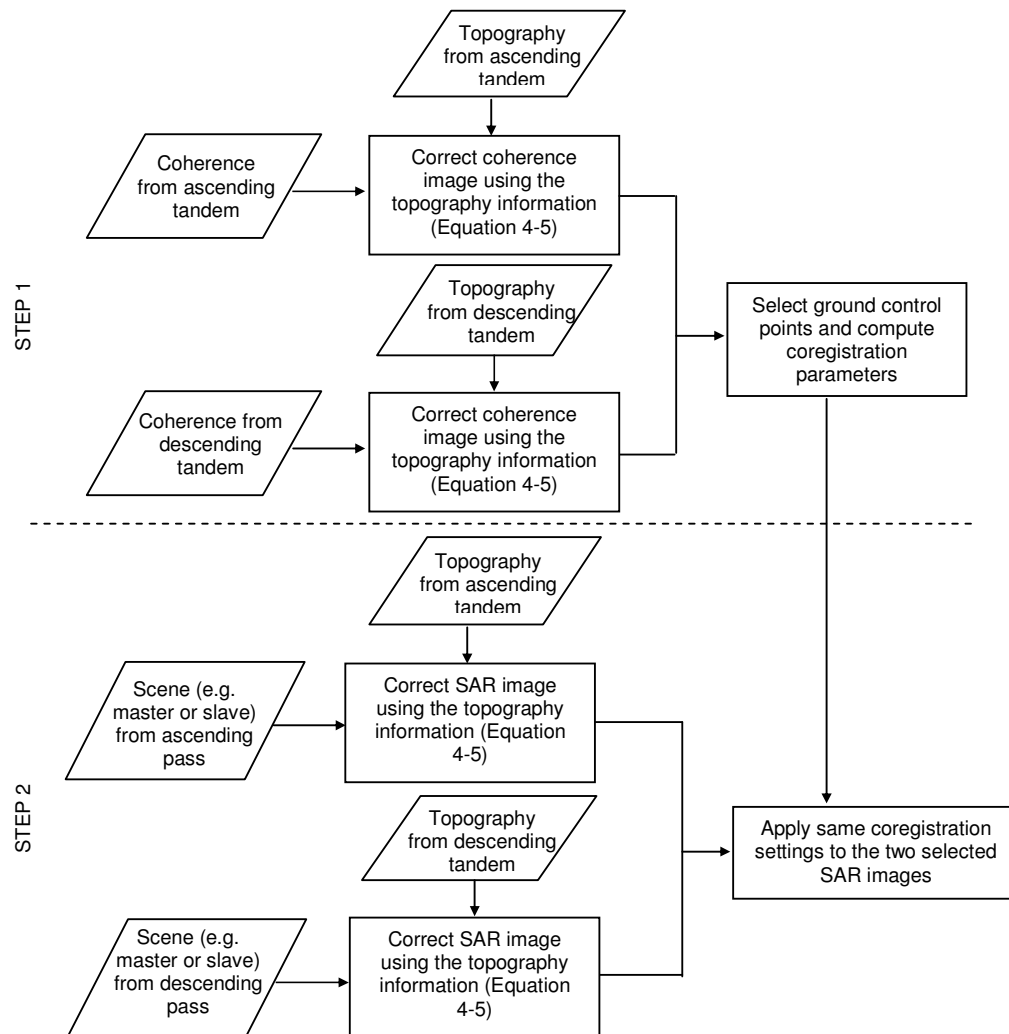


Figure 4-33. Flow chart of ascending and descending SAR sub-scenes coregistration.

In the research, this procedure is carried out interactively via already existing ENVI functionalities by selecting over 70 ground control points in the selected area of interest (usually of circa 10000 pixels) and applying a Delaunay triangulation with the Nearest Neighbour resampling method. This solution is selected after testing other methodologies such as a simple two-dimension translation and rotation algorithm or more complex cubic convolution resampling functions which do not achieved accurate results or lose the speckle characteristics of SLC data. Once the coregistration settings have been computed for the coherence image, they can be used to coregister the SLC data as well. Clearly, these latter images must have the same ground resolution as the

coherence image and must also be terrain-corrected. This procedure is extremely suitable for the gentle topographic characteristics of the region around Cranfield University. Certain areas might present more irregular height features, therefore they require the selection of additional locally close ground control points in the coherence image to assure an accurate coregistration.

4.9 Land-Use Classification

As mentioned in Section 2.1.6.1, some classification techniques for SAR images merge interferometric products such as the coherence magnitude together with the backscatter data. Four recent papers of particular relevance to this research (Tansey et al., 2004; Okhimamhe, 2003; Weydhal, 2001 and Wegmuller et al., 2000) demonstrate the great potential of such algorithms. A short review of these papers follows.

Wegmuller et al. (2000) investigate the applicability of surface characterisation of arid land by using 35-day repeat pass ERS tandem pairs. Applying preset thresholds to the degree of coherence, the backscattering coefficient and the backscatter ratio between master and slave scenes, they develop 18 different surface classes related to the parameters detectable by a radar system. Some examples are: rough dry salt crust, high vegetation density or strong erosion activity, stable bare surface, moisture decrease at high correlation. They also model the decorrelation effects to the soil cover fraction of vegetation and to an erosion parameter.

Weydhal (2001) applies these classification algorithms on a 105 km² area about 40 km north of Oslo in Norway. Plotting the coherence magnitude against the SAR backscatter amplitude, Weydhal identifies 9 classes which are related to both land-cover and land-use features. These are: lake, forest, fields, gravel pit, runway, hangar, large buildings, sawmill, city area. The second part of the paper focuses on high-coherence targets only, analysing the correlation to their backscatter amplitude and using crisp thresholds to classify data into groups.

Okhimamhe (2003) investigates the information content of ERS SAR tandem scenes over a savanna environment in Africa. He develops a similar classification methodology of Wegmuller et al. (2000) by combining, in a red-green-blue (RGB) composite, the coherence image, the master-slave average backscatter and the backscatter intensity difference image. This Interferometric Landuse (ILU) product is then compared with a Landsat ETM scene. This latter image is classified using a supervised maximum likelihood classification technique and the initial twelve different classes are reduced to only three for ease of comparison with the ILU image. These are: dense canopy vegetation, low canopy vegetation and bare soil. Ground truth data validate the ILU results with an accuracy 89 %.

Finally, Tansey et al. (2004) investigate the potential to retrieve growing stock volume of forested areas in four different test sites in the world by analysing scatter plots of the coherence magnitude against the backscattering intensity as in Weydhal (2001). Different non-forest and forest classes were identified: water bodies; smooth surfaces (in L-band radar terms) such as bogs and agricultural area; open areas (e.g. a non-forest class including vegetation in the early stages); rough agricultural surfaces and burnt or cleared forest; areas presenting a growing stock volume of 20-50 m³ha⁻¹; others between 51-80 m³ha⁻¹; and finally zones with a growing stock volume higher than 80 m³ha⁻¹ which are associated with commercially important forests resources and mature forest. Their results show an accuracy greater than 70 %.

The aim of this review is to point out two key aspects common to all four studies. Firstly, land-cover and land-use classes are often mixed. These two concepts are very different from each other and should be separated. As explained by the Global Land Cover Network (GLCN, 2007), land cover is the observed (bio)physical cover on the Earth's surface whilst land use refers to how land is employed by humans. Therefore, two different areas may have similar land cover, but different land use. For example, a vegetated area may be used for recreational or agricultural purposes. Sometimes a land-cover descriptor might be more appropriate than a land-use one, and often there might not actually be a specific use of the area under consideration. This is probably why the papers previously presented tend to mix the two types of classification groups. Doing so, they can decrease the number of unclassified pixels. In all four papers, the developed classes are tailored to the specific purpose of the application and as a result the classification procedures use both specific land-use categories and other more general land-cover classes.

The second aspect is that these studies apply strict thresholds to categorize these classes. This solution is used even when, as in the case of Okhimamhe (2003), it is recognised that the appearance of the land cover categories is better described with approximate terms such as low, medium or high.

Initially, the author investigated a variety of data fusion RGB combinations similar to the ones presented above. For example, Section 6.3 uses an RGB composite of the coherence magnitude, the backscatter amplitude and again the coherence magnitude. Another example is shown in Figure 4-34. This image of the Brogborough landfill is obtained by merging three different coherence magnitude images as an RGB colour composite. It is immediately evident how the fusion of various levels of information enhances the classification potential of SAR data. Ultimately, the research develops a new classification methodology that uses only land-use classes and applies a Fuzzy Logic (FL) based analysis. As explained in the following sections, FL is able to take into account a certain level of vagueness for the description of the classes, as noticed in the literature review presented above.

Although the wording of the second objective of this research (i.e. can SAR data be correlated with landfill on-site conditions and operational procedures?) intrinsically refers to both land-cover and land-use aspects, the research considers strictly land-use classes specific to landfill conditions.

The following sections first provide the reader with introductory concepts of FL and then explain the overall classification methodology. For a more comprehensive description of the FL algorithms and their implementation the reader can refer to Cox (1999).

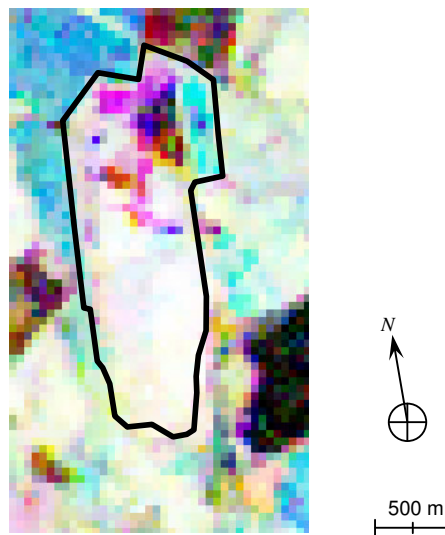


Figure 4-34. RGB colour composite with three coherence magnitude images derived from three different 1-day ERS tandem pairs. The black contour identifies the Brogborough site boundary.

4.9.1 Fundamentals of Fuzzy Logic

Fuzzy logic is an analysis techniques based on the concept of fuzzy sets introduced by Zadeh (1965): “A fuzzy set is a class of objects with a continuum of grades of membership.” As such, FL allows for set membership values to range between 0 and 1, rather than the conventional crisp full-membership or non-membership definition (e.g. true or false, yes or no). This flexibility and the introduction of specific mathematical procedures make FL a very suitable tool to handle imprecise information for a variety of applications and specifically for the classification of remote sensing images.

Two examples of fuzzy sets are given in Figure 4-35. The graph on the left shows the degree of coherence $|\gamma|$, which has a value in the range between 0 and 1, subdivided into three overlapping grades: low, medium and high. The graph on the right shows the

backscatter amplitude, normalised from 0 to 1, again described in three intersecting classes. The curves describing these grades are commonly known as membership functions. The number of classes, the degree of overlap and the shape of each function is flexible and is defined based on the user's knowledge and experience.

The fuzzy sets are then used to develop a number of "if-then rules" expressed in a very natural way using linguistic variables. The IF part is called the antecedent and the THEN part is called the consequent. For instance, in the case of the classification of water bodies based on the two fuzzy sets previously presented (Figure 4-35), it is possible to define the two following rules:

- Rule 1: IF (Degree of Coherence is Low) AND (Backscatter Amplitude is Low) THEN (Pixel is a Water Body: True)
- Rule 2: IF (Degree of Coherence is Medium) AND (Backscatter Amplitude is High) THEN (Pixel is a Water Body: False)

Here the Water Body class is again defined with a fuzzy set as in Figure 4-36. The AND, OR and NOT operators (i.e. respectively the fuzzy intersection, union or inverse operators) implemented in this research follow respectively the minimum operator, the maximum and the inverse operator. Therefore in mathematical terms the antecedent part of Rule 1 can be written as:

$$Antecent = \min(f_{low}(coh) , f_{low}(ampl)) \quad \text{Equation 4-7}$$

where $f_y(x)$ represents the value of the membership function y for a given input x . This process is called fuzzification.

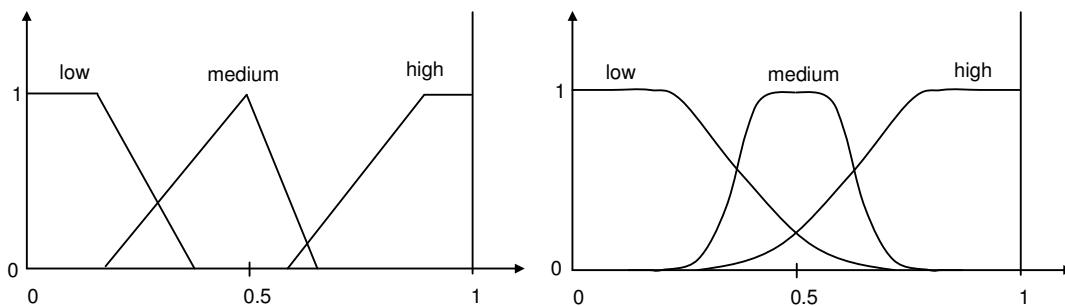


Figure 4-35. Fuzzy sets for the degree of coherence (left) and the backscatter amplitude (right). Note the different functions used to model the membership grades and the overlapping difference between them which is left at the discretion of the developer.

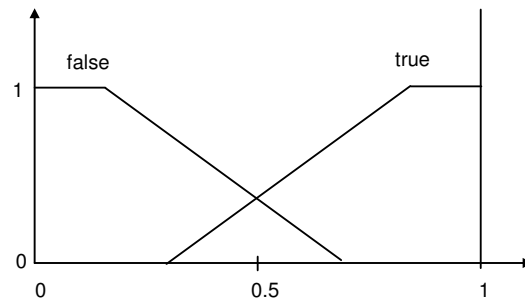


Figure 4-36. Fuzzy set for the Water Body class.

It is now possible to compute the membership level of a given input for each variable of the fuzzy system. This process determines the degree to which the input belongs to the relative fuzzy sets via the membership functions.

For instance, the inputs to the fuzzy system described above can be a degree of coherence equal to 0.25 and a normalised backscatter amplitude of 0.4. As shown in Figure 4-37 and Figure 4-38, the membership levels for the two rules are:

- Rule 1: Degree of Coherence is Low = 0.55
- Rule 1: Backscatter Amplitude is Low = 0.45
- Rule 2: Degree of Coherence is High = 0.2
- Rule 2: Backscatter Amplitude is High = 0.1

The fuzzified level is subsequently used in the fuzzy rules. If the antecedent of a given rule has more than one part, as the given example, the fuzzy operator is applied to obtain one number that represents the result of the antecedent for that rule. This result is then applied to the consequent. Given the AND (i.e. min) operator in the two rules of the example, Rule 1 outputs a level of 0.45 and Rule 2 outputs a level of 0.1.

Before applying the consequent part of the fuzzy rules, each output level can also be weighted in order to increase or decrease its importance. In this example, the weight is 1 for both rules, so it has no effect on the consequents. Generally, once the weighting has been computed for each rule, the consequent statements can be processed.

The consequent fuzzy set (Figure 4-36) is reshaped based on the antecedent weighted output. This research uses the minimum operator, which truncates the consequent fuzzy set as shown in Figure 4-39. The truncated functions of the consequent fuzzy rules are aggregated into one single fuzzy set as illustrated in Figure 4-40. This is then defuzzified in order to obtain a single output value from the overall fuzzy system. The defuzzification method applied in this research is the centroid calculation, which returns the centre of area under the curve.

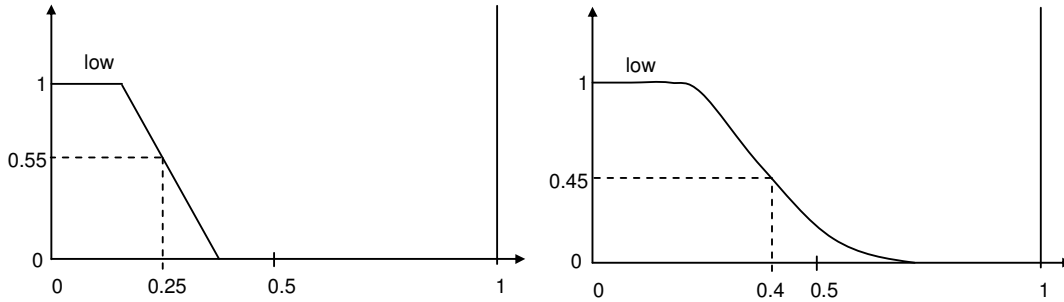


Figure 4-37. Fuzzy membership of Rule 1 for the degree of coherence (left) and backscatter amplitude (right). The results are approximate and for explanation purposes only.

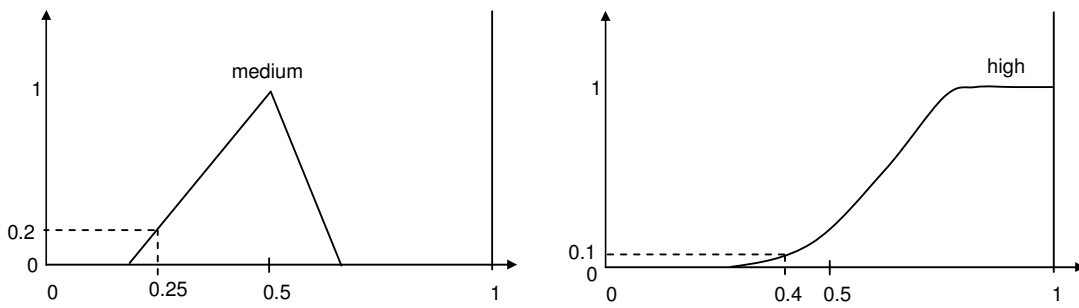


Figure 4-38. Fuzzy membership of Rule 2 for the degree of coherence (left) and backscatter amplitude (right). The results are approximate and for explanation purposes only.

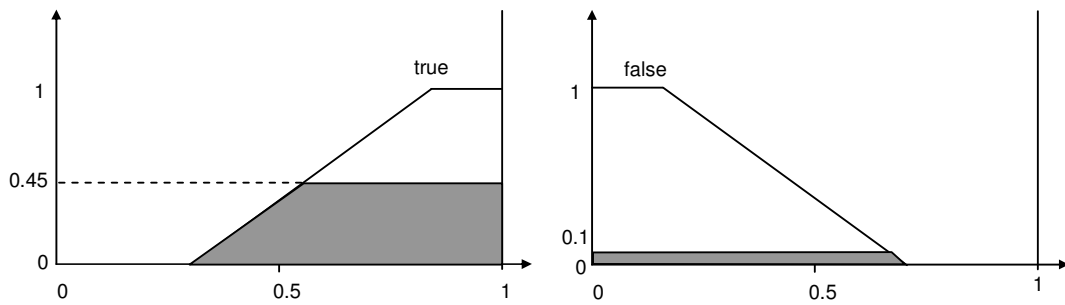


Figure 4-39. Application of the consequent fuzzy rules. Rule 1 on the left and Rule 2 on the right. The results are approximate and for explanation purposes only.

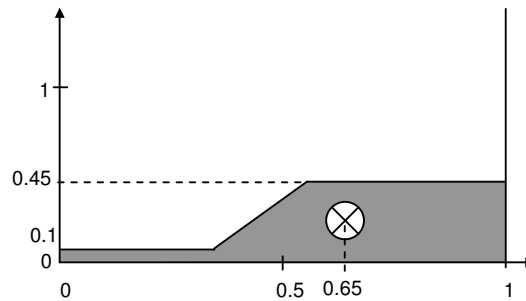


Figure 4-40. Aggregation of the consequent fuzzy rules and defuzzification through the centroid calculation. The results are approximate and for explanation purposes only.

For the example presented in this section, this final result identifies the level of membership of the selected pixel to the class Water Body. Therefore, the pixel is 65 % a Water Body and is 35 % not a Water Body. It is important to explain that FL does not provide a probabilistic result. As explained by Cox (1999) a probabilistic approach for the example provided in this section would yield the statement: "there is a 65 % chance that the pixel is a water body". Instead, the fuzzy terminology corresponds to "the pixel's degree of membership to a water body is 65 %." Clearly, there is a significant semantic difference. Still today, the relationship between probability theory and FL continues to be an object of controversy. This discussion is beyond the scope of this research.

In the field of EO images classification, FL has been applied for a variety of purposes. Fisher and Pathirana (1990) are the first to successfully use FL to investigate sub-pixel spectral mixing. As explained by Zhang and Foody (1998) a fuzzy classification allows for multiple and partial classes membership properties. This achieves the integration of more information on the relative strengths of the class membership at a pixel level. Foody (1999) also emphasise that the applicability of fuzzy classifier is of even greater relevance when an image has a large proportion of mixed pixels (i.e. coarse ground spatial resolution). As reported by Bãrdossy and Samaniego (2002), since the early applications the literature presents a large spectrum of fuzzy classifiers and there are great differences regarding how they handle the data as well as the algorithms employed for the membership allocation procedures. In this research, a rule-based fuzzy classifier similar to the one presented by Bãrdossy and Samaniego (2002), is applied to allow individual pixels to be assigned to different classes with different memberships. This is presented in more details in Section 4.9.4.

4.9.2 Overall Classification Procedure

As shown in Figure 4-41, instead of simply plotting the coherence and backscatter data in the red-green-blue channels to create a colour composite image such as the ILU, the procedure applies both featured-based and fuzzy classification techniques on many levels of information derived from three 1-day ERS tandem pairs. Figure 4-41 also

specifies the time separation between these acquisitions, namely 9 days between the initial ascending-orbit pair and the first descending-orbit pair, and 35 days between the two descending-orbit pairs. This specific time separation is only dependent on the ERS mission orbit characteristics. The algorithm is structured so that the final result describes the land-use conditions at the time of the first descending-orbit pair (i.e. Master 2, Slave 2).

The coherence images are bias-corrected and multilooked with a 2 by 10 window, in range and azimuth respectively, obtaining an image with a 50 m ground resolution (refer to Section 4.5.11). No range band filtering is applied during the interferometric processing (refer to Section 4.5.4). For the backscatter intensity images, the Enhanced Lee filter implemented in IDL ENVI (Lopes et al., 1990) is first applied. This reduces speckle while preserving texture information. It uses local statistics within the computing window (i.e. 3 by 3 pixels) and determines whether the central pixel is part of a homogeneous or heterogeneous region, or if it acts as a point target. Each class is treated differently. For the homogeneous class, the pixel value is replaced by the average of the filter window. For the heterogeneous class, the pixel value is replaced by a weighted average. For the point target class, the pixel value is unchanged.

Subsequently, the filtered intensity images are averaged to achieve the same ground resolution as the coherence magnitude image, and their values are then normalised from 0 to 1. The ascending images are coregistered as explained in Section 4.8. Following the classification steps, presented in more details in Sections 4.9.4 and 4.9.5, the final result is stored in three bands corresponding to the red-green-blue channels of the classification image. These values are stored with a band interleaved by pixel (BIP) format which has the first pixel for all bands in sequential order, followed by the second pixel for all bands, followed by the third pixel for all bands and so on.

The overall classification procedure is developed in Matlab and presented in Appendix A (i.e. `land_use_classification.m`).

4.9.3 Definition of the Land-Use Classes

As discussed in Chapter 2, the amount of surface change over time describes processes occurring on time scales of the orbit repeat time and size scales on the order of the ground resolution and radar wavelength. Section 4.9 has clarified that this research uses only land-use classes, therefore, these must be defined also according to the actual possibility of detecting them. Eight land-use classes are identified: lagoons, buildings, roads, capped areas, tipping areas, clay operation zones, restored areas with low vegetation, restored areas with high vegetation. The analysis of these classes with respect to the fuzzy logic classifier is presented in Table 6-2 in Chapter 6. Additionally there is the possibility that a pixel remains unclassified or it has multiple membership characteristics.

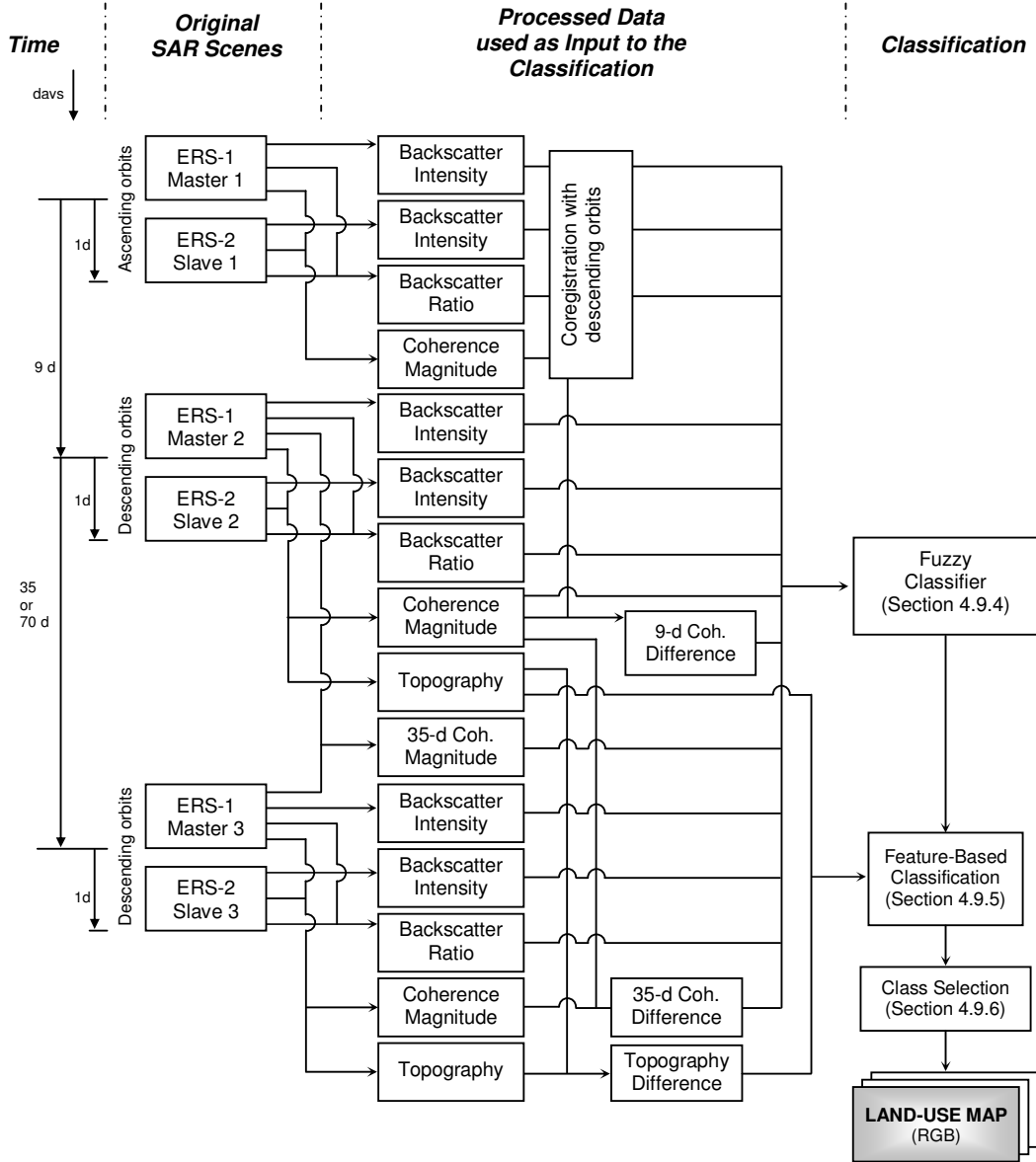


Figure 4-41. Land-use classification algorithm.

4.9.4 Rule-Based Fuzzy Logic Classifier

The rule-based FL classification implemented in the research is a pixel-based procedure. This is programmed in Matlab (i.e. 3Tandem_Fuzzy_Classifier.fis) with the support of the Matlab FL Toolbox. As illustrated in Figure 4-42, for each pixel the values of 13 information channels are used as input variables to the FL classifier. Based on the defined membership functions and on the fuzzy rules, the FL classifier outputs the degree of membership of each pixel to all land-use class. Each pixel, $P(x, y)$, is therefore associated to row vector $\mathbf{M}(P)$ that stores the degree of membership, M_c , for each of the 8 land-use classes c , with c varying from 1 to 8 and M_c from 0 to 1.

An example of an input fuzzy set is illustrated in Figure 4-43. All input fuzzy sets are described by a low, medium and high membership functions. These are modelled with a two-sided composite of two different Gaussian curves (i.e. Matlab function gauss2mf). An example is given in Figure 4-43. In the FL jargon, the adjustment of the membership function is called fine-tuning and is often based on the experience of the developer and user.

All output fuzzy sets for the land-use classes are instead described by two linear functions as illustrated in Figure 4-44.

Overall, the FL classifier is based on 27 fuzzy rules derived from the analysis presented in Table 6-2, in Chapter 6. Figure 4-45 shows a FL Matlab toolbox that allows the developer to interactively test the fuzzy rules. These tools have enabled the author to fine-tune specific membership functions of the input fuzzy sets.

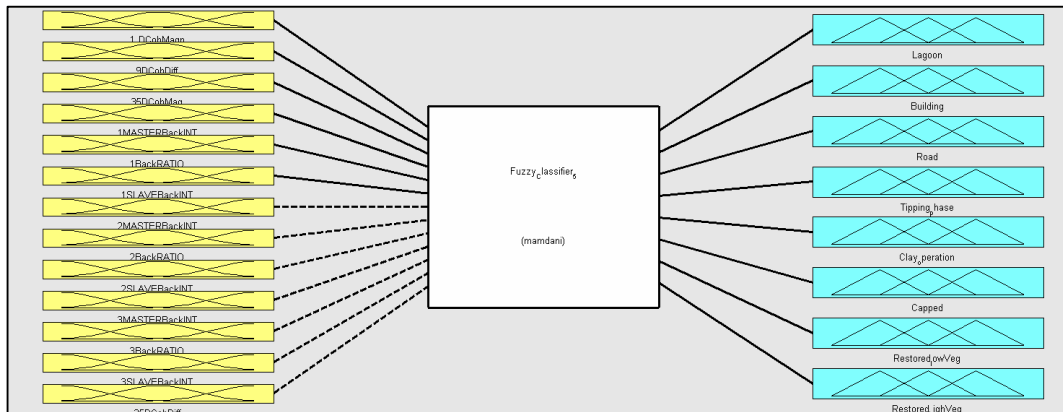


Figure 4-42. Fuzzy logic classifier structure. It uses a Mamdani defuzzification algorithm. It has 13 input variables and 8 output variables and it uses 27 fuzzy rules.

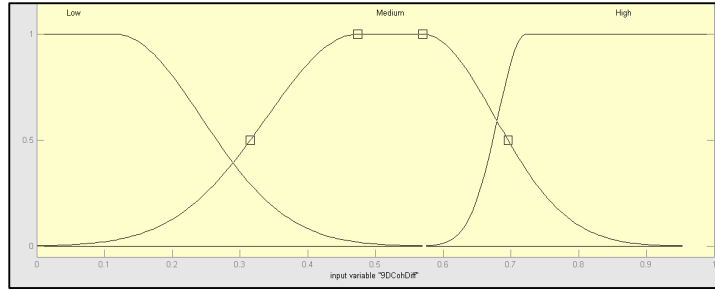


Figure 4-43. Example of a fuzzy set and membership functions developed for the FL classifier. This examples shows the 9-day coherence difference fuzzy set. The transition from a low to medium value is smoother than from a medium to high value. This is used to make a more defined separation between the latter two levels.

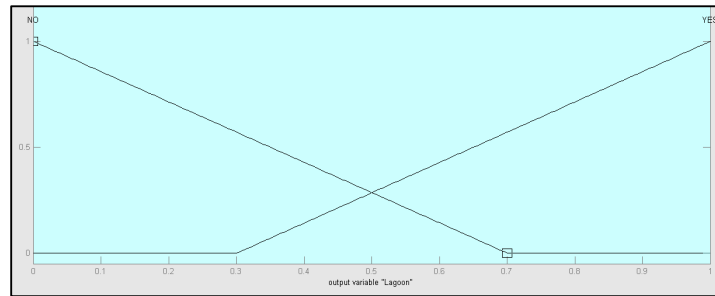


Figure 4-44. Example of a fuzzy set and membership functions for the land-use classes. All classes are modelled by the same linear membership functions.

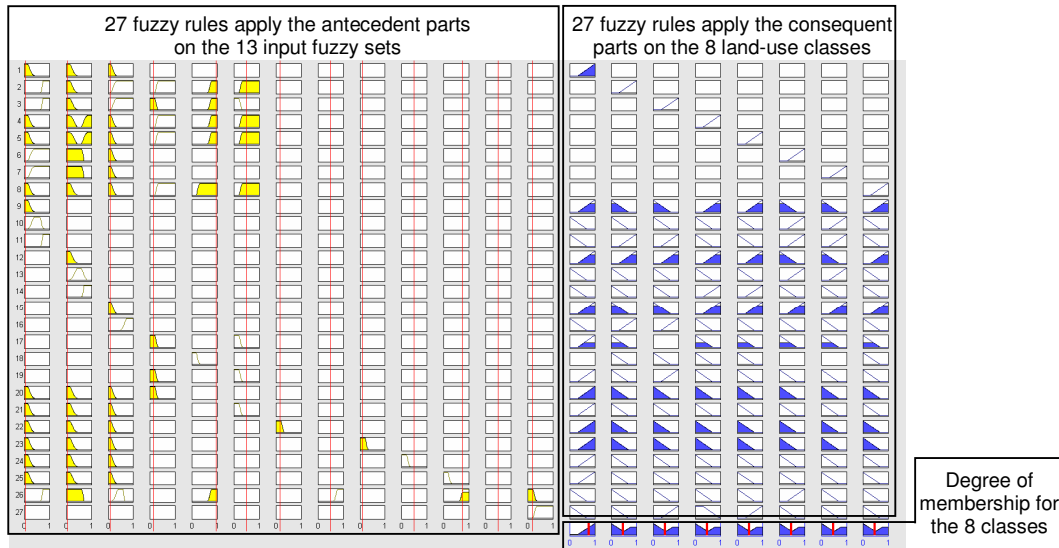


Figure 4-45. Example of a fuzzy set and membership functions for the land-use classes. All classes are modelled by the same linear membership functions.

As in the study by Bãrdossy and Samaniego (2002), this classification methodology has the advantage that a measure of the classification uncertainty can be defined for each pixel. Novel concepts are proposed in this thesis to describe the fitness of the classification: the degree of ownership, the degree of ambiguity and the degree of classification success. These coefficients do not actually refer to the accuracy of the overall classification, which is instead addressed in Section 4.9.7. The degree of ownership $O(P)$ for a pixel $P(x, y)$ is the maximum level of membership that the pixel has between the land-use classes and can be defined as:

$$O(P) = \max_{c=1}^8 M(P) \quad , \quad \text{with } O(P) \in [0,1] \quad \text{Equation 4-8}$$

where $M(P)$ is the vector containing the level of membership, M_c , for each of the 8 land-use classes c . In other words, $O(P)$ is equivalent to the higher level of class membership for the pixel under consideration.

The degree of ambiguity $A(P)$ for a pixel $P(x, y)$ represents the uniqueness of the maximum level of membership previously identified. This can be defined as:

$$A(P) = 1 - [\max_{c=1}^8 M(P) - 2^{nd} \max_{c=1}^8 M(P)] \quad , \quad \text{with } A(P) \in [0,1] \quad \text{Equation 4-9}$$

where $2^{nd} \max_{c=1}^8$ is the second highest level of membership, M_c , found in $M(P)$. Therefore a degree of ambiguity equal to 0 corresponds to the optimal and in most cases unachievable situation in which a pixel has a complete degree of membership (e.g 1) to a specific class and the second highest is 0. On the contrary, a degree of ambiguity equal to one identifies the most adverse situation in which a pixel has the same degree of membership for the strongest two classes, irrespective of what the level of membership is.

The final step is to define the degree of classification success $S(P)$. This is:

$$S(P) = O(P) \cdot (1 - A(P)) \quad , \quad \text{with } S(P) \in [0,1] \quad \text{Equation 4-10}$$

The degree of classification success $S(P)$ represents the confidence with which a land-use class can be assigned to a pixel.

A practical example can be useful to clarify the meaning of these coefficients. For instance, a pixel $P(x, y)$ with a $[\max_{c=1}^8 M(P)]$ equal to 0.95 has a very high degree of ownership. This apparently means that one of the land-use classes can be appropriately assigned to the pixel. Nonetheless, if the same pixel P has $[2^{nd} \max_{c=1}^8 M(P)]$ equal to 0.85, its degree of ambiguity $A(P)$ is also very high (i.e. equal to 0.9). Therefore, the

obtained degree of classification success $S(P)$ is very low and equal to 0.095. This confirms that there is actually a substantial level of uncertainty in assigning any land-use class to the pixel despite the fact that there is one class with a very high degree of membership.

To properly use these parameters, one must appreciate the rarity of obtaining a result for $S(P)$ higher than 0.3. This would be achieved for instance with a $[\max_{c=1}^8 M(P)]$ equal to 0.75 and a $[\max_{c=1}^8 M(P)]$ equal to 0.35. Figure 4-46 shows that the relationship between $O(P)$ and $S(P)$ for different values of the $[\max_{c=1}^8 M(P)]$ is not linear.

As explained in the next sections, these three parameters describing the fitness of the classification are used during featured-based classification and the class selection steps previously illustrated in Figure 4-41.

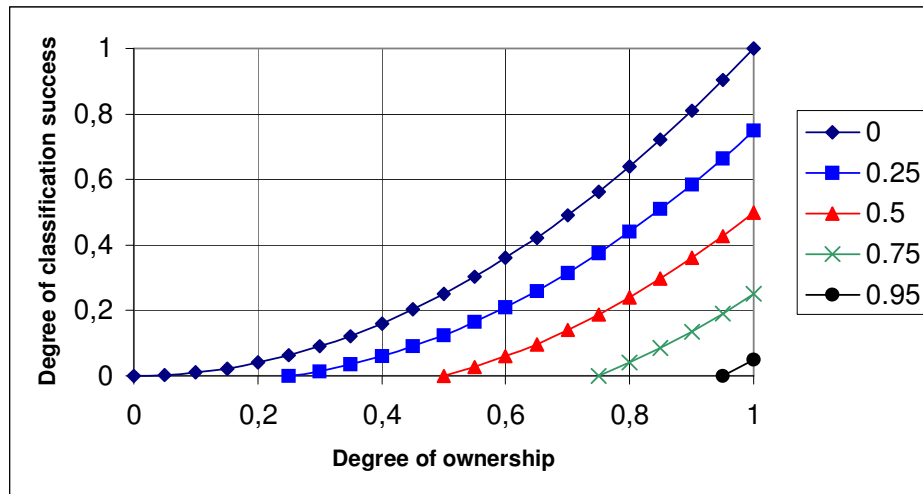


Figure 4-46. Relationship between $O(P)$ and $S(P)$ for different values of the second highest degree of membership as specified in the legend.

4.9.5 Featured-Based Classification

Before assigning a land-use class to each pixel, three additional feature-based rules are applied in order to further distinguish the classes. These rules are applied pixel-by-pixel. They improve the degree of ownership $O(P)$ and decrease the degree of ambiguity $A(P)$ of the pixel, therefore achieving a higher degree of classification success $S(P)$.

In the presence of a pixel P whose $O(P)$ correspond to the lagoon or restored area with high vegetation classes and which has a high $A(P)$ (i.e. higher than 0.8) between the same two classes, the first rule uses the 1-day topography information. This procedure finds the first pixels with high coherence (i.e. higher than 0.65) in the vertical, horizontal and diagonal directions from the selected pixel and checks their height. If these eight pixels have a similar height (i.e. within 5 m) then the level of membership M_1 (i.e. for the lagoon land-use class) of the pixel is increased by 0.2 or up to 1 not to exceed the maximum value. This rule is based on two assumptions. First that the borders of a lagoon have all the same height and second that the borders of a restored area covered with high vegetation do not necessarily have the same height.

Based on the degree of ownership and classification success of the pixels, the second rule is that no capped or restored areas or can be completely surrounded by a lagoon or a tipping area. Also, no tipping areas or clay operation zones can be completely surrounded by a lagoon. By moving along the vertical, horizontal and diagonal directions from the pixel under consideration, this procedure checks if the land-use classes (based only on the respective degree of ownership and classification success) of the first encountered pixels that have a different degree of ownership from the pixel under consideration satisfy this second rule. If so, the procedure sets the membership level of all classes of the pixel under consideration to 0.5. As explained in the next section, this will cause the pixel to be left undefined in the class selection step.

The third rule is used to help distinguishing tipping areas from clay operation zones which may presents very similar attributes relative to the input variables used in the fuzzy classifier. In the presence of a pixel P whose $O(P)$ correspond to a clay operation zone or tipping area and which has a high $A(P)$ (i.e. higher than 0.8) between the same two classes, the third rule uses concurrently the coherence and topography information. Usually these areas have small coherence. This rule finds the first pixels with high coherence (i.e. higher than 0.65) in the vertical, horizontal and diagonal directions from the selected pixel in the second tandem pair and checks their height. If the average height of these surrounding pixels in the second tandem pair is lower than their height in the third tandem pair, then the area with a low 1-d degree of coherence is more probable to be a tipping area. Therefore, the level of membership for the tipping area land-use class of these pixels is increased by 0.2 or up to 1 not to exceed the maximum value. In the opposite situation (i.e. the average height is lower), the level of membership for the clay operation zone land-use class is increased by 0.2 or up to 1 not to exceed the maximum value. This can only be achieved if the DEM computed from the third ERS interferometric scenes is reliable (i.e. coherence magnitude higher than 0.65) in the area under examination. The two relative interferometric heights are put in reference by using four pixels on the bottom left corner of the image.

If none of the rules are satisfied, then the land-use degree of membership for all classes of the pixel is left unchanged. Finally, each pixel goes through the selection process.

4.9.6 Class Selection

For the allocation of a specific land-use class to a pixel, the degree of ownership $O(P)$ must be higher than 0.6 and the degree of classification success $S(P)$ must be higher than 0.18. This means that as the degree of ownership $O(P)$ increases, the degree of ambiguity $A(P)$ is also allowed to increase without affecting the classification of the pixel. If $O(P)$ satisfies this requirement but $S(P)$ is lower than 0.18, then the pixel is described as a multiple class pixel (refer to Table 6-2). In all other cases (i.e. $O(P)$ lower than 0.6), the pixel is considered undefined (refer to Table 6-2). The influence of these threshold parameters on the classification result is also tested.

4.9.7 Land-use Classification Accuracy Assessment

The assessment of the overall classification procedure is carried out with standard error techniques measure the accuracy of the classification maps against ground reference data. For a detail discussion on their implementation, the reader is referred to Jensen (2005).

5. Landfill Site Identification

This chapter addresses the first research objective: can SAR data support the identification of landfill sites by distinguishing them from other disturbed areas which present similar optical spectral signatures?

As reviewed in Section 1.1.5, several studies of optical multispectral data report that landfill sites have spectral signatures similar to areas undergoing some type of development or derelict areas. The spectral and spatial resolutions of the optical space-based instruments used in such studies are similar to what most current and future space systems offer or plan to provide. Some examples are the Moderate-resolution Imaging Spectroradiometer (MODIS) on the NASA Terra satellite (NASA, 2006), the Indian Remote Sensing Resourcesat-1 mission (Indian Space Research Organisation, 2005) and the ESA Global Monitoring for Environment and Security (GMES) Sentinel 2 mission (ESA, 2005b). As a consequence, future optical data will suffer the same identification ambiguity between landfills and disturbed areas. This strengthens the need to assess whether SAR data can distinguish landfill sites from other areas which present similar optical spectral signatures.

This chapter initially presents a brief analysis of optical data to corroborate what is presented in Section 1.1.5. It then tackles the research objective by investigating the spatial characteristics of SAR backscatter amplitude data of landfills and disturbed areas (Section 5.2) and by observing their temporal variability (Section 5.3).

5.1 Optical Data Spectral Analysis

Initially, an image provided by DMCII Ltd. (Disaster Monitoring Constellation International Imaging) is used to show the feasibility and simplicity of identifying landfills in mid-resolution multispectral EO scenes when their location is well known. The map in Figure 5-1 shows the location of the Buckden site (i.e. 52° 18' 30.93" North 0° 13' 26.87" West), an average size landfill managed by Anti Waste Ltd. This map was freely obtained from the online Environment Agency service "What's in your backyard" (Environment Agency, 2005).

The aerial photo in Figure 5-2 illustrates the Buckden landfill. This photo was formed by creating a mosaic of the free preview images available on the online GetMapping service (GetMapping, 2004). The commercial aerial photographs provided by this company have a 250 mm resolution, while the free preview has only a resolution of 2 m. This is an approximate value as the area of the preview tile (i.e. 0.5 x 0.5 km) might be slightly incorrect.



Figure 5-1. As pointed by the label, the Buckden landfill (located at 52° 18' 31.39'' North and 0° 13' 28.32'' West) is identified by the red area in the bottom left corner of the map. (Environment Agency, 2005).



Figure 5-2. An aerial photo of the Buckden landfill at a 2 m resolution taken in the second half of 1999 (GetMapping, 2004).

The Buckden landfill is now identified on the DMCII image (i.e. UK_Cambridge_Agriculture.jpg) which is a compressed image (i.e. using the Joint Photographic Experts Group (jpeg) method) distributed in the standard false colour composite band combination (Campbell, 2002). Being compressed, it has a ground resolution lower than its original 32 m. Nevertheless, as shown in Figure 5-3, the Buckden landfill can be easily found.

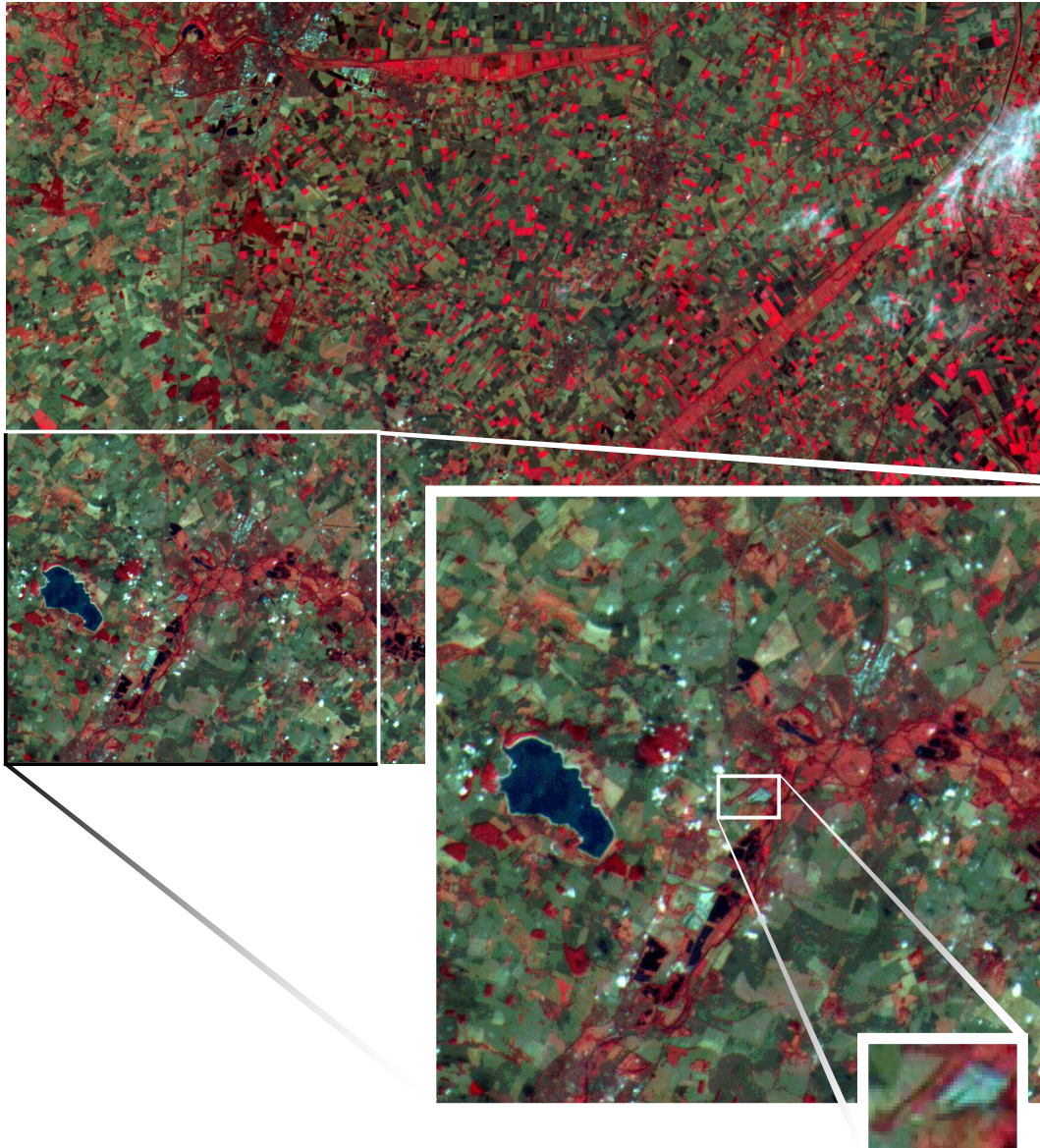


Figure 5-3. The wide image is the original UK_Cambridge_Agriculture.jpg available from the DMCII DVD. Two enlargements highlight the Buckden landfill.

To improve the visual comparison of the two results, the Getmapping and DMCII images are resampled to the same resolution as shown in Figure 5-4. It must be clarified that the acquisition time of both images is unknown but this is of no particular importance for the specific aim of the research. This basic exercise shows the feasibility of using optical data to detect waste disposal sites. Nonetheless, without the a priori knowledge of the landfill location, the site identification remains ambiguous. This is shown in the following spectral analysis.

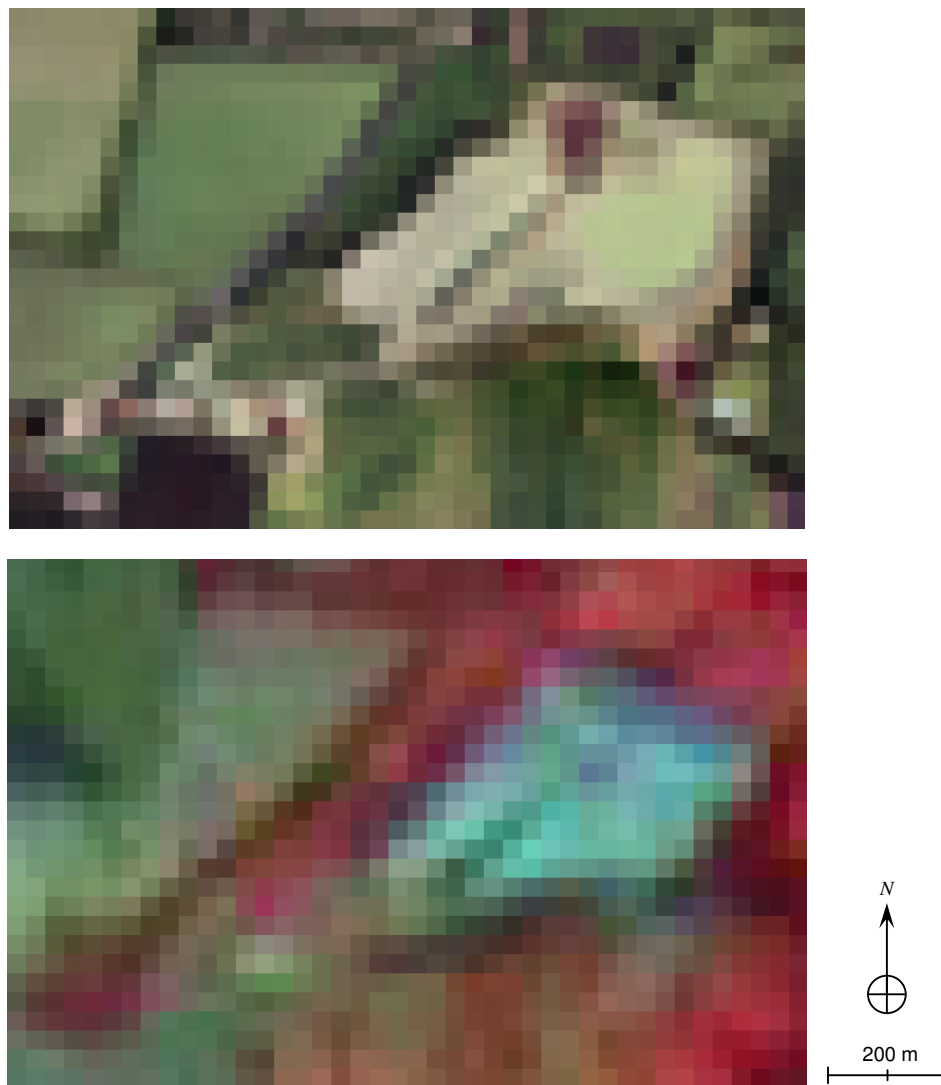


Figure 5-4. Top: the aerial photo of the Buckden landfill at a 32 m resolution, obtained by simple averaging of the original image. Bottom: image of the Brampton landfill available from the DMCII DVD.

The analysis of the spectral signatures is carried out on three orthorectified sub-scenes of Bedfordshire that covers three areas of interest (AOI): the Brogborough landfill, the Stewartby landfill and the Quest Pit of the Stewartby brickwork site. These sub-scenes have been acquired from the SPOT 2 imaging system on 16th May 1992 (Figure 5-5), the Landsat 5 Thematic Mapper (TM) on 12th June 1992 (Figure 5-6) and the Landsat 7 Enhanced Thematic Mapper Plus (ETM+) on 12th May 2001 (Figure 5-7).

After testing various spectral transformations, the standard false colour composite (Campbell, 2002) is found to be the most suitable combination for visual interpretation. Active vegetation appears red and pink, water bodies are dark blue or black and the white areas are fields covered with bright yellow flowering rapeseeds (*Brassica napus*) widely cultivated for the production of animal feed, vegetable oil for human consumption, and biodiesel.

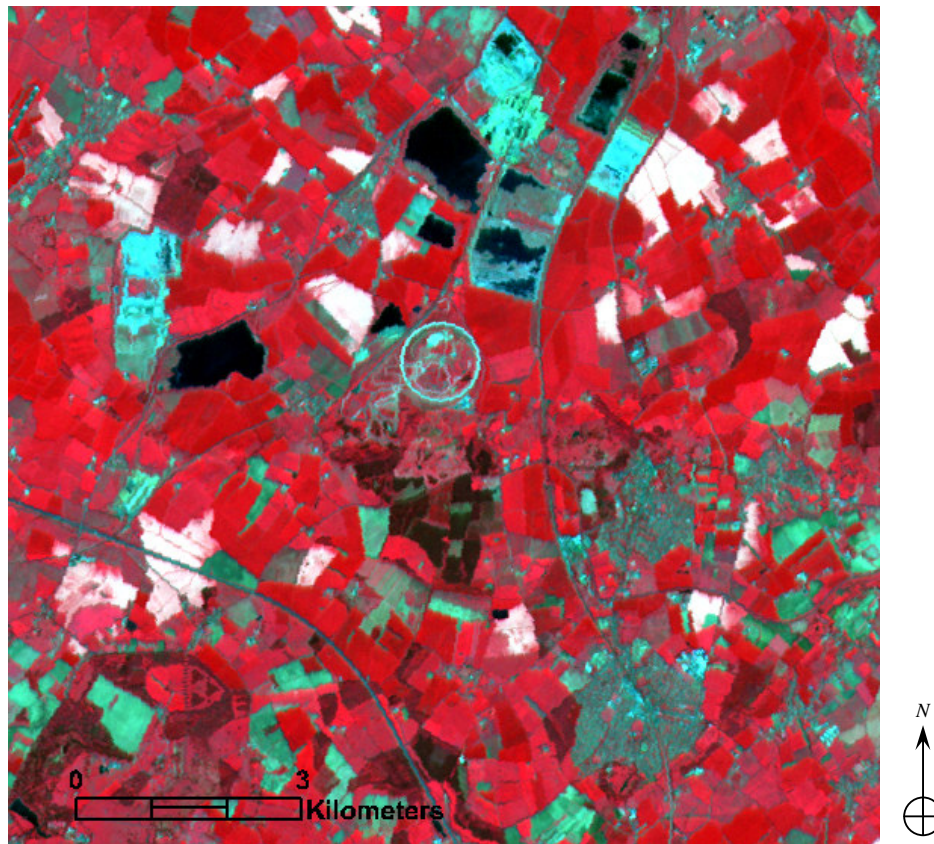


Figure 5-5. SPOT 2 sub-scene of Bedfordshire with 20 m ground resolution acquired on 16th May 1992. The image is obtained with a standard false colour composite with Band 1 (wavelength from 0.50 to 0.59 μm – green) as Blue, Band 2 (0.61 - 0.68 μm – red) as Green, and Band 3 (0.78 - 0.89 μm – NIR) as Red. The image is centred at 52° 2' 12'' N and 0° 31' 53'' W. The image was provided by the Cranfield University Centre for Geographical Information Management. Copyright CNES 1992.

The three AOI appear with a distinctive green-blue colour. In all three optical images, the Brogborough landfill can be seen in the middle left side of the image, the Stewartby landfill is in the middle top part and the tilted rectangle on its right is the brickwork site. The unusual circle in the centre is the Millbrook automotive test and validation centre.

Taking into consideration only the non-vegetated surfaces, each of the three AOIs are represented by a different number of pixels in every sub-scene. This is summarised in Table 5-1.

Table 5-1. Number of representative pixels per AOI in each sub-scene.

AOI	Optical Images		
	SPOT 2	Landsat 5	Landsat 7
Brogborough landfill	1021	442	686
Stewartby landfill	880	317	258
Disturbed area (Quest pit)	682	238	326



Figure 5-6. Landsat 5 TM sub-scene of Bedfordshire with 30 m ground resolution acquired 12th June 1992. The image is obtained with a standard false colour composite with Band 2 (wavelength from 0.525 to 0.605 μm – green) as Blue, Band 3 (0.630 - 0.690 μm – red) as Green, and Band 4 (0.75 - 0.90 μm – NIR) as Red. The image is centred at 52° 2' 12'' N and 0° 31' 53'' W as Figure 5-5. Its printed size appears smaller than Figure 5-5 due to the coarser spatial ground resolution. Copyright University of Manchester/University College London Year 2001 (Landmap, 2005). Original Landsat 5 distributed by Infoterra International.

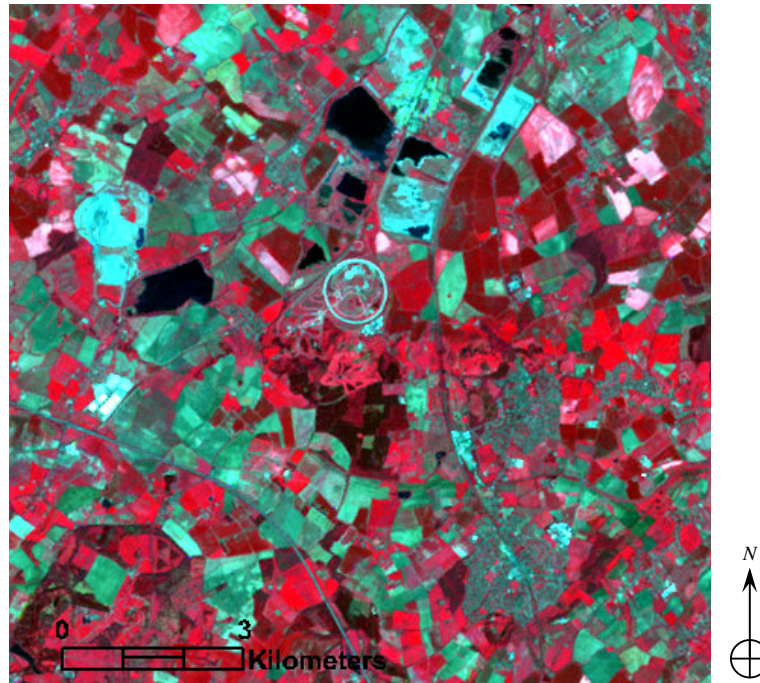


Figure 5-7. Landsat 7 ETM+ sub-scene of Bedfordshire with 30 m ground resolution acquired 12th May 2001. The image is obtained with a standard false colour composite as for Figure 5-6. The image is centred at 52° 2' 12'' N and 0° 31' 53'' W as Figure 5-5. Its printed size appears smaller than Figure 5-5 due to the coarser spatial ground resolution. Copyright University of Manchester/University College London Year 2001 (Landmap, 2005). Original Landsat 7 distributed by Infoterra International.

By computing the mean and standard deviation values for each band, the graphs in Figure 5-8 confirm that the three AOI have the same spectral signatures and therefore the two landfills cannot be readily distinguished from the brickwork site. As briefly presented in Section 1.1.5, a different analysis approach is presented by Brivio et al. (1993) in a paper titled “Aspects of spatial autocorrelation of Landsat TM data for the inventory of waste-disposal sites in rural environments”. They investigate the spatial variability in optical data achieving promising results, therefore such a methodology could also represent a valuable tool to discriminate waste disposal sites from other similar areas with SAR data. The study by Brivio et al. (1993) computes the semivariogram function using the matrix method. For each selected site, this method evaluates the semivariograms in each of the 6 Landsat TM bands for all rows and all columns and then takes the overall average. Such a method is selected by Brivio et al. (1993) under the assumption that the spatial structure of waste disposal sites and disturbed areas is isotropic. This assumption may be suitable when dealing with optical data, but cannot be applied a priori when using SAR data. In order to avoid this assumption, this research investigates the spatial structure of SAR backscatter amplitude data by applying the rotationally averaged power spectrum method as presented in Chapter 4.

It is important to reiterate that previous studies on SAR data texture characteristics have focused on segmentation techniques that apply a sliding processing window over an entire image whilst this research uses the spatial analysis to classify pre-selected areas of interest.

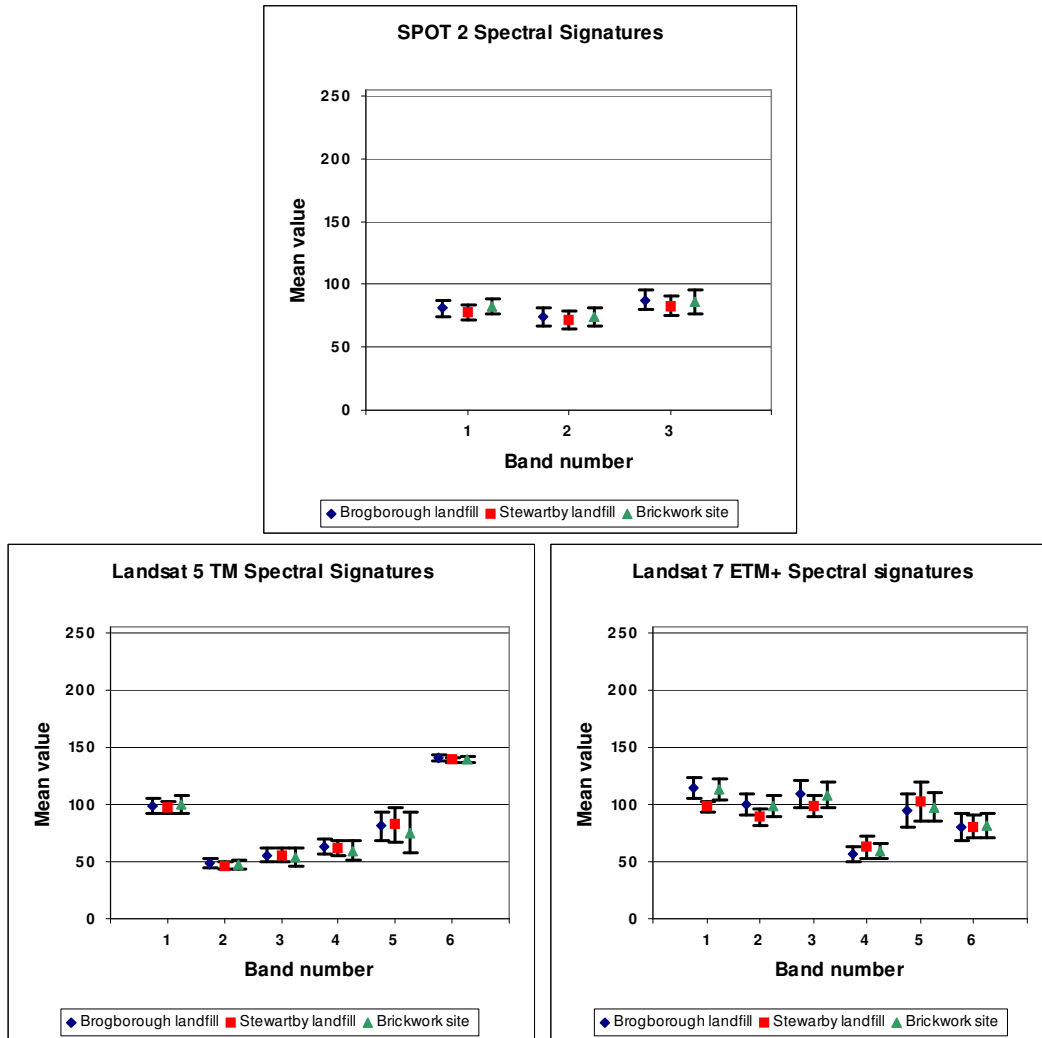


Figure 5-8. Spectral signatures for the three selected AOI in the three sub-scenes. The Landsat band number 6 in the graphs actually represents the official band number 7 (2.08 - 2.35 μm – reflected IR).

5.2 Analysis of SAR Amplitude Spatial Structure

The analysis starts by selecting in a SAR backscatter amplitude image waste disposal sites and disturbed areas which have the same spectral signature in an optical image. This requires the acquisition dates of the SAR and optical scenes to be close in time. The only available optical scenes for the research are the ones presented in the previous section. With the only requirement that the SAR images must cover the Brogborough landfill, a search on the ESA EoliSA database led to the selection of an ERS-2 scene acquired on 11th June 2001 during an ascending pass (i.e. orbit 32119, track 201, frame 1035, acquired at 22:03:56 GMT). The Landsat 7 ETM+ image (12th May 2001) and this SAR scene have only a one-month separation in time. This difference is small enough to infer that the disturbed zones have not changed characteristics in a significant way and would present the same spectral signature at the SAR acquisition time.

Figure 5-9 illustrates that the two scenes only partially cover the same ground allowing the research to identify 20 areas of interest (AOI). These are selected by visually examining a colour composite of the first three bands generated by a PCA applied on the Landsat 7 scene. The PCA technique transforms the multispectral remote sensing data into a smaller set of uncorrelated bands that represent most of the information present in the original data. Jensen (2005) provides a detailed explanation of the processing algorithm.

The corresponding areas in the SAR backscatter amplitude data are shown in Table 5-2. As it is possible to notice, 10 AOI are landfill sites and 10 AOIs are disturbed areas. It is important to explain that no additional information on the selected disturbed areas is available. They might be for example clay and gravel extraction pits, borrow pits, quarries or construction sites. Through the Environment Agency website (2005) it is only possible to establish that these zones are not and were not waste-disposal sites.

It must be specified that the original SAR scene is first flipped vertically and then averaged by 5 in the azimuth direction in order to obtain a realistic orientation and pixels with the same resolution in both azimuth and range directions (i.e. 25 by 25 m). The azimuth averaging is performed using a pixel aggregate routine which simply averages the 5 pixel values that contribute to the output pixel. This process is also known as incoherent averaging because all phase information is discarded. The SAR backscatter amplitude values of the AOI are neither radiometrically corrected nor expressed in decibels. The backscatter amplitude is left as computed from the raw in-phase and quadrature channels. The SAR AOI are saved in jpeg format making sure that no information is lost and they are subsequently imported into Matlab to compute their backscatter histogram, mean, standard deviation and rotationally averaged power spectrum.

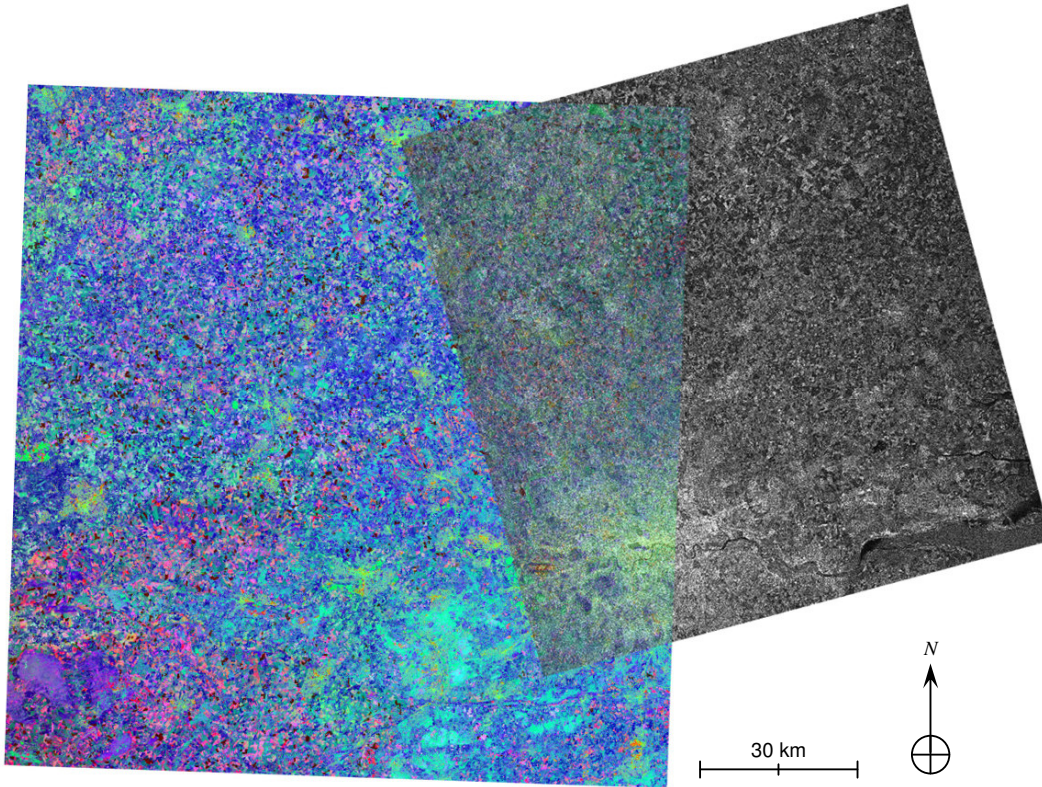



















Figure 5-9. Landsat 7 ETM+ image (12th May 2001) and ERS-2 scene (11th June 2001).

Table 5-2. List of the twenty AOI selected in the SAR scene. The columns specify the name of the AOI, the coordinates of its centre location, the number of pixels and the actual SAR backscatter amplitude image.

AOI No.	Name	Coordinates of Area of Interest Centre (North and West) (Proj : Transverse Mercator Datum: Ord. Survey G. Britain 1936)	No. of Pixels (AOI are squared with ground resolution of 25x25 m per pixel)	Image (Shown with a resolution of 28.346 pixels/cm). The SAR look direction is from left to right.
1	Brogborough landfill - 01	52° 03' 22.68" 0° 35' 32.62"	1296	
2	Brogborough landfill - 02	52° 02' 55.07" 0° 35' 24.30"	484	
3	Stewartby landfill	52° 04' 57.27" 0° 31' 00.35"	784	

Table 5.2. cont.

4	Disturbed area 01	52° 03' 23.56" 0° 31' 13.95"	784	
5	Disturbed area 02	52° 04' 18.17" 0° 29' 36.28"	484	
6	Elstow landfill	52° 06' 13.78" 0° 28' 26.67"	784	
7	Arlesey landfill	52° 00' 02.83" 0° 16' 21.05"	1444	
8	Disturbed area 03	52° 07' 41.84" 0° 14' 39.15"	484	
9	Potton landfill	52° 07' 23.02" 0° 13' 31.52"	484	
10	North Herts landfill	51° 58' 29.60" 0° 18' 01.62"	676	
11	Hatfield Quarry landfill	51° 46' 44.00" 0° 16' 21.60"	676	
12	Waterhall Quarry landfill	51° 46' 54.49" 0° 06' 40.51"	484	
13	Pollards Quarry landfill	51° 46' 08.43" 0° 06' 45.04"	256	
14	Disturbed area 04	51° 54' 07.42" 0° 32' 07.57"	324	
15	Disturbed area 05	51° 51' 57.79" 0° 30' 52.04"	256	
16	Disturbed area 06	51° 58' 24.48" 0° 11' 23.42"	324	
17	Disturbed area 07	52° 04' 56.72" 0° 17' 32.97"	324	
18	Disturbed area 08	51° 40' 29.29" 0° 26' 00.86"	324	
19	Disturbed area 09	51° 43' 09.89" 0° 19' 34.81"	256	
20	Disturbed area 10	51° 54' 49.30" 0° 20' 40.44"	400	

5.2.1 Spatial Analysis Results

The analysis results are presented in a way that facilitates the assessment of any difference between waste disposal sites and disturbed areas, considered as two separate groups.

A preliminary examination, illustrated in Figure 5-10 shows that there is no specific correlation between the size of the AOI and the two groups. Also, the histograms do not highlight any aspect that can differentiate waste disposal sites from disturbed areas. Figure 5-11 shows that the difference between the backscatter mean and standard deviation of the two groups is insignificant.

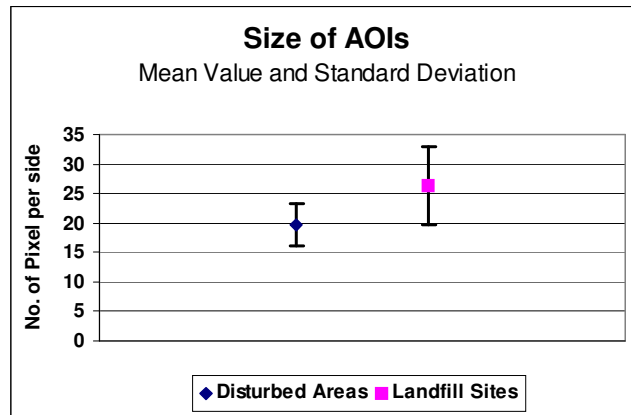


Figure 5-10. Mean value and standard deviation of the AOI size.

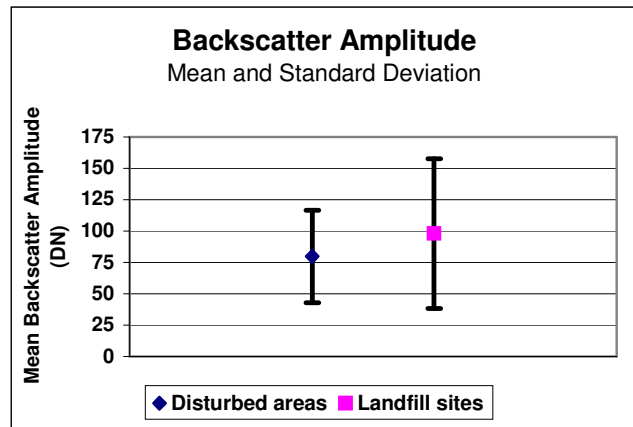


Figure 5-11. Mean value and standard deviation of SAR backscatter.

Conversely, the power spectra illustrated in log-log plots in Figure 5-12 present valuable attributes. This analysis technique is presented in Section 4.4. The power-law exponents β for every AOI are summarised in Table 5-3. As shown in Figure 5-13, their means appear to be associated to two different groups. The difference of the power law exponents indicates that landfills present a higher spatial correlation with relatively more structure at large spatial scales. This difference in correlation is related to the ground variables detected by the radar electromagnetic signal, which are different from the sun radiation scattered and reflected to the sensor in an optical system.

The hypothesis that the AOI can be classified based on the parameter β (i.e. null hypothesis H_0 : Disturbed areas = Landfill sites, versus the alternative hypothesis H_1 : Disturbed areas \neq Landfill sites) is tested by analysing whether there is a significant difference between the two means. The separation between the means of the β values for the two groups is confirmed by a t-test considering non-homogeneous variance even with a 99 % confidence level. This statistical test, presented in more details by Kennedy and Neville (1986) is used to compare the mean values of two populations for the purpose of determining whether the observed difference is due to chance only or whether it is statistically significant. This assessment is based on the key assumption that the two groups follow a normal distribution. Montgomery and Runger (2003) clarify that possible moderate departures from normality do not adversely affect this procedure. Therefore, it is possible to argue that landfill sites can be separated from disturbed areas on the basis of their SAR backscatter amplitude spatial structure. The same t-test is carried out considering the power-law exponents of AOI 13 as an outlier. This procedure decreases the degree of freedom of the data sets but it is found again that the two groups are separable even with a 99 % confidence level. The discussion presented in the next sections address in more details the interpretation of this result.

Table 5-3. Power-law exponents, β , of the model fitted on the rotationally averaged power spectrum of each AOI.

Disturbed areas		Landfill sites	
AOI Number (Refer to Table 5-2)	Power-law exponent	AOI Number (Refer to Table 5-2)	Power-law exponent
4	-0.69	1	-1.28
5	-0.51	2	-0.75
8	-0.52	3	-0.90
14	-0.45	6	-0.75
15	-0.61	7	-1.19
16	-0.67	9	-0.71
17	-0.41	10	-1.12
18	-0.54	11	-1.29
19	-0.39	12	-1.26
20	-0.40	13	-1.70
Mean = -0.52 Standard Deviation = 0.11		Mean = -1.10 Standard Deviation = 0.32	

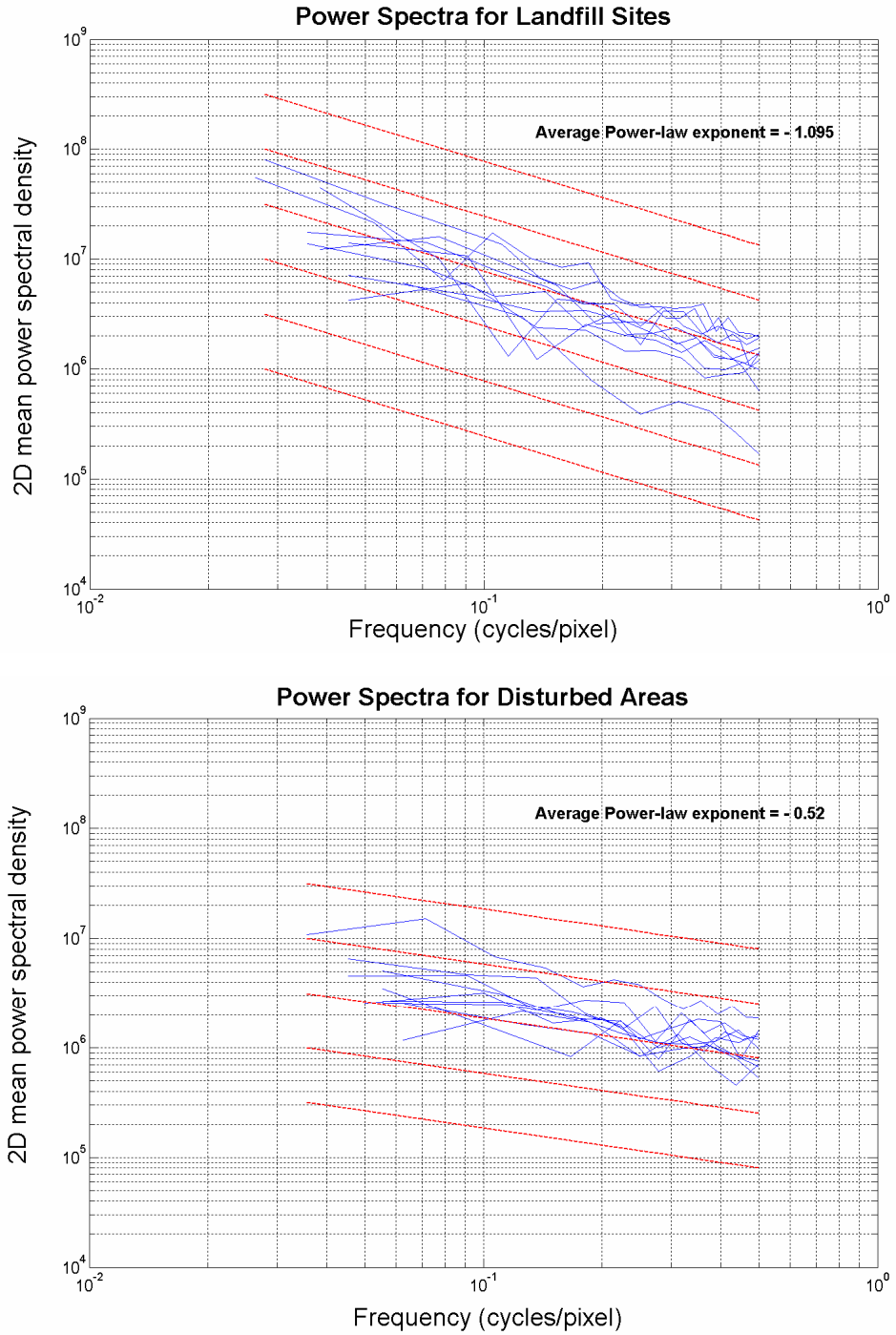


Figure 5-12. Power spectra for landfill sites (above) and disturbed areas (below). The red dotted line represents the average power-law exponent of the two groups.

Another inspection is carried out on the correlation between the AOI size and the computed power-law exponents. The correlation for disturbed areas has a negative value equal to -0.42 , which suggests that smaller areas tend to have smaller values of the power-law exponent. Nonetheless, the computed correlation for landfill sites is almost zero (i.e. 0.099), thus refuting such suggestion.

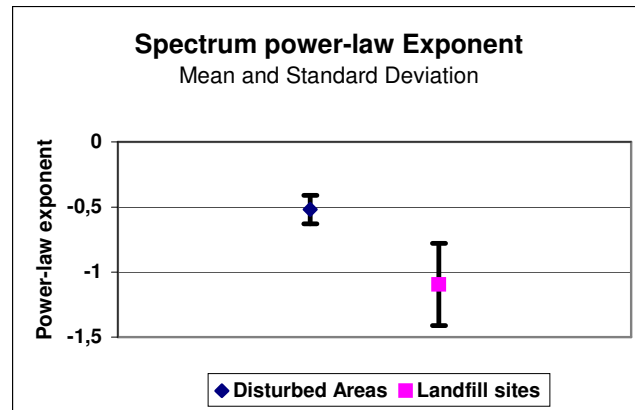


Figure 5-13. Mean value and standard deviation of spectrum power-law exponents.

5.2.2 Validation

In order to validate these results, the Brogborough and Stewartby landfills are selected in four additional SAR scenes. It is not possible to select disturbed areas as no reference optical image is available.

As the SAR scene used in the previous analysis is an ERS-2 ascending-pass acquired over the summer, the other four scenes cover other possible combinations. The new AOI and the specifications of their respective SAR scene are listed in Table 5-4. Ground truth data are provided by historical survey maps produced by the landfill operator.

The rotationally averaged power spectra (refer to Section 4.4) of the 8 AOI have very similar trends between each other. These are summarised in Table 5-5 and illustrated in Figure 5-14. The mean of the power law exponents is -1.41 , even lower than the one previously computed for waste disposal sites. This result corroborates the hypothesis that such sites can be distinguished on the basis of their SAR backscatter amplitude spatial structure.

These validation tests also prove that in both winter and summer conditions and with both ascending and descending orbits (i.e. different look angles and acquisition times), waste disposal sites present similar spatial characteristics.

Table 5-4. AOI used as validation sites. The columns specify the name of the SAR platform, the orbit specifications, the acquisition date and time, the number of pixels and the actual SAR backscatter amplitude image.







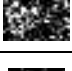

Validation AOI No.	SAR Platform	Orbit Parameters (i.e. Ascending / Descending; orbit number; track number; frame number)	Acquisition date and time	No. of Pixels (AOI are squared with ground resolution of 25x25 m per pixel)	Image (Shown with a resolution of 28.346 pixels/cm). For Ascending orbits the SAR look direction is from left to right, whilst for descending orbits it is from right to left)
01 Brog.	ERS-1	D; 21124; 94; 2547	30/07/1995 11am	784	
02 Stew.	ERS-1	D; 21124; 94; 2547	30/07/1995 11am	676	
03 Brog.	ERS-1	A; 24008; 473; 1035	16/02/1996 10.06pm	1024	
04 Stew.	ERS-1	A; 24008; 473; 1035	16/02/1996 10.06pm	576	
05 Brog.	ERS-2	D; 4457; 94; 2547	26/02/1996 11am	784	
06 Stew.	ERS-2	D; 4457; 94; 2547	26/02/1996 11am	676	
07 Brog.	ERS-2	D; 55559; 94; 2547	05/12/2005 11am	676	
08 Stew.	ERS-2	D; 55559; 94; 2547	05/12/2005 11am	484	

Table 5-5. Power-law exponents β of each AOI.

AOI Number (Refer to Table 5-4)	Power-law exponent
1	-1.76
2	-1.46
3	-1.57
4	-1.31
5	-1.79
6	-1.34
7	-0.91
8	-1.13
	Mean = -1.41 Standard Deviation = 0.30

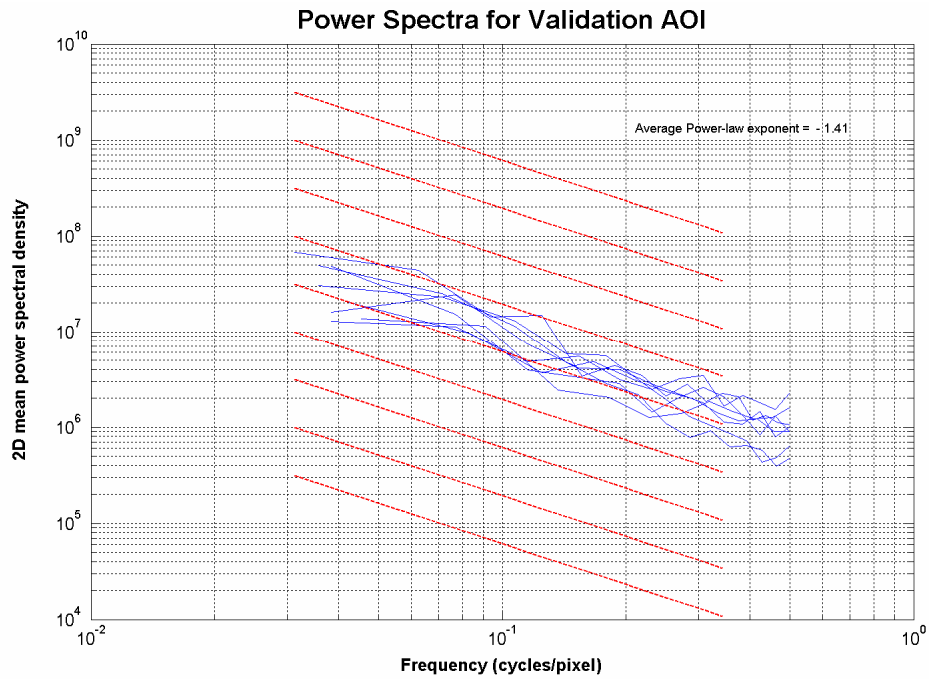


Figure 5-14. Power spectra for Brogborough and Stewartby landfills used as validation sites. The red dotted lines represent the average power-law exponent.

5.2.3 Discussion

Statistical considerations are not the sole basis for drawing inferences. A physical appreciation of the problem, judgement and experience should also be brought into the picture. The statistical results on the rotationally averaged power spectra must be correlated with qualitative observations of the AOI. The disturbed areas in fact appear to be characterised by high-frequency speckle changes. In contrast, waste disposal sites tend to present distinct features with high radar backscatter. Furthermore, the power-law exponents β can be related to the fractal number D_2 (Pentland, 1984). As comprehensively described by Sun et al. (2006), fractal geometry represents a valuable tool for characterising complex shapes and land surface patterns in remote sensing images. As such, the value of D_2 is intimately linked to a notion of “complexity” or “roughness” of an image (Pentland, 1984). It is beyond the scope of this research to discuss the potentials and limitations of the various fractal dimension estimation methodologies. The reader is referred to Mandelbrot (1977, 1982) for a more complete discussion of fractal geometry and to Peitgen and Saupe (1998) for an introduction to fractal analysis of images. In the context of this research it is important to recognise that the mean values of β for the two groups lead to a fractal dimension, D_2 , equal to 3.29 and 2.95 for the disturbed areas and landfill sites respectively. Turcotte (1997) explains that the first fractal value corresponds to “white noise” while the second value represents self-affine images in which the scale variability in the two dimensions is different. This latter property can consequently be linked to a certain level of anisotropy.

The presence of anisotropic features in the landfill SAR backscatter images can be confirmed by a visual examination. This can also be corroborated by applying a Radon transform (refer to section 4.4.3) as shown for example in Figure 5-15. Here the transform is applied to the disturbed area number 04 (AOI number 14) and to the Pollard landfill (AOI number 13). The graph for the disturbed area is homogeneous with high values for all θ angles, whilst for the landfill site the transform shows the presence of a specific feature.

The preliminary ground observations carried out in Chapter 3 can explain the presence of such directional dependent properties. In fact, landfill sites are characterised by a distinctive topography and variable soil properties that significantly affect the microwave signal and its backscattered amplitude. For instance, as confirmed by the survey map in Figure 5-16, the strong backscatter amplitude linear element visible in the Brogborough validation AOI number 1 and 5 is produced by a 35 m high slope.

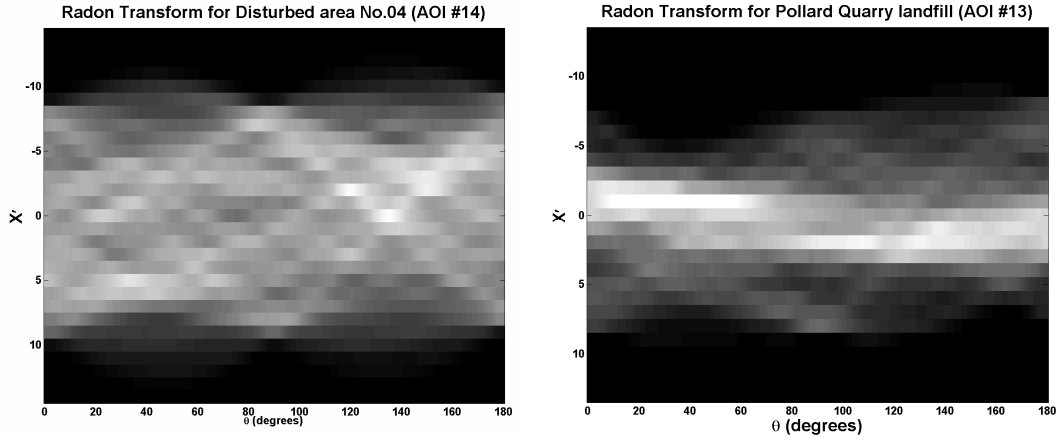


Figure 5-15. Radon transform for two AOI.

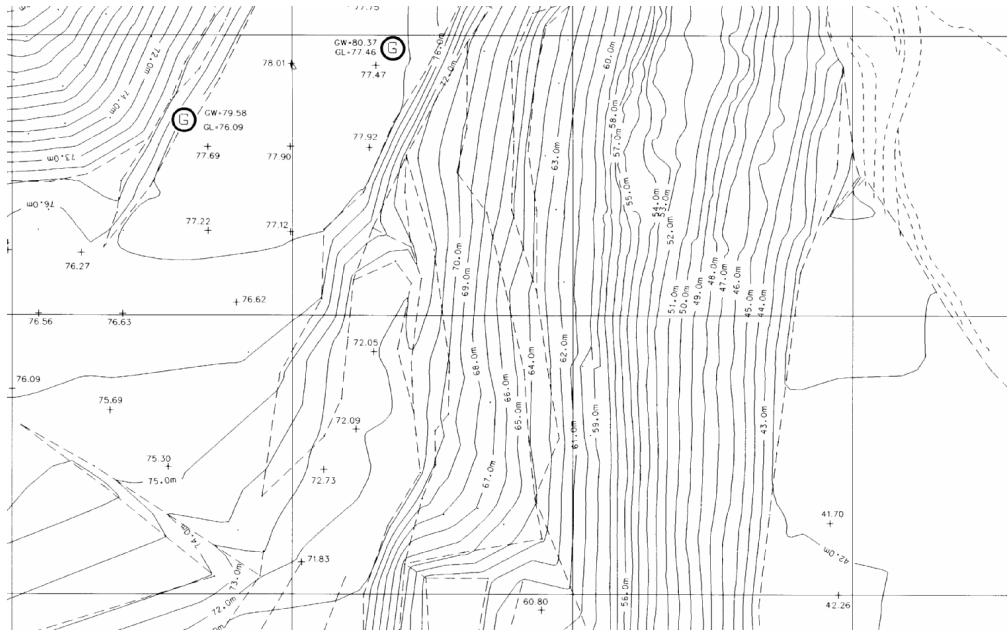


Figure 5-16. Particular of a survey map with a 100 m spacing grid of Brogborough landfill provided by Waste Recycling Group Ltd. (Void Take Up Survey 24th January 1996). It highlights a 35 m high step occurring in about 180 m across.

A number of studies have questioned the applicability of the fractal model to remotely sensed images (Lam, 1990; Emerson et al., 1999; De Jong and Burrough, 1995; Lam et al, 2002). These studies have shown that the estimated D_2 varies with the resolution of the image used and the region and direction in which it is computed. As argued by Sun et al. (2006), even though it is not necessary to relate the power-law exponents β to the fractal dimension in order to extract textural information, the dependence of the fractal dimension on the scale of the image highlights the limitation of all spatial statistics estimation methodologies, including the power spectrum method used in this research.

As examined by Emerson et al. (1999), changes in scale, or resolution, affect the estimation of any spatial structure analysis. This is easily noticeable by comparing Figure 5-2 and Figure 5-4. In the low resolution image the fields on the left of the landfill do not present the spatial structure associated with the furrows which is instead clearly detectable in the high-resolution image. Fisher (1997) and Stein et al. (1999) stress that such issues are often not fully covered in the literature therefore leading to erroneous conclusions.

With regard to SAR images, the influence of pixel size for distributed targets has been partially examined by Nesti et al. (1996). They conclude that the same target appears different depending on the spatial resolution of the SAR processor. This has an immediate impact on the estimation of the backscattering coefficient σ^0 . Their results show that with spatial resolutions smaller than 2 AC length of the target, the statistics of the backscattered signal do not follow those of the speckle model presented in Section 2.1.3. For larger pixel sizes, the experimental data become instead consistent with the Rayleigh model. This finding substantially confirms the results presented in Sarabandi and Oh (1995) which, based on numerical simulations, show that a correct estimate for the σ^0 can be obtained with pixel sizes above 2 AC length. Nesti et al. (1996) do not specifically discuss the spatial structure variation. They simply notice that “in the high resolution image, there are many bright spots sparsely distributed over the surface, whereas in the low resolution image, there are fewer and larger spots almost uniformly covering the entire surface”. In other words, an increasing resolution progressively reveals a different structure of the target, theoretically reaching the point at which each individual scatterer becomes observable and dominates the return in the pixel. This does not mean that the wave-target scattering mechanism which is directly linked to the frequency and polarisation of the SAR system actually changes. For instance, the 5 multilook averaging process in azimuth described in Section 5.2 suitably reduces the speckle effect of SAR imagery but it may also hide texture features which are unrelated to the speckle models of homogeneous targets. Furthermore, this analysis can also be linked to the Ulaby et al. (1982) criteria used in Section 3.1.3 such that horizontal spacing distance in the AC length estimation must be $\leq 0.1\lambda$.

These key considerations lead to the conclusion that the optimal SAR resolution and SAR wavelength depend on the scale of the ground phenomena under investigation. For instance, although it would not correctly estimate the backscatter coefficient σ^0 (Nesti et

al., 1996; Sarabandi and Oh, 1995), a very high resolution below 2 AC length may be required in order to fully appreciate the spatial characteristics of certain ground elements. In the specific context of this research, the 25 by 25 m resolution appears adequate to appreciate anisotropic features in landfills and to generate speckle-characterised images for the other disturbed areas. This same argument is presented by Curran and Atkinson (1999). They discuss that, in the simplest case, the optimal pixel size to study a feature of interest is about 10 times smaller than the autocorrelation value of the feature itself. For the 35 m slope shown in Figure 5-16, the optimal resolution would be about 18 m (i.e. a 10th of the dimension in which the slope occurs). Therefore, the 25 m ground resolution of the SAR images used in this study is not far from the optimal one. A coarse ground resolution would smooth out both the distinctive attributes of landfills and also the speckle noiselike quality of disturbed areas. Such an effect would limit the applicability of the spatial analysis as a classification tool between the two groups.

As landscape attributes seem to be the key to distinguishing landfill sites from other disturbed areas, it becomes necessary to investigate what are the typical characteristics of areas such as sand and gravel pits, engineering earthworks, construction sites, borrow pits and quarries, which all present similar signatures with optical multispectral instruments. It is found that the first three types of sites have features similar to the batter present in landfills, which is on average between 2 to 6 m high, but overall they tend to be flat. Sometimes they present cone-shaped piles of processed material which may reach heights of 10 m. Borrow pits and quarries instead can present those larger topographic features analogous to landfills (e.g. the 35 m slope detected in Brogborough shown in Figure 5-16). Indeed, once terminated their initial purpose, they are often used as waste disposal sites in order to restore the original landscape. This fact can be also noticed by the name of the AOI in Table 5-2. Therefore, the SAR backscatter amplitude spatial analysis does not prove to be a definite solution. Additionally, it is also necessary to appreciate that as the overall landfill size decreases, the more significant topographic features become smaller as well (Smith, 2005). Therefore, even if the results do not show such correlation, smaller landfills might appear more similar to sand and gravel pits, engineering earthworks and construction sites. This issue is further discussed in Section 7.2.1.

Finally, it is important to appreciate that this study focuses on landfill representative of a specific country in the world. Indeed, the site operators have to follow strict procedures to deposit and handle waste. These operational practices may not be the same for other countries, and most probably not for illegal sites. Examples investigating this matter are presented in Section 7.4.

5.3 Analysis of Temporal Change Characteristics

The preliminary ground based observations presented in Chapter 3 have highlighted that capped areas of a landfill may not undergo any significant change for days, weeks and even months (apart from variations related to weather conditions), whilst due to the landfilling operations the open cells are affected by significant changes even at very small time scales (e.g. minutes and hours). It was also discussed that in large sites, there might be multiple open cells in which the tipping location may vary day by day depending on decisions taken by the site operator.

Two recent studies by Drezet and Quegan (2006) and Koskinen et al. (2001) show the complementary value of SAR backscatter and the coherence magnitude. They monitor the environmental effects of forests in time and relate the average backscatter and coherence variation to forest growth, vegetation density and stem volume. Even though the average backscatter amplitude cannot be used in the same way because this research does not treat a distributed target, valuable information can still be extracted by computing the interferometric degree of coherence. It is also necessary to remind the reader that the aim of this analysis is to find features that can help distinguish landfill sites from other disturbed areas and not to correlate data with onsite conditions and operations. This latter issue is discussed in the next chapter.

A preliminary analysis shows that with the typical ERS and Envisat interferometric 35-day repeat pass too much decorrelation occurs between the master and slave SAR scenes, thus resulting in no specific value. Conversely, the 1-day repeat pass of the ERS 1-2 tandem mission suitably detects specific changes of the ground conditions. The 11 available coherence images listed in Table 4-2 are used to observe the 1-day change. The time separation of the tandem pairs acquired in 1995 and 1996 is shown in Figure 5-17. This shows the intervals at which these 1-day change detection snapshots are performed. The ascending orbit pairs are separated by 70 days, double as much as the descending ones. Also, two of the ascending pairs occur just 9 days before the other descending ones. The 1999 and 2000 tandem pairs have a separation of 79 days.

The development of this study has the main drawback that it requires specific ground information at the time of the ERS tandem mission. This limits the analysis only on the Brogborough and Stewartby landfills. Additionally, only one disturbed area is selected. This is the Quest pit of the Stewartby brickwork site that was initially considered in Section 5.1.

The 11 coherence images are computed with an estimating window of 2 by 10 pixels in range and azimuth respectively. The resulting images have a ground resolution of 50 by 50 m. In order to obtain a ground orientation close to reality, the scenes have been flipped horizontally or vertically depending on whether the acquisition orbit was respectively descending or ascending. The procedure to correct the coherence bias is

explained in Section 4.5.11. The average ENL over the three areas of interest in the 11 images is 48, with a standard deviation of 21.

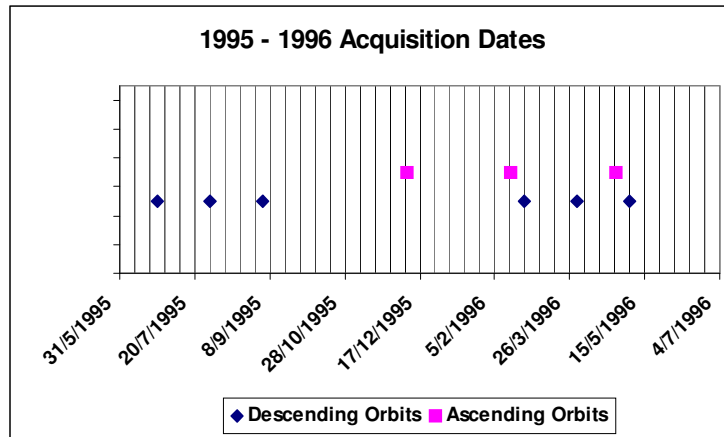


Figure 5-17. 1995 – 1996 acquisition dates of the ERS 1-2 tandem pairs.

5.3.1 Analysis of Historical Weather and Ground Reference Data

The only available weather data for the 1995 acquisitions is obtained from the British Atmospheric Data Centre (BADC, 2006) as a special data request submitted by the author. The daily soil temperature and rainfall records from the Woburn Station (i.e. located 52.014° North and -0.594° East, 3.5 km from the Brogborough landfill) are summarised in Figure 5-18. The graphs show the average weather conditions on the days of the satellite passes and on the one immediately before. The scales in the graphs is not constant so it is important to refer to the relevant axis. These daily records shows that no noticeable weather events occurred between the tandem acquisitions. The 1 mm of rain on 3rd September and the soil temperature close to zero on 9th December 1995 are the only two features that can potentially change the surface dielectric constant between the two tandem acquisitions and consequently the magnitude and phase of the SAR backscatter.

Weather conditions at the time of the 1996 acquisitions, shown in Figure 5-19, are instead extracted from the Cranfield University Automatic Weather Station, managed by the Space Research Centre. The graphs show the temperature and rainfall data during the two days of the satellite passes and during the one immediately before. Again, the scale in the graphs is not always the same. The 15-min sampling data accurately shows the daily oscillation of the temperature and the lag between the variation of the air and soil temperatures. The magnitude of this lag, known as the soil temperature phase space, has an average of circa 2 hours. The graphs in Figure 5-19 illustrate that two of the tandem pairs (i.e. 16-17 and 25-26 February 1996) might be affected by decorrelation

due to rain events. In the first case, the rain starts just half an hour before the slave scene acquisition.

For the 1999 and 2000 ERS scenes, the average weather conditions are presented in Figure 5-20. These are again retrieved from the British Atmospheric Data Centre and refer to the Stagsden weather station located 52.128° North and -0.568° East, 8 km from the sites. In both cases a rain event is observed between the tandem acquisitions, potentially reducing the coherence values. It must be clarified that as the three sites have a maximum distance of 7.2 km from each other, the research assumes the same weather condition for all of them at any one time.

With regards to the conditions of the three sites, valuable information has been obtained from the respective operators.

Figure 5-21 to Figure 5-23 illustrate the location of the open cells in 1994/95, 1995/96 in the Brogborough landfill and present a VTU survey carried on 15th February 1996. As it is possible to see, activities were mainly localised in the northern part of the landfill. No specific information on ground cover is available on the lower part of the site. Figure 5-24 draws attention to the site extension that was permitted at the end of 1998 (Tucker, 2006) and the supplementary area leased at the end of 2006 used for a provisional clay stock pile.

Figure 5-25 provides the reader with the overall VTU of the Stewartby landfill carried out 28th January 2004. Even if much more recent than the interferometric passes this illustration can be used to clearly interpret the area covered by other partial drawings provided by the landfill operators. For example, the red line identifies the zone presented in Figure 5-26. This is an image of an open cell in 1995 and it is possible to recognise a lagoon just on the north border. Additionally, a surveyor of the site (Haycock, 2005) confirmed that in 1995-1996 parts of the central and lower areas of the landfill were already capped but not fully restored.

The Quest pit was officially opened in February 1983 and it is still being worked today as pictured in Figure 5-27. Once in the pit it is impossible to ignore the sheer scale of the crane that extracts the clay. Its bucket removes approximately 6.25 m^3 of clay at a time. There is also a conveyor belt that runs all around the site taking the freshly crushed clay from the navvy to the brick sheds where the brickmaking process begins. Any unsuitable clay is left on site and used to landscape the pit area already worked. Some of these areas are currently already covered by short grass and often small ponds are present.

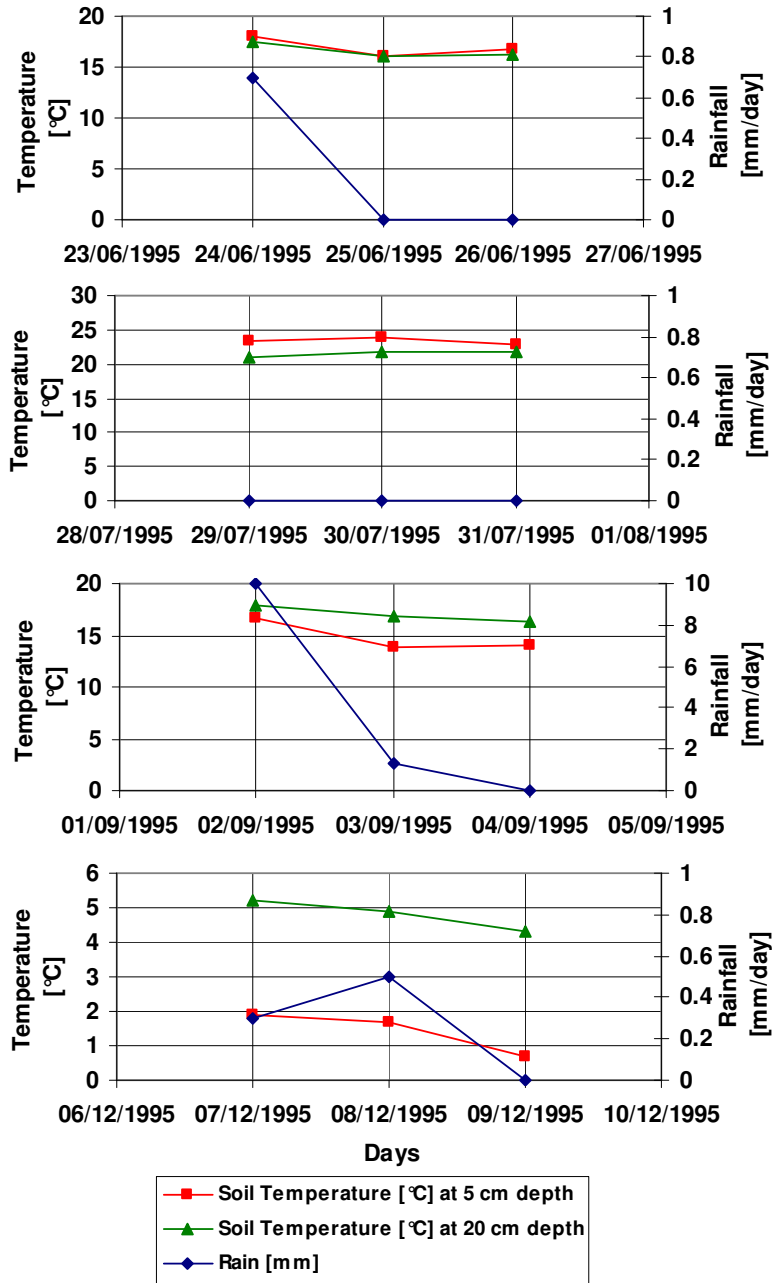


Figure 5-18. Daily soil temperature and rainfall during the 1995 ERS tandem pairs acquisitions.

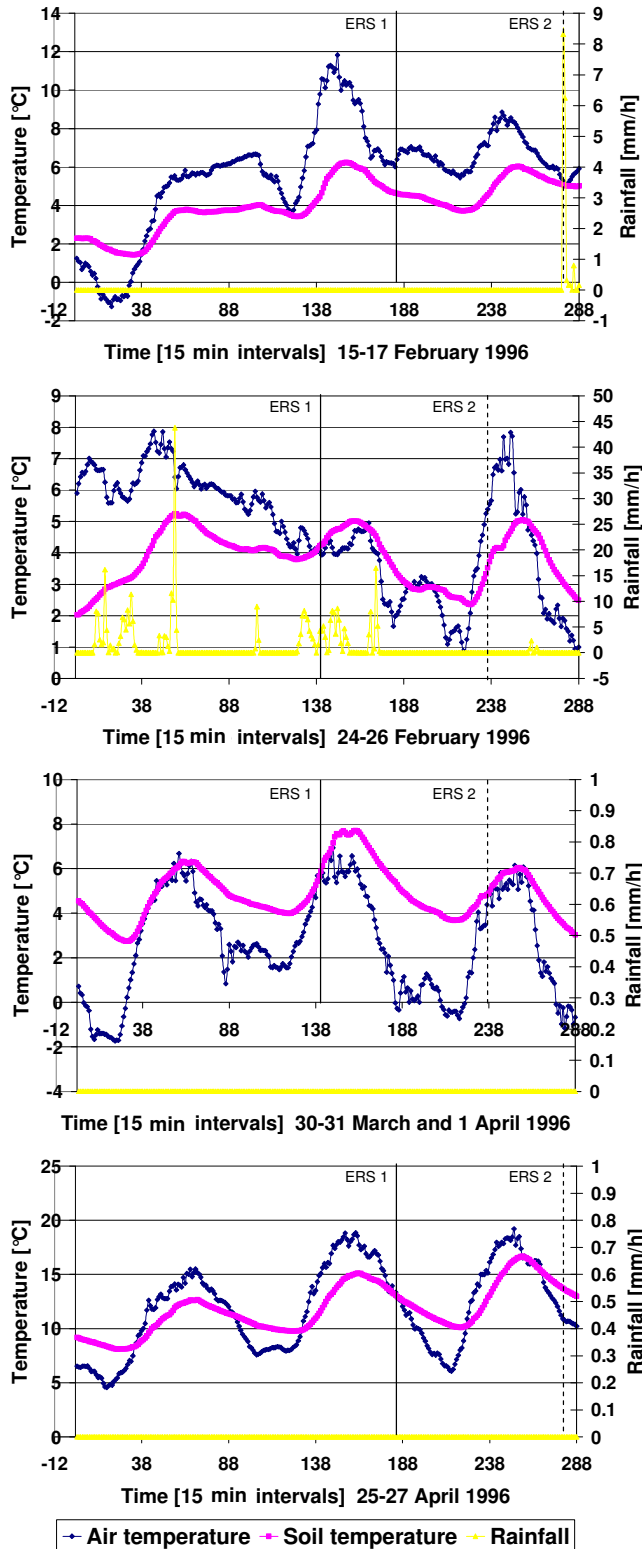
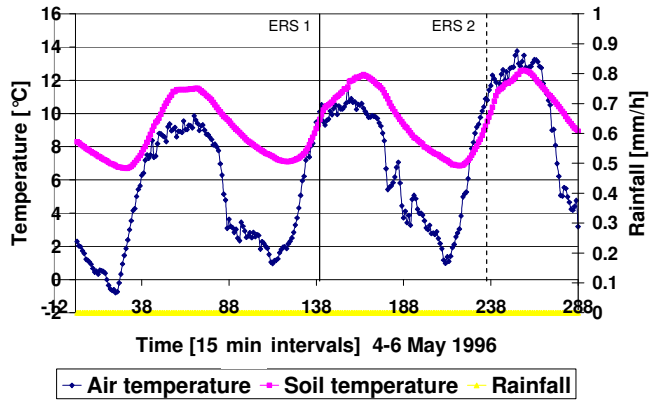


Figure 5-19. Soil temperature and rainfall data at 15-min intervals during the 1996 ERS tandem pairs acquisitions. The vertical and dotted lines respectively identify the time of the ERS 1 and ERS 2 passes. Cont.



End of Figure 5-19.

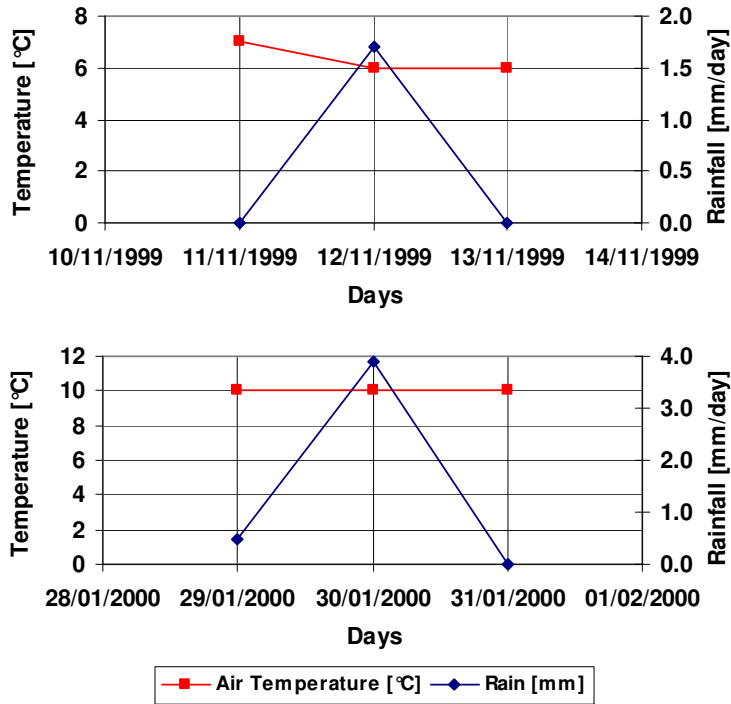


Figure 5-20. Daily soil temperature and rainfall during the 1999 and 2000 ERS tandem pairs acquisitions.

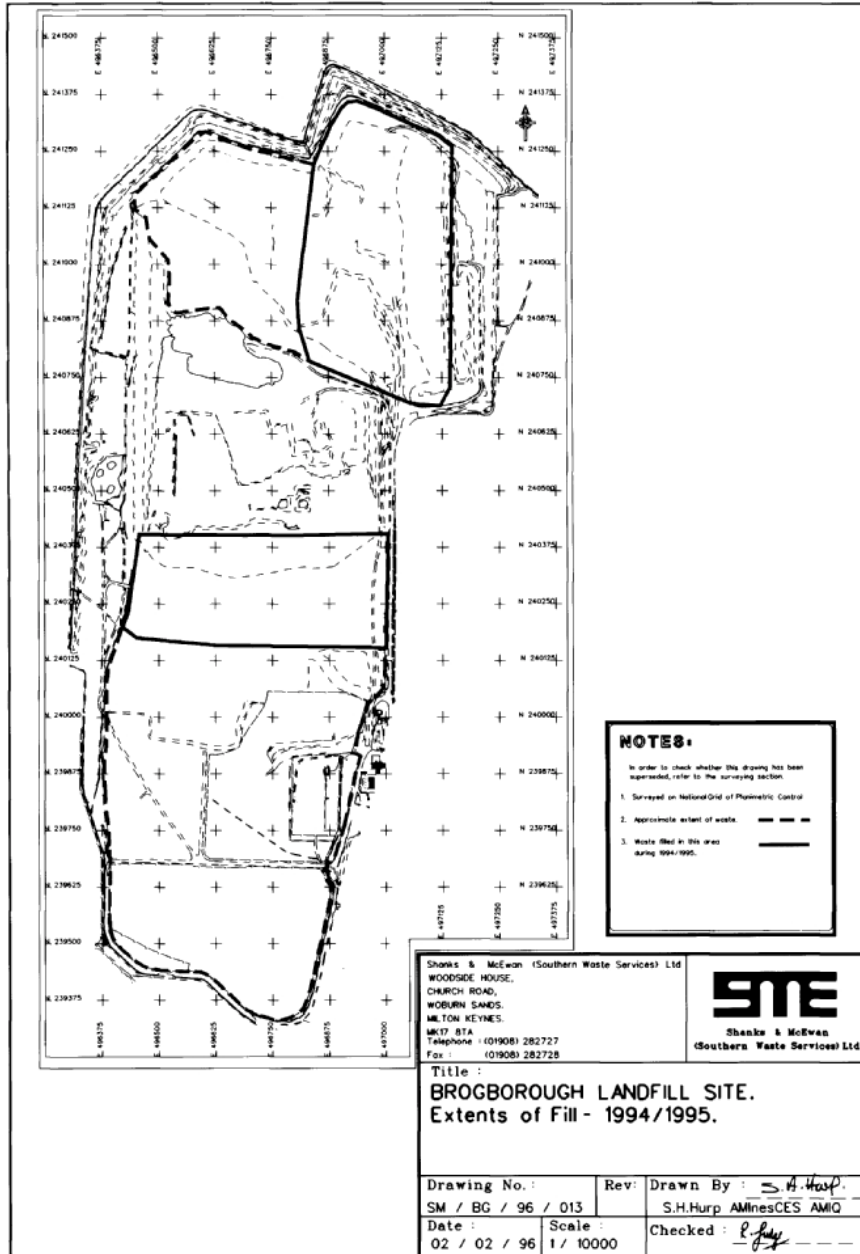


Figure 5-21. Survey map with a 125 m spacing grid of Brogborough landfill provided by Waste Recycling Group Ltd. The two solid lines indicate the areas in which waste was filled during 1994/1995.

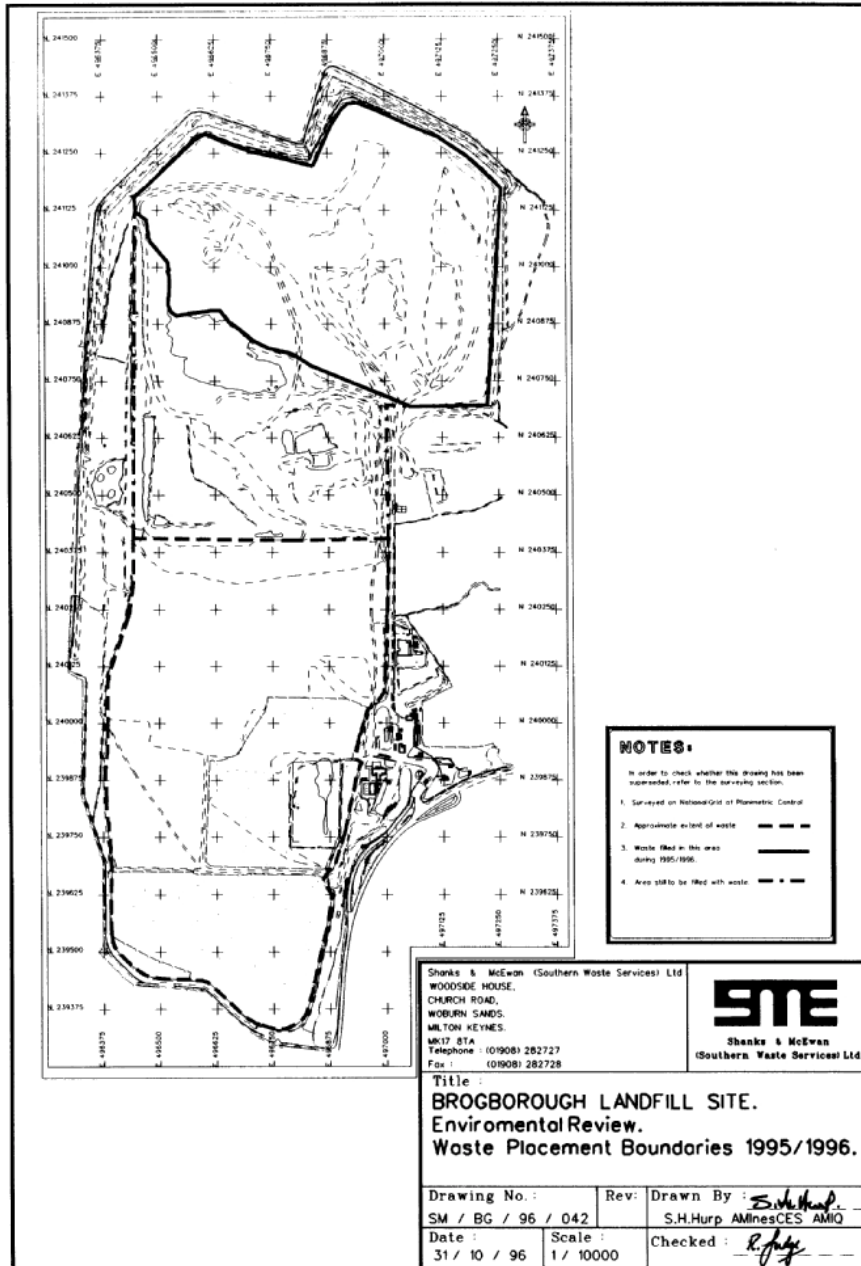


Figure 5-22. Survey map with a 125 m spacing grid of Brogborough landfill provided by Waste Recycling Group Ltd. The solid line in the northern part of the landfill indicates the area in which waste was filled during 1995/1996.



Figure 5-23. Topographic survey with a 100 m spacing grid of Brogborough landfill provided by Waste Recycling Group Ltd. 15th February 1996. These surveys specify the exact location of the tipping areas and the presence of any lagoon used to monitor run of water or the presence of leachate.

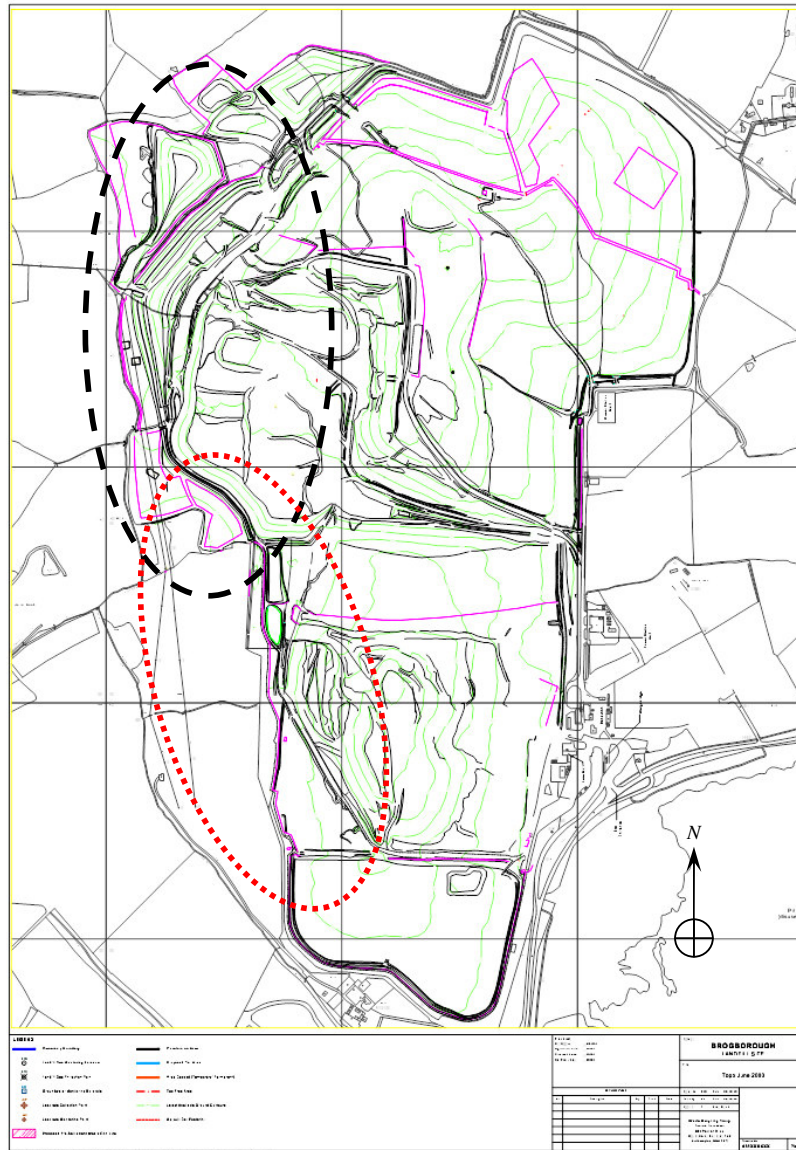


Figure 5-24. Topographic survey of Brogborough landfill provided by Waste Recycling Group Ltd. June 2004. The black dashed line indicates the site extension permitted towards the end of 1998. The red dotted line refers to an area leased at the end of 2006 used for a provisional clay stock pile. The grid has a 500 m spacing.

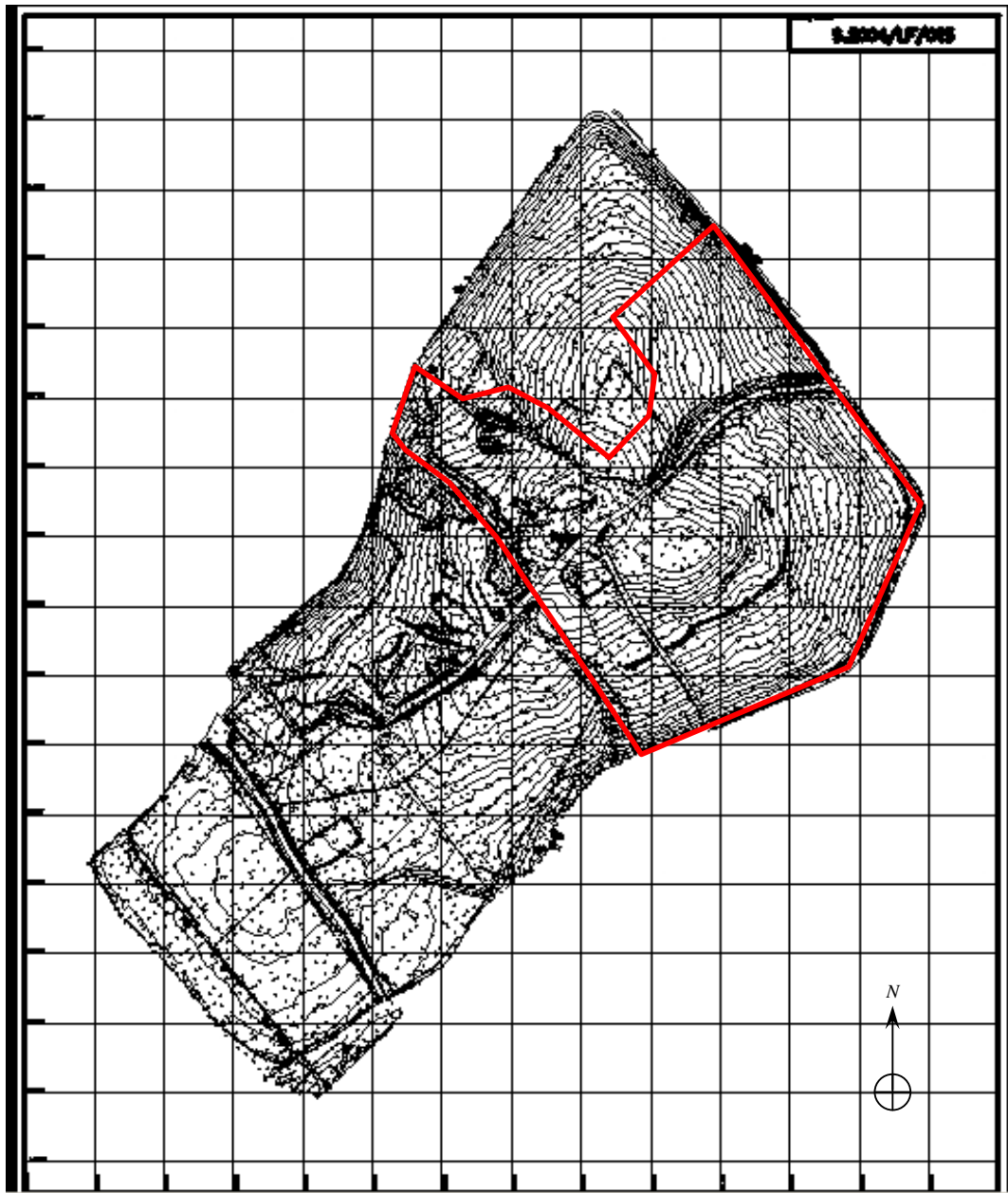


Figure 5-25. Topographic survey with a 100 m spacing grid of Stewartby landfill provided by Waste Recycling Group Ltd. 28th January 2004. The red line refers to the area covered in Figure 5-26.

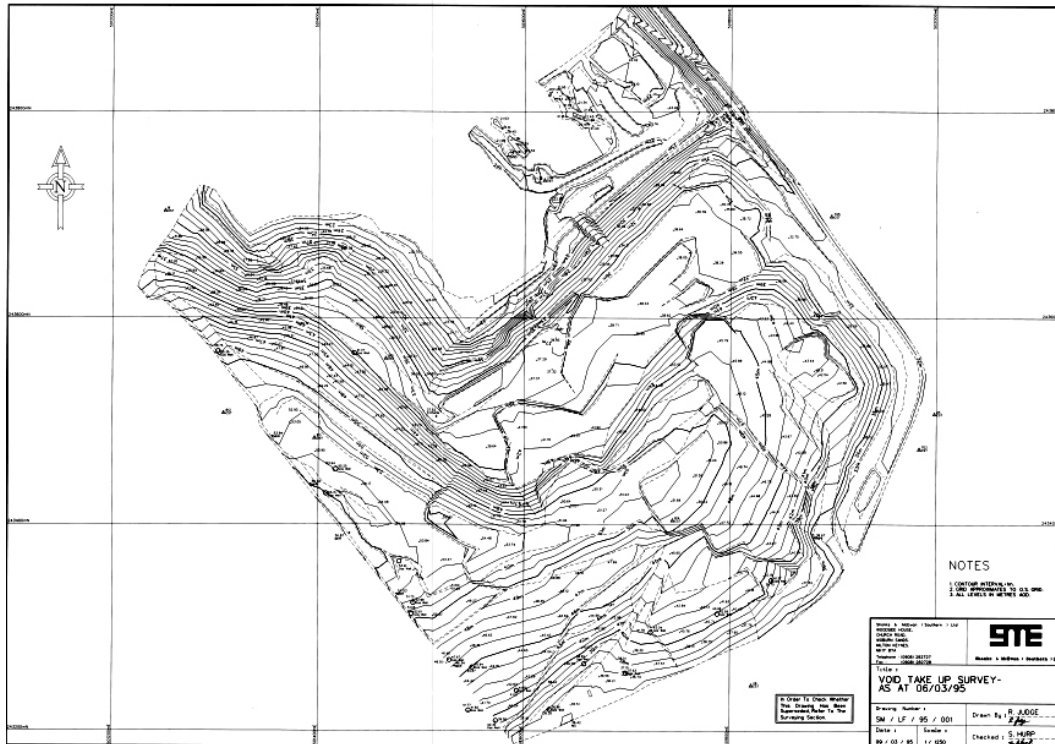


Figure 5-26. Topographic survey with a 200 m spacing grid of Stewartby landfill provided by Waste Recycling Group Ltd. 6th March 2004.



Figure 5-27. Quest pit of the Stewartby clay extraction site. Particular of the activities during a site visit on 22nd November 2006.

5.3.2 Coherence Magnitude Results

All coherence magnitude images are shown below. Each identified by a roman number, they are grouped as one single figure (i.e. Figure 5-28) and are arranged depending on the site, acquisition date and orbit type. All images are magnified four times, with each pixel corresponding to a 50 m² area. The approximate site boundaries are identified with a red contour in the first image of each group.

1995 – 1996 Brogborough Landfill – Descending orbits

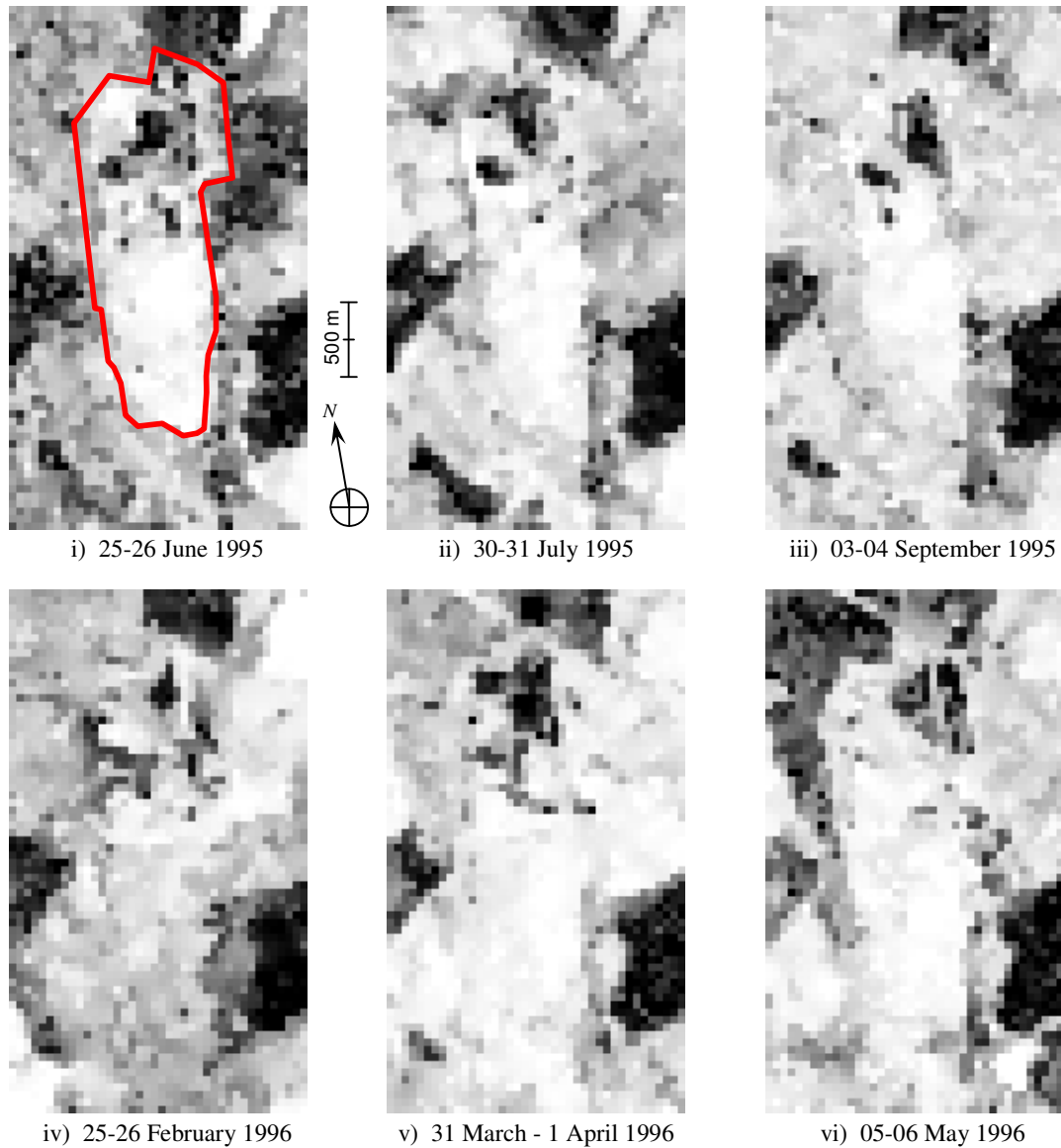


Figure 5-28. Coherence magnitude images of the three selected sites.

1995 – 1996 Brogborough Landfill – Ascending orbits

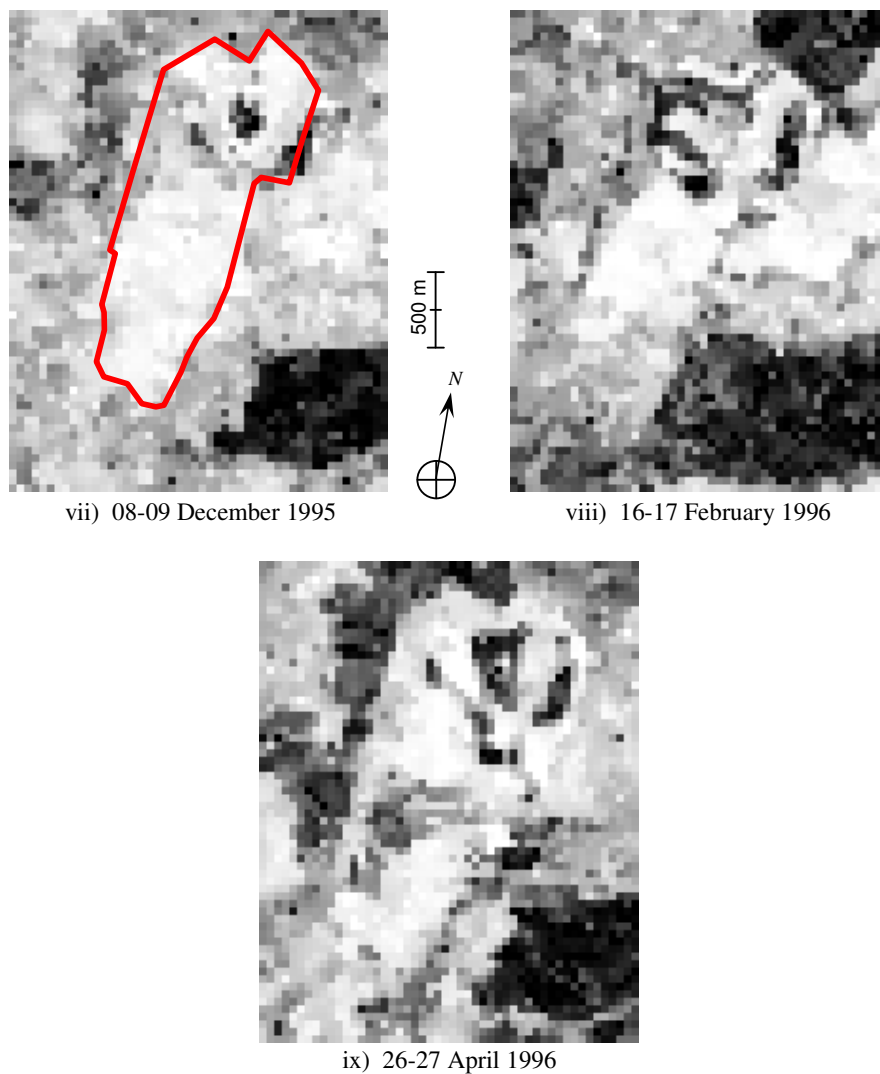
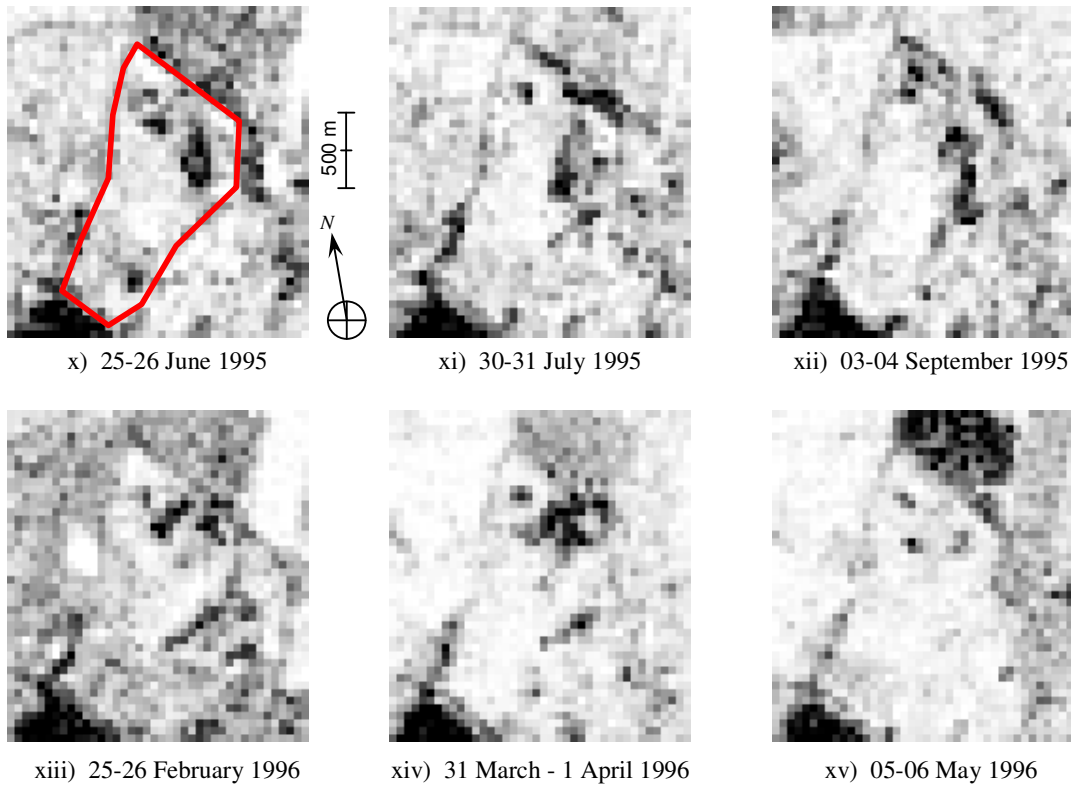


Figure 5-28 Cont.

1995 – 1996 Stewartby Landfill – Descending orbits



1995 – 1996 Stewartby Landfill – Ascending orbits

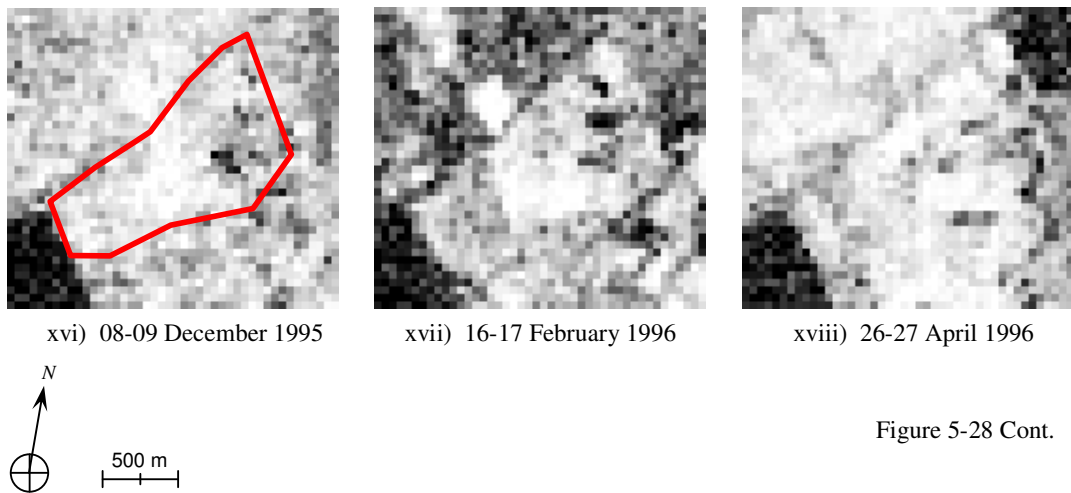


Figure 5-28 Cont.

1995 – 1996 Stewartby Quest Pit – Descending orbits



xix) 25-26 June 1995



xx) 30-31 July 1995



xxi) 03-04 September 1995



xxii) 25-26 February 1996

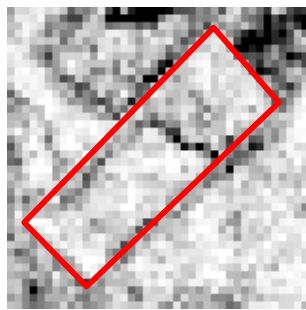


xxiii) 31 March-1 April 1996

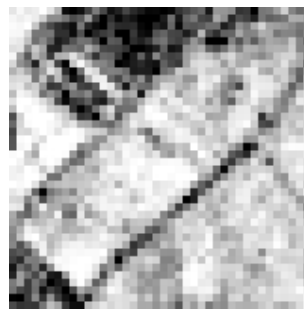


xxiv) 05-06 May 1996

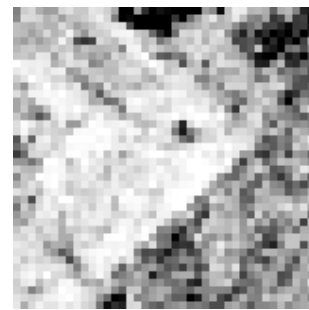
1995 – 1996 Stewartby Quest Pit – Ascending orbits



xxv) 08-09 December 1995



xxvi) 16-17 February 1996



xxvii) 26-27 April 1996

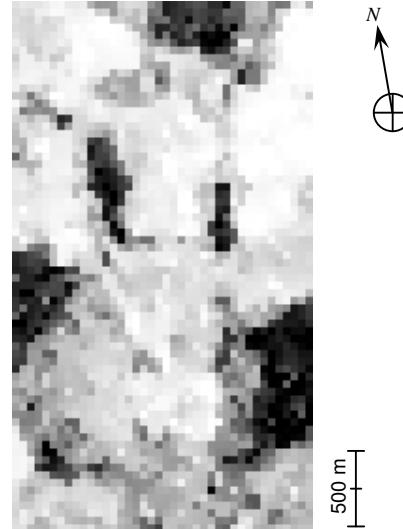
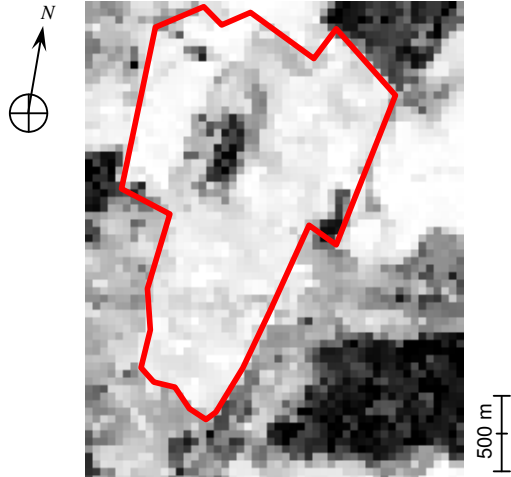
Figure 5-28 Cont.

12-13 November 1999 (Asc.)

30-31 January 2000 (Desc.)

Brogborough Landfill

Brogborough Landfill



The red contour is needed to show the site extension.
xxviii)

xxix)

Stewartby Landfill

Stewartby Landfill

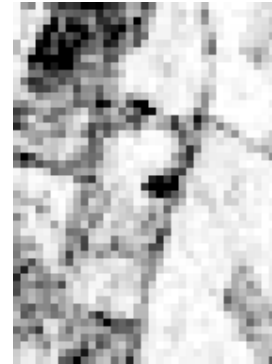


xxx)

xxxi)

Stewartby Quest Pit

Stewartby Quest Pit



xxxii)

xxxiii)

End of Figure 5-28

5.3.3 Discussion

The occurrence of the rain and frost events observed respectively on 3rd September and 9th December 1995 does not seem to have affected in any significant and noticeable way the interferometric coherence of the AOI. In contrast, for the 25-26 February 1996 tandem pair of the Brogborough and Stewartby landfills (i.e. number iv and xiii), the degree of coherence appears to have generally lower values. Even if this immediately suggests that the rain events presented in Figure 5-19 might be the cause of such decorrelation, image xxii of the Quest pit contradicts such suggestion. Here the lower part of the pit has an average coherence level of 0.89. Therefore, the observed decorrelation in the landfills must be caused by other types of change.

The 1999 interferometric tandems do not present any overall significant loss of coherence that might be related to rain events presented in Figure 5-20. As the weather data are daily average readings, it is possible that the master and slave scenes have both been acquired after the precipitation on 12th November. The same applies for the tandem pairs of year 2000.

The analysis also examines these images in more quantitative terms. The coherence mean and standard deviation of tandem pairs that could be negatively affected by weather conditions do not present any noteworthy difference from all other coherence images.

Having established this key point, a visual inspection of the 22 coherence magnitude images of the landfill sites (i.e. 11 images per site) confirms what the preliminary observations highlighted: changes in landfills are substantial, occur very rapidly and not always in the same location. This is clearly noticeable by comparing Figure 5-28 viii with iv, and ix with vi. Even with only 9 days of separation, the locations of the low coherence areas on the top half of the Brogborough landfill have completely changed. Additionally, image ix presents a high level of alteration on the whole site. Following an image to image registration as discussed in 4.8, it is possible to compute a difference map between viii and iv and between ix and vi. This is shown in Figure 5-29. In both cases, the difference is computed by subtracting the coherence magnitude of the first tandem pair (i.e. from the ascending orbit) from the coherence of the second tandem pair (i.e. from the descending orbit), and subsequently dividing the results into 11 classes defined by change thresholds. A positive change identifies pixels that became brighter, represented in red, while a negative change identifies pixels that became dimmer which are represented in blue. Zones that have not changed their coherence magnitude characteristics tend to a grey shade. Figure 5-29 shows that within the landfill boundary there are many areas that have substantially changed (i.e. coherence magnitude difference > 0.6) even with only a 9-day separation.

Overall, the fast changing location characteristics of decorrelated areas is also evident on the Stewartby landfill. Even if the decorrelated areas in xvii are also present in xiii, a

new major zone of low coherence is observable. Large areas of decorrelation are again present in the 1999 and 2000 (i.e. images xxviii , xxix, xxx and xxxi).

With regards to the Quest pit of the brickwork site, all images with the exception of the 1999 and 2000 tandem pairs show smaller regions of decorrelation, roughly equal to 200 to 400 m² each. These are about half or even less the size of the low coherence areas observable in the landfills. Additionally, the areas undergoing change in the clay extraction site do not tend to vary their location, in contrast with the waste disposal sites. This might be related to the fact that the excavating crane was operating only in a couple of locations over the 1995 and 1996 period and activities were therefore mainly taking place around that specific area. The Quest pit coherence magnitude images also present fixed linear features that can be correlated to transportation roads within the site.

Overall, it seems that coherence magnitude images of landfill sites are characterised by large decorrelated areas with transient attributes, whilst the Quest pit presents smaller areas of low coherence with a permanent location. This is a distinct difference that can certainly support the achievement of the first research objective. With a SAR spaceborne system similar to the ERS 1-2 tandem mission, the coherence magnitude computed from an ascending interferometric pair can be compared with the results obtained from the immediately following (i.e. 9 days apart) descending tandem pair. The occurrence of large decorrelated areas with frequently changing location can establish the presence of a landfill.

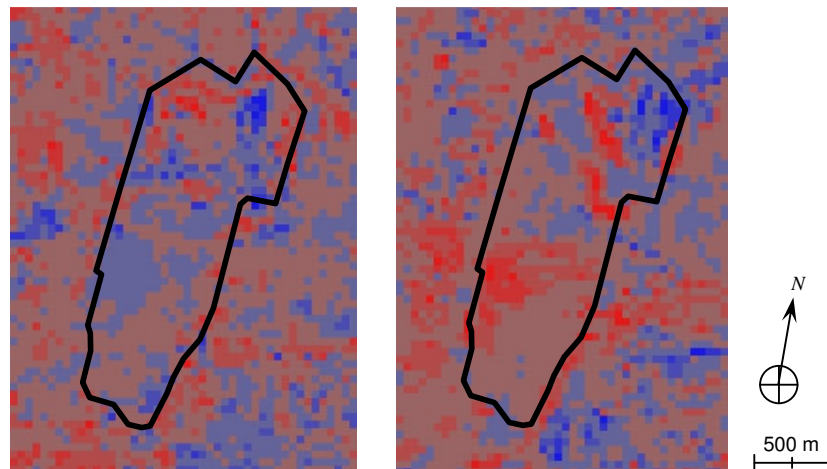


Figure 5-29. Difference map between the coherence magnitude images of (a) 16-17 February 1996 and 25-26 February 1996 and (b) 26-27 April 1996 and 05-06 May 1996. Red pixels represent areas in which change is detected in the first coherence image but not in the second, while blue pixels identify areas in which change occurred in the second coherence image but not in the first. Zones that have not changed their coherence magnitude characteristics between the 9 days of the two tandem pairs have a grey colour. The approximate site boundary is shown by the black contour.

However, the analysis has a number of limitations. As previously underlined, it takes under consideration only two landfills and only one disturbed area. Additionally, the waste disposal sites are managed by the same operator and the disturbed area is a clay extraction pit in which the specific operational procedures put in place are most certainly not representative of other disturbed areas such as a derelict area, sand and gravel pits, engineering earthworks, construction sites, borrow pits and quarries. The dependence of the finding of this analysis on the practical daily operations that take place in these sites can be confirmed by investigating images xviii) and xv) of the Stewartby landfill. Both of them, but more predominantly the first of the two (i.e. the ascending interferometric pair), show an overall level of high coherence in the whole of the site. By checking the 1996 calendar, it is found that these specific ascending master and slave scenes are always acquired respectively on Fridays and Saturdays at 10pm. As confirmed by the site operators (Kirkland, 2005), landfilling activities on Saturday are usually reduced or sometimes even stopped, and therefore not much change can take place in 24 hours between Friday 10pm and Saturday 10pm. The descending master and slave scenes instead are acquired on Sunday and Monday at 11am, therefore allowing for substantial change to occur.

Evidently, practical operational procedures are of key importance when considering coherence images. If a site handles a limited amount of waste or for other reasons activities are temporarily reduced or stopped, then the coherence image would not lead to reliable conclusions.

It is also important to appreciate that the separation between the ascending and descending tandem pairs is a key aspect. This time gap can become inadequate if too short or too long. For instance, with a sampling separation between the two tandem pairs of one day (i.e. day one ascending master acquisition, day two ascending slave acquisition, day three descending master acquisition and day four descending slave acquisition), no change of the location of the decorrelated areas in a landfill might be observed. This matter can be considered as the opposite of the Nyquist critical rate when sampling a signal. The shortcoming of this empirical assessment can be overcome by making a priori ground observations of other possible disturbed areas. In the timeframe of 24 hours, such places might undergo no change at all, or might in contrast completely vary. Others might present coherence magnitude characteristics very similar to the Quest pit, with decorrelated areas always located in the same position but maybe of smaller or larger sizes. Additionally, seasonality aspects may also play as a variable.

It is beyond the scope of the research to describe the extent and temporal characteristics of changes that can possibly occur on every single type of disturbed areas. What is important to understand is that with an accurate selection of the day of the week of the SAR scenes' acquisitions and the time separation between the two tandem pairs, it can be possible to distinguish landfills from other disturbed areas as demonstrated in this research. This constraint clearly poses requirements on the overall SAR mission design.

5.3.4 Analysis and Discussion of Interferometric DEM

As mentioned in section 5.3.1, no exact ground cover information is available on the lower part of the Brogborough landfill. Nonetheless, Figure 5-23 shows that this zone presents homogeneous topographic contours. At the same time, high coherence is observed even during months for which vegetation would cause a certain level of decorrelation (e.g. ERS tandems of 25-26 June 1995, 30-31 July 1995, 05-06 May 1996). It is therefore possible to infer that this southern half of the site is probably covered by bare soil, presenting an optical signature similar to disturbed areas as initially discussed. Consequently, with such high coherence values it is possible to compute an accurate DEM. Should the bare soil cover assumption be inaccurate, the examination of the overall topography of the sites remains of significant interest with regards to the first objective of the report.

The tandem scene with the highest average coherence for the three sites of interest (i.e. 31 March - 1 April 1996) is processed in order to compute their DEM. The result is illustrated in Figure 5-30. The high coherence regions in both waste disposal sites have a distinctive positive topography whilst the Quest pit clay extraction site corresponds to a void with higher surrounding land. This result is obtained with the other tandem pairs as well, corroborating the general conclusion that, with a priori considerations on operational procedures of other possible disturbed areas, topography can help to distinguish waste disposal sites from other disturbed areas.

Clearly, this analysis would only distinguish waste disposal sites that are in the middle or end of their operational lifetime. In fact, landfills are often put in place to restore areas previously used as extraction pits in the first place. Therefore, during their early stages, landfills would present topography characteristics similar to the pits. Such consideration highlights again that every technique has its constraints.

A further exercise explores the value of subtracting two DEMs derived from two different ERS tandem pairs (i.e. acquired on 25th and 26th June 1995 and on 3rd and 4th September 1995). As presented in Figure 5-31, a substantial difference is visible in the open cells. This topographic difference of great value is in fact applied in the land-use classification algorithm as presented in Section 4.9.5. Nonetheless, it is important to appreciate that the height difference might also be affected by errors during the unwrapping procedure as the tipping areas are often characterised by low coherence as presented in the next chapter. Overall, this result also highlights the possibility of applying DInSAR techniques if the interferometric scenes are not too decorrelated (i.e. acquired closely in time). It is worthy of note to underline that no evident sign of waste settlement is instead detected in the lower half of the site with the dome like features as shown in Figure 5-30.

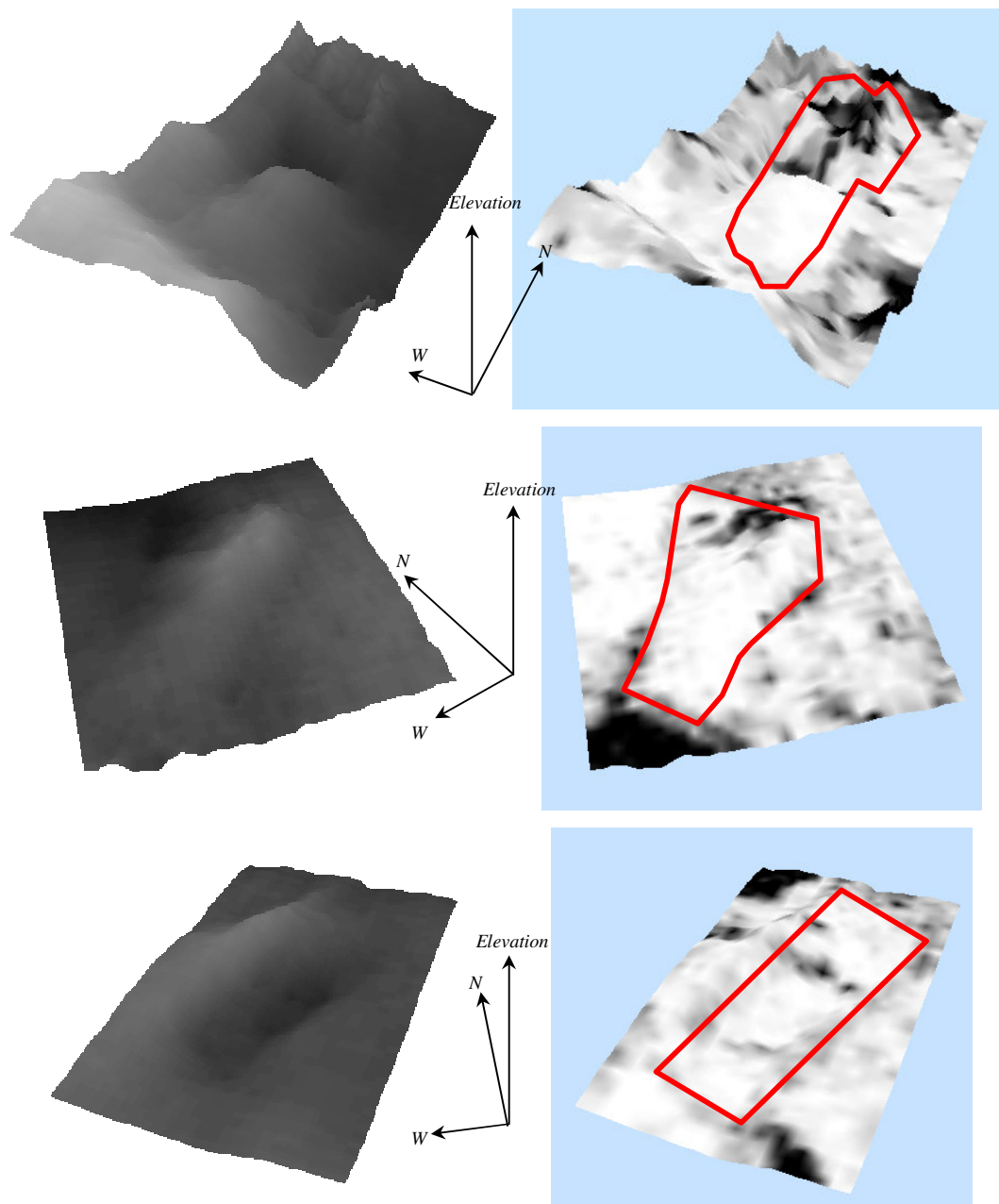


Figure 5-30. DEM of the three sites of interest for the ERS tandem scenes of 31 March - 1 April 1996. From top to bottom: Brogborough landfill, Stewartby landfill, Quest pit. The three DEM have a different scale from each other. The right column shows the topography values with a vertical exaggeration of 10 times. In the left column the coherence magnitude values are added on the topography. The red contours identify the approximate sites boundaries. The three axes in the middle show the approximate direction of the North (N), West (W) and the elevation.

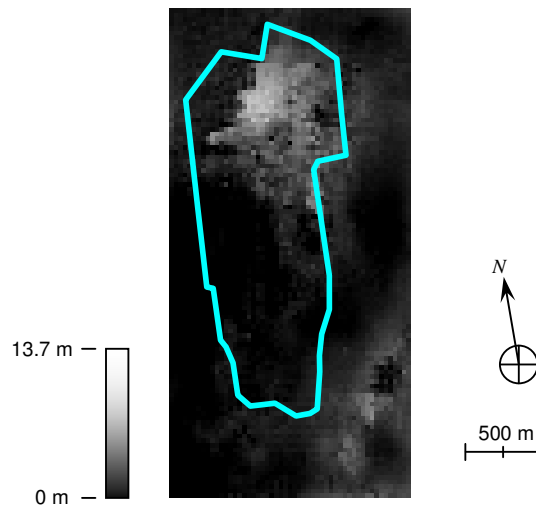


Figure 5-31. Subtraction of two DEMs over Brogborough landfill derived from two different ERS tandem pairs (i.e. acquired on 25th and 26th June 1995 and on 3rd and 4th September 1995). The white colour represents areas that have increased in height. The white zones south east of the waste disposal site correspond to vegetation areas next to the Brogborough lake over which the DEM might not be accurate due to the decorrelation effects. The turquoise contours identify the approximate sites boundaries.

5.4 Conclusions of Landfill Site Identification Analysis

This chapter has presented opportunities and limitations of different analysis techniques that address aspects in both the space and time dimensions and also topographic features. Overall, SAR data can help distinguish landfills from other disturbed areas but each technique has its shortcomings, therefore implying that they should be used concurrently. Table 5-6 pulls together the findings with the aim of giving all-embracing concluding remarks. All results highlight the strong dependency on the practical operational procedures carried out on the ground. These operations and the on-site conditions are the subject of the analysis presented in the next chapter.

Table 5-6. Concluding remarks on landfill site identification.

Analysis Technique	Capability	Ground features of interest	Constraints	Recommendations
SAR Amplitude Spatial Structure	Applicable to distinguish open cells	Irregular steep-slope elevation features generally higher than 20m	SAR ground resolution around 10 times smaller than the autocorrelation value of the feature of interest	Apply these two techniques together to corroborate the results
Interferometric coherence magnitude	Applicable to distinguish open cells	Large decorrelated areas with transient attributes	Two interferometric pairs with a 1-day temporal baseline and a separation between the two pair of 7 to 15 days	
Overall site topography	Applicable to distinguish capped areas of landfills in the middle or end of their operational lifetime	Regular topographic contours	High coherence values to allow the computation of an accurate DEM	Examine the topography if the other two techniques do not lead to any clear conclusion

6. On-site Conditions Monitoring

This chapter addresses the second research objective: is it possible to monitor on-site operational procedures with SAR data?

Apart from the general survey maps presented in the previous chapter, no exact ground reference information relative to the historical SAR data is available to relate SAR backscatter values with on-site conditions. Additional measurements are therefore required in order to obtain the SAR backscatter coefficient values for areas common to waste disposal sites and whose surface characteristics were investigated in Section 3.1.3. These data are obtained with the use of a ground based SAR (GB-SAR) system. Simulations based on the RT2 backscatter model are subsequently used to carry out a sensitivity analysis on the variables affecting the radar backscatter. The objective of this analysis is not to provide a detailed discussion of the modelling of the interaction of the radar signal with bare soils, but to quantitatively assess the parameters which have an effect on it.

Following this analysis, historical ERS SAR scenes are used to develop a novel classification methodology to identify different land-use areas on the Brogborough landfill. This method is based on a Fuzzy Logic classifier and on featured-based pixel-by-pixel classification procedures.

6.1 GB-SAR Acquisitions

In order to have a complete understanding of the interaction between the radar wave and the target surface of interest, the research makes use of a fully portable and polarimetric GB-SAR system. This is presented in section 4.6.

6.1.1 Acquisitions on Tipping and Capped Area

The GB-SAR system in the deployed configuration is shown in Figure 6-1. A comparative analysis is carried out between two different areas at the Brogborough landfill. The first is a relatively smooth surface of a capped area and the second is a rougher surface of a tipping area covered by temporary clay in an open cell. These are pictured in Figure 6-2.

The ground properties of these two surfaces are presented in Table 3-1 in Section 3.1.3. The volumetric soil moisture measured in the top 50 mm presented very dry conditions (i.e. equal to 0.08) for both areas. This value should be taken as approximate because air voids in the temporary clay of the tipping area and the hard ground condition of the

capped area introduce errors during the Theta probe measurements. This is explained in more detail in Section 4.3.2. The capped area is made of engineered highly compacted Oxford clay and due to the dry conditions during the GB-SAR acquisitions, wide cracks of approximately 20 mm were observed.

The two fully polarised acquisitions are obtained with a C-band antenna and the beam centre tilted at 50 degrees incidence angle. The data are polarimetrically calibrated against a known reference target and the 4° slope of the tipping surface is taken into account to correct the backscatter coefficient. The comparative analysis is carried out on the backscattering coefficient σ^0 [dB] computed with the new data processing algorithm for the GB-SAR (Bennett, 2005) as explained in Section 4.6.3. The system resolution is 100 mm in azimuth and 200 mm in range.

Figure 6-3 and Figure 6-4 show the σ^0 variation with respect to the incidence angle for all polarisations over the two areas. These graphs also include additional comparable experimental results taken from the literature (Oh et al., 1992).

An example of the imaging product generated by the GB-SAR is shown in Figure 6-5. These two images represent the HH polarisation acquisitions. Here, the ground range varies from 3 m at the top of the image (i.e. incidence angle of circa 17°), to 23 m at the bottom of the image (incidence angle of circa 63°). The incidence angle variation explains the stronger return obtained at close range. The azimuth resolution is halved for visualisation purposes only to obtain the same range resolution.



Figure 6-1. GB-SAR deployed configuration at the Brogborough landfill.



Figure 6-2. Acquisitions surfaces: capped (left) and tipping areas (right).

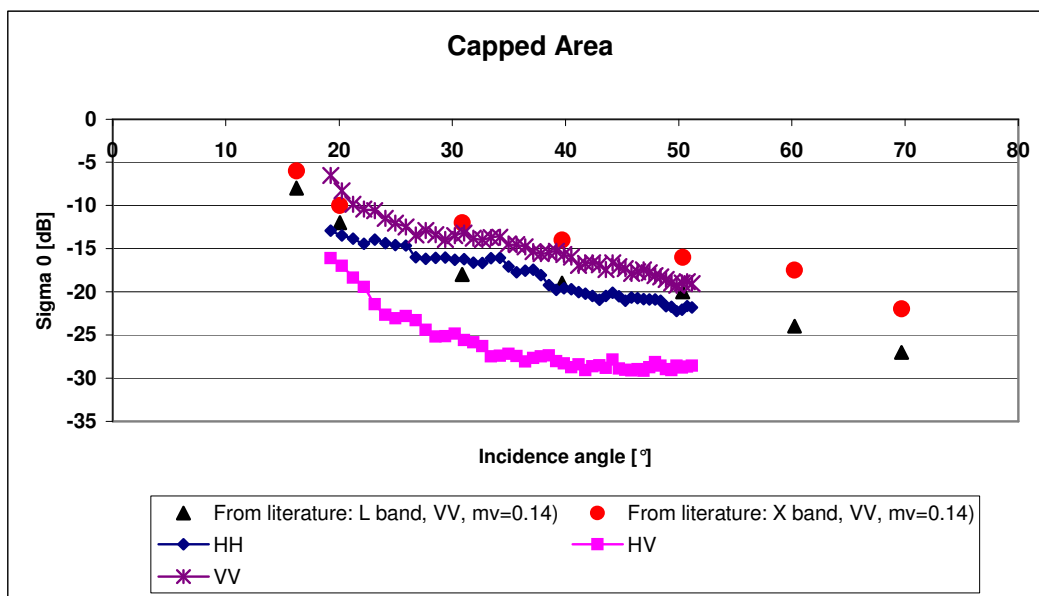


Figure 6-3. Angular response of σ_0 for all polarisations acquired over the capped area.

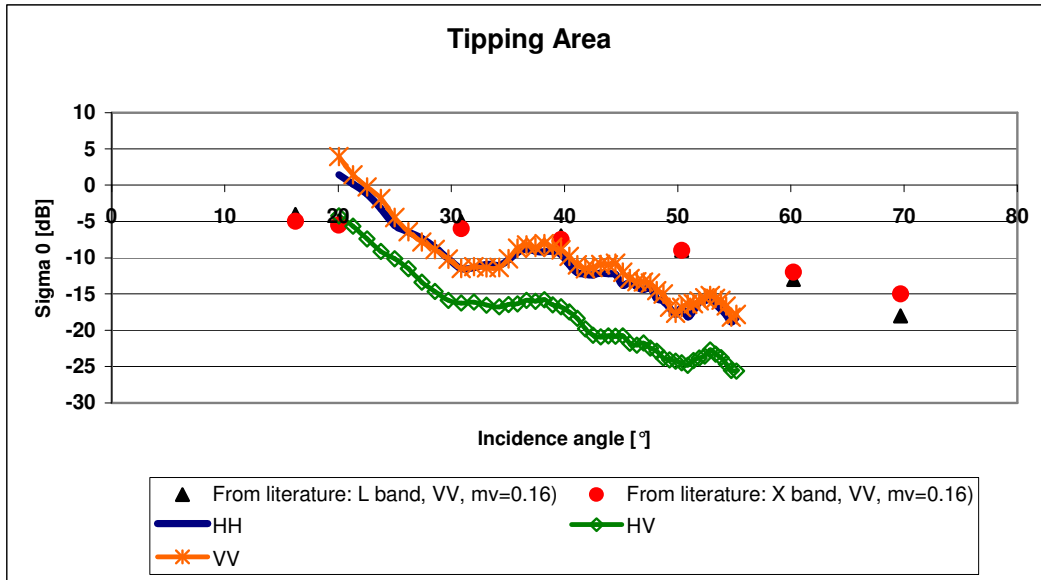


Figure 6-4. Angular response of σ_0 for all polarisations acquired over the tipping area.

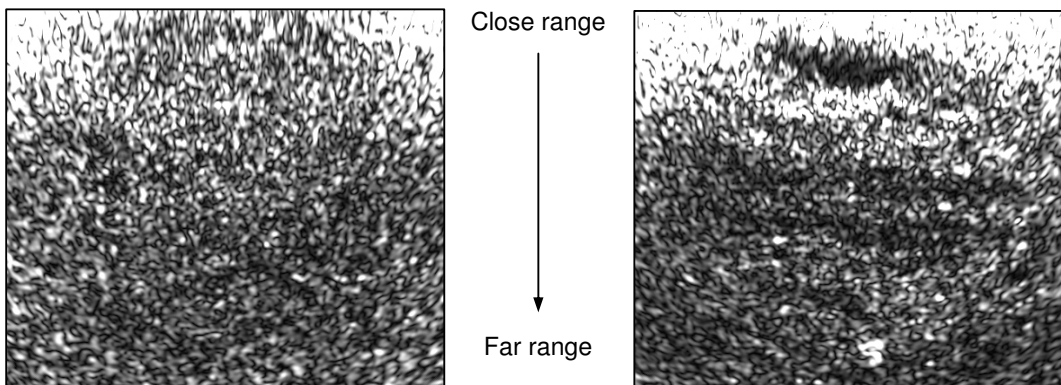


Figure 6-5. Amplitude values of the HH polarisation acquisitions of the capped cell (left) and of the tipping area (right). The images' histograms have been optimised independently of each other to improve the visualisation. The SAR system point of view is in the middle top of each image. Light pixels represent a stronger backscatter signal.

6.1.2 Comparative Analysis and Discussion

The HH backscattered values are initially investigated. Figure 6-6 shows the normalised histogram of the σ^0 distribution for the two scenes. The mean value for the tipping surface is circa 7 dB higher than the capped area. By applying a stretched histogram from -40 to -10 dB on both images, it is evident that the backscatter values from the tipping surface have a stronger return. This is shown in Figure 6-7.

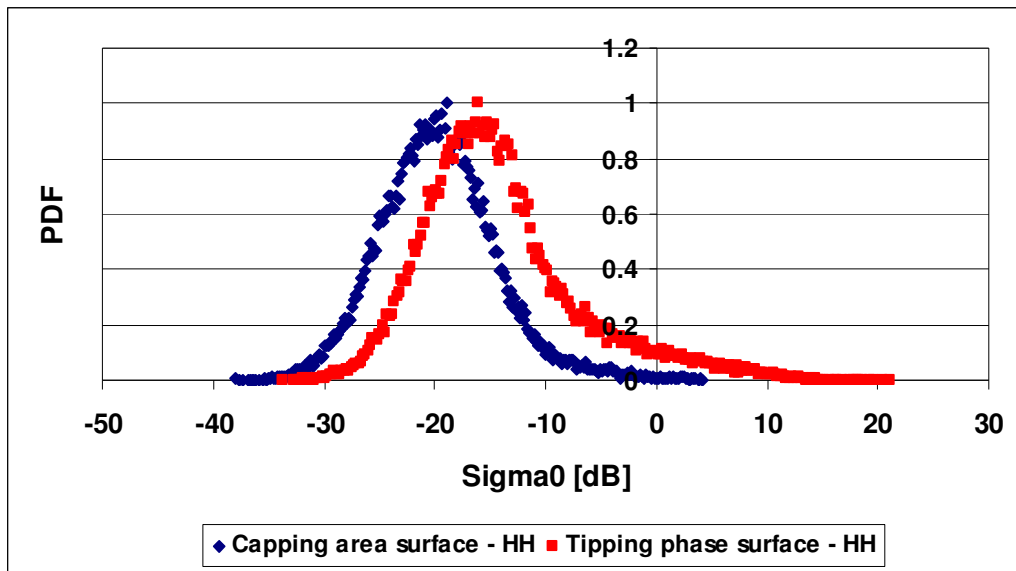


Figure 6-6. Normalised histograms of the HH backscattering coefficients of the two acquisitions.

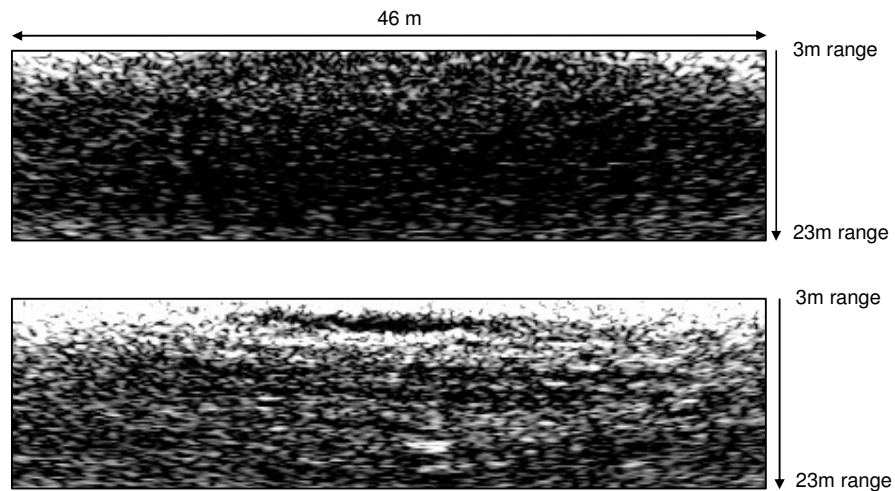


Figure 6-7. HH backscattering coefficient values for the capped surface (top) and for the tipping surface (bottom).

It is important to appreciate that at C band the capped area surface satisfies the Rayleigh criterion for smoothness but not the Fraunhofer one, which is more consistent to experimental observation (Ulaby et al., 1982), even for incidence angles larger than 50° . With an L band SAR instead, the capped area surface can be considered as smooth, while the tipping area would still act as a rough surface.

An immediate aspect of the capped area is the uniformity of the return with respect to range, in contrast with the more inhomogeneous characteristics of the tipping surface (Figure 6-7). This latter surface has a high k_s parameter (i.e. 3.75 from Table 3-1) therefore shadowing and multiple bounce effects might occur especially at higher incidence angles. The darker patch at close range in this rougher image is due to the presence of a high negative slope which probably causes shadowing in the radar signal. Two additional darker horizontal linear feature can also be observed towards the middle of the image. These are related to a highly compacted road way and is also detectable in Figure 6-4 with low backscatter values at about 32° . The bright patch in the lower central region is instead caused by a large mound of debris containing metals.

The small discrepancy of the backscattering coefficient in Figure 6-3 and Figure 6-4 from the additional literature data is mostly due to the fact that the ground properties are not exactly the same. The lower values obtained for the tipping surface might be also related to the higher soil moisture conditions of the literature data.

Additionally, it is observed that the cross polarisation acquisitions for the capped area becomes stable at circa -28 dB with $\theta > 45^\circ$. This can be related to the presence of randomly oriented wide cracks on the ground previously mentioned. Such affect is also analysed by Li (2003), who models surface cracks as lossy dielectric cylinders obtaining backscatter coefficient values of -30dB even at 80° incidence angles.

It remains critical to understand the relation of these results with respect to the applicability of space-borne SAR imaging. As presented by Nesti et al. (1996) and as extensively discussed in the previous chapter, the same target appears completely different by changing the spatial resolution of the SAR processor. A space-borne acquisition with a ground resolution in the order of 40 AC lengths (i.e. 5 m ground resolution) would not be able to appreciate the same detailed spatial variability of the backscattered signal obtained with the GB-SAR.

Hence, only the backscattering coefficient σ^0 is the parameter of interest. On top of the average 7dB difference between the mean backscatter of the two surfaces, an aspect worthy of note is the exact similarity of the trend between σ_{HH}^0 , σ_{VV}^0 and σ_{HV}^0 for the tipping area in contrast with the capped area. Figure 6-8 shows that the mean of the correlation coefficients computed between the various backscattering coefficients for the tipping surface is 0.95 and it has a very low standard deviation. On the contrary, the mean value for the capped area is 0.7 with a standard deviation of 0.2. For example, the correlation between σ_{HV}^0 and σ_{VV}^0 of the capped area is only 0.59.

It is also observed that the co-polarised ratio $\sigma_{HH}^0/\sigma_{VV}^0$ can support the analysis of the on-site landfill conditions and distinguish smooth and rough surfaces, hence the capped from the tipping areas, with the assumption of a flat topography. In fact, as shown in Figure 6-9, the co-polarised ratio for the tipping surface is always smaller than the one of the capped area. The first has a mean value of 0.45 and the second of 2.76, both with a standard deviation of about 0.7.

As confirmed by Mattia et al. (1997), these results corroborate that the co-polarised ratio and the vertical-horizontal correlation coefficient can be used as roughness discriminators. Generally, the rougher the surface, the more depolarisation generated (Long, 2001). Therefore even though the two surfaces under examination do not strictly satisfy the smoothness criteria as previously discussed, the roughness difference is observable from the co-polarised ratio.

The cross-polarised ratio does not show any significant difference in terms of backscatter. This confirms the preliminary ground observations that no volume scattering occurs.

The steep slope for the tipping area ratios when approaching the 23°, or the large difference between to cross-polarised ratios of the two surfaces around 30° should not be considered relevant. Small variation specifically related to the surface of interest would have a considerable effect on the ratio. It is instead essential to focus on the more consistent features, such as the constant difference between the co-polarised ratios previously pointed out.

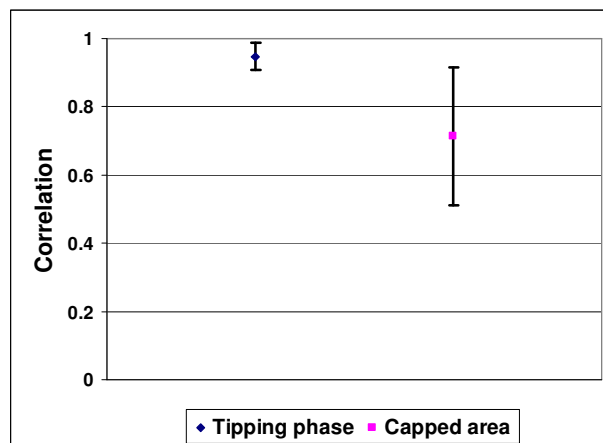


Figure 6-8. Mean and standard deviation of the correlation coefficients computed between the various backscattering coefficients for each acquisitions.

Ground observations also highlighted the frequent presence of conductive materials on the surface. If the distribution of such objects has an overall orientation within one SAR resolution cell, then they would act as one single oriented dipole, whose co-polarised ratio $\sigma_{HH}^0/\sigma_{VV}^0$ varies as \tan^4 of the orientation angle. This is shown in Figure 6-10. Hence, two acquisitions of the same area, from different perspectives but with the same incidence angle (e.g. ascending and descending orbits), would highlight the presence of such features, assuming the other parameters affecting the SAR backscatter do not change. Clearly, the backscatter return would also be affected by the rest of the ground “clutter”, nonetheless, for angles higher than 50° a small variation in the orientation would still cause a high change in the polarisation ratios. Although, the analysis predicted such behaviour, this was not observed in the acquired images and therefore it is possible to assume that it is not a significant feature.

The reader must be reminded that no phase information was available from GB-SAR acquisitions, preventing the research from examining the interchannel phase information such as the complex polarimetric correlations, the coherency matrix and the entropy factor. Nonetheless, as introduced in Section 2.1.4 and demonstrated in recent polarimetry and interferometric polarimetry studies (ESA, 2007d), the phase information is mainly used to differentiate between targets presenting dihedral and double bounce characteristics (e.g. urban areas) and diffuse targets (e.g. vegetation), therefore not specifically of direct use to this research.

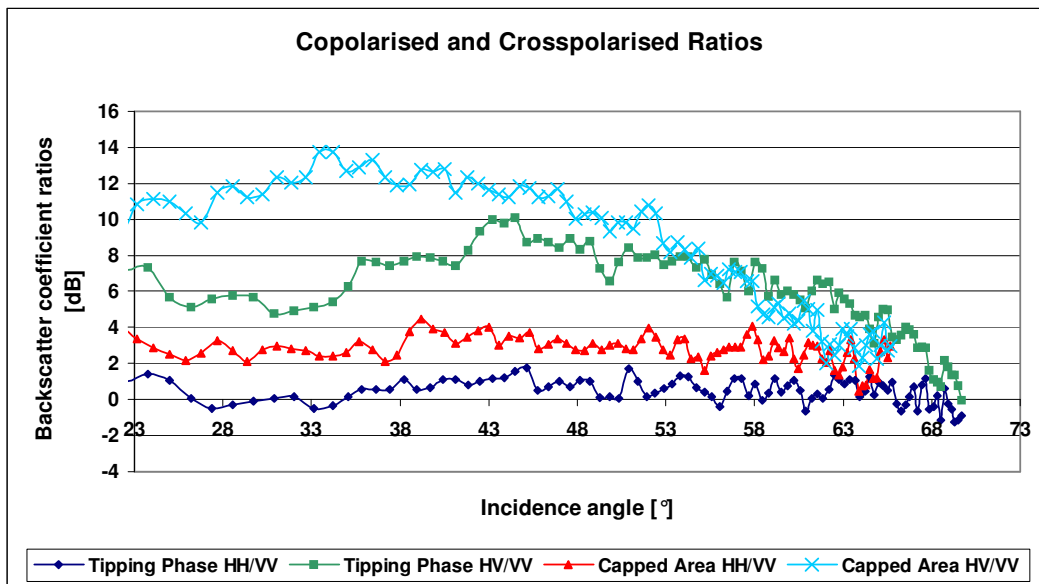


Figure 6-9. Angular response of the co- and cross-polarised ratios for both surfaces.

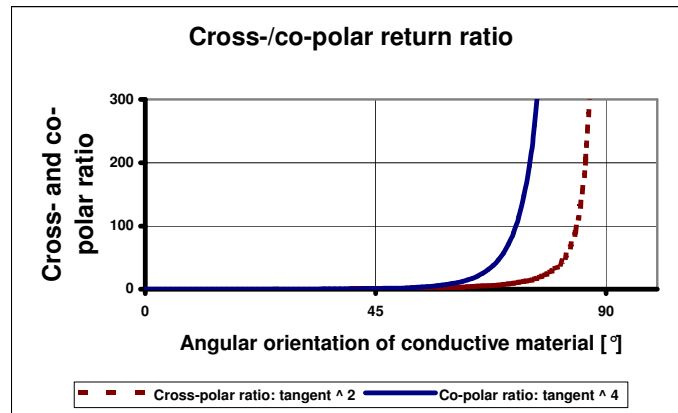


Figure 6-10. Variation of the cross and co-polar ratios as a function of a dipole orientation.

6.2 Sensitivity Analysis: RT2 Simulations

Before performing the sensitivity analysis on the variables affecting the SAR backscatter, tests are carried out to verify the accuracy and suitability of the RT2 software. The GB-SAR HH polarisation acquisitions for the two surfaces are compared with the RT2 output for the same ground conditions. As shown in Figure 6-11, the Ulaby and Siquiera model (1995) implemented in RT2 closely follows the trend of the GB-SAR backscatter. There is only the evident divergence for the tipping area return at incidence angles smaller than 28° degrees, which is also noticeable in Figure 6-4. This problem has been recently discussed by Fung and Cheng (2004), suggesting modifications in the electromagnetic model. Excluding such incidence angles, the root mean square error for the tipping surface backscatter is 1.42 dB with a standard deviation of 1.54 dB and for the capped area is 1.64 dB with a deviation of 1.54 dB. These small differences can be linked to the variability of the ground conditions and the 18 % accuracy of the ground measurements as discussed in Section 3.1.3. Therefore, such disagreement does not prevent the use of RT2 for the sensitivity analysis.

The sensitivity analysis can therefore be carried out on five different variables: the radar wavelength, soil moisture, soil texture, surface roughness and incidence angle. Figure 6-12 show the variation in backscatter with different soil moisture conditions for a 100% clay soil with a 9 mm roughness. This is plotted for all polarisations for the X, C and L bands. The higher the volumetric soil moisture, the more the difference between the HH and VV return. The X band tends to have the strongest return, while the L band presents the lowest values with the -50 dB for the HV polarisation at very low soil moisture conditions. Overall the backscatter varies in a range of 5 to 7 dB, a difference similar to the one observed between the capped and tipping area GB-SAR acquisitions which was instead mainly related to soil roughness.

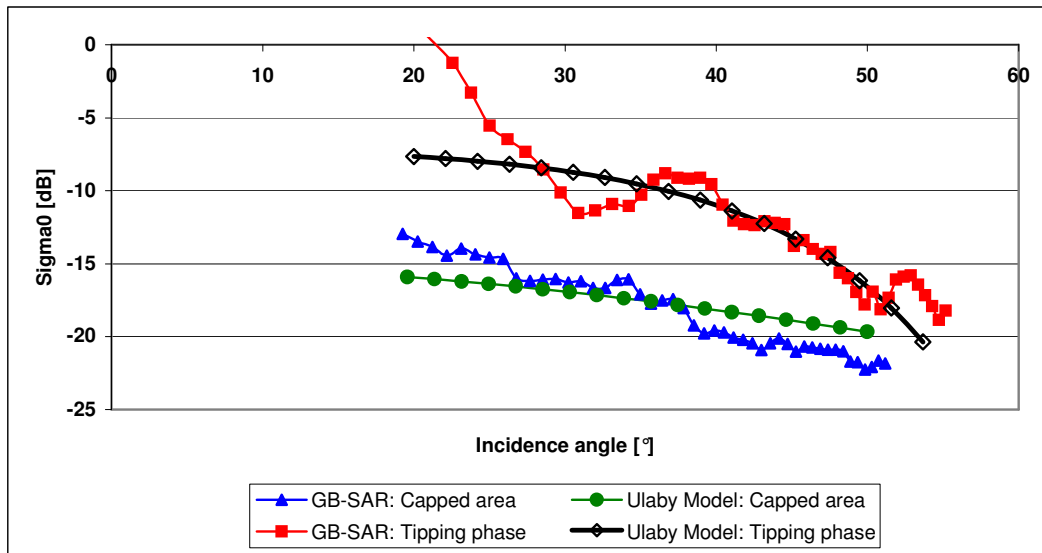


Figure 6-11. Variation of the cross and co-polar ratios as a function of a dipole orientation.

Figure 6-13 shows the sensitivity to soil roughness. This simulation highlights that X and C band radars are not able to detect soil roughness variations for values higher than respectively 10 and 20 mm. An L band radar instead does not have this sort of saturation with respect to soil roughness.

Figure 6-14 and Figure 6-15 instead show the σ^0 variation with soil moisture for a 100% sand soil and a 100% silt soil at different wavelengths. In addition to the lower L band backscatter values with respect to the X and C band return, these graphs highlight that for such soil texture combinations, variations of the volumetric soil moisture have a significantly lower effect than for a clay soil texture. They present a variation of approximately only 4 dB, whilst Figure 6-12 shows an average change of 10 dB.

The highest backscatter variation range observed for the L band with respect to change in both soil moisture (Figure 6-12) and soil roughness (Figure 6-13) conditions, leads the analysis to investigate only L band data, and in particular the HH backscatter, which represents a good compromise between the higher VV and the lower HV returns. Figure 6-16 presents the backscatter dependence to soil texture composition under variable soil moisture conditions. As previously observed, fine texture soils dominated by clay cause the largest change in backscatter. Finally, Figure 6-17 presents a similar graph to the GB-SAR results, showing the angular response at L band for a mixed soil texture at fixed soil moisture and roughness values.

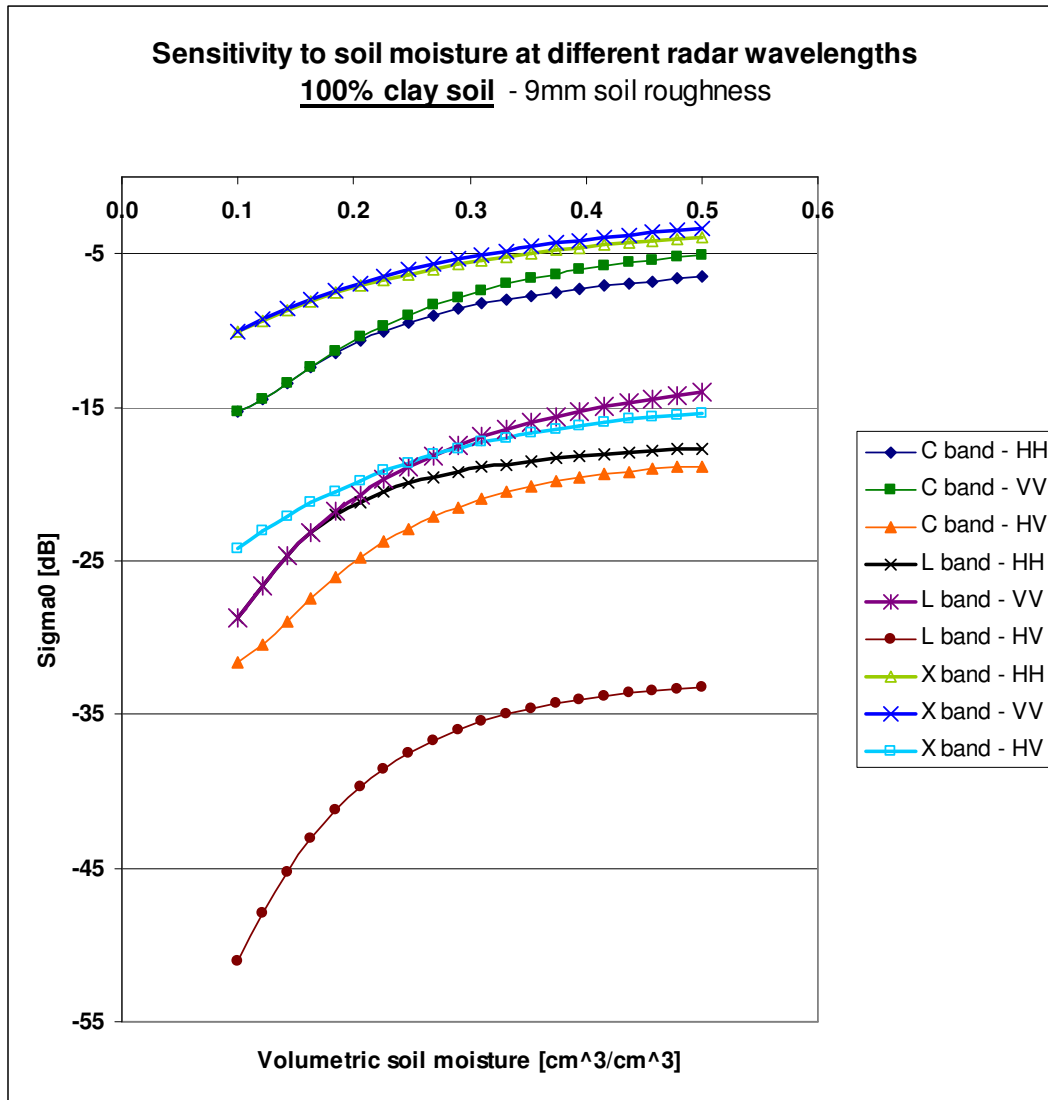


Figure 6-12. Backscatter variation with soil moisture at different radar wavelengths and polarisations for a 100 % clay soil texture. Fixed incidence angle at 23°.

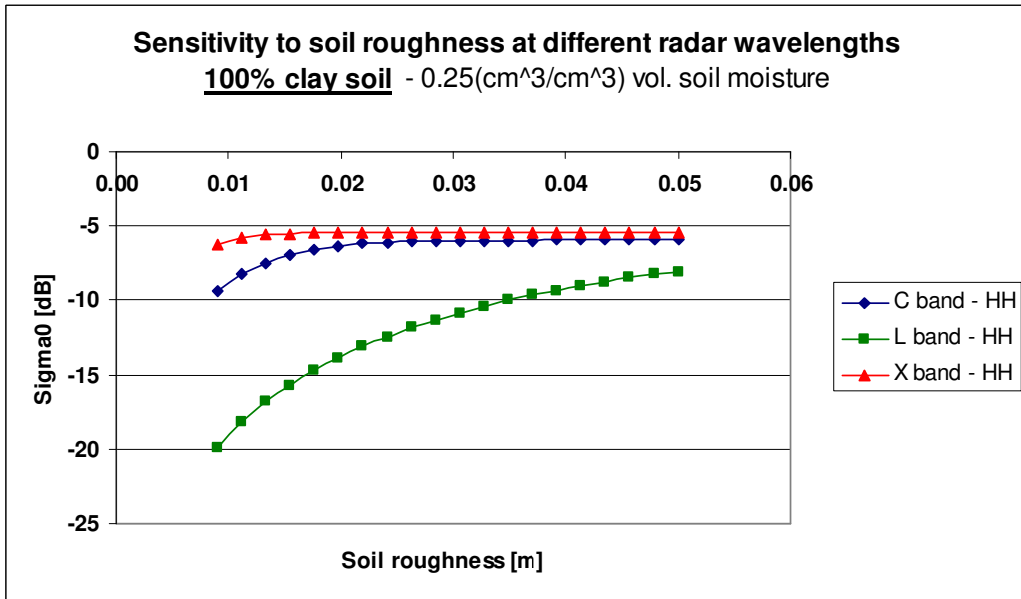


Figure 6-13. Backscatter variation with soil roughness at different radar wavelengths. Fixed incidence angle at 23°.

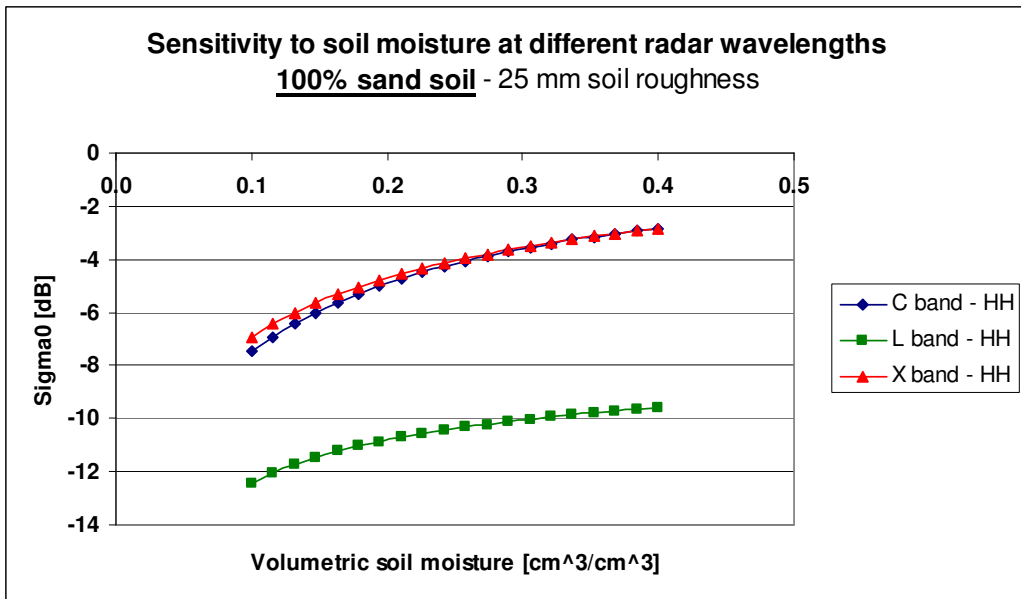


Figure 6-14. Backscatter variation with soil moisture at different radar wavelengths for a 100 % sand soil texture. Fixed incidence angle at 23°.

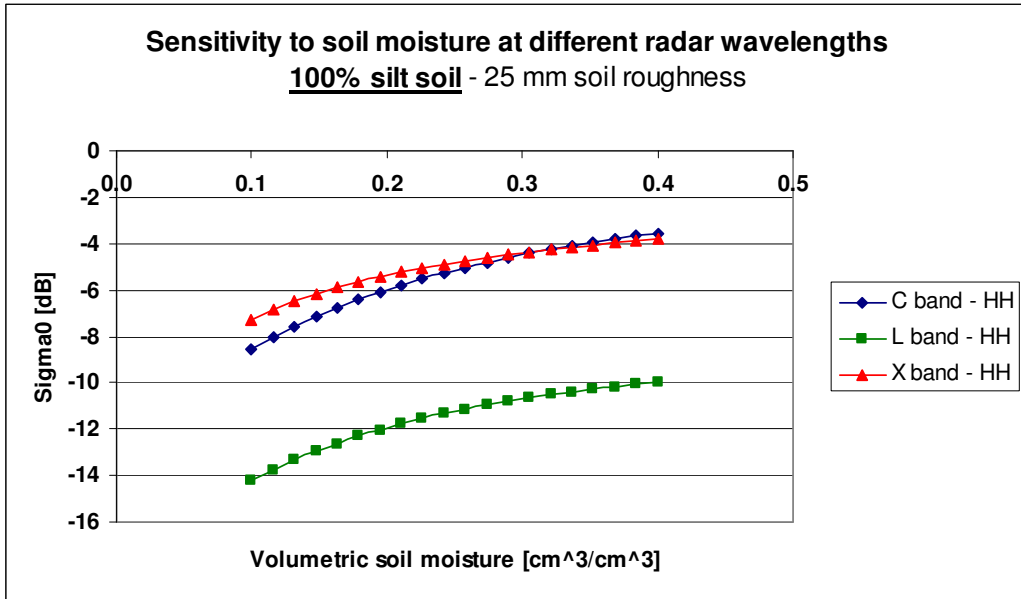


Figure 6-15. Backscatter variation with soil moisture at different radar wavelengths for a 100 % silt soil texture. Fixed incidence angle at 23°.

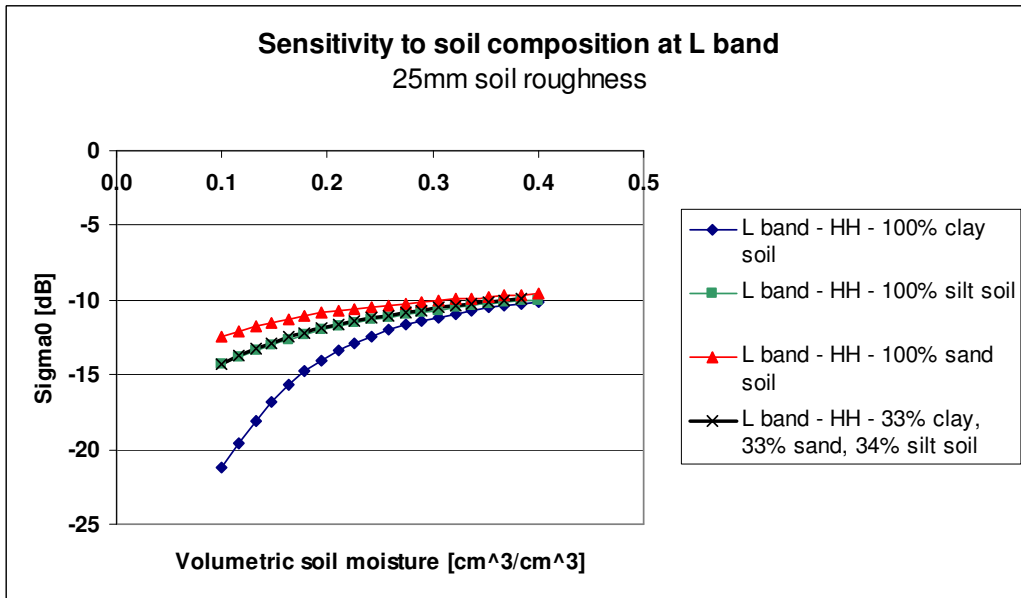


Figure 6-16. Backscatter variation with soil texture at L band. Fixed incidence angle at 23°.

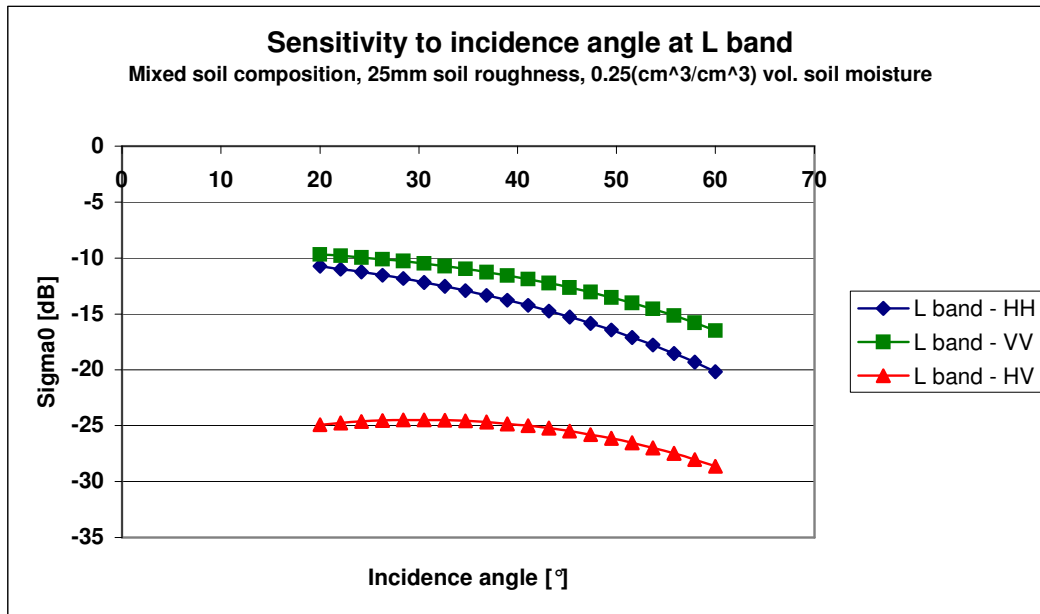


Figure 6-17. Backscatter variation with incidence angle at L band.

6.2.1 Conclusion of Sensitivity Analysis

The sensitivity analysis highlights that the variables taken into consideration (i.e. soil moisture, soil texture, surface roughness and incidence angle) have the same magnitude of influence on the SAR backscatter. It is therefore extremely challenging to relate backscatter changes to soil conditions, and assumptions are often required to allow the examination of a SAR scene and its land-cover classification. Without the accurate knowledge of topographic and weather conditions, one single-polarisation acquisition can hardly provide correct land-cover information, and consequently knowledge on land-use. A clear example is the SAR backscatter from water bodies. Figure 6-18 provides the reader with a clear example of how wind induced surface capillary waves can completely change the lakes' radar reflectivity. Indeed, in (b) all water bodies are not readily distinguishable from bare ground, forested areas or urban environments.

Therefore, with regards to a single scene acquisition, it is evident that fully polarimetric complex data offer a major benefit. Even if it generally presents lower backscattering values, an L band SAR has a better sensitivity to surface roughness and soil moisture, hence providing results that can be more accurately linked to ground conditions. This factor, together with a lower sensitivity to vegetation, makes an L band SAR more suitable for bare soil studies.

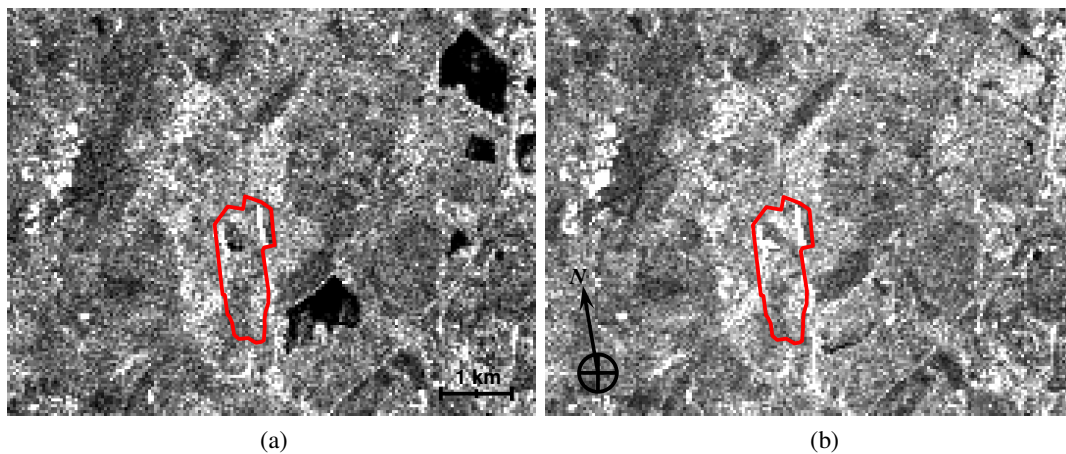


Figure 6-18. Backscatter amplitude of (a) ERS-1 acquisition of 30th July 1995 (i.e. orbit 21124, track 94, frame, 2547, VV pol) and (b) ERS-2 acquisition of 31st July 1995 (i.e. orbit 1451, track 94, frame 2547, VV pol). These sub scenes, which also include Cranfield University with its airfield, confirm the difficulty of extracting land-cover information with one single-polarisation SAR image. The red lines identify the Brogborough landfill boundary.

Recent studies (Bujor et al., 2003; Karszenbaum, et al., 2003 and Wang et al., 2001) have shown the valuable utilisation of single polarisation acquisitions by applying analysis in the temporal dimension through time series, temporal averaging and ratios. They achieve very promising results, demonstrating how a temporal analysis can improve certain classification routines by detecting or averaging out certain temporal fluctuations of the targets' reflectivity properties. In general, these methods are used to reduce speckle effects of distributed targets. Unfortunately, with respect to the specific objective of this research, these techniques are not actually valuable. Due to the large temporal repeat pass of current SAR space borne systems (e.g. 35 days for Envisat and ERS-2) long periods are needed to acquire a substantial number of scenes. During such a timeframe the ground conditions of a landfill change considerably and therefore no accurate information can be extracted on the land-cover and land-use at a specific moment in time. Much shorter revisit times are therefore required in order to make such techniques applicable to improve short-term classification methodologies.

For each of the 2005 and 2006 ERS and Envisat acquisitions, the author examined the radar backscatter of the Brogborough landfill site and compared it to its ground conditions. These scenes confirm that a single polarisation SAR image with no additional ground information (e.g. DEM) cannot distinguish the variables affecting the SAR backscatter (i.e. topography, the target surface roughness and correlation length, the occurrence of volume scattering in the presence of vegetation and the target dielectric constant). Hence, the need to merge more levels of information into one single image as discussed in Section 4.9. The importance of the application of these techniques is demonstrated in the following two sections.

6.3 Detection of Subsidence: Results and Discussion

The research initially examines the fusion of the interferometric coherence magnitude obtained from a 1-day ERS tandem pair (i.e. 25th and 26th June 1995) and the backscatter amplitude of the master. This analysis is carried out to demonstrate the immediate benefit of merging different information channels into one single image and the key importance of such results in support of the interpretation of an interferometric DEM. The specific land classification is presented in the next section.

An RGB composite is created by using respectively for each channel the coherence, backscatter and again coherence information. This is superimposed on the computed interferometric DEM as illustrated in Figure 6-19. By means of a visual investigation, it is immediately possible to distinguish a number of different regions. Areas appearing in green are those with a low degree of coherence and relatively high backscatter. Areas with an evident purple colour are instead those characterised by a low backscatter and high coherence. Furthermore, white pixels are those with both high coherence and high backscatter, whilst areas with a black colour are those with both low coherence and low backscatter. This RGB composite is preferred to the ILU combination by Okhimamhe (2003) presented in Section 4.9. This is mainly because this analysis is not specifically aimed at the land classification of the image, and therefore this RGB composite simplifies its interpretation.

The information provided by this colour composite can also be used to interpret the interferometric DEM computed with the same 1-day ERS tandem pair. In Figure 6-19 a circle highlights a 45 m spike in the DEM in the northern part of the landfill. As analysed in Section 4.5 such a spike can be generated by problems in the phase unwrapping due to the presence of noise, or as explained in the literature review chapter, it can be caused by subsidence mistakenly interpreted as a high topographic peak. The white colour of the spike establishes that such a pixel has both high coherence and backscatter. The immediately surrounding pixels also have a relatively high coherence (i.e. average of 0.59). Consequently, it becomes possible to assert that subsidence is detected in the interferogram and the spike is not caused by a phase unwrapping problem. By applying Equation 2-21, the 3.31 rad of phase difference can therefore be linked to a subsidence of approximately 1.48 cm occurred between 11am of Sunday 25th June 1995 and 11 am of Monday 26th June 1995.

This phenomenon was also observed by Elder (2002). In his work, he applies an additional adaptive filter to eliminate noise in the interferometric phase. This allows any detected spike to be related to subsidence. The phase noise filter by Elder is not applied in this research because a preliminary verification of the obtained results shows that the filter can smooth out some phase variations that are instead related to actually existing ground heights.

The occurrence of such rapid waste subsidence phenomena, most probably linked to compression under the self weight, is confirmed by waste management experts (Smith, 2006) and Brogborough landfill surveyors (Haycock, 2005). Together with Haycock, in February 2005 the author also carried out measurements of topography with differential GPS equivalent to a VTU survey (Figure 6-20). Due to the many errors introduced when placing the instrument, Haycock highlighted that such GPS point measurements are not suitable to detect ground movements in vast areas in the cm order of magnitude.

It is important to reiterate that the detection of such spikes with SAR is only possible over areas of with a high degree of coherence (i.e. low phase noise). As illustrated in Figure 2-10, decorrelation is more sensitive to vertical changes than to horizontal changes for incidence angles less than 45° . This means that movements of track over the area would already cause a significant level of decorrelation, preventing the accurate computation of subsidence. Additionally, the event must occur over an area wide enough with respect to the SAR system ground resolution. The scatterers within the ground resolution must move concurrently in the same direction in order not to lose coherence and to detect the ground displacement. If the SAR spatial resolution only partially covers the subsidence area, the phase of the scatterers not involved in the ground movement would negatively affect the detection of such events. With the 50 m ground resolution of the interferometric products obtained in this research it becomes in fact a rare case to detect such ground displacements. Indeed, the tandem of 25th and 26th June 1995 is the only one for which a spike is obtained in an area with high degree of coherence.

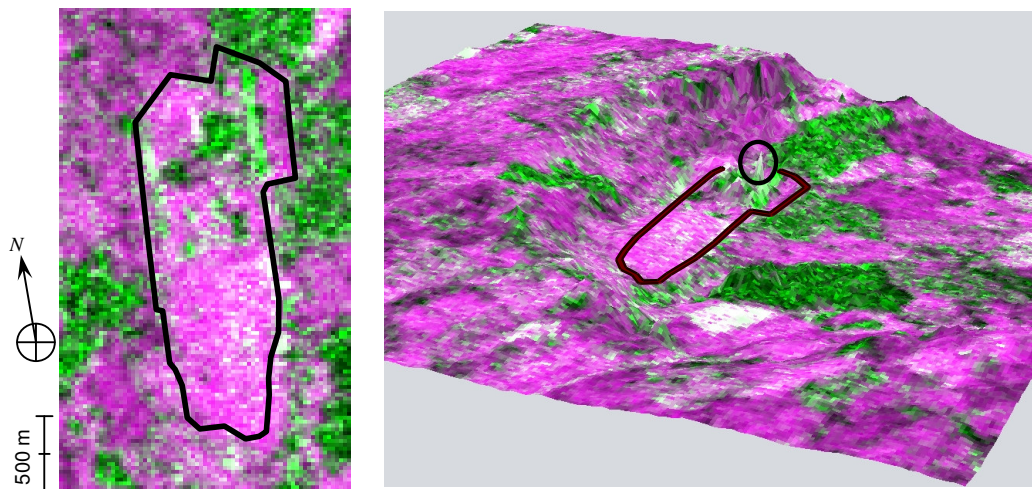


Figure 6-19. Left: red-green-blue composite using respectively the coherence magnitude, backscattered amplitude and coherence magnitude for each colour band. Data of the SAR interferometric pair of 25th and 26th June 1995. The radar view direction is from right to left. The black contour identified the boundaries of the Brogborough landfill in 1995. Right: Same colour composite superimposed on the interferometric DEM. The black circle highlights the spike in the DEM.



Figure 6-20. Left: topographic survey over the Brogborough landfill (22nd February 2005). Right: surveying data download and processing.

6.4 Land-use Classification Results

This section presents the results of the land-use FL featured-based classification algorithm presented in Section 4.9. The procedure is applied using the ERS scenes listed in Table 6-1. This is the only available set of three ERS tandem acquisitions satisfying the processing requirements.

Based on the preliminary ground observations and on the findings presented in the previous and current chapters, each land-use class is assessed against the parameters used in the classification procedure. This analysis, based on qualitative terms and observations, is summarised in Table 6-2 and is the foundation to develop the rules for the fuzzy classifier (refer to Appendix C). The classification focuses on the Brogborough landfill only, for which more accurate historical reference data are available. Figure 6-21 shows an example of class selection from a topographic survey carried out by the operators. The land-use classification algorithm is also applied on the areas surrounding of the site (i.e. outside the turquoise contour that identifies the site boundary). The results are shown in Figure 6-22.

Table 6-1. SAR scene used in the land-use classification.

SAR Scene	Platform	Acquisition Date	Orbit	Track	Frame	Perp. Baseline [m]
Master 1	ERS 1	16/02/1996	24008	473	1035	172.3
Slave 1	ERS 2	17/02/1996	4335	473	1035	
Master 2	ERS 1	25/02/1996	24130	94	2547	38.0
Slave 2	ERS 2	26/02/1996	4457	94	2547	
Master 3	ERS 1	31/03/1996	24631	94	2547	-92.1
Slave 3	ERS 2	01/04/1996	4958	94	2547	

Table 6-2. Qualitative analysis of land-use classes.

Class No.	Name	Classification Parameters							Colour Definition in RGB, 24-bit representation
		1-d Coherence	9-d Asc/Desc Coherence Difference	35-d Coherence and 35-d Coh. Difference	Backscatter Intensity	1-d Master Slave Backscatter Ratio	1-d Topography	35-d Topography Difference	
1	Lagoon	Low	Low	Low Low	Variable. Very low if no wind	Variable	Pixel around the area have the same height	---	[0, 0, 255] Blue
2	Building	High	Low	High Low	Variable. Generally high	Close to 1	Possibly Higher than surrounding pixels if correct unwrapping procedure	---	[255, 255, 255] White
3	Road	High	Low	High Variable	Generally low	Close to 1	Variable	---	[0, 0, 0] Black
4	Tipping area	Low	Variable. Either high or low.	Low Variable	High	Close to 1	Usually present unwrapping problems	If DEM from last ERS pair is reliable, then surrounding pixels of the original low coherence area can present lower values	[255, 0, 0] Red
5	Clay operation zone	Low	Variable. Either high or low.	Low Variable	High	Close to 1	Usually present unwrapping problems	---	[128, 0, 128] Purple
6	Capped area with no vegetation	Medium High	Medium	Low Low	Medium (strongly depends on incidence angle, and therefore topography)	Variable	Variable	---	[255, 255, 0] Yellow
7	Restored area with low vegetation	Medium High	Medium	Low Medium Low	Variable	Variable	Variable	---	[127, 255, 0] Chartreuse
8	Restored area with high vegetation	Low	Low	Low Low	Generally high	Close to 1	Usually present unwrapping problems	---	[0, 128, 0] Green
--	Undefined	---	---	---	---	---	---	---	[128, 128, 128] Grey
--	Multiple Class	---	---	---	---	---	---	---	[189, 183, 107] Dark Khaki

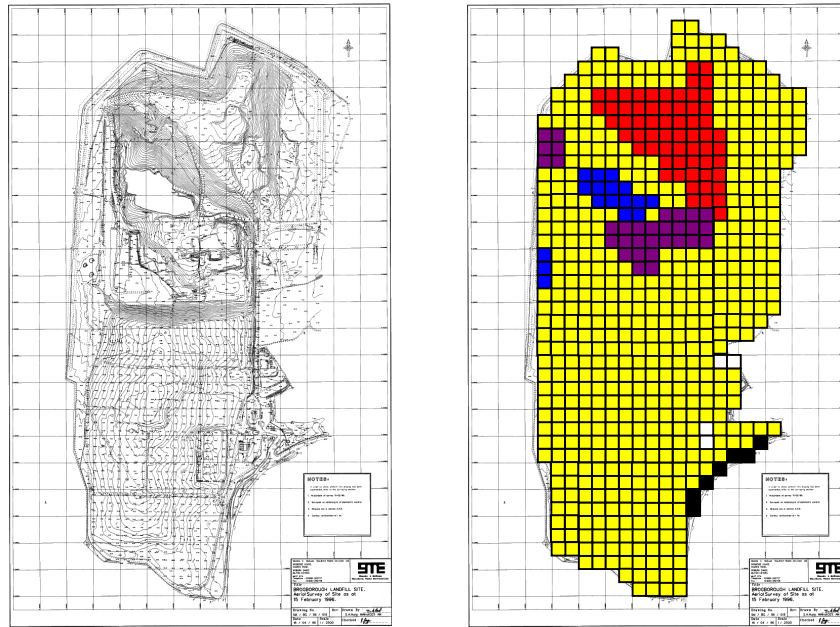


Figure 6-21. Left: topographic survey with a 100 m spacing grid of Brogborough landfill provided by Waste Recycling Group Ltd. 15th February 1996. Right: example of land-use class selection based on the topographic survey and additional reference data provided by the operators. Areas of no specific use are grouped into the capped area with no vegetation class.

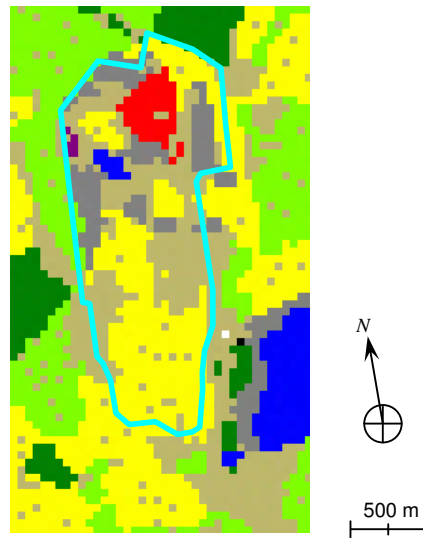


Figure 6-22. Land-use classification results. The map is obtained by setting the degree of ownership $O(P)$ higher than 0.6 and the degree of classification success $S(P)$ higher than 0.18. The turquoise contour identifies the site boundary.

By using reference data presented in the previous chapter, an error matrix for the landfill pixels is developed. This is presented in Table 6-3. The ground reference data are obtained by drawing a 50m grid on the survey map provided by the operators and selecting the most appropriate land-use class. This method of deriving ground reference data approximates the detailed survey map to a coarser resolution therefore generating mixed class pixels. They are nonetheless described with a single definite class. As explained in Section 5.3.4, based on the interferometric coherence computed with other 1-day ERS tandems for which a low level of coherence would be expected if the area was covered with vegetation (i.e. 25-26 June 1995, 30-31 July 1995, 05-06 May 1996), the research assumes that the southern half of the site is covered by bare soil. The accuracy of the classification is discussed in the next section.

Table 6-3. Error matrix for the land-use map obtained setting $O(P)$ higher than 0.6 and $S(P)$ higher than 0.18. It is assumed that the southern half of the site is covered by bare soil and is not a restored area with low or high vegetation.

Classified Pixels	Reference Data								
	Lagoon	Building	Road	Tipping	Clay operat.	Capped	Rest. low veg.	Rest. high veg.	Row Total
Lagoon	12	0	0	0	0	0	0	0	12
Building	0	0	0	0	0	0	0	0	0
Road	0	0	0	0	0	0	0	0	0
Tipping	0	0	0	45	0	11	0	0	56
Clay operation.	0	0	0	0	6	0	0	0	6
Capped	0	0	0	0	17	289	0	0	306
Rest. low veg.	0	0	0	0	0	14	0	0	14
Rest. high veg.	0	0	0	0	0	0	0	0	0
Column Total	12	0	0	45	23	314	0	0	394
Undefined	6	0	0	0	56	32	0	0	94
Multiple Class	0	0	0	8	48	183	0	0	239
Column Total	18	0	0	53	127	529	0	0	727

6.4.1 Discussion

Before discussing the classification accuracy, it is necessary to address the main question made by the landfill operators when considering the results of Figure 6-22: “if you can classify what is happening on the site, why is it so hard to detect it in the first place?”. It is important to appreciate that there is a key conceptual difference when examining SAR data between this land classification study and the identification

analysis presented in the previous chapter. This difference is the a priori knowledge that the area under examination is actually a landfill. Such knowledge allows other subsequent assumptions on the SAR data and relative products to be made. To better explain this distinction, it is possible to investigate the classified areas surrounding the Brogborough landfill in Figure 6-22. Clearly, the land-use classes lose their specific meaning and can be interpreted as general land-cover classes. For example, site lagoons used to monitor run off water and leachate can be simply considered as water bodies and restored areas with high vegetation can be considered as woodland. This is confirmed by a Ordnance Survey map (Figure 6-23). The two woodland areas on the north and west of the landfill are respectively the Marston Thrift and the Holcot Wood. The water body south east of the site is the Brogborough lake.

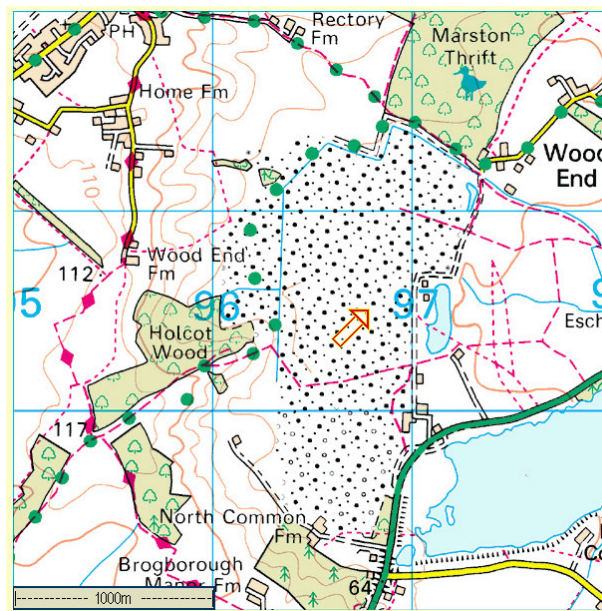


Figure 6-23. Ordnance Survey map. The red arrow identifies the centre of the Brogborough landfill (copyright Ordnance Survey).

From the error matrix, it is possible to compute that within the landfill boundary, only 54 % of the pixels have been classified correctly (i.e. satisfying the degree of ownership and classification success thresholds). Around 13 % are left undefined (i.e. the degree of ownership is lower than 0.6) and the remaining third corresponds to multiple class pixels (i.e. the degree of classification success is lower than 0.18). The physical significance of all these unclassified pixels (i.e. 46 %) is most probably due to the coarse ground resolution if the used images. The 50 m pixels often contain multiple classes as observed when generating the historical ground reference data. For instance, the roads present on the site are often too small (ie. 3 to 10 m wide) to be detectable.

This major issue can be verified by increasing the required degree of classification success threshold to 0.25. The obtained result is shown in Figure 6-24. As expected, this image presents many additional multiple class pixels due to the stricter requirements on the degree of ambiguity. It goes beyond the scope of this research to investigate the sensitivity of the classification results with respect to $O(P)$ and $S(P)$. The key aspect to be appreciated is the limitation produced by the coarse resolution. The classes more affected are tipping areas, clay operation zones, capped areas and restored areas with low vegetation. A detailed analysis brings to light that the degree of ambiguity $A(P)$ is the limiting factor. The tipping area and the clay operation zone classes often have a very similar degree of membership in the $M(P)$ vector. The same applies for the capped area class and restored area with low vegetation class. On the contrary, restored areas with high vegetation (or woodlands in land-cover terms) and lagoons (or water bodies) do not lose their classification level.

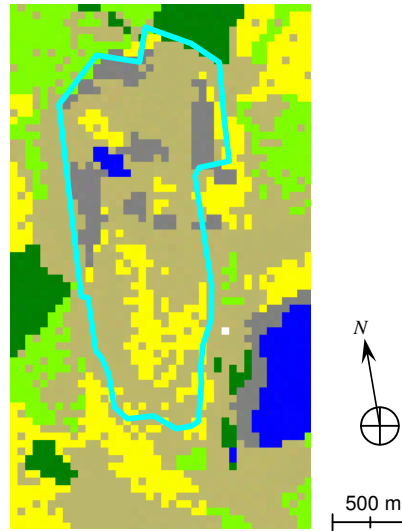


Figure 6-24. Land-use classification results obtained by increasing the degree of classification success $S(P)$ threshold to 0.25. The turquoise contour identifies the site boundary.

Overall, the class selection methodology based on the developed coefficients acts as a filter, allowing only certain pixels to be assigned a land-use class. Therefore, considering only the classified pixels in the landfill perimeter of Figure 6-22 (i.e. excluding undefined and multiple class pixels), the Kappa analysis yields a coefficient of agreement equal to 71%. As explained by Jensen (2005), such a result represents a reasonable accuracy between the fuzzy-logic featured-based classification map and the ground reference information. From the landfill site regulator's perspective, being able to remotely map the site operations is recognised to be a very successful outcome. The only limitation is that this methodology needs 6 SAR images acquired over a 44-day period and therefore is not an immediate result.

As expected, with 50 m pixels the road class can hardly fill a resolution cell and subsequently be accurately classified. The same applies to buildings if not in the presence of a urban area. Nonetheless, just outside the site perimeter two pixels are actually classified respectively as a road and a building. By investigating this area on the ground, the author suggests a possible validation of this result. This is shown in Figure 6-25. The solid-line black squares superimposed on the image identify the possible position of the pixels and specifically the road and building class pixels. The pixels are tilted due to the actual SAR look direction of ERS descending orbits. This plausible ground validation of the classification results consequently highlights an additional shortcoming of the 50 m spatial resolution. In fact, if the squares are shifted by half their size both in the azimuth and ground range directions, as illustrated by the dashed black squares in Figure 6-25, the two pixels under examination would most probably not be classified as observed in the results. It is also vital to understand that the relative position of the pixels also depends on the cropping coordinates used to select the area of interest in the original 5 m to 25 m resolution SAR scenes. This factor strengthens the need for a higher spatial resolution.

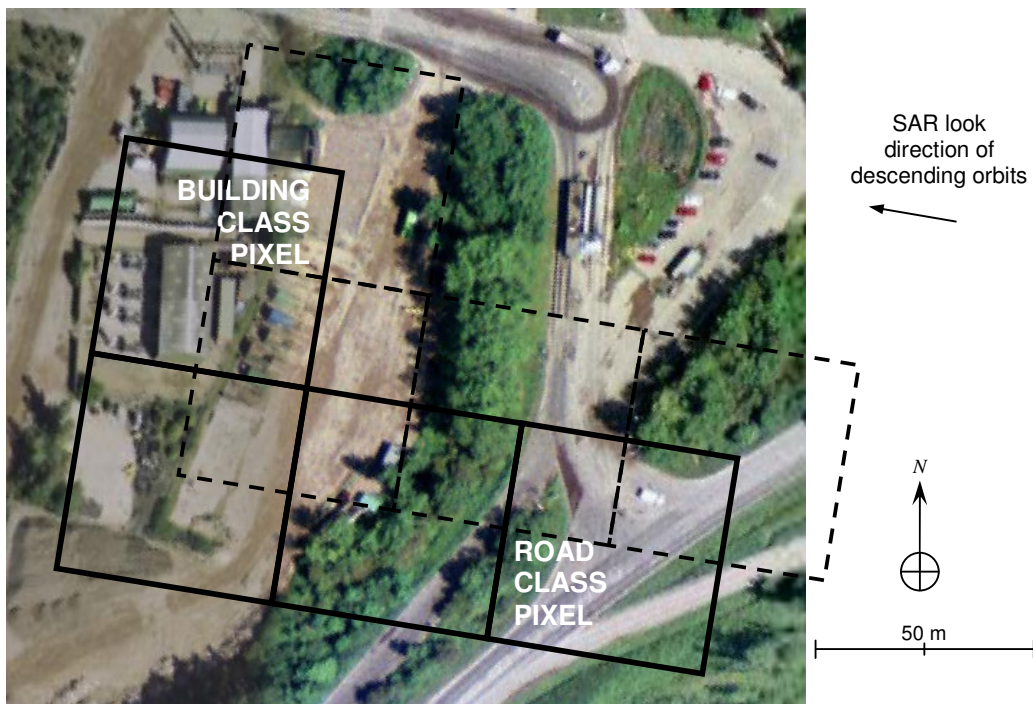


Figure 6-25. Ground validation of the road and building class pixels observed in the results. (Google Earth, 2007; with the education setting reproduction agreements).

The research must acknowledge the fact that a validation of this classification technique should be carried out with additional sets of appropriate SAR scenes and for other landfills. The lack of available historical ground reference information for other sites and the difficulty of ordering and acquiring additional SAR satellite data have prevented such validation.

Finally, it is also important to appreciate the high computing requirements involved in this classification approach. As it carries out 5 pixel-by-pixel routines (i.e. the FL classification, the three featured-based rules and the class selection), the routine takes about 1.5 h to process approximately 3000 pixels with a Pentium III processor (i.e. 934 MHz 512 Mb of RAM).

6.5 Conclusion of On-site Conditions Monitoring

Overall, this chapter has demonstrated the key value of merging together complementary information such as backscatter amplitude, interferometric coherence magnitude and topography acquired at different times. A single polarisation SAR image is unable to correctly identify ground conditions or on-site operations. Thus, spatial and temporal information is used concurrently to monitor and classify the land-use ground conditions in a landfill.

Empirical data have demonstrated the value of the co-polarised ratio and the vertical-horizontal correlation coefficient to discriminate rough and smooth surfaces. This can be highly beneficial in the classification of ground conditions in landfill sites. Simulations have also shown that an L band SAR system has a better sensitivity to surface roughness and soil moisture, hence providing results that can be more accurately linked to ground conditions.

The novel classification approach has proved to be fairly accurate for most land-use classes. A more evident level of ambiguity is observed for certain classes especially when increasing the degree of classification success level. The multiple class pixels are most probably caused by detecting various classes within one 50 m SAR spatial resolution cell.

7. Overall Discussion

Chapter 7 develops the results and discussion previously presented. It investigates the applicability of the developed techniques in an operational context.

Section 7.2 examines the impact of the main SAR system parameters with respect to the specific research objectives. The discussion identifies the data specification requirements linked to the techniques developed in this research. The chapter then reviews whether future SAR missions would satisfy these requirements.

It is also critical to address the possibility of extrapolating the developed SAR data analysis methodologies beyond the UK (Section 7.4). The study explores a number of optical data sets to investigate issues related to the spectral and spatial resolutions.

Ultimately, Section 7.5 presents an analysis of the different user groups and their needs for a sustainable operational use of such remote sensing products. Remarks also cover issues such as data accessibility, processing speed and cost-effectiveness.

7.1 Summary of Previous Analysis and Discussion

The analysis and discussion presented in the previous chapters has highlighted opportunities and limitations of SAR data for 1) the identification of landfill sites by distinguishing them from other disturbed areas which present similar optical spectral signatures 2) the possibility of correlating SAR data with on-site conditions and operational procedures.

A spatial analysis of the SAR backscatter amplitude over these sites showed that landfills are characterised by evident anisotropic features that can support their identification. Information about the status of the sites during the used SAR acquisitions and additional ground observations have revealed that such anisotropic features are linked to topography. Validation tests also proved that in both winter and summer conditions and with both ascending and descending orbits (i.e. different look angles and acquisition times), waste disposal sites present distinctive SAR backscatter spatial characteristics.

The analysis of the degree of coherence over both landfills and a disturbed area demonstrated that waste disposal sites are characterised by large decorrelated areas with transient locations, whilst the disturbed area presents smaller areas of low coherence in a permanent position.

Finally, the distinctive positive elevation of landfills can also help to distinguish them from other disturbed areas presenting similar optical signatures.

Overall, the discussion pointed out the constraints of such analysis techniques linked to the daily operational landfilling procedures carried out on the sites and to the spatial resolution of the SAR imaging system.

With regards to the second objective, both ground based and space-borne SAR data have shown that one single polarisation acquisition is not able to distinguish land-cover nor land-use ground properties. Nonetheless, the integration of information derived from multiple interferometric pairs has allowed the research to achieve satisfactory land-use classification results.

The key point is the dependence of the results on the specific operations taking place on the landfill sites. For this reason, the analysis methodologies for the first research objective take into consideration both time and spatial variables and should therefore be used concurrently in order to corroborate their findings.

The research pointed out the value of merging many levels of information in both the time and space dimensions. These techniques helped in interpreting unusual spikes observed in the computed interferometric DEM and classifying the SAR images into land-use classes. In both cases, the temporal resolution between the acquisitions and the spatial resolution of the final product proved to be key factors for the effective or less successful application of these techniques.

Overall, SAR scenes acquired from different geometries, interferometric products, polarimetric data and information in the temporal dimension are all of high value to the two research objectives.

7.2 Analysis of SAR System Parameters

In order to appreciate the applicability in an operational context of the analysis techniques presented in the previous chapters, this section addresses the key SAR system parameters that have an influence on them.

7.2.1 Ground Resolution

The discussion in Section 5.2.3 and 6.4.1 has extensively highlighted the importance of the SAR ground resolution for the effective applicability of the analysis techniques. Based on the preliminary ground observations and dialogue with landfill operators, an analytical approach is developed to identify the constraints on the SAR ground resolution depending on the landfill features.

Information provided by the Environment Agency (Butcher, 2005) allows the research to model the size distribution of the landfills with a gamma distribution (Equation 7-1). In Wales and England there are about 2160 operating landfills. The graphs in Figure 7-1 show their size distribution and the normalised modelled cumulative distribution that assumes there are no landfills with a zero area. The gamma distribution is defined as:

$$y = f(x | a, b) = \frac{1}{b^a \Gamma(a)} x^{a-1} e^{-\frac{x}{b}} \quad \text{Equation 7-1 (James, 1999)}$$

where $a > 0$ is the shape parameter and $b > 0$ is the scale parameter of the gamma distribution.

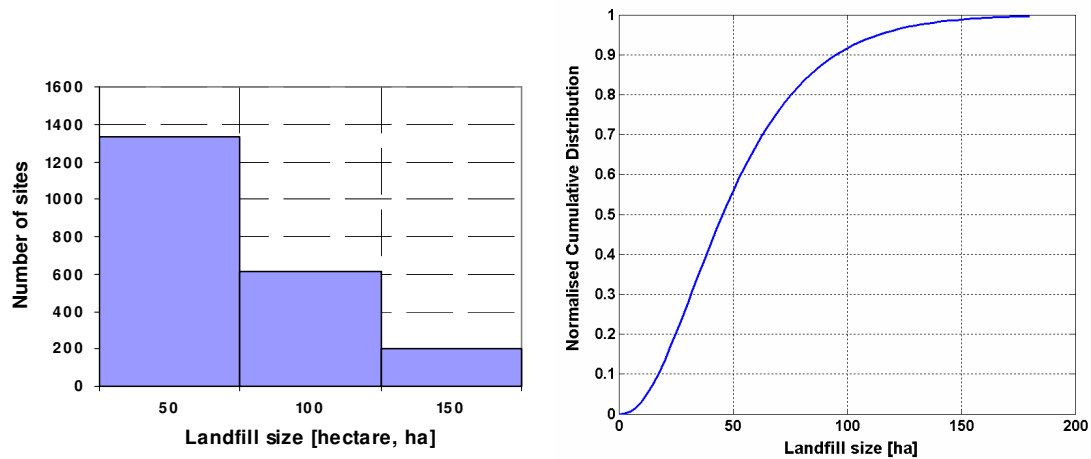


Figure 7-1. Size of landfills in England and Wales (left) and normalised modelled cumulative distribution using a gamma distribution (right). The gamma parameters a and b are respectively equal to 2.5 and 2.

Further discussion with experts and landfill operators has allowed the research to develop a polynomial function to model the relationship between the landfill size and its topographic characteristics. As discussed in Section 5.2.3, the optimal SAR ground resolution to study a feature of interest should be about 10 times smaller than the autocorrelation value of the feature itself. For vertical features, this consideration refers to the horizontal dimension across the slope and not the vertical topography itself. As suggested by the landfill operators (Kirkland, 2005), by considering features with a slope of roughly 40%, Figure 7-2 shows the relation between the landfill size to its vertical topographic characteristics. As previously mentioned, this relationship is developed based on the experience of experts and landfill operators and therefore must not be considered absolute. A variation of even ± 15 m is acceptable. For example, vertical topographic features of 30 m, occurring in 75 m horizontally, can be found in

landfills of 60 ha and larger. Considering the uncertainty of the model, such features could also be found in sites of 40 ha. In fact, from the graph in Figure 7-2, the specific feature height for such a landfill size is around 15 m, which would occur in about 37 m across (i.e. 40% slope). The gamma function used to model the landfill size distribution highlights that the mode of the distribution is close to 40 ha, therefore the optimal SAR ground resolution to effectively appreciate these topographic features is about 4 m (i.e. 37/10 m).

With regards to the computation of the degree of coherence, larger pixels (i.e. a lower SAR ground resolution) would cause a decrease in coherence. Indeed, by applying the model developed by Wegmuller et al. (2000), which assumes that in each resolution cell there are a number of independent scatterers each with specific temporal decorrelation characteristics, it is possible to argue that the bigger the resolution cell the more the stable scatterers will be affected by the temporally unstable ones.

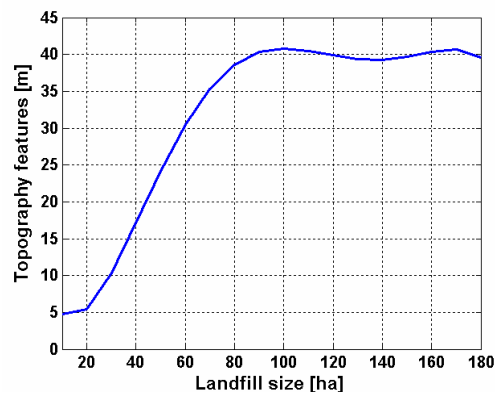


Figure 7-2. Relation between landfill size and its topography features. The polynomial used to model this relationship is: $y = -0.0007 x^3 + 0.0549 x^2 - 1.1354 x + 11.2672$.

7.2.2 Temporal Resolution and Interferometry

The temporal resolution between two SAR acquisitions, whether from different geometries or for interferometric processing, is of critical importance to the application addressed in this study. The discussion presented in the previous chapters has highlighted how the temporal dimensions plays a key role for the identification of a landfill and the monitoring of the on-site conditions.

With relation to the on-site monitoring application, an optimal space-borne SAR system should be able to acquire interferometric scenes at both very short (e.g. 5 to 24 hours), medium (e.g. 5 to 10 days) and large (e.g. 25 to 40 days) intervals. The coherence computed at each temporal baseline can be related to specific weather conditions and/or on-site operations. Multiple successive acquisitions (i.e. more than just two as in the

ERS tandem mission) could also be extremely effective in developing a dynamic model of the land-use ground properties and not just for a snapshot classification as developed in the previous chapter. This is illustrated in Figure 7-3. In these images, each vertical line along the time axis represents an interferometric pair (i.e. two SAR acquisitions). The crossed circled identifies the time t that the on-site classification map is related to.

Hence, the top image refers to the methodology presented in the previous chapter, in which an ascending interferometric pair is used together with two additional descending pairs separated by 9 and 44 days. As explained in 4.9.2, the obtained land classification map is related to the acquisition time of the first descending pair. The second example of Figure 7-3 presents an hypothetical case in which the interferometric scenes have a temporal baseline of 12 h and each pair is separated by 48 h. Each classification map could be obtained by merging three interferometric products respectively with temporal baselines of 12 hours, 2 and 4 days. Such configuration would deliver land-use maps of the site every 2 days, therefore potentially achieving the development of change dynamics models. Additionally, a smaller temporal baseline would also reduce decorrelation effects and consequently produce more accurate digital elevation models.

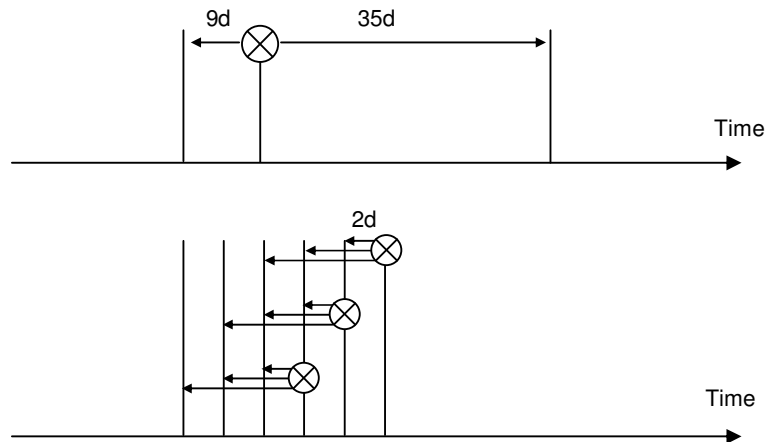


Figure 7-3. Examples of how temporal resolution can support the development of change dynamics models of land-use characteristics.

7.2.3 Wavelength

As presented in the analysis in the previous chapter, an L band SAR system has a better sensitivity to surface roughness and soil moisture, hence providing results that can be more accurately linked to ground conditions. This factor, together with a lower sensitivity to vegetation, makes an L band SAR more suitable for bare soil studies. The drawback of an L band radar is that it generally presents lower backscattering values and it has a coarser range resolution due to the smaller bandwidth.

7.2.4 Polarisation

The GB-SAR acquisitions have demonstrated the value of the co-polarised ratio and the vertical-horizontal correlation coefficient to discriminate rough and smooth surfaces. As examined by a vast amount of research, polarimetry and interferometric polarimetry are extremely powerful tools for both the classification of vegetation (i.e. volume scattering) and bare soil (i.e. surface scattering) and accurate digital elevation and terrain models.

7.2.5 Ascending and Descending Orbits and SAR Incidence Angle

Acquiring scenes from different perspectives can prove to be very valuable. Topography parallel to the look direction can go completely undetected and a multiple view angle is the only solution to such shortcoming.

With respect to the SAR incidence angle, Figure 6-17 shows that an incidence angle between 40 and 50 degrees has more sensitivity than at lower incidence angles. An additional significant advantage of higher incidence angles is also the reduced terrain distortion. Severe foreshortening and layover of slopes facing the radar would be avoided at the expense of increased shadow effects. The benefit linked to the higher incidence angle is the extra information that can be observed on the bright steep slopes facing the radar. This can greatly improve the value of the image for surface classification. A space-borne SAR system should therefore be capable of pointing at different incidence angles. The Envisat ASAR instrument can for instance acquire data from an incidence angle of 15° (i.e. image mode swath 1) to one of 45° (i.e. image mode swath 7). Such a flexibility allows the user to select optimum angles for different applications, or to use two distinct angles for two separate passes to carry out a multi-angle analysis. As demonstrated with the GB-SAR, the combination of different incidence angles is of interest for soil roughness studies, with the condition that the temporal resolution between acquisitions is small with respect to the changes occurring on the ground. A practical difficulty is that changes in incidence angle may conflict with other users that need a specific setting or a constant incidence angle

7.2.6 Conclusion of the Key SAR System Parameters Analysis

The results of the previous chapters and the analysis of the key SAR system parameters have shown that for an effective and more widely applicable implementation of the techniques developed in this research there are a number of requirements: the SAR spatial ground resolution should be around 4 m; the system should allow the acquisition of interferometric pairs with a temporal baseline of maximum 24 hours; L-band wavelength with full polarimetry; multi-geometry view acquisitions.

The next session reviews the characteristics of future SAR missions to appreciate whether such specifications will be met.

7.3 Review of Future SAR Space-borne Missions

This section reviews SAR missions planned to be launched in the near future (i.e. 2007-2010) to understand whether the system requirements identified in the previous analysis will be satisfied. The missions presented here are the Italian COSMO-SkyMed constellation, the German TerraSAR-X and TanDEM-X satellites, the Canadian Radarsat-2 mission, the Israeli TecSAR satellite and the European Sentinel-1 satellite linked to the GMES programme (European Commission, 2006). The following description focuses on the space segment only. For a detailed explanation of some of the terminology used on these sections the reader is advised to refer to Wertz and Larson (1999).

7.3.1 COSMO-SkyMed

COSMO-SkyMed (Constellation of Small Satellites for Mediterranean basin Observation) is a 4-spacecraft constellation, funded by the Italian Space Agency and the Italian Ministry of Defence. Most of the information provided in this section is obtained from the EOPortal (2006). The four satellites are three-axis stabilized and each is equipped with a X-band SAR instrument. With a mass of about 1700 kg, the envisaged operational lifetime of the spacecraft is 5 years. The used orbit for the satellites is a circular sun-synchronous dawn-dusk one, with nominal altitude of 619.6 km and inclination of 97.86°. The nominal repeat cycle is 16 days, however the full constellation achieves a revisit time of a few hours on a global scale. This refers to the capability to fly again over a given geographic site and to image the site under different conditions (e.g. with a varying incidence angle). All four spacecraft are planned to be positioned in the same orbital plane with a phasing angle of 90°.

As described by Candela and Caltagirone (2003), the SAR-2000 instrument, designed and developed by Thales Alenia Space (formerly Alenia Spazio), is a multi-mode programmable system providing different performance characteristics in terms of swath size, spatial resolution, and polarization configurations. “The SAR transmitter/receiver system operates through an electrically steerable multi-beam antenna which concentrates the transmitted energy into narrow beams in the cross-track direction while the characteristics of the transmitted pulses and the echo signal determine the spatial resolution and coverage.” With such a flexibility, the system can span from a spotlight mode (i.e. single polarisation with ground spatial resolution less than 1 m, an observation area of 10 by 10 km) to “huge region” mode (i.e. single polarisation with a spatial resolution of 100 m and a swath width of 200 km).

7.3.2 TerraSAR-X and TanDEM-X

Developed by the German Aerospace Agency and EADS Astrium in a public-private partnership, TerraSAR-X is a high resolution observation satellite operating in the X-

band. The satellite has a mass of 1200 kg and its envisaged operational lifetime is 5 years. The system is planned to have a sun-synchronous orbit with a 514 km altitude and 97.44° inclination. This achieves a 11 days revisit interval. The active steering ability of the SAR antenna can achieve both a right and left looking capability with full polarisation. The various acquisition modes can span from a spotlight mode with 10 x 10 km scenes at a resolution of 1-2 m, to a "ScanSAR" mode with 100 km wide strips at a resolution of 16 m. More detailed information can be found at DLR (2007).

The TanDEM-X spacecraft is envisaged to be an enhanced copy of TerraSAR-X and fly in formation with it, forming a huge radar interferometer. These two satellites would deliver timely, high-precision DEM (i.e. ground resolution of circa 12 m and 2 m height accuracy).

7.3.3 Radarsat-2

As described in MacDonald, Dettwiler and Associates Ltd. (2007), Radarsat-2 has been developed under a public and private collaboration between the Canadian Space Agency and MacDonald, Dettwiler and Associates Ltd. This mission represents the follow-on to Radarsat-1, launched in 1995. The new satellite has a C-band antenna and has been designed for a minimum lifetime of 7 years. The satellite orbit will be sun-synchronous with an altitude of 798 km and an inclination of 98.6°. This has a period of 100.7 minutes and a repeat cycle 24 days.

The instrument has flexible acquisition modes, full polarization and left and right-looking imaging options. The beam modes range from an "ultra-fine" configuration (i.e. covers an area of 20 km by 20 km, with 3 m ground resolution) to "ScanSAR Wide" mode (i.e. covers an area of 500 km by 500 km, with 100 m resolution). A number of incidence angles are available within each beam mode.

7.3.4 TecSAR

The TecSAR satellite has been developed by the Israel Aerospace Industry (2007). The spacecraft is 3-axis stabilized, with a launch mass of 300 kg. This includes the 100 kg X-band parabolic antenna. This is made of a deployable umbrella reflector, with a rigid carbon fibre reinforced plastic central dish and a set of knitted mesh gores stretched by skeleton ribs. This low mass design and the spacecraft configuration with low moments of inertia provide a high degree of pointing agility therefore increasing the viewing capabilities from the spacecraft. The spacecraft/antenna system may be dynamically redirected into any direction of the flight path (i.e. in the cross-track as well as in the along-track direction). Thus, a wide field of view within the incidence-angle range may be obtained on either side of the ground track for event monitoring coverage. The envisaged orbit is a sun-synchronous circular orbit with an altitude of 550 km, an inclination of 143.3° and a ground track repeat cycle of 36 days.

Combining high manoeuvrability with electronic antenna beam steering, the TecSAR acquisition modes can vary from “spotlight” configuration achieving a 1 m ground resolution to a wide coverage “ScanSAR” mode with an 8 m ground resolution.

7.3.5 GMES Sentinel-1

Within the European GMES programme, the Sentinel-1 satellite will ensure continuity of radar data for the European technical and scientific community. Indeed, this community has a strong expertise in the utilisation of C-band data from ERS-1/2 and Envisat satellites. The Sentinel-1 mission is still in its design phase but it is envisaged to offer full polarisation at C-band and a high acquisition mode flexibility (Davidson, 2007).

7.3.6 Conclusion of the Review of Future SAR Space-borne Missions

This review shows that future SAR missions will achieve both high spatial resolution and temporal coverage. In addition to this, polarimetry and interferometry capabilities are also satisfied. The only drawback is the lack of future L-band systems. Apart from the already operating Japanese Advanced Land Observing Satellite (ALOS) with its Phased Array type L-band Synthetic Aperture Radar (PALSAR) instrument, there is no other future mission planning for an L-band system.

This is quite surprising. A longer wavelength is in fact more suitable for all those studies that need to penetrate vegetation and observe the ground. Therefore, applications such as the monitoring of areas prompt to landslides, the analysis of surface deformation in active tectonic zones (e.g. earthquakes) and the monitoring of volcano activities would therefore not fully benefit from the future C and X band missions. Flood monitoring would also benefit more from an L-band system. A possible explanation to this matter could be the presence of a stronger user group dedicated to the observation of vegetation. This can be confirmed by examining the topic of the papers presented at the last ESA International Workshop on Science and Applications of SAR Polarimetry and Polarimetric Interferometry in January 2007. This workshop had one session dedicated entirely to forestry studies. One of other application sessions was on land/agriculture research, therefore including again vegetation monitoring. Therefore, even of there was indeed a session for subsidence monitoring by using permanent scatterers (refer to 2.1.7), most of the studies focused on vegetation monitoring.

Because of the lack of future L-band missions, the research explores a system design that would achieve the requirements set in Section 7.2.6. These specifications would also satisfy the other applications listed above. The aim of this analysis, summarised in Appendix D, is to demonstrate the possibility of designing an L-band mission that

satisfies the set specifications and to consider the subsequent operational needs that such a mission would generate in terms of data handling and distribution.

7.3.7 Results of the L-band SAR Mission Analysis and Design

As presented in Appendix D, a suitable spatial ground resolution can be achieved by an L-band SAR system. A 4-day repeat pass is obtained with a single satellite capable of agile steering. This solution also satisfies the full coverage requirement. A 4-satellite constellation similar to the COSMO-SkyMed system could therefore achieve the required 24-h temporal baseline for interferometric acquisitions. The mission analysis also highlights that such a system would generate a large amount of remote sensing data. This issue also applies to the previously presented missions that will provide users with fully polarimetric data at a relative high temporal resolution. Such practical matter is considered in Section 7.5.

7.4 Extrapolation of the Analysis Techniques Beyond the United Kingdom

One of the secondary objectives of the research is to consider the extrapolation potentials of the analysis techniques developed in this study beyond the United Kingdom. Landfills can be found in completely different environments and operational procedure can also be quite different from the ones applied in the UK. For instance, as mentioned in Section 1.1.2, in low- and middle-income countries the open dump approach remains the predominant disposal option, and often waste is deposited without following any specific procedure.

The first selected landfill is illustrated in Figure 7-4. This picture shows the Eagle Mountain site, located $33^{\circ} 53' 24.25''$ North and $115^{\circ} 33' 24.60''$ West in Southern California. Currently, the site is still not active and its purchase and eventual operation by the Sanitation Districts are contingent upon successful resolution of pending federal litigation (SDLA, 2007). The Eagle Mountain landfill would occupy the site of an abandoned iron mine and would have an enormous total capacity of 708 million tons potentially allowing the facility to operate for over 100 years. What is important to notice is that the mountainous environment surrounding the landfill would produce strong distortions in the SAR image. Foreshortening and shadows effects would reduce the possibility of extracting useful information from the radar scene and consequently would prevent the achievement of successful results from the techniques developed in this research.

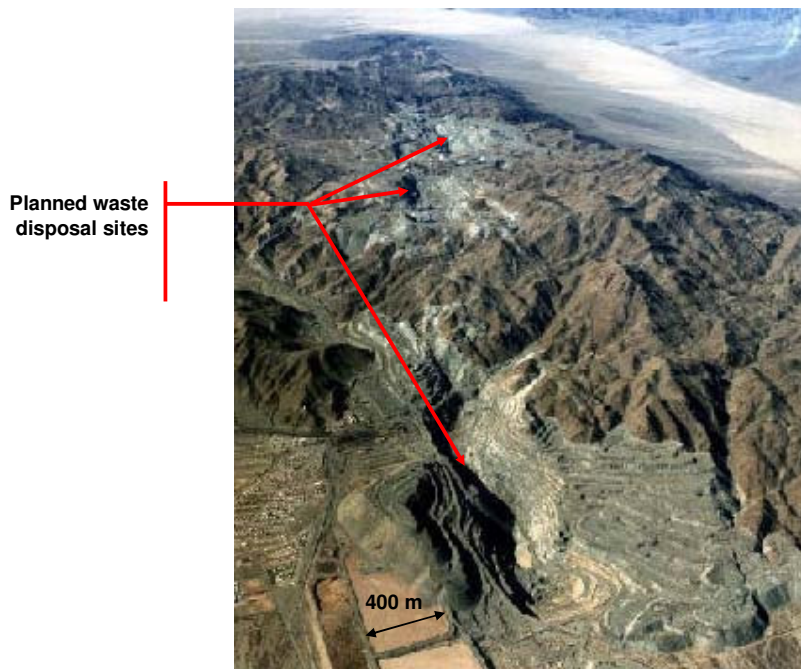


Figure 7-4. Aerial view of the planned Eagle Mountain landfill (SDLA, 2007).

The author also established a number of contacts with landfill operators and remote sensing experts in South Africa (SA) and Ghana (GH). Jarrod Ball (2005), from Jarrod Ball & Associates Ltd., and Stephen Opoku-Duah (2005), from Durham University, provided the author with information on a number of landfills located in different environments and which follow different operational procedures. Ball specified that in SA waste disposal sites are usually located very close to urban areas to facilitate the transport of material to the dump.

The second site presented in this section is the Bisasar Road site, located $29^{\circ} 48' 59''$ South and $30^{\circ} 58' 49''$ East in Durban (SA). This landfill, pictured in Figure 7-5, has been the cause of major controversy due to the type of waste accepted over the years. Today, the site is based on a modern cellular sanitary landfill approach with a methane recovery system built into the newest cells, and flaring systems installed to dispose of a portion of the methane being generated in an environmentally acceptable manner (Ball, 2005). The aspect of interest of this site is linked to the weather conditions. Durban has a tropical coastal climate, and the frequent rain comes in the form of thunderstorms. These regular precipitation events might significantly affect the classification methodology developed in the previous chapter by altering the interferometric coherence magnitude even for short temporal baselines (e.g. 24 h) and consequently leading to the misinterpretation of the SAR data.



Figure 7-5. Aerial view of the Bissasar Road landfill (Google Earth, 2007; with the education setting reproduction agreements).

Finally, the third landfill of interest is the Oblogo disposal site located $5^{\circ} 34' 04.19''$ N and $0^{\circ} 18' 0''$ W on the western peri-urban fringe of Accra, the Ghanaian capital city. As described by Demanya (2006) and Paris (2005), operations on this site do not follow strict regulations. The landfill is practically controlled by the local chief. Demanya (2006) explains that “customary rites have to be performed and a monthly royalty has to be paid to the chiefs as custodian of the land for the people and their ancestors, so as to perform rituals for cleansing the land, and appeasing the land gods for any abomination that such use of the land might bring.” The Oblogo site does not even have an exact perimeter establishing the permitted landfilling operations. Such difference in the operational procedures can significantly limit the applicability of both the landfill identification spatial analysis methodology and the land-use classification algorithm.

Overall, the analysis of these three sites highlights the limitations of the techniques developed in the research. These limitations can be linked to a different setting of the landfill (e.g. mountainous area or sandy desert), and/or particular weather conditions that can significantly affect the radar signal, and/or unusual landfilling procedures applied by the operators.

The difficulty and cost of ordering and acquiring additional SAR satellite data has not permitted these valuable a-priori remarks to be validated. However, because the starting point of the research addresses optical multispectral images of medium resolution, the following section investigates the potentials of additional optical data sets to monitor on-site conditions and therefore support the radar analysis in presence of these more challenging situations.



Figure 7-6. Aerial view of the Oblogo landfill (Google Earth, 2007; with the education setting reproduction agreements).

7.4.1 Analysis of Optical High Spatial and Spectral Resolution Data

As reviewed in Section 1.1.5, Jago and Curran (1997), Folkard and Cummins (1998) and Jensen (2005) have already demonstrated that airborne hyperspectral sensors that acquire high spatial resolution data in many small contiguous or non-contiguous bands of the electromagnetic spectrum can capture spectral information with sufficient resolution for the direct identification of certain materials and therefore successfully monitor the site conditions. Still, space-borne instruments do not achieve a fine resolution in both the spatial and spectral dimensions. For instance the future French Pleiades satellites (CNES, 2006) will acquire images with an enhanced spatial resolution of 2.8 m but with a coarse multispectral resolution (i.e. four wide bands in the blue, green, red and near infrared spectrum). It remains therefore important to separately consider high spatial resolution images with low spectral capabilities, and medium to low spatial resolution images with a fine spectral resolution. As a result, the following analysis investigates multispectral high spatial resolution CASI data and hyperspectral medium spatial resolution images collected by the CHRIS instrument onboard of the ESA PROBA spacecraft.

7.4.1.1 CASI

In 2002, the UK Environment Agency acquired an airborne image with 1 m ground resolution of the Bletchley landfill site near Milton Keynes (exact Ordnance Survey grid location $x = 486173$, $y = 232520$) (Hambidge, 2005). The instrument, flown on a Cessna aircraft operated from Coventry airport, acquired data in only 7 bands (Table

7-1) and not in the standard 288 available bands at 1.9 nm intervals varying between 400 and 1000 nm (Itres, 2005). Even if it is an airborne instrument, the small number of bands makes the delivered data similar to a future Pleiades satellite image.

Table 7-1. Spectral bands acquired by the CASI instrument.

1-	446.0nm +/- 6.6 nm
2-	470.0nm +/- 6.6 nm
3-	550.0nm +/- 6.7 nm
4-	670.9nm +/- 6.8 nm
5-	751.0nm +/- 6.8 nm
6-	780.6nm +/- 5.9 nm
7-	880.0nm +/- 11.6 nm

Two colour composites of the data are shown in Figure 7-7. The bottom image is obtained combining bands 1, 4 and 7. This RGB composite is suggested by Sabins (1996) as the optimal colour combination for bare soil studies. Figure 7-8 zooms on the tipping area of the landfill, while Figure 7-9 shows a simple Normalized Difference Vegetation Index (Schowengerdt, 1997) applied on the data.

A vast number of additional spectral combinations could be produced, but the examples provided so far already evidently demonstrate that even with a small set of wide bands, space-borne high resolution data could support the detailed monitoring of ground activities. As discussed with Smith (2005), the images shown here can provide useful information such as the scale of tipping areas, monitor clay transportation activities, assess depressions due to desiccation cracks which are often source of harmful methane emissions, and monitor surface water sediments in ponds. This information could be of interest to both regulators and private individuals. For instance, in 2001 unregulated activities at the Bletchley landfill led to expensive legal litigations between the landfill operator and private citizens. In such instances, high-resolution satellite images would definitively be of great value.

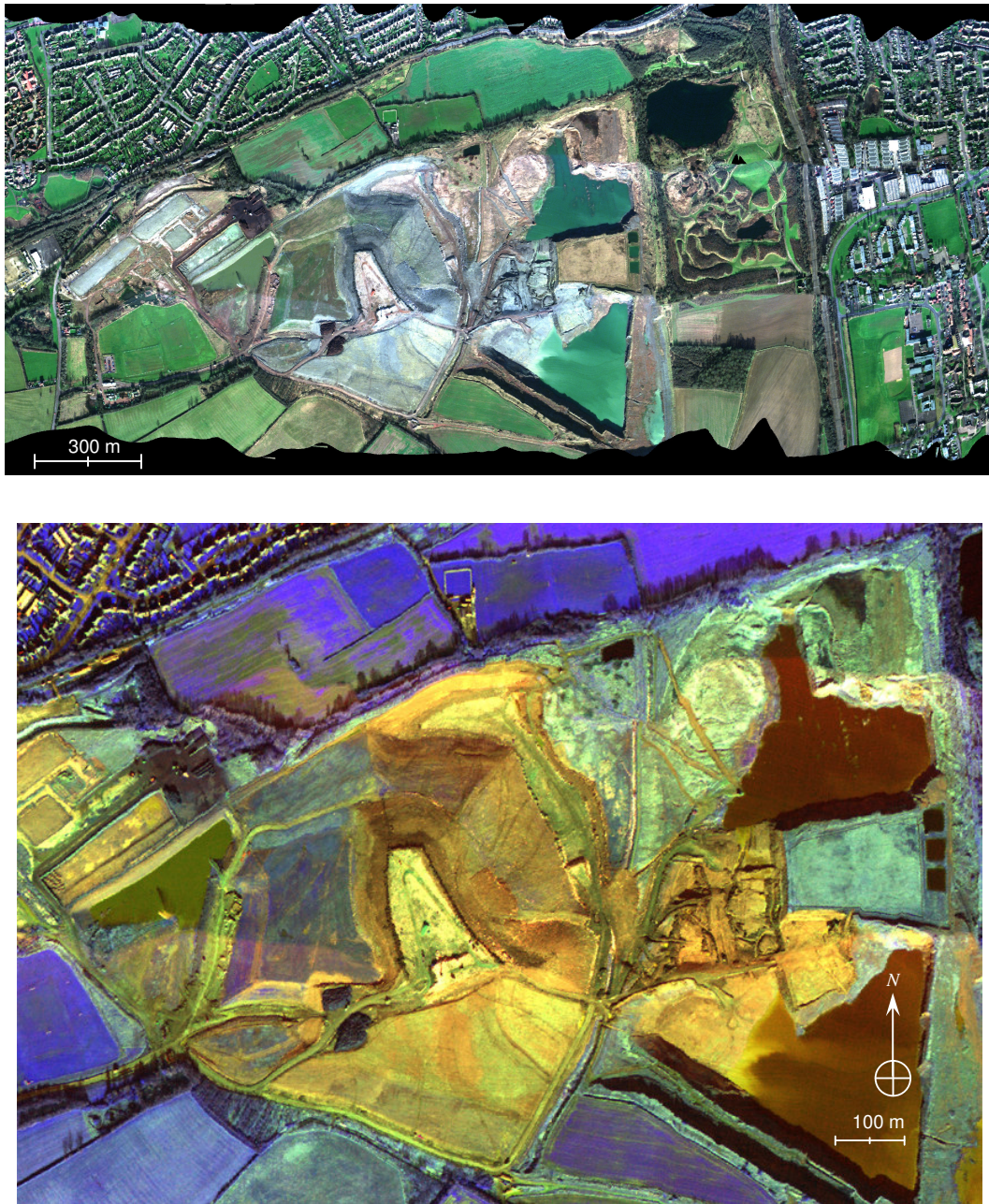


Figure 7-7. Colour composites of a CASI image with 1 m ground resolution of the Bletchley landfill site near Milton Keynes. Top: original data, true colour composite with bands 4 3 2 as RGB. Top: landfill site, false colour composite with bands 1 4 7 as RGB. Copyright 2005 Environment Agency

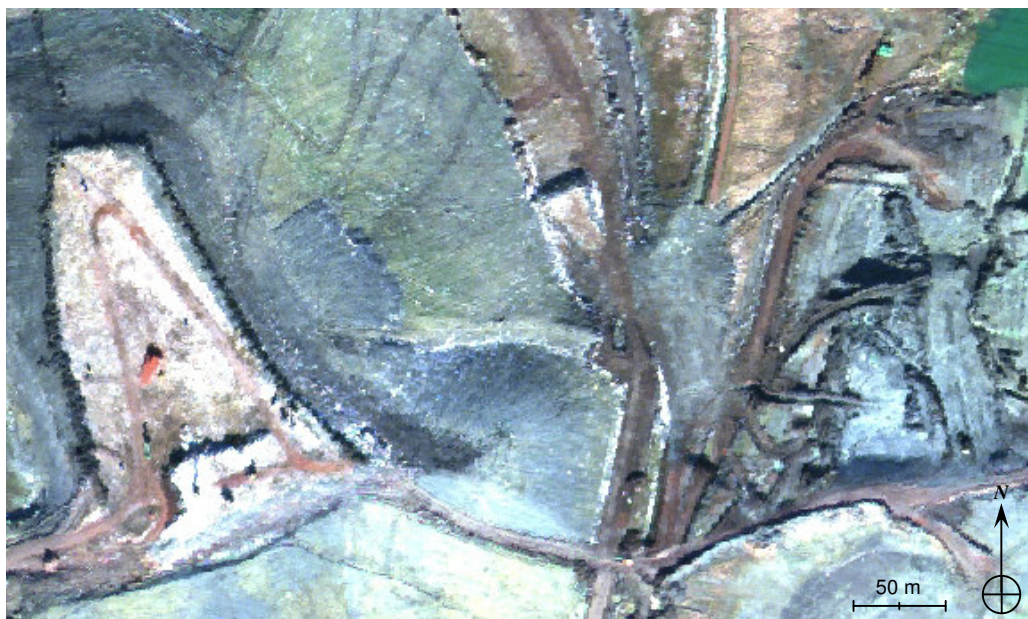


Figure 7-8. True colour composites of a CASI image with 1 m ground resolution of the Bletchley landfill site near Milton Keynes, UK. true colour composite with bands 4 3 2 as RGB. Copyright 2007 Environment Agency.

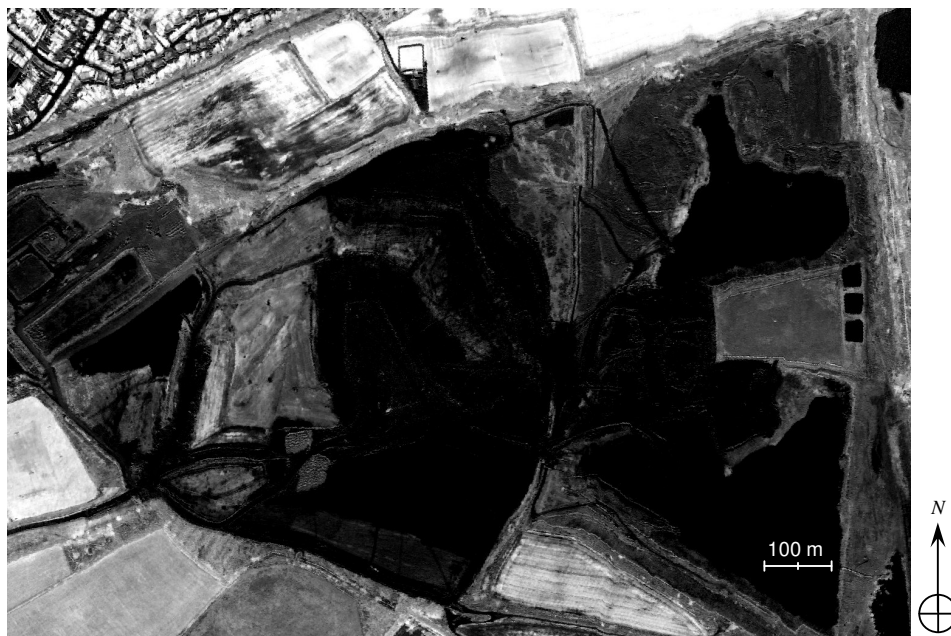


Figure 7-9. Bletchley landfill. Normalized Difference Vegetation Index (Schowengerdt, 1997). Bright areas corresponds to vegetation, whilst dark areas correspond to bare zones. Copyright 2007 Environment Agency.

7.4.1.2 PROBA CHRIS

As explained in Section 4.1, CHRIS data were obtained through an ESA Category-1 research proposal (proposal identification number: 3138). From a 600 km orbit, CHRIS can offer 14 km x 14 km images with a spatial resolution approximately of 19 m. The satellite has agile steering capabilities in both the along and across track directions and this enables observation of selectable targets well outside the nominal field of view of 1.3°. As a result, images are generally be acquired in sets of 5, these being taken at along track angles of +/- 55°. +/- 36°, and as close to nadir as possible. CHRIS operates with spectral bandwidths that vary from 1.3 nm at 410 nm to 12 nm at 1050 nm. The spectral bands are illustrated in Figure 7-10.

Unfortunately due to technical failures and cloud cover (Fletcher, 2005), every window of opportunity has been partially or totally unsuccessful. The only acquisition that has in part satisfactory characteristics is illustrated in Figure 7-11. This corresponds to the nadir image acquired on 30th August 2005. As pointed out by the arrow, the landfill is covered by a cloud and its shadow. Because the 5 images per acquisition of Proba are obtained at different times, the position of the clouds changes between each image. Luckily, the -36° view angle image shows the northern part of the landfill unaffected by clouds or shadows. Overall, the obstacles for acquiring a successful image can be translated into an important conclusion, not to be underestimated when considering the operational application of EO data. Optical data can certainly reveal valuable information, nonetheless they are dependent on atmospheric conditions, which is a critical constraint for many areas of the world. SAR systems therefore have the advantage of being effective in all-weather conditions.

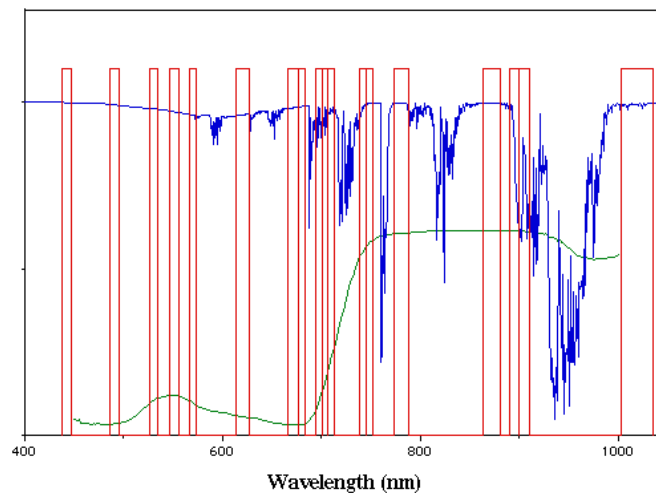


Figure 7-10. CHRIS Proba spectral windows (ESA, 2007e). The instruments in Mode 3 acquires 18 bands (in red). A spectrum of healthy vegetation is shown in green. The blue spectrum depicts the atmospheric absorption.



Figure 7-11. CHRIS Proba acquisition centred on the Brogborough landfill. Partial cloud cover and relative shadows limit the utilisation of the image.

As the delivered images were affected by striping, the author applied a Fourier Transform to the image and filtered it in the frequency domain. A detailed explanation of this technique can be found in Jensen (2005). This process is carried out with the filtering tools implemented in ENVI. Then, the Minimum Noise Fraction (MNF) Transformation is applied. This is a useful algorithm that reduces the dimensionality of hyperspectral data and minimizes the noise in the imagery. Again, the reader is referred to Jensen (2005) for an explanation of this technique. The first three components of the MNF transformation are used to create the RGB composite shown in Figure 7-12.

The image is cropped because the band reduction analysis was carried out specifically on this northern part of the landfill only and not on the overall image. As presented in Ottavianelli et al. (2006), the blue marine areas are clouds, the red pixels represent water, pink and white areas correspond to vegetation, and purple, violet and blue shades identify other land cover types. The aerial view in Figure 7-13 acquired by the author shortly after the CHRIS acquisition confirmed that the blue areas highlighted by the four arrows in Figure 7-12 correspond to the tipping areas. This analysis demonstrates that hyperspectral data even with a relatively coarse resolution are adequate to monitor the activities carried out in a landfill.

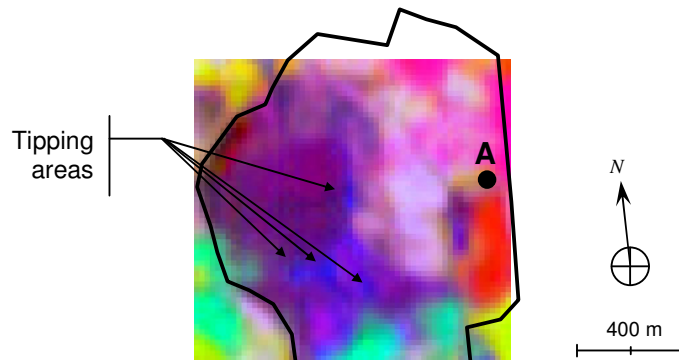


Figure 7-12. Proba CHRIS red-green-blue composite using the first three components after the image dimensionality reduction. Image acquired on 30th August 2005. The blue areas indicated by the arrows refer to the open cells. Red areas correspond to water, while blue marine corresponds to clouds. The black line identifies the perimeter of the northern part of the landfill.



Figure 7-13. Aerial view of the tipping areas of the Brogborough landfill acquired by the author on 5th September 2005 in collaboration with the Cranfield National Flying Laboratory Centre. The three axes show the approximate direction of the North (N), West (W) and the elevation. Point A north of the landfill facilitates the comparison of this picture with the Proba CHRIS colour composite in Figure 7-12 as a ground truthing tool.

7.4.2 Conclusion of the Analysis on the Extrapolation Potentials

This analysis has demonstrated that if a landfill is located in particular regions (e.g. mountainous area or sandy desert), and/or if meteorological conditions can significantly affect the SAR backscatter, and/or different landfilling procedures are followed, the analysis techniques developed in this research suffer a number of limitations.

The research has also established that despite their cloud cover constraints, optical data with a fine spatial resolution (i.e. < 3 m) or with a high spectral resolution (i.e. > 15 narrow bands) are able to accurately monitor on-site landfill conditions and therefore support the SAR data analysis. Given the coarser spatial resolution of SAR images currently available, it remains more advantageous to use the hyperspectral data which would allow the two datasets to be merged without losing information.

7.5 Analysis of End-Users Needs for the Utilisation of EO Data in an Operational Context

The section focuses on the end-user needs related to the initial utilisation of the EO data and the subsequent continuous application in an operational context.

In seeking to define the long-term relationship sought with users, one must consider the all-inclusive structure that goes from the space infrastructure provider and user policy aspects, to EO data acquisition, processing and product delivery. It must be underlined that the different bodies can simultaneously have different roles. For instance, an end-user can also be the product/service provider, directly acquiring the raw data and subsequently processing them to obtain the required knowledge and information.

The great diversity of users and applications leads to an even larger variety of users' needs. A list indicating the range of needs follows below:

- Initial implementation programmes needs:
 - legal framework and policy related issues,
 - bureaucracy elimination in agreement formulation and implementation,
 - capacity building (i.e. infrastructure and know-how),
 - demonstrated benefits for the application,
 - clear economic added value for the user,
 - product/service accuracy and reliability,
 - product/service prompt delivery,
 - affordability,
 - diversification of product/service level (e.g. the need of already extracted knowledge or preliminary product still to be analysed for information extraction),

- need for integration of additional in situ data and ancillary non geo-referenced data,
- final product format,
- utilisation complexity (e.g. software requirements and integration of Geographical Information Systems (GIS) services with EO products).

- The long-term needs
 - product/service certification and standardisation that satisfies their regulations,
 - product/service delivery continuity,
 - resourceful support availability throughout the operational phase,
 - effortless implementation of new techniques for more accurate and efficient products/services,
 - low operational maintenance costs,
 - product/service flexibility to accommodate changes in application needs,
 - inter-usability of data for different applications,
 - standardisation of product/service delivery chain,
 - users programme empowerment,
 - full integration of local expertise,
 - efficient dialogue and feedback between user and provider.

From the actual space-borne infrastructure implementation and product/service distribution point of view, it is possible to identify a number of other issues and requirements regarding:

- data storage and access
- data availability
- processing complexity (e.g. data mining, data fusion)
- more powerful information and communication technology and resources.
- need for dedicated space-borne instruments/platforms/systems and data specifications requirements (i.e. area coverage rate, area access rate, ground resolution, radiometric resolution, spectral resolution, footprint area, and instantaneous access area).

7.5.1 Example for Landfill Regulators

The landfill regulators (e.g. the UK Environment Agency) are selected as an example of user group to identify critical issues related to the application of EO data for solid waste landfill monitoring.

Landfill regulators must gather information on landfilling activities on a regular basis and they often report to other national and international bodies. In many cases, EO data, whether SAR or optical, can provide such information but these are not used for a variety of reasons.

First of all, sometimes there are standards related to the monitoring of a landfill that not only state the accuracy of the observation, but often refer to the actual methodology. Therefore, the regulators follow this set specification even if the application of EO data might result more beneficial (e.g. in economic or precision terms).

Secondly, in order to use remote sensing data, the regulator would have to build new capacity related to EO data handling and processing. This implies investing or redirecting resources (i.e. time, money and manpower) into new technologies (e.g. acquire knowledge, buy hardware and software) which in the short term is usually not convenient. A solution would be to directly use EO products developed by a third party, but this would raise issues of accuracy assessment, liability issues and product certification which are often disregarded in the EO community (Campbell, 2007).

As raised in Section 4.1.1 and 7.4.1.2, remote sensing data can be problematical to order and obtain, even for commercial purposes as most missions are primarily dedicated to research. Common examples are: conflict with other instruments onboard the same satellite, instrument unavailability due to calibration and validation procedures, the need to submit a data request three months in advance, clash with other requests for the same instrument (e.g. different radar polarisation), simple errors in the data request software cloud cover for optical data, time required for the production and delivery of the images. Appendix D also points out that scenes from future SAR missions will have a very large size in terms of bytes, therefore posing critical data handling and processing requirements to the final user or the service provider.

A fourth and final point is that once a satellite reaches the end of its operational life, there is no assurance on the future availability of remote sensing data with similar characteristics.

7.5.2 Conclusion of the Analysis of the End-User Needs

The analysis demonstrates that there are a number of aspects, ranging from practical and managerial matters to legal and technical issues, that discourage the utilisation of EO data by new potential users.

An independent provider of the final required product should have a stronger role in filling the gap between the satellite manufacturers and the final end-users. They should initially show the concrete benefits of EO data utilisation in a practical way. They should then encourage dialogue with the final users in order to implement a sustainable utilisation of the remote sensing products.

Many of these practical problems with using EO data are not unique to the landfill application. For example, the ESA Epidemio and European Terrafirma programmes

(Epidemio, 2006; Terrafirma, 2007) corroborate that the role of an information provider delivering the EO final products based on a close dialogue with the end-user is essential.

7.6 Concluding Remarks of the Overall Discussion

The discussion presented in this chapter addressed the applicability of the developed techniques in an operational context. It focused on three different aspects: the impact of the main SAR system parameters, the extrapolation potential beyond the UK and the end-user needs.

Several key point were made. For an effective and more widely applicable implementation of the techniques developed in this research there are a number of requirements linked to SAR system parameters: the achievable spatial resolution should be around 4 m; the system should allow the acquisition of interferometric pairs with a temporal baseline of maximum 24 hours; L-band wavelength with full polarimetry; multi-geometry view acquisitions. A review of future SAR missions shows that both high spatial resolution and temporal coverage requirements will be met. In addition to this, polarimetry and interferometry capabilities are also satisfied. The only drawback is the lack of future L-band systems.

With regards to the extrapolation potentials, the research demonstrated that if a landfill is located in particular regions (e.g. mountainous area or sandy desert), and/or if meteorological conditions can significantly affect the SAR backscatter, and/or different landfilling operational procedures are followed, the analysis techniques developed in this research suffer a number of limitations. The research has also established that despite their cloud cover constraints, optical data with a fine spatial resolution (i.e. < 3 m) or with a high spectral resolution (i.e. > 15 narrow bands) are able to accurately monitor on-site landfill conditions and therefore support the SAR data analysis. Given the coarser resolution of current SAR systems, it remains more advantageous to use the hyperspectral data which would allow the two data sets to be merged without losing information.

Finally, the end-user community is acknowledged to be heterogeneous across several dimensions leading to a variety of needs that should be extensively addressed when formulating and implementing a sustainable operational use of EO data. The analysis shows that there are a number of aspects, including simply practical and managerial matters to more complex legal to technical issues, that discourage the utilisation of EO data by new potential users. The role of third party providers of the final required product to the end-user is envisaged to have a key function. They should fill the gap between the satellite manufacturers and the final end-users by initially showing the concrete benefits of EO data and subsequently encouraging dialogue with the final users in order to implement a sustainable utilisation of the remote sensing products.

In conclusion, considering the SAR missions planned to be launched in the coming years and overcoming the main obstacles preventing new users to apply EO data, the analysis techniques presented in this thesis could be effectively used in an operational context.

8. Conclusions and Further Work

Overall, the justification for the research has been comprehensively addressed in the thesis and the objectives have been met within the limits of the acquired SAR data and time. It is important to clarify again that the research aim is not to directly compare optical data with SAR data. Also, it is beyond the scope of the research to investigate the application of additional techniques such as Light Detection and Ranging (LIDAR) sensors. This is identified as further work.

The following sections provide a concise summary of the main findings and conclusions related to the two research objectives. They also summarise the limitations and applicability of the developed techniques in an operational context. Proposed areas of future work are also presented in Section 8.5.

8.1 Summary of the Research

The work presented in this thesis has investigated the qualitative and quantitative interpretation and analysis of SAR data applied to the monitoring of solid waste landfills.

In particular, the research objectives are to: 1) assess whether SAR data can support the identification of landfill sites by distinguishing them from other disturbed areas which present similar optical spectral signatures, and 2) assess the possibility of correlating SAR data with on-site conditions and operational procedures.

The author initially carried out fieldwork to appreciate those spatial, temporal and biophysical characteristics of a landfill that can influence SAR data. These preliminary ground measurements and observations examined general features and characteristics that can subsequently support the data analysis. They also facilitated the physical interpretation of the results.

With the financial support of the Royal Aeronautical Society Centennial Scholarship awarded to the author and the Remote Sensing and Photogrammetry Society, historical and new programmed acquisitions were obtained from the ESA ERS-1 and -2 satellites and from the Envisat ASAR instrument. These scenes were delivered within the framework of a Category-1 research project proposed by the author to ESA.

Different approaches are used to address the two research objectives. The first is tackled by means of a spatial analysis of SAR backscatter amplitude data and by qualitatively investigating the temporal decorrelation of interferometric coherence magnitude images.

The significance of the digital elevation models derived from the InSAR processing is also assessed.

With regards to the second objective, the analysis initially explored the backscatter signal to correlate SAR images with on-site conditions and operational procedures. Ground measurements were required in order to obtain the SAR backscatter coefficient values for areas common to waste disposal sites. These data were obtained with the use of a ground based SAR system. Simulations based on the RT2 backscatter model were subsequently used to carry out a sensitivity analysis on the variables affecting the radar backscatter. The objective of this analysis was to quantitatively assess the parameters which have an effect on the SAR backscatter coefficient. Following this analysis, historical ERS SAR scenes were used to develop a novel classification methodology to identify different land-use areas on the Brogborough landfill. This method is based on a Fuzzy Logic classifier and on featured-based pixel-by-pixel classification procedures and merger information both in the space and time dimensions.

Ultimately, the research provided an appreciation of the applicability of the developed techniques in an operational context and of the possibility to extrapolate the SAR data analysis methodologies beyond the UK. Concluding remarks also covered issues related to the needs of the potential end-users of such remote sensing products.

8.2 Objective 1: Landfill Site Identification

The analysis initially confirmed the findings of previous research presented in the literature with regards to the limitation of medium spatial resolution multispectral optical data to readily distinguish landfill sites from other disturbed areas.

A spatial analysis of the SAR backscatter amplitude over these sites showed that landfills are characterised by evident anisotropic features that can support their identification. Information about the status of the sites during the used SAR acquisitions and additional ground observations have revealed that such anisotropic features are linked to topography and the presence of distinctive areas with smooth and rough soil properties. Validation tests also proved that in both winter and summer conditions and with both ascending and descending orbits (i.e. different look angles and acquisition times), waste disposal sites present distinctive SAR backscatter spatial characteristics.

The analysis of the degree of coherence over both landfills and a disturbed area demonstrated that waste disposal sites are characterised by large decorrelated areas with transient locations, whilst the disturbed area presents smaller areas of low coherence in a permanent position.

Finally, the distinctive positive topography of landfills can also help to distinguish them from other disturbed areas presenting similar optical signatures.

Overall, the discussion pointed out the constraints of such analysis techniques linked to the daily operational landfilling procedures carried out on the sites and to the spatial resolution of the SAR imaging system.

8.3 Objective 2: On-site Conditions Monitoring

The GB-SAR measurements showed that there is an average difference of circa 7dB between the mean backscatter of capped areas and rougher tipping areas common to landfills. An additional aspect worth of notice is the exact similarity of the trend between σ_{HH}^0 , σ_{VV}^0 and σ_{HV}^0 for the tipping area in contrast with the capped area.

It is also observed that the co-polarised ratio $\sigma_{HH}^0/\sigma_{VV}^0$ can support the analysis of the on-site landfill conditions and distinguish smooth and rough surfaces, hence the capped from the tipping areas. This would require the assumption of a flat topography.

Overall, these results corroborate that the co-polarised ratio and the vertical-horizontal correlation coefficient can be used as roughness discriminators. Also, the cross-polarised ratio does not show any significant difference in terms of backscatter. This confirms the preliminary ground observations that no volume scattering occurs.

The RT2 sensitivity analysis highlighted that the variables taken into consideration (i.e. soil moisture, soil texture, surface roughness and incidence angle) have the same magnitude of influence on the SAR backscatter. It is therefore extremely challenging to relate backscatter changes to soil conditions, and assumptions are often required to allow the examination of a SAR scene and its land-cover classification. Without the accurate knowledge of topographic and weather conditions, one single-polarisation acquisition can hardly provide correct land-cover information, and consequently knowledge on land-use. Therefore, with regards to a single scene acquisition, it is evident that fully polarimetric complex data offer a major benefit. Even if it generally presents lower backscattering values, an L band SAR has a better sensitivity to surface roughness and soil moisture, hence providing results that can be more accurately linked to ground conditions. This factor, together with a lower sensitivity to vegetation, makes an L band SAR more adequate for bare soil studies.

The research pointed out the value of merging coherence and magnitude data to interpret unusual spikes observed in the computed interferometric DEM. With regards to the image classification of SAR data, the research highlighted that in the literature land-cover and land-use classes are often mixed. Additionally, these studies apply strict thresholds to categorize the various classes even though it is often acknowledged that

the appearance of the land cover categories is better described with approximate terms such as low, medium or high. The research therefore developed a new classification methodology that uses only land-use classes and applies a Fuzzy Logic (FL) and a feature-based analysis. These novel classification approach proved to be fairly accurate for most land-use classes (i.e. Kappa coefficient of 71%). A more evident level of ambiguity is observed for certain classes especially when increasing the degree of classification success threshold. The multiple class pixels were most probably caused by detecting various classes within one 50 m SAR spatial resolution cell.

8.4 Conclusions of the Overall Discussion

The analysis of the key SAR system parameters showed that for an effective and more widely applicable implementation of the techniques developed in this research there are a number of requirements: the SAR spatial ground resolution should be around 4 m; the system should allow the acquisition of interferometric pairs with a temporal baseline of maximum 24 hours; L-band wavelength with full polarimetry; multi-geometry view acquisitions.

The investigation of the extrapolation potentials also demonstrated that if a landfill is located in particular regions (e.g. mountainous area or sandy desert), and/or if meteorological conditions significantly affect the SAR backscatter, and/or different landfilling procedures are applied by the site operators, the analysis techniques developed in this research suffer a number of limitations.

The research has also established that despite their cloud cover constraints, optical data with a fine spatial resolution (i.e. < 3 m) or with a high spectral resolution (i.e. ~ 20 narrow bands) are able to accurately monitor on-site landfill conditions and therefore support the SAR data analysis. Given the coarser spatial resolution of SAR images currently available, it remains more advantageous to use the hyperspectral data which would allow the two datasets to be merged without losing information.

8.5 Further Work

Overall, the analysis has revealed a number of areas for further investigation and research. These are summarised below:

- Explore the potential of high resolution and/or fully polarimetric space-borne SAR data. As mention in Chapter 4.1, additional data requests have already been submitted by the author and successfully accepted by the Canadian Science and Operational Applications Research programme (research project reference number: 1719) for high resolution C-band SAR data from Radarsat-2 (i.e. ultra-

fine beam mode, 20 km swath, 3x3 m ground resolution), and by the Japanese Advanced Land Observing Satellite (ALOS) (research project reference number: 3568) for L-band fully polarimetric data through a cooperative agreement between ESA and the Japan Aerospace Exploration Agency (JAXA). These data should be used to further explore both the landfill identification and classification techniques. The Radarsat-2 data in particular could assess the value of a finer spatial resolution.

- Apply the analysis methodologies in a variety of environments to address their extrapolation potential and eventually implement modifications and enhancements of the techniques. Such application could be carried out within the framework and with the financial support of the European GMES programme.
- Investigate pixel, feature and decision data fusion algorithms to merge SAR and hyperspectral optical data in order to improve both the identification and on-site monitoring analysis.
- Address end-users needs related to accuracy assessment, liability and product certification issues. Findings should be translated into sensor calibration requirements and the standardisation of remote sensing image analysis.
- Study the possibility of implementing the subsidence monitoring by employing corner reflectors on capped and restored areas of landfill sites. Short revisit times or large number of SAR scenes could support the accurate detection of both fast and slow ground movements.
- Study more accurate solutions for the co-registration of SAR scenes acquired from ascending and descending orbits especially not ERS tandem pairs.
- Investigate the application of Light Detection and Ranging (LIDAR) sensors.
- Explore the value of relating these EO products to environmental economics matters.

9. References

9.1 References

- Armour, B., Tanaka, A., Ohkura, H., and Saito, G. (1999). Radar Interferometry for Environmental Change Detection. In: Lunetta, R. S. and Elvidge, C. D. (Editors), *Remote Sensing Change Detection*. Taylor and Francis Ltd, London.
- BADC (2006). *British Atmospheric Data Centre*. Available at: <http://badc.nerc.ac.uk/home/index.html> (last accessed 30th November 2006).
- Bagchi, A. (2004). *Design of Landfills and Integrated Solid Waste Management*. 3rd ed. John Wiley and Sons, Hoboken, New Jersey.
- Baldock, C., Environment Agency. (2005). *Waste Management - Business*. Available at: http://www.environment-agency.gov.uk/business/444304/444641/?version=1&lang=_e&lang=_e (last accessed 18th Feb 2005).
- Ball, J. (Jarrod Ball & Associates Ltd.) (2005). *Personal communication*.
- Bamler, R. (Alpbach Summer School 2006) (2006). *Radar Interferometry for Surface Deformation Assessment*.
- Bamler, R. and Hartl, P. (1998). Synthetic Aperture Radar Interferometry. *Inverse Problems*. Vol. 14, pp. R1–R54.
- Bamler, R. and Just, D. (1993). Phase Statistics and Decorrelation in SAR Interferograms. In: *Geoscience and Remote Sensing Symposium, IGARSS '93*. Tokyo, Japan, August 18-21, 1993, Vol. 3, pp. 980-984. IEEE.
- Barber, B. C. (1993). The Phase Statistics of a Multichannel Radar Interferometer. *Waves in Random Media*. Vol. 3, pp. 257-266.
- Bardossy, A. and Samaniego, L. (2002). Fuzzy Ruled-Based Classification of Remotely Sensed Imagery. *IEEE Transactions on Geoscience and Remote Sensing*. Vol. 40, No. 2, pp. 362-374.
- Beaven, R. P. (2001). *Integration of Monitoring Data Management Systems for Landfill Sites*. Environment Agency Technical report EA/TR-P1-428. DoE, London.
- Bedford Borough Council (2007). *Development Planning of Former Grain Storage*

- Depot, Station Road, Turvey, Bedfordshire. 06/02284/MAF. Bedford Council, Bedford .*
- Bennett, J. C. (Sheffield University) (2005). *Private communication in July 2005.*
- Bennett, J. C. and Morrison, K. (1996). Development of a Ground-Based, Polarimetric Synthetic Aperture Radar. In: *Aerospace Applications Conference*. Snowmass, CO, February 3-10, 1996, Vol. 4, pp. 139-146. IEEE, New York.
- Bennett, J. C., Morrison, K., Race, A. M., Cookmartin, G., and Quegan, S. (2000). The UK NERC Fully Portable Polarimetric Ground-Based Synthetic Aperture Radar (GB-SAR). In: *Geoscience and Remote Sensing Symposium, IGARSS 2000*. Honolulu, July 24-28, 2000, Vol. 5, pp. 2313-2315. IEEE.
- Berardino, P., Fornaro, G., Lanari, R., and Sansosti, E. (2002). A New Algorithm for Surface Deformation Monitoring Based on Small Baseline Differential SAR Interferograms. *IEEE Trans. Geoscience and Remote Sensing*. Vol. 40, No. 11, pp. 2375-2383.
- Blaes, X. and Defourny, P. (2003). Retrieving Crop Parameters Based in Tandem ERS 1/2 Interferometric Coherence Images. *Remote Sensing of Environment*. Vol. 88, pp. 374-385.
- Blumberg, D. G. (2007). High Resolution X-band SAR Imagery for Precise Agriculture and Crop Monitoring. In: *ESA POLinSAR 2007 Workshop*. ESA/ESRIN, Frascati, Italy, Jan. 22-26, 2007 . ESA, Paris.
- Bobolina, E. (2005). *Optimising temporal resolution of soil moisture measurement using synthetic aperture radars* (unpublished M.Sc. thesis). Cranfield University, Cranfield.
- Boerner, W.-M., Mott, H., Lunenburg, E., Livingstone, C., Brisco, B., Brown, R. J., and Patterson, J. S. (1998). Polarimetry in Remote Sensing: Basic and Applied Concepts. In: Henderson, F. M. and Lewis, A. J. *Manual of Remote Sensing*. 3rd ed. Vol. 2: Principles and Applications of Imaging Radar. Wiley, Chichester.
- Breton, M. R. and Chorowicz, J. (1997). Utilisation de la Télédétection et des Systemes d'Information Géographiques dans la Recherche et le Suivi des Centres d'Enfouissement Techniques. In: *International Symposium on Engineering Geology and the Environment*. Athens, Greece, June 23-27, 1997, Vol. 1-3, pp. 1643-1648. Balkema, Rotterdam.
- Brivio, P. A., Doria, I., Gomasasca, M. A., Moriondo, S., Pagnoni, F., Tomasoni, R., and Zilioli, E. (1991). *Potenzialita del Telerilevamento da Satellite e da Aereo nella Ricerca di Aree Soggette ad Inquinamento e Degrado, anche Finalizzata*

- alla Individuazione di Discariche Abusive, Tramite Analisi di Stress Ambientale e Alterazione delle Caratteristiche Pedologiche di Zone Campione*. L. 441/87 CNR-TEI-ENEA, Second and Third Progress Report. Ministry for the Environment of Italy, Rome.
- Brivio, P. A., Doria, I., and Zilioli, E. (1993). Aspects of Spatial Autocorrelation of Landsat TM Data for the Inventory of Waste-Disposal Sites in Rural Environments. *Photogrammetric Engineering and Remote Sensing*. Vol. 59, No. 9, pp. 1377-1382.
- Bruno, D. (2003). *Radar Measurement of Topography* (unpublished M.Sc. thesis). Cranfield University, Cranfield.
- Bryce, D., Hall, R. S., and Young, R. I. (2003). *Greenhouse Gases Detection*. Technical Report E1-127. Environmental Agency, Bristol.
- Bujor, F. T., Nicolas, J.-M., Trouve, E., and Rudant, J.-P. (2003). Application of Log-Cumulants to Change Detection on Multi-Temporal SAR Images. In: *Geoscience and Remote Sensing Symposium, IGARSS 2003*. Toulouse, France, July 21-25, 2003, Vol. 2, pp. 1386-1388. IEEE.
- Butcher, K. (Environment Agency) (2005). *List of Landfill Sites*. (unpublished Excel spreadsheet provided on 29th November 2004).
- Campbell, J. B. (2002). *Introduction to Remote Sensing*. 3rd ed. The Guilford Press, New York.
- Campbell, G. (Science and Applications Department, European Space Agency) (2007). *Personal communication*.
- Candela, L. and Caltagirone, F. (2003). COSMO-SkyMed: Mission Definition, Main Applications and Products. In: *ESA POLinSAR Workshop*. ESA/ESRIN, Frascati, Italy, January 14-16, 2003. ESA, Paris.
- Carrasco, D., Díaz, J., Broquetas, A., Arbiol, R., Castillo, M., and Palr, V. (1997). Ascending-descending orbit combination SAR interferometry assessment. In: *3rd ERS SYMPOSIUM*. Florence, Italy, March 17-21, 1997. ESA.
- Casu, F., Manzo, M., and Lanari, R. (2006). A Quantitative Assessment of the SBAS Algorithm Performance for Surface Deformation Retrieval from DInSAR Data. *Remote Sensing of Environment*. Vol. 102, pp. 195-210.
- Chen, C. W. and Zebker, H. A. (2001). Two-dimensional Phase Unwrapping with the use of Statistical Models for Cost Functions in Nonlinear Optimisation. *Journal of the Optical Society of America A*. Vol. 18, No. 2, pp. 338-351.

- Cliff, A. D. and Ord, J. K. (1973). *Spatial Autocorrelation*. Pion Ltd., London.
- CNES (2006). *Pleiades Satellites*. Available at: http://smc.cnes.fr/PLEIADES/GP_satellite.htm (last accessed 10th January 2006).
- Colesanti, C., Ferretti, A., Novali, F., Prati, C., and Rocca, F. (2003). SAR Monitoring of Progressive and Seasonal Ground Deformation Using the Permanent Scatterers Technique. *IEEE Transactions On Geoscience And Remote Sensing*. Vol. 41, No. 1, pp. 1685-1701.
- Coltelli, M., Fornaro, G., Franceschetti, G., Lanari, R., Puglisi, G., Sansosti, E., and Tesauro, M. (1998). ERS-1/ERS-2 Tandem Data for Digital Elevation Model Generation. In: *Geoscience and Remote Sensing Symposium, IGARSS 1998*. Seattle, July 6-10, 1998, Vol. 2, pp. 1088-1090. IEEE.
- Committee on Earth Observation Satellites (2006). *Earth Observation Handbook*. Available at: <http://www.eohandbook.com/index.html> (last accessed 14th August 2006).
- Congalton, R. G. and Green, K. (1999). *Assessing the Accuracy of Remotely Sensed Data: Principles and Practices*. Lewis, Boca Raton, FL.
- Conklin, A. R. (2004). *Field Sampling*. Marcel Dekker, New York.
- Cox, E. (1999). *The Fuzzy Systems Handbook: A Practitioner's Guide to Building, Using, and Maintaining Fuzzy Systems*. Academic Press Professional, New York.
- CSA (2007). *Radarsat 1 and 2*. Available at: <http://www.space.gc.ca/asc/eng/satellites/default.asp> (last accessed 7th January 2007).
- Curlander, J. C. and McDonough, R. N. (1991). *Synthetic Aperture Radar. Systems and Processing*. Wiley, Chichester.
- Curran P. J. and Atkinson, P. M. (1999). Issues of Scale and Optimal Pixel Size. In: Stein, A. et al. *Spatial Statistics for Remote Sensing*. Kluwer Academic Publisher, Dordrecht, The Netherlands.
- Davidson, M. (European Space Agency, European Space Research and Technology Centre (ESA/ESTEC)) (2007). *Personal communication*.
- de Guijter, J. (1999). Spatial Sampling Schemes. In: Stein, A. et al. *Spatial Statistics for Remote Sensing*. Kluwer Academic Publisher, Dordrecht, The Netherlands.

- De Jong, S. M. and Burrough, P. A. (1995). A Fractal Approach to the Classification of Mediterranean Vegetation Types in Remotely Sensed Images. *Photogrammetric Engineering and Remote Sensing*. Vol. 61, pp. 1041-1053.
- DEFRA (2004). *Sustainable Development Indicators in Your Pocket 2004*. Defra Publications, London.
- DEFRA (2000). *Waste Strategy 2000 for England and Wales*. Available at: <http://www.defra.gov.uk/environment/waste/strategy/cm4693/index.htm> (last accessed 20th January 2005).
- Delft (2005). *Delft Object-oriented Radar Interferometric Software*. Available at: <http://enterprise.lr.tudelft.nl/doris/> (last accessed 6th April 2007).
- Dell'Acqua, F. and Gamba, P. (2003). Texture-based Characterization of Urban Environments on Satellite SAR Images. *IEEE Trans. Geoscience and Remote Sensing*. Vol. 41, pp. 153-159 .
- Delta-T Devices Ltd (1999). *Theta Probe Soil Moisture Sensor*. Delta-T Devices Ltd, Cambridge.
- Demanya, B. K. (2006). *The Role of Local Knowledge in planning and managing urban solid waste: the tale of two (2) West African Cities, Accra and Kumasi, Ghana*. (PhD thesis). University of Waterloo (CA), Waterloo.
- Dewidar, Kh. M. (2002). Landfill Detection in Hurghada, North Red Sea, Egypt, Using Thematic Mapper Images. *International Journal of Remote Sensing*. Vol. 23, No. 5, pp. 939-948.
- DLR (2007). *TerraSAR-X*. Available at: <http://wwwserv2.go.t-systems-sfr.com/tsx/documentation/Satellite.pdf> (last accessed 25th March 2007).
- DoE (Department of Environment) (1997). *Landfill Design, Construction and Operational Practice*. Waste Management Paper 26. DoE, London.
- Dong, Y., Forster, B., and Ticehurst, C. (1997). Radar Backscatter Analysis for Urban Environments. *International Journal of Remote Sensing*. Vol. 6, pp. 1351-1364.
- Dousset, B. (1997). Interpretation of ERS-SAR Images Over Urban Surfaces. In: *3rd ERS Symposium*. Paris. ESA.
- Drezet, P. M. L. and Quegan, S. (2006). Environmental Effects on the Interferometric Repeat-Pass Coherence of Forests. *IEEE Transactions On Geoscience And Remote Sensing*. Vol. 44, No. 4, pp. 825-837.

- Eastman, J. R. and Fulk, M. (1993). Long Sequence Time Series Evaluation Using Standardized Principal Components. *Photogrammetric Engineering and Remote Sensing*. Vol. 59, No. 6, pp. 991-996.
- Elachi, C. (1988). *Spaceborne Radar Remote Sensing: Applications and Techniques*. IEEE Press, New York.
- Elder, K. (2002). *The Detection and Measurement of Landfill Subsidence Using SAR* (unpublished MSc Astronautics and Space Engineering thesis). Cranfield University, Cranfield.
- Emerson, C. W., Lam, N. S. N., and Quattrochi, D. A. (1999). Multiscale Fractal Analysis of Image Texture and Pattern. *Photogrammetric Engineering and Remote Sensing*. Vol. 65, pp. 51-61.
- Environment Agency (1996). *Guidance on Good Practice for Landfill Engineering*. R&D Technical Report CWM-106/94(C). DoE, London. Available from Environment Agency, Bristol.
- Environment Agency (1999). *Methane Emissions from Different Landfill Categories*. Technical report EA/TR-P233a. DoE, London.
- Environment Agency (2005). *What's in Your Backyard*. Available at: <http://www.environment-agency.gov.uk/maps/> (last accessed 28th July 2005).
- Environment Agency (2006). *Waste Overview*. Available at: <http://www.environment-agency.gov.uk/subjects/waste/> (last accessed 20th August 2006).
- EOHelpDesk (ESA) (2005). *Personal communications in 2005*.
- EOHelpDesk (ESA) (2006). *Personal communications in 2006*.
- eoPortal (2006). *COSMO-SkyMed*. Available at: http://directory.eoportal.org/pres_COSMOSkyMedConstellationof4SARSatellites.html#foot7%29 (last accessed 18th November 2006).
- Epidemio (2006). *EO in Epidemiology*. Available at: <http://www.epidemio.info/> (last accessed 30th October 2006).
- Erb, T., Philipson, W. M., Teng, W., and Liang, T. (1981). Analysis of Landfills with Historic Airphotos. *Photogrammetric Engineering and Remote Sensing*. Vol. 47, No. 9, pp. 1363-1369.
- ESA (2004). *Annex C ERS SAR.SLC/SLC-I CCT and EXABYTE FORMAT SPECIFICATIONS*. Available at:

- <http://earth.esa.int/rootcollection/sysutil/sarslc.html> (last accessed 15th July 2004).
- ESA (2005a). *ESA Online Radar Courses*. Available at: http://earth.esa.int/applications/data_util/SARDOCS/spaceborne/Radar_Courses/ (last accessed 5th January 2005).
- ESA (2005b). *GMES Sentinel Family Definition Studies*. Available at: http://www.esa.int/esaLP/SEMZHMODU8E_LPgmes_0.html (last accessed 10th January 2006).
- ESA (2006a). *Earth Observation Market Development*. Available at: <http://www.eomd.esa.int/index.asp> (last accessed 18th August 2006).
- ESA (2006b). *Envisat*. Available at: <http://envisat.esa.int/> (last accessed 7th January 2007).
- ESA (2007a). *Principal Investigator Portal*. Available at: <http://eopi.esa.int> (last accessed 8th January 2007).
- ESA (2007b). *Display Earth remote sensing Swath Coverage for Windows*. Available at: <http://earth.esa.int/descw/> (last accessed 8th January 2007).
- ESA (2007c). *Earthnet On-Line Interactive Stand Alone*. Available at: <http://eoli.esa.int> (last accessed 8th January 2007).
- ESA (2007d). *3rd International Workshop on Science and Applications of SAR Polarimetry and Polarimetric Interferometry (22-26 January 2007)*. Available at: <http://earth.esa.int/workshops/polinsar2007/> (last accessed 8th February 2007).
- ESA (2007e). *Project for On-Board Autonomy (Proba)*. Available at: <http://earth.esa.int/probal> (last accessed 20th March 2006).
- European Commission (2006). *Global Monitoring for Environment and Security*. Available at: <http://www.gmes.info/index.php?id=home> (last accessed 18th August 2006).
- European Environment Agency (2006). *Waste Indicators*. Available at: http://themes.eea.europa.eu/IMS/IMS/ISpecs/ISpecification20041007131809/IAssessment1116426884700/view_content (last accessed 14th August 2005).
- European Union (1999). *Landfill Directive*. Available at: http://europa.eu.int/eur-lex/pri/en/oj/dat/1999/l_182/l_18219990716en00010019.pdf (last accessed 3rd February 2005).

- Evans, B. M. and Mata, L. (1984). Aerial Photographic Analysis of Hazardous Waste Disposal Sites. In: *Hazardous Wastes and Environmental Emergencies* . Hazardous Materials Control Research Institute Publication, Silver Spring, Maryland.
- GLCN (2007). *Land Cover Classification System*. Available at: <http://www.glcnlccs.org/index.php?name=Content&pa=showpage&pid=2> (last accessed 10th March 2007).
- Ferretti, A., Prati, C., and Rocca, F. (2000). Nonlinear Subsidence Rate Estimation Using Permanent Scatterers in Differential SAR Interferometry. *IEEE Transactions On Geoscience And Remote Sensing*. Vol. 38, No. 5, pp. 2201-2212.
- Ferretti, A., Prati, C., and Rocca, F. (2001). Permanent Scatterers in SAR Interferometry. *IEEE Transactions On Geoscience And Remote Sensing*. Vol. 39, No. 1, pp. 8-20.
- Ferretti, A., Prati, C., Rocca, F., and Monti Guarnieri, A. (1997). Multibaseline SAR interferometry for Automatic DEM Reconstruction. *3rd ERS Workshop*
- First Research (2005). *Waste Management Industry Profile Excerpt*. Available at: <http://www.firstresearch.com/Industry-Research/Waste-Management.html> (last accessed 8th July 2005).
- Fisher, P. (1997). The Pixel: a Snare and a Delusion . *International Journal of Remote Sensing*. Vol. 18, No. 3, pp. 679-685 .
- Fisher, P. F. and Pathirana, S. (1990). The Evaluation of Fuzzy Membership of Land Cover Classes in the Suburban Zone. *Remote Sensing of the Environmnet*. Vol. 34, pp. 121-132.
- Fitzpatrick-Lins, K. (1981). Comparison of Sampling Procedures and Data Analysis for a Land-use and Land-Cover map. *Photogrammetric Engineering and Remote Sensing*. Vol. 47, pp. 349-366.
- Fletcher, P. (Remote Sensing Applications Consultants) (2005). *Personal communication*.
- Folkard, A. M. and Cummins, D. I. (1998). Hyper-Spectral Remote Sensing of the Spread of Soil Contaminants from Landfill Sites. In: *6th International Conference on Contaminated Soil*. Edinburgh, Scotland, May 17-21, 1998, pp. 153-161. Thomas Telford, London.
- Foody, G. M. (1999). The Continuum of Classification Fuzziness in Thematic Mapping.

- Photogramm. Eng. Remote Sens.* Vol. 65, No. 4, pp. 443-451.
- Fung, A. K. (1994). *Microwave Scattering and Emission Models and Their Applications*. Artech House, Norwood, Mass.
- Fung, A. K. and Chen, K. S. (2004). An Update on the IEM Surface Backscattering Model. *IEEE Geoscience and Remote Sensing Letters*. Vol. 1, No. 2, pp. 75-77.
- Garofalo, D. and Wobber, F. (1974). Solid Waste and Remote Sensing. *Photogrammetric Engineering*. Vol. 40, No. 1, pp. 45-59.
- GetMapping (2004). *UK Aerial Maps*. Available at: <http://www2.getmapping.com/home.asp> (last accessed 28th October 2004).
- Ghiglia, D. C. and Pritt, M. D. (1998). *Two-Dimensional Phase Unwrapping*. Wiley, New York.
- Goldstein, R. (1995). Atmospheric Limitations to Repeat-Track Radar Interferometry. *Journal Geophysical Research*. Vol. 22, pp. 2517-2520.
- Goldstein, R. M. and Werner, C. L. (1998). Radar interferogram filtering for geophysical applications. *Geophysical Research Letters*. Vol. 25, No. 1, pp. 4035-4048.
- Goodman, N. R. (1963). Statistical Analysis Based on a certain Multivariate complex Gaussian Distribution (an Introduction). *Annals of Mathematical Statistics*. Vol. 34, No. 1, pp. 152-177.
- Google Earth (2007). *Google Earth*. Available at: <http://earth.google.com> (last accessed 9th April 2007).
- Gregory, R. G., Revans, A. J., and Hill M. D. (2000). *Framework to Assess the Risks to Human Health and the Environment from Landfill Gas*. Environment Agency Technical Report EA/TR-P271. DoE, London.
- Grey, W. M. F., Luckman, A. J., and Holland, D. (2003). Mapping Urban Change in the UK Using Satellite Radar Interferometry. *Remote Sensing of Environment*. Vol. 87, pp. 16-22.
- Hagberg, J. O., Ulander, L. M. H., and Askne, J. (1995). Repeat-Pass SAR Interferometry over Forested Terrain. *IEEE Trans. Geoscience and Remote Sensing*. Vol. 33, No. 2, pp. 331-340.
- Hambidge, C. (Environment Agency) (2005). *Personal communication*.

- Hanssen, R. F. (2001). *Radar Interferometry*. Kluwer Academic, Dordrecht, The Netherlands.
- Haralick, R. M., Shanmugan, K., and Dinstein, I. (1973). Texture Features for Image Classification. *IEEE Transactions on Systems, Man, and Cybernetics*. Vol. SMC-3, pp. 610-621.
- Haycock, R. (Waste Recycling Group Ltd) (2005). *Personal communication*.
- Heer, C. and Shutie, P. F. (2005). Digital Beam Forming Synthetic Aperture Radar. In: *IEEE MTT-S International Microwave Symposium Digest*. Long Beach, California, USA, June 12-7 2005 . IEEE,
- Hein, A. (2004). *Processing of SAR data. Fundamentals, Signal Processing and Interferometry*. Springer-Verlag, Heidelberg, Germany.
- Henderson, F. M. and Lewis, A. J. (Editors) (1998). *Manual of Remote Sensing. Volume 2: Principles and Applications of Imaging Radar*. 3rd ed. Wiley, New York.
- Hopper, A. J. (1996). Remote Sensing Detection of Landfill Pollutant Migration. In: *22nd Annual Conference of the Remote Sensing Society*. Durham, UK, 1996, pp. 281-289.
- Ichoku, C., Karnieli, A., Arkin, Y., Chorowicz, J., Fleury, T., and Rudant J-P. (1998). Exploring the Utility Potential of SAR Interferometric Coherence Images. *International Journal of Remote Sensing*. Vol. 19, No. 6, pp. 1147-1160.
- Indian Space Research Organisation (2005). *IRS-P6 (Resourcesat-1)*. Available at: <http://www.isro.org/pslvc5/index.html> (last accessed 10th January 2006).
- Infoterra GmbH (2006). *TerraSAR-X*. Available at: <http://www.terrasar.de/> (last accessed 7th January 2007).
- International Maritime Organization (1972). *London Convention*. Available at: <http://www.londonconvention.org/documents/lc72/LC1972.pdf> (last accessed 20th August 2006).
- Irvine, J. M., Evers, T. K., Smyre, J. L., Huff, D., King, A. L., Stahl, G., and Odenweller, J. (1997). The Detection and Mapping of Buried Waste. *International Journal of Remote Sensing*. Vol. 18, No. 7, pp. 1583-1595.
- Israel Aerospace Industries (2007). *TecSAR*. Available at: <http://www.iai.co.il/ELTA.aspx?docID=34550&FolderID=33778&lang=en&res=0&pos=0> (last accessed 25th March 2007).

- Iters (2005). *Airborne Hyperspectral Remote Sensing Systems and Solutions*. Available at: <http://www.itres.com/> (last accessed 3rd April 2005).
- James, G. (1999). *Advanced Modern Engineering Mathematics*. 2nd ed. Addison-Wesley, Harlow.
- Jago, R. A. and Curran, P. J. (1996). Estimating Canopy Chlorophyll Concentration From Field and Airborne Spectra to Infer Levels of Land Contamination. In: *23rd Annual Conference of the Remote Sensing Society*. Reading, UK, 1996, pp. 274-279.
- Jaxa (2004). *Advanced Land Observing Satellite Home Page*. Available at: <http://alos.nasda.go.jp/index-e.html> (last accessed 7th January 2007).
- Jensen, J. R. (2005). *Introductory Digital Image Processing. A Remote Sensing Perspective*. 3rd ed. Pearson Prentice Hall, Upper Saddle River, NJ, USA.
- Johannessen, L. M. and Boyer, G. (1999). *Observations of Solid Waste Landfills in Developing Countries: Africa, Asia, and Latin America*. The World Bank, Washington.
- Johnson, E., Klein, M., and Mickus, K. (1993). Assessment of the Feasibility of Utilizing Landsat for Detection and Monitoring of Landfills in a Statewide GIS. *Environmental Geology*. Vol. 22, pp. 129-140.
- Jones, H. K. (1991). *The Investigation of Vegetation Change Using Remote Sensing to Detect and Monitor Migration of Landfill Gas* (unpublished Ph.D. thesis). Aston University, Birmingham.
- Jones, H. K. and Elgy, J. (1994). Remote Sensing to Assess Landfill Gas Migration. *Waste Management and Research*. Vol. 12, pp. 327-337.
- Justice, C. O. and Townshend, J. R. G. (1981). Integrating Ground Data with Remote Sensing. In: Townshend, J. R. G. (Editor), *Terrain Analysis and Remote Sensing*. Allen & Unwin, London.
- Kampes, B., Delft University of Technology. (2005). *Delft Object-oriented Radar Interferometric Software (DORIS). User's Manual and Technical Documentation*. Available at: <http://enterprise.lr.tudelft.nl/doris/usermanual/> (last accessed 15th January 2007).
- Kampes, B. (Delft Technical University) (2006). *Personal communication*.
- Kandaswamy, U., Adjeroh, D. A., and Lee, M. C. (2005). Efficient Texture Analysis of SAR Imagery. *IEEE Transaction on Geoscience and Remote Sensing*. Vol. 43,

No. 9, pp. 2075-2083.

- Karszenbaum, H., Tiffenberg, J., Grings, F., Martinez, J. M., Kandus, P., and Pratalongo, P. (2003). A SAR time series analysis toolbox for extracting fire affected areas in wetlands. In: *Geoscience and Remote Sensing Symposium, IGARSS 2003*. Toulouse, France, July 21-25, 2003, Vol. 6, pp. 4107-4109. IEEE.
- Kennedy, J. B. and Neville, A. M. (1986). *Basic Statistical Methods for Engineering and Scientists*. 3rd ed. Harper & Row Inc., New York.
- Kirkland, J. (Waste Recycling Group Ltd) (2005). *Personal communication*.
- Kirkland, J. (Waste Recycling Group Ltd) (2006). *Personal communication*.
- Koskinen, J. T., Pulliainen, J. T., Hyypä, J. M., Engdahl, M. E., and Hallikainen, M. T. (2001). The Seasonal Behaviour of Interferometric Coherence in Boreal Forest. *IEEE Transactions On Geoscience And Remote Sensing*. Vol. 39, No. 4, pp. 820-829.
- Knight, P. A. (1997). *Backscatter Software User Guide, SAR Interaction Modelling Software*. Technical Report Ref. Y/BD/970283/BA402. GEC-Marconi Research Centre, Space Division, Avionics Laboratory.
- Kwarteng, A. Y. and Al-Enezi, A. (2004). Assessment of Kuwait's Al-Qurain Landfill Using Remotely Sensed Data. *Journal of Environmental Science and Health. Part A: Toxic/Hazardous Substances and Environmental Engineering*. Vol. A39, No. 2, pp. 351-364.
- Lam, N. S. N. (1990). Description and Measurement of Landsat TM Images Using Fractals. *Photogrammetric Engineering and Remote Sensing*. Vol. 56, pp. 187-195.
- Lam, N. S. N., Qiu, H. L., Quattrochi, D. A., and Emerson, C. W. (2002). An Evaluation of Fractal Methods for Characterising Image Complexity. *Cartography and Geographic Information Science*. Vol. 29, pp. 25-35.
- Landmap (2005). *The Landmap Project*. Available at: <http://www.landmap.ac.uk/index.html> (last accessed 2005).
- Lee, W. K. (2001). Analytical Investigation of Urban SAR Features Having a Group of Corner Reflectors. In: *Geoscience and Remote Sensing Symposium, IGARSS 2001*. Sydney, July 9-13, 2001, Vol. 3, pp. 1282-1284. IEEE, New York.
- Lee, J.-S., Cloude, S., Papathanassiou, K. P., Grunes, M. R., and Woodhouse, I. H.

- (2003). Speckle Filtering and Coherence Estimation of Polarimetric SAR Interferometry Data for Forest Applications. *IEEE Transactions on Geoscience and Remote Sensing*. Vol. 41, No. 10, pp. 2254-2263.
- Lee, J.-S., Grunes, R., and de Grandi G. (1999). Polarimetric SAR Speckle Filtering and its Implication for Classification. *IEEE Trans. Geoscience and Remote Sensing*. Vol. 37, No. 5, pp. 2363-2373.
- Lee, J. S., Hoppel, K. W., Mango, S. A., and Miller, A. R. (1994). Intensity and Phase Statistics of Multilook Polarimetric and Interferometric SAR Imagery. *IEEE Trans. Geoscience and Remote Sensing*. Vol. 32, No. 5, pp. 1017-1028.
- Lefort, A., Grippa, M., Walker, N., Stewart, L. J., and Woodhouse, I. H. (2004). Change Detection Across the Nasca Pampa Using Spaceborne SAR Interferometry. *International Journal of Remote Sensing*. Vol. 25, No. 10, pp. 1799-1803.
- Li, E. S. (2003). Physical Optics Model for the Backscatter Response of Road-Surface Faults and Roadside Pebbles at Millimeter-Wave Frequencies. *IEEE Transactions on Antenna and Propagation*. Vol. 51, No. 10, pp. 2862-2868.
- Long, M. W. (2001). *Radar Reflectivity of Land and Sea*. 3rd ed. Artech House, Boston.
- Long, T. (1999). *Surveillance of Greenhouse Gas Releases*. Project E1-058. Environment Agency, Bristol.
- Lopes, A., Touzi, R., and Nezry, E. (1990). Adaptive Speckle Filters and Scene Heterogeneity. *IEEE Trans. Geoscience and Remote Sensing*. Vol. 28, No. 6, pp. 992-1000.
- Luckman, A., Frery, A. C., Yanasse, C. C. F., and Groom, G. B. (1997). Texture in airborne SAR imagery of tropical forest and its relationship to forest regeneration stage . *International Journal of Remote Sensing* . Vol. 18, No. 6, pp. 1333-1349 .
- Lyon, J. (1982). Use of Aerial Photography and Remote Sensing in the Management of Hazardous Wastes. In: Sweeney, T. et al. (Editors), *Hazardous Waste Management for the 80's*. Ann Arbor Science, Ann Arbor, MI.
- Lyon, J. (1987). Use of Maps, Aerial Photographs, and Other Remote Sensor Data for Practical Evaluation of Hazardous-Waste Sites. *Photogrammetric Engineering and Remote Sensing*. Vol. 53, No. 5, pp. 515-519.
- MacDonald, Dettwiler and Associates Ltd. (2007). *Radarsat-2*. Available at: <http://www.radarsat2.info/> (last accessed 25th March 2007).

- Mallat, S. G. (1989). A Theory for Multi-resolution Signal Decomposition: the Wavelet Representation. *IEEE Transactions on Pattern Analysis and Machine Intelligence*. Vol. 11, pp. 674-693.
- Mandelbrot, B. B. (1982). *The Fractal Geometry of Nature*. W. H. Freeman and Company, New York.
- Mandelbrot, B. B. (1977). *Fractals: Form, Chance and Dimension*. W. H. Freeman and Company, San Francisco.
- Marsh, S. E., Walsh, J. L., Lee, C. T., and Graham, L. A. (1991). Multitemporal Analysis of Hazardous-Waste Sites Through the Use of a New Bi-Spectral Video Remote-Sensing System and Standard Color-IR Photography. *Photogrammetric Engineering and Remote Sensing*. Vol. 57, No. 9, pp. 1221-1226.
- Massonnet, D. (2001). The Interferometric Cartwheel: a Constellation of Passive Satellites to Produce Radar Images to be Coherently Combined. *International Journal of Remote Sensing*. Vol. 22, No. 12, pp. 2413-2430.
- Massonnet, D., Rossi, M., Carmona, C., Adagna, F., Peltzer, F., Feigl, K., and Rabaute, T. (1993). The Displacement Field of the Landers Earthquake Mapped by Radar Interferometry. *Nature*. Vol. 364, No. 8, pp. 138.
- Mattia, F., Davidson, M. W. J., Le Toan, T., D'Haese, C. M. F., Verhoest, N. E. C., Gatti, A. M., and Borgeaud, M. (2003). A Comparison Between Soil Roughness Statistics Used in Surface Scattering Models Derived From Mechanical and Laser Profilers. *IEEE Trans. Geoscience and Remote Sensing*. Vol. 41, No. 7, pp. 1659-1671.
- Mattia, F., Le Toan, T., Souyris, J.-C., De Carolis, G., Floury, N., Posa, F., and Pasquariello, G. (1997). The Effect of Surface Roughness on Multifrequency Polarimetric SAR Data. *IEEE Transactions On Geoscience And Remote Sensing*. Vol. 35, No. 4, pp. 954-966.
- McCoy, R. (2005). *Field Methods in Remote Sensing*. The Guilford Press, New York.
- McDougall, F., White, P., Franke, M., and Hindle, P. (2001). *Integrates Solid Waste Management: A Life Cycle Inventory*. Blackwell Science, Oxford.
- Montgomery, D. C. and Runger, G. C. (2003). *Applied Statistics and Probability for Engineers*. 3rd ed. John Wiley and Sons, New York.
- Monti Guarnieri, A. and Prati, C. (1997). SAR Interferometry: A "Quick and Dirty" Coherence Estimator for Data Browsing. *IEEE Trans. Geoscience and Remote*

- Sensing*. Vol. 35, No. 3, pp. 660-669.
- Moody, R. O., Puckett, D. A., and Rodwell, W. R. (1991). *Experimental and Theoretical Studies of Gas Migration from Landfill Sites*. Environment Agency Report EA/CWM-029/91. DoE, London.
- Moody, R. O., Rodwell, W. R., and Ghabaee, K. (1992). *Numerical Simulation of the Migration of Gas Produced in Landfills*. Environment Agency Report EA/CWM-030/91. DoE, London.
- Nair, C., Environmental Resources Management. (1993). *Solid Waste Management in Emerging Industrialised Countries*. Available at: <http://www.eco-web.com/cgi-local/sfc?a=/editorial/index.html&b=/editorial/01060.html> (last accessed 8th November 2004).
- NASA (2006). *Moderate-resolution Imaging Spectroradiometer*. Available at: <http://terra.nasa.gov/About/MODIS/index.php> (last accessed 10th January 2006).
- Neeff, T., Dutra, L. V., Dos Santos, J. R., Freitas, C. C., and Araujo, L. S. (2005). Power Spectrum Analysis of SAR Data for Spatial Forest Characterization in Amazonia. *International Journal of Remote Sensing*. Vol. 26, No. 13, pp. 2851-2864.
- Nesti, G., Fortuny, J., and Sieber, A. J. (1996). Comparison of Backscatter Signal Statistics as Derived from Indoor Scatterometric and SAR Experiments. *IEEE Transactions On Geoscience And Remote Sensing*. Vol. 34, No. 5, pp. 1074-1083.
- Northern Ireland Audit Office (2005). *Northern Ireland's Waste Management Strategy*. Available at: <http://www.ehsni.gov.uk/pubs/publications/NIWMS.pdf> (last accessed 7th July 2005).
- Ogawa, H. (1996). Sustainable Solid Waste Management in Developing Countries. In: *7th International Solid Waste Association International Congress and Exhibition*. Yokohama, October 27 - November 1, 1996, Vol. Parallel Session 7, "International Perspective". International Solid Waste Association, Denmark.
- Oh, Y. and Kay, Y. C. (1998). Condition for Precise Measurement of Soil Surface Roughness. *IEEE Trans. Geoscience and Remote Sensing*. Vol. 36, No. 2, pp. 691-695.
- Oh, Y., Sarabandi, K., and Ulaby, F. T. (1992). An Empirical Model and an Inversion Technique for Radar Scattering from Bare Soil Surfaces. *IEEE Transactions on Geoscience and Remote Sensing*. Vol. 30, No. 2, pp. 370-381.

- Okhimamhe, A. A. (2003). ERS SAR Interferometry for Land Cover Mapping in a Savanna Area. *International Journal of Remote Sensing*. Vol. 24, No. 18, pp. 3583-3594.
- Oliver, C. J. (2000). Rain Forest Classification Based on SAR Texture. *IEEE Trans. Geoscience and Remote Sensing*. Vol. 38, No. 2, pp. 1095-1104 .
- Oliver, C. and Quegan, S. (1998). *Understanding Synthetic Aperture Radar Images*. Artech House, Norwood, MA, USA.
- Opoku-Duah, S. (Durham University) (2005). *Personal communication*.
- Ottavianelli, G. (Cranfield University) (2004). *SAR and Image Processing Techniques for Change Detection of Human-Made Structures*. (unpublished PhD Progress Report).
- Ottavianelli, G., Hobbs, S., Smith, R., and Bruno, D. (2005). Assessment of SAR data and Interferometric Products for Solid Waste Landfill Management. In: *RSPSoc Annual Conference 2005 - Measuring, Mapping and Managing a Hazardous World*. Portsmouth, September 6-9, 2005. RSPSoc, Nottingham.
- Ottavianelli, G., Hobbs, S., Smith, R., Morrison, K., and Bruno, D. (2006). SAR Interferometric Products and Hyperspectral Data for Monitoring Solid Waste Landfill Operations. In: *Fourth ESA CHRIS Proba workshop*. Frascati, Italy, 19 - 21 September 2006. European Space Agency, Paris.
- Paris, I. (2005). Are Sanitary Landfills Really Necessary? In: *Urban Forum 2005. Cities: Grounding the Development Agenda*. World Bank, Washington, DC, March 9-10, 2005. World Bank.
- Parsons, P. J. (2000). *Effectiveness of Liners in Inhibiting the Migration of Landfill Gas*. Environment Agency Technical Report EA/TR-P256. DoE, London.
- Peitgen, H. O. and Saupe, D. (1988). *The Science of Fractal Images*. Springer Verlag, New York.
- Pentland, A. P. (1984). Fractal-based Descriptions of Natural Scenes. *IEEE Transactions on Pattern Analysis and Machine Intelligence*. Vol. 6, pp. 661-674.
- Perakis, K., Malliaros, D., Soulakellis, N., Silleos, G., and Kungolos, A. (2004). Remote Sensing and Statistics for the Investigation of Uncontrolled Landfill Sites: a Case Study in Lesvos Island, Greece. *Fresenius Environmental Bulletin*. Vol. 13, No. 5, pp. 378-384 .
- Philipson, W. R., Barnaba, E. M., Ingram, A., and Williams, V. L. (1988). Land-Cover

- Monitoring with SPOT for Landfill Investigations. *Photogrammetric Engineering and Remote Sensing*. Vol. 54, No. 2, pp. 223-228.
- Pottier, E. (2005). SAR Polarimetry and Applications. In: *POLINSAR2005 Workshop* . Opening Session, Frascati, Italy, January 17-21, 2005. ESA, Paris.
- Preiss, M., Gray, D. A., and Stacy, N. J. S. (2006). Detecting Scene Changes Using Synthetic Aperture Radar Interferometry. *IEEE Transactions On Geoscience And Remote Sensing*. Vol. 44, No. 8, pp. 2041-2054.
- Rees, W. G. (2003). *Physical Principles of Remote Sensing*. 2nd ed. Cambridge University Press, Cambridge.
- Rees, W. G. and Steel, A. M. (2001). Simplified Radar Mapping Equations for Terrain Correction of Space-borne SAR Images. *International Journal of Remote Sensing*. Vol. 22, No. 18, pp. 3643-3649.
- Rignot, E. J. M. and van Zyl, J. (1993). Change Detection Techniques for ERS-1 SAR Data. *IEEE Trans. Geoscience and Remote Sensing*. Vol. 31, No. 4, pp. 896-906.
- Rugge, C. D. and Ahlert, R. C. (1992). Ground and Aerial Survey of a Peninsular Landfill. *Water Research* . Vol. 26, No. 4, pp. 519-526.
- Sabins, F. J. (1996). *Remote Sensing: Principles and Interpretation*. 3rd ed. W.H. Freeman and Company, New York.
- Sandwell, D. T. (1987). Biharmonic Spline Interpolation of GEOS-3 and SEASAT Altimeter Data. *Geophysical Research Letters*. Vol. 2, pp. 139-142.
- Sansosti, E., Lanari, R., Fornaro, G., Franceschetti, G., Tesauro, M., Puglisi, G., and Coltelli, M. (1999). Digital Elevation Model Generation Using Ascending and Descending ERS-1/ERS-2 Tandem Data. *International Journal of Remote Sensing*. Vol. 20, No. 8, pp. 1527-1547.
- Sarabandi, K. and Oh, Y. Effect of Antenna Footprint on the Statistics of Radar Backscattering from Random Surfaces. In: *Proc. International Conference Geoscience Remote Sensing Symposium*. Florence, Italy, July 10-14, 1995, pp. 927-929. IEEE, Los Alamitos, CA.
- Schowengerdt, R. A. (1997). *Remote Sensing. Models and Methods for Image Processing*. 2nd ed. Elsevier, San Diego, USA.
- SDLA (2007). *Website of Sanitation District of the Los Angeles County*. Available at: <http://www.lacsd.org/default.asp> (last accessed 25th October 2006).

- Seynat, C. (2000). *Quantification of the Effect of Wind Driven Wheat Motion on SAR Interferometric Coherence* (Ph.D. thesis). Cranfield University, Cranfield.
- Skolnik, M. (2001). *Introduction to Radar Systems*. 3rd ed. McGraw-Hill, Singapore.
- Smith, R. (Cranfield University, School of Applied Sciences, Centre for Resource Management and Efficiency) (2006). *Personal communication*.
- Smith, R. (Cranfield University, School of Applied Sciences, Centre for Resource Management and Efficiency) (2005). *Personal communication*.
- Smith Korfmacher, K. (1997). Solid Waste Collection Systems in Developing Urban Areas of South Africa: An Overview and Case Study. *Waste Management & Research*. Vol. 15, pp. 477-494.
- Soumekh, M. (1999). *Synthetic Aperture Radar Signal Processing with Matlab Algorithms*. Wiley, Chichester.
- Stein, A., van der Meer, F., and Gorte, B. (1999). *Spatial Statistics for Remote Sensing*. Kluwer Academic Publisher, Dordrecht, The Netherlands.
- Stohr, C., Darmody, R. G., Frank, T. D., Elhance, A. P., Lunetta, R., Worthy, D., and O'Connor-Shoresman, K. (1994). Classification of Depressions in Landfill Covers Using Uncalibrated Thermal-Infrared Imagery. *Photogrammetric Engineering and Remote Sensing*. Vol. 60, No. 8, pp. 1019-1028.
- Stohr, C., Su, W. J., DuMontelle, P. B., and Griffin, R. A. (1987). Remote Sensing Investigations at a Hazardous-Waste Landfill. *Photogrammetric Engineering and Remote Sensing*. Vol. 53, No. 11, pp. 1555-1563.
- Sun, W., Xu, G., Gong, P., and Liang, S. (2006). Fractal Analysis of Remotely Sensed Images: a Review of Methods and Applications. *International Journal of Remote Sensing*. Vol. 27, No. 22, pp. 4963-4990.
- Tammenagi, H. (1999). *The Waste Crisis. Landfills, Incinerators, and the Search for a Sustainable Future*. Oxford University Press, Oxford.
- Tansey, K. J., Luckman, A. J., Skineer, L., Balzter, H., Strozzi, T., and Wagner, W. (2004). Classification of Forest Volume Resources Using ERS tandem Coherence and JERS Backscatter Data. *International Journal of Remote Sensing*. Vol. 25, No. 4, pp. 751-768.
- Terrafirma (2007). *Pan-European Ground Motion Hazard Information Service*. Available at: <http://www.terrafirma.eu.com/> (last accessed 20th January 2007).

- Terunuma, T., Nishida, K., Amada, T., Mizuyama, T., Sato, I., and Urai, M. (2005). Detection of Traces of Pyroclastic Flows and Lahars with Satellite Synthetic Aperture Radars. *International Journal of Remote Sensing*. Vol. 26, No. 9, pp. 1927-1942.
- Titus, S. (1984). Exemplary Projects of Environmental Assessment from Analysis of Remotely Sensed Imagery. Survey and Analysis of Present or Potential Environmental Impact Sites in Woburn, Massachusetts. In: *48th Annual Meeting of the American Society of Photogrammetry*. Denver, 1984, pp. 538-549. American Society of Photogrammetry, Falls Church.
- Toft, P. (1996). *The Radon Transform: Theory and Implementation* (unpublished PhD thesis). Technical University of Denmark, Lyngby.
- Tough, R. J. A., Blacknell, D., and Quegan, S. (1995). A Statistical Description of Polarimetric and Interferometric Synthetic Aperture Radar. *Proceedings of the Royal Society London*. Vol. 34, pp. 519-531.
- Touzi, R., Goze, S., Le Toan, T., Lopes, A., and Mougin E. (1992). Polarimetric discriminators for SAR images. *IEEE Trans. Geoscience and Remote Sensing*. Vol. 34, No. 5, pp. 973-980.
- Touzi, R. and Lopes, A. (1994). The Principle of Speckle Filtering in Polarimetric SAR Images. *IEEE Trans. Geoscience and Remote Sensing*. Vol. 32, No. 5, pp. 1110-1114.
- Touzi, R. and Lopes, A. (1996). Statistics of the Stokes Parameters and of the Complex Coherence Parameters in One-Look and Multilook Speckle Fields. *IEEE Transactions on Geoscience and Remote Sensing*. Vol. 34, No. 2, pp. 519-531.
- Touzi, R., Lopes, A., Bruniquel, J., and Vachon, P. W. (1999). Coherence Estimation for SAR Imagery. *IEEE Transactions on Geoscience and Remote Sensing*. Vol. 37, No. 1, pp. 135-149.
- Tucker, R. (Waste Recycling Group Ltd) (2005). *Personal communication*.
- Turcotte, D. L. (1997). *Fractals and Chaos in Geology and Geophysics*. Cambridge University Press, Cambridge.
- UK Legislation (2002). *The Landfill (England and Wales) Regulations 2002*. Available at: <http://www.legislation.hmso.gov.uk/si/si2002/20021559.htm> (last accessed 15th November 2004).
- UK Legislation (2000). *The Pollution Prevention and Control (England and Wales) Regulations 2000*. Available at:

- <http://www.legislation.hmso.gov.uk/si/si2000/20001973.htm> (last accessed 15th November 2004).
- Ulaby, F. T. and Siquiera, P. (1995). *Polarimetric SAR Soil Moisture Inversion Algorithm*. Tech. Memorandum 95-12. University of Michigan, University of Michigan.
- Ulaby, F. T. and Elachi, C. (1990). *Radar Polarimetry for Geoscience Applications*. Artech House, Norwood, MA, USA.
- Ulaby, F. T., Moore, R. K., and Fung, A. K. (1982). *Microwave Remote Sensing: Active and Passive*. Vol. II - Radar Remote Sensing and Surface Scattering and Emission Theory. Artech House, Norwood, MA, USA.
- United Nations (1989). *Basel Convention*. Available at: <http://www.basel.int/text/con-e-rev.pdf> (last accessed 20th August 2006).
- United Nations (1992). *Agenda 21. Chapter 21: Environmentally Sound Management of Solid Wastes and Sewage-Related Issues*. United Nations, Washington.
- United Nations Environment Programme (2001). *Stockholm Convention on Persistent Organic Pollutants*. Available at: http://www.pops.int/documents/convtext/convtext_en.pdf (last accessed 20th August 2006).
- United Nations Environment Programme (2004). *Rotterdam Convention*. Available at: <http://www.pic.int/en/ConventionText/ONU-GB.pdf> (last accessed 20th August 2006).
- USDA (2007). *Natural Resources Conservation Service. Technical References. Soil Properties and Qualities*. Available at: <http://soils.usda.gov/technical/handbook/contents/part618p5.html> (last accessed 30th January 2007).
- US EPA (2003). *Municipal Solid Waste Generation, Recycling, and Disposal in the United States: Facts and Figures for 2003*. Available at: <http://www.epa.gov/epaoswer/non-hw/muncpl/pubs/msw05rpt.pdf> (last accessed 7th July 2005).
- USGS (2005). *Digital Spectral Library*. Available at: <http://speclab.cr.usgs.gov/spectral-lib.html> (last accessed 10th April 2005).
- Vincent, F., Raucoules, D., Degroevé, T., Edwards, G., and Abolfazl Mostafavi, M. (2005). Detection of River/Sea Ice Deformation using Satellite Interferometry. *International Journal of Remote Sensing*. Vol. 25, No. 18, pp. 3555-3571.

- Vincent, R. K. (1994). Remote Sensing for Solid Waste Landfills and Hazardous Waste Sites. *Photogrammetric Engineering and Remote Sensing*. Vol. 60, No. 8, pp. 979-982.
- Waltz, E. (2001). The Principles and Practice of Image and Spatial Data Fusion. In: Hall, D. L. and Llinas, J. (Editors), *Handbook on Multisensor Data Fusion*. CRC Press, Boca Raton, FL.
- Wang, C. T., Chen, C. T., and Kuo, J. M. (2001). A Study of Target Identification from Multi-temporal SAR Images. In: *22nd Asian Conference of Remote Sensing*. Singapore, November 5-9, 2001. Centre for Remote Imaging, Sensing and Processing, National University of Singapore.
- Warner, W. S. (1994). Evaluating a Low-Cost, Non-Metric Aerial Mapping System for Waste Site Investigators. *Photogrammetric Engineering and Remote Sensing*. Vol. 60, No. 8, pp. 983-988.
- Wegmuller, U., Strozzi, T., Farr, T., and Werner, C. L. (2000). Arid Land Surface Characterization with Repeat-Pass SAR Interferometry. *IEEE Transactions on Geoscience and Remote Sensing*. Vol. 38, No. 2-1, pp. 776-781.
- Werner, C., Strozzi, T., Wegmuller, U., and Wiesmann, A. (2002). SAR Geocoding and Multi-Sensor Image Registration. In: *Geoscience and Remote Sensing Symposium, IGARSS 2002*. Toronto, June 24-28, 2002, Vol. 2, pp. 902-904. IEEE.
- Wertz, J. R. and Larson, W. J. (editors) (1999). *Space Mission Analysis and Design*. 3rd ed. Microcosm Press, El Segundo, USA.
- Weydahl, D. J. (2001). Analysis of ERS SAR Coherence Images Acquired over Vegetated Areas and Urban Features. *International Journal of Remote Sensing*. Vol. 22, No. 14, pp. 2811-2830.
- Woodcock, C. E. and Strahler, A. H. (1987). The Factor of Scale in Remote Sensing. *Remote Sensing of Environment*. Vol. 21, pp. 311-332.
- Woodcock, C. E., Strahler, A. H., and Jupp, D. L. B. (1988a). The Use of Variograms in Remote Sensing: I. Scene Models and Simulated Images. *Remote Sensing of Environment*. Vol. 25, No. 3, pp. 323-348.
- Woodcock, C. E., Strahler, A. H., and Jupp, D. L. B. (1988b). The Use of Variograms in Remote Sensing: II. Real Digital Images. *Remote Sensing of Environment*. Vol. 25, No. 3, pp. 349-379.
- Yhdego, M. (1995). Urban Solid Waste Management in Tanzania. Issues, Concepts and

- Challenges. *Resources, Conservation and Recycling*. Vol. 14, pp. 1-10.
- Zadeh, L. (1965). Fuzzy Sets. *Information and Control*. Vol. 8, pp. 338-353.
- Zebker, H. A. and Chen, K. (2005). Accurate Estimation of Correlation in InSAR Observations. *IEEE Geoscience and Remote Sensing Letters*. Vol. 2, No. 2, pp. 124-127.
- Zebker, H. A. and Goldstein, R. M. (1986). Topographic Mapping From Interferometric Synthetic Aperture Radar Observations. *Journal of Geophysical Research*. Vol. 91, No. B5, pp. 4993-4999.
- Zebker, H. A., Rosen, P. A., Goldstein, R. M., Gabriel, A., and Werner, C. L. (1994). On the Derivation of Coseismic Displacements Fields Using Differential Radar Interferometry: The Landers Earthquake. *Journal of Geophysical Research*. Vol. 99, No. B10, pp. 19617-19634.
- Zebker, H. A. and Villasenor, J. (1992). Decorrelation in Interferometric Radar Echoes. *IEEE Transactions on Geoscience and Remote Sensing*. Vol. 30, No. 5, pp. 950-959.
- Zhang, J. and Foody, G. M. (1998). A Fuzzy Classification of Sub-Urban Land Cover from Remotely Sensed Imagery. *International Journal of Remote Sensing*. Vol. 19, No. 14, pp. 2721-2738.


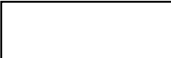

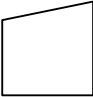

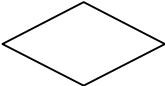
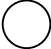
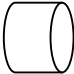
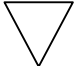
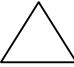


Appendix A - Matlab and IDL Routines

This section presents the Matlab and IDL routines developed by the author during the research. Due to constraints on the report length, the full script is presented only for two routines (i.e. A.4 SARcrop.pro and A.7 coherence_correction.m). These two examples show the software has been extensively commented and explicitly validated as explained in Section 4.2.

List of Matlab and IDL routines:

- A.1 soil_profile.m
- A.2 PowerSpectrum.m and rotagv.m
- A.3 SAR_2or4B_read.pro
- A.4 SARcrop.pro
- A.5 SARmodify.pro
- A.6 terrain_correction.m
- A.7 coherence_correction.m
- A.8 coherence_sd.m
- A.9 GBSAR_min_RCS.m
- A.10 GBSAR_read.pro
- A.11 GBSAR_proportional.pro
- A.12 GBSAR_sigma0.pro
- A.13 land_use_classification.m

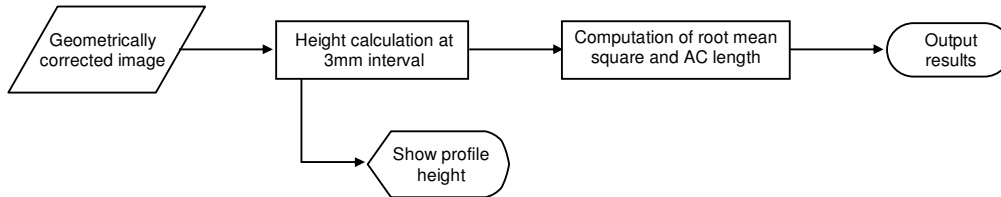
Flowcharts are used when necessary to clarify the routine structure. An explanation of the shapes used in the flowcharts follows in the next page.

	Starting or terminating process
	Process (e.g entire procedure or function, or single operation)
	Automatic input/output. Data
	Manual input
	Use of document
	Decision
	Connector
	Direct access memory
	Data Fusion
	Data extraction
	Graphic visualisation
	Preparation

A.1 soil_profile.m

This Matlab function is used to calculate the soil profile height from the corrected picture and compute the root mean square height and the profile AC length.

FUNCTION STRUCTURE:



SCRIPT:

```

function elements = soil_profile(profile)

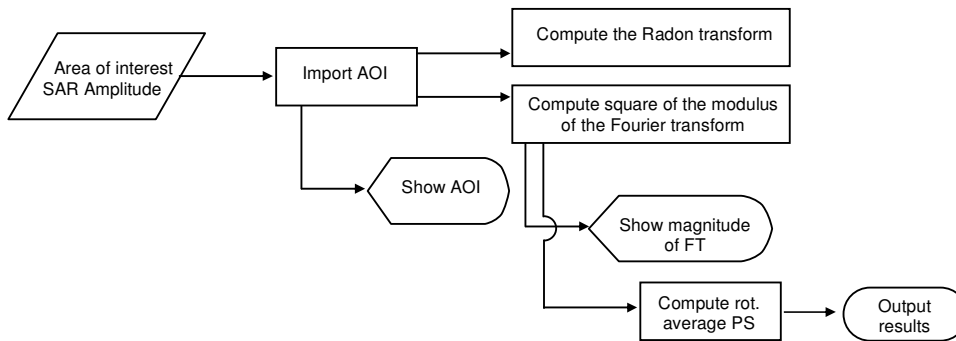
% ;+
% ; NAME:
% ;     soil_profile
% ;
% ; PURPOSE:
% ;     The purpose of this program is to compute the height of a soil
% ;     profile. The imported image has to be ready for processing.
% ;
% ;
% ; INPUT PARAMETERS:
% ;     profile      Already processed file of the soil profile.
% ;
% ; OUTPUTS:
% ;     A vector with the height values.
% ;
% ; CALLING SEQUENCE EXAMPLE:
% ;     elements = soil_profile('profile_01_01_ave')
% ;

```

A.2 PowerSpectrum.m and rotavg.m

PowerSpectrum.m and rotavg.m are two Matlab routines used to calculate the power spectrum and its rotational average. It also computes the Radon transform of the selected image.

FUNCTION STRUCTURE:



SCRIPT:

```

% ;+
% ; NAME:
% ;     PowerSpectrum
% ;
% ; PURPOSE:
% ;     The purpose of this program is to compute a Radon transform of an
% ;     image and then the rotationally averaged PowerSpectrum.
% ;     The image must be squared and with an even number of pixels per
% ;     side.
% ;
% ; INPUT PARAMETERS:
% ;     picture_name      The picture file name.
% ;     This routine calls the 'rotavg.m' routine.
% ;
% ; OUTPUTS:
% ;     The new image is saved with the suffix:
% ;     " _cohcorrL(multilooknumber)"
% ;
% ; CALLING SEQUENCE EXAMPLE:
% ;     Modify manually the name of the image to be imported directly in
% ;     the script, then highlight the calls you would like to run.
% ;     Right click and then select 'Evaluate Selection'

```

A.3 SAR_2or4B_read.pro

This IDL routine reads ERS SLC data files.

SCRIPT:

```

; PROGRAM IN BRIEF
;
; - Opens the selected file
; - Creates a jpg image for a quick look if required
; - Show immediately the image in IDL
;
; PROGRAM DESCRIPTION
;
; The programme runs interactively and requests inputs from the user
; to be specified on the IDL terminal.
;
; The number of rows and columns of the file must be known.
;
; As you can see in the program, if required the byte order is
; swapped for use on a SUN
; rather than PC or Unix. The image orientation is changed in order to
; view it in its natural (map-like) display.
;
; The program supports both 2 bytes (2B) and 4 bytes (4B) per value.
; i.e. one pixel defined by 2B for the real
; and 2B for the imaginary part or defined by 4B for the real
; and 4B for the imaginary part
;
;
; EXAMPLE IMAGE - STRUCTURE of 1 ROW
;
; Pixel no.      : | 1 | 2 | 3 | 4 | 5 | ...
; Im. Struct.    : | Re Im | Re Im | Re Im | Re Im | Re Im | ...
;
; 2-Byte         : | 2B 2B | 2B 2B | 2B 2B | 2B 2B | 2B 2B | ...
;
; 4-Byte (Doris) : | 4B 4B | 4B 4B | 4B 4B | 4B 4B | 4B 4B | ...
;
;
; It is important to notice that even if the number of lines (rows)
; is not exactly divisible by 5 (i.e. for the azimuth averaging),
; the image immediately showed by IDL and the IPG image might
; have 1 to 4 lines missing at the bottom.
;
;
; PROGRAM HISTORY
;
; Developed by G. Ottavianelli (June 2004)
; g.ottavianelli@tiscali.it
;
; V0.2 :
; - (August 2004) the 4B reading procedure has been
;   modified as it was not working properly
;
; COMPILE AND RUN from IDL "Run" menu

```

A.4 SARcrop.pro

This IDL routine crops an area of interest from ERS SLC data files. The full programming script is provided below.

SCRIPT:

```
; PROGRAM IN BRIEF
;
; - Opens the selected ERS1/2 file (Big Endian)
; - Asks user what part to crop
; - Crops the file
; - Creates a 2B real 2B imag cropped file (Small Endian)
; - Creates a 4B real 4B imag cropped file (Small Endian)
; - Creates a TXT file with the cropping parameters used,
;   and the required text to emulate the Doris cropping routine.
; - Creates a jpg image for a quick look
; - Show immediately the image in IDL
;
;
;#####
;#####          CHECK          #####
;#####
; In the script you will find sections headed with the above 3 'check' lines.
; These sections are used to make cross validations on the data while the
; program is running. If you want you can delete these section or simply
; make them comments by adding semicolons at the beginning of the line.
;
;
;
; PROGRAM DESCRIPTION
;
; This program crops ERS1/2 SLC SAR files and quickly views them in order to
; make sure the cropping has been carried out correctly.
;
; The programme runs interactively and requests inputs from the user to be
; specified on the IDL terminal.
;
; This routine has been developed for the ERS1/2 SLC SAR original data files
; currently stored in /rh/u09b/SharedDrives/SARdata/
; Make sure you copy the file of interest in your own folder before
; running this program.
;
; The number of rows and columns of these files must be known.
; This information can be found in the Leader file relative to each SLC file,
; located in the same folder.
;
; The SLC files contain a 12 byte header at the beginning of every row.
; Each pixel is pixel is defined by 2 bytes for its Real in-phase value, and
; 2 bytes for its Imaginary quadrature value.
; For instance, the SAR SLC file dated 06 June 1995 has 4900 columns and
; 26320 lines (or rows). The total size of the file is equal to:
; (12 * 26320) + (4 * 4900 * 26320) = 516187840 bytes
;
;
;
```

```
;
; IMAGE - STRUCTURE of 1 ROW
;
; Pixel no.      : | HEADER |  1  |  2  |  3  |  4  |  5  | ...
; Image structure : |        | Re Im | Re Im | Re Im | Re Im | Re Im | ...
; Byte content   : | 12B   | 2B 2B | 2B 2B | 2B 2B | 2B 2B | 2B 2B | ...
;
;
; When providing the coordinates of the area to be cropped, do NOT consider
; the 12 byte header.
;
; As you can see in the program, to visualise the image the byte order
; is swapped for use on PC rather than SUN Unix, and the image orientation is
; changed in order to view it in its natural (map-like) display.
;
; The cropped images is saved in Small Endians for compatibility with Linux
; and Windows systems.
;
; It is important to notice that even if the number of lines (rows) is not
; exactly divisible by 5 (i.e. for the azimuth averaging), the cropping
; process is not affected.
; The image immediately showed by IDL and the IPG image might have 1 to 4
; lines missing at the bottom. Even so, the cropped image is fine and
; fully compatible with Doris.
;
;
;
;
; PROGRAM HISTORY
;
; Developed by G. Ottavianelli (May 2005)
; g.ottavianelli@tiscali.it
;
; V0.1 :
;   - Final reading procedure based on S.E. Hobbs routine, 20 Jun 2002
;
; V0.2 : (May 2005)
;   - Creates a cropped file compatible with DORIS
;     (i.e. 4B real and 4B imaginary)
;   - Creates a JPEG file of the cropped image;
;
; V0.3 : (June 2005)
;   - Odd and Even case of cropping procedure modified.
;   - Added a number of checks on the Doris compatible (4B) image values
;   - Added comments
;   - Major bug found: extra line was being read before starting
;     cropping procedure
;
; V0.4 : (June 2005)
;   - Cropped images are stored in Small Endians!
;   - Outputs a txt file listing the cropping parameters used.
;     This is useful for DORIS.
;
;
; COMPILER AND RUN from IDL "Run" menu
```

```

;-----
;-----
;-----
; Initialise the variable image_exist equal to 0 as this is used later to
; check if the file specified by the user exists.
image_exist = 0

; Start a REPEAT...UNTIL loop that is terminated if the specified file exist
REPEAT BEGIN

    ; Define image_location as a string before reading:
    image_location = ''

    ; Write on the main IDL screen some explanations:
    PRINT, ''
    PRINT, 'Please, specify the path of the directory where the image is
located (e.g. C:\Data\ERS12\1995_06_06\).'
    PRINT, 'NOTE: If you want to use the default folder (i.e. C:\crop\)' leave
the field empty and press Return.'

    PRINT, ''

    ; Read input from the terminal:
    READ, image_location, PROMPT='Directory path (empty if default is OK): '

    ; Remove leading and trailing white spaces
    image_location = STRTRIM(image_location,2)

    ; If the image_location is an empty string then its given the default
value
    IF image_location EQ '' THEN BEGIN
        ;image_location = 'C:\crop\'
        image_location = 'Y:\linux\COHERENCE\19950625\Outdata\'
        ;image_location = 'F:\- PhD WORK -\Data\COHERENCE\OutData_19950606\'
    ENDIF

    ; Check that the last character of the path is a backward slash (\)
    Result = STRMATCH(image_location, '*\ ', /FOLD_CASE)
    IF Result NE 1 THEN BEGIN
        image_location = image_location + '\'
    ENDIF

    ; Print the current path
    PRINT, '- Selected folder -'
    PRINT, image_location

    ; Define image_name as a string before reading:
    image_name = ''

    ; Write on the main IDL screen some explanations:
    PRINT, ''
    PRINT, 'Please, specify the name of the SAR image file to be cropped (e.g.
950606 ).'
    PRINT, 'NOTE: The file extension is not required. This is assumed to be
equal to DAT.'
    PRINT, ''

    ; Read input from the terminal:
    READ, image_name, PROMPT='File name (without extension):'

```

```

; Remove leading and trailing white spaces
image_name = STRTRIM(image_name,2)

; Concatenating the user inputs to create the overall path of the file
image_tocrop = image_location+image_name+'.DAT'

; Print the path as a check
PRINT,'- Selected file -'
PRINT, image_tocrop

; Testing for the file existence and that it is readable by the user,
without opening it
image_exist = FILE_TEST(image_tocrop,/READ)

; If file does not exist then inform the user and ask to re-write the
names
IF image_exist NE 1 THEN BEGIN
    PRINT,''
    PRINT,'The specified file does NOT exist or is not readable!'
    PRINT,'Please, re-enter the information.'
ENDIF

; Exit the loop if the file exists and is readable
ENDREP UNTIL (image_exist EQ 1)

; Confirm to the user that the image file exist and is readable
PRINT,''
PRINT,'The file ', image_tocrop,' exists and is readable.'

;-----
;-----
;-----
; The user is now asked the name to give to the output file
; If the field is left empty, the output file is named with
; the original name and the suffix _crop

PRINT,''
PRINT,'What name do you want to give to the output cropped file?'
PRINT,'NOTE: If left empty, it will be named ', image_name, '_crop.dat .'
PRINT,'NOTE: If already existing, its old contents are overwritten.'

; Define image_out & image_out_doris as a string before reading:
image_out = ''
image_out_doris = ''

; Read input from the terminal:
READ, image_out, PROMPT='Output file name (empty if default is OK): '

; Remove leading and trailing white spaces
image_out = STRTRIM(image_out,2)

; If image_out is an empty string then its given the default value
; image_out_doris is given the same name of image_out with attached at the end
'_doris'
IF image_out EQ '' THEN BEGIN
    image_out = image_name+'_crop'
    image_out_doris = image_out+'_doris'

```

```

ENDIF ELSE BEGIN
    image_out_doris = image_out+'_doris'
ENDELSE

;#####
;#####          CHECK          #####
;#####
; Inform the user on the output name
PRINT, ''
PRINT, 'The output cropped file will be named ', image_out, '.dat .'
PRINT, 'The DORIS compatible output file will be named ', image_out_doris, '.dat .'
PRINT, ''
PRINT, 'CHECK'
READ, PAUSING, PROMPT='Pausing - Enter any number to continue: '
;#####

;-----
;-----
;-----
; The user is now asked the specify the dimensions
; (columns & rows) of the original file.

; Initialise the variable image_exist equal to 0 as this is used later to
; check if the file specified by the user exists.
compare_size = 0

; Start a REPEAT...UNTIL loop that is terminated if the dimensions are correct
REPEAT BEGIN

    PRINT, ''
    PRINT, 'How many columns (pixels per line) does the file have?'
    PRINT, 'NOTE: This information can be found in the Leader file relative to
each SLC file.
    PRINT, 'NOTE: Do NOT consider the 12 byte header at the beginning of every
line.'
    PRINT, 'NOTE: Start Counting from 1 and not from 0.'
        ; Read input from the terminal:
    READ, Ncol, PROMPT='Number of columns (e.g. 4900): '
        ; Make sure it is a integer type (32-bit Unsigned integer with absolute
value range from 0 to 2^32 - 1)
    Ncol = ULONG(Ncol)

    PRINT, ''
    PRINT, 'How many lines (or rows) does the file have?'
    PRINT, 'NOTE: This information can be found in the Leader file relative to
each SLC file.
    PRINT, 'NOTE: Start Counting from 1 and not from 0.'
        ; Read input from the terminal:
    READ, Nrow, PROMPT='Number of lines (e.g. 26320): '
        ; Make sure it is a integer type
    Nrow = ULONG(Nrow)

        ; Number of rows to average over to equalise row and col ground resolution
    Navg = 5

```



```

; Calculate the file size from the user inputs
; and check it corresponds to the actual one
Header_bytes = 12
Image_size = (Header_bytes * Nrow) + (Ncol * 4 * Nrow)

; Open the file for input only
OPENR, lun_in, image_tocrop, /GET_LUN
; Obtain information about the file (e.g. name, size)
Temp_Var = FSTAT(lun_in)

; If the size is not correct then inform the user and ask to re-write the
dimensions
compare_size = 1
IF Temp_Var.SIZE NE Image_size THEN BEGIN
  PRINT, ''
  PRINT, 'The specified dimensions are NOT correct!'
  PRINT, 'Please, re-enter the information.'
  compare_size = 0
ENDIF

; Exit the loop if the file exists and is readable
ENDREP UNTIL (compare_size EQ 1)

PRINT, ''
PRINT, 'File: ', Temp_Var.NAME, ' is ', Temp_Var.SIZE, ' bytes long.'

;-----
;-----
;-----
; The user is now asked the specify the centre and the dimentions
; of the image to crop.

PRINT, ''
PRINT, 'What is the column value of the centre of the sub-image to be cropped?'
; Read input from the user:
READ, Ncol_crop, PROMPT='Column number of sub-image centre (e.g. 2858): '
; Make sure it is a integer type
Ncol_crop = FIX(Ncol_crop)

PRINT, ''
PRINT, 'What is the row (line) value of the centre of the sub-image to be
cropped?'
; Read input from the user:
READ, Nrow_crop, PROMPT='Row number of sub-image centre (e.g. 25275): '
; Makes sure it is a integer type
Nrow_crop = FIX(Nrow_crop)

PRINT, ''
PRINT, 'What is the width (in number of columns) to be cropped? (Specify the
entire width)'
PRINT, 'NOTE: If the number is not ODD (i.e. allowing for a central pixel),'
PRINT, '      its value is decreased by one. '
; Read input from the user:
READ, Ncol_delta, PROMPT='Width to be cropped (e.g. 1195): '
; Makes sure it is a integer type
Ncol_delta = FIX(Ncol_delta)

```

```

; If the number is not ODD, its value will be decreased by one
IF ((Ncol_delta MOD 2) EQ 0) THEN BEGIN
    Ncol_delta = Ncol_delta - 1
    ; Print check
    PRINT,'The total width (in number of columns) to be cropped is:
',Ncol_delta
ENDIF

PRINT,''
PRINT,'What is the height (in number of rows) to be cropped? (Specify the
entire width)'
PRINT,'NOTE: Remember that in ground resolution, 5 rows (azimuth) correspond
to 1 columns '
PRINT,'NOTE: If the number is not ODD (i.e. allowing for a central pixel),'
PRINT,' its value is decreased by one.
; Read input from the user:
READ, Nrow_delta, PROMPT='Height to be cropped (e.g. 2043): '
; Makes sure it is a integer type
Nrow_delta = FIX(Nrow_delta)
; If the number is not ODD, its value will be decreased by one
IF ((Nrow_delta MOD 2) EQ 0) THEN BEGIN
    Nrow_delta = Nrow_delta-1
    ; Print check
    PRINT,'The total height (in number of lines) to be cropped is:
',Nrow_delta
    PRINT,''
ENDIF

; Compute which one will be the first column of the new cropped image
; with respect to the original image. The 12 byte header is not included.
First_col = Ncol_crop - ((Ncol_delta-1)/2)
; Compute which one will be the first row of the new cropped image
; with respect to the original image.
First_row = Nrow_crop - ((Nrow_delta-1)/2)

;-----
;-----
;-----
; The image is now cropped and saved into a new file.

; Define the path of the output file
path_out = image_location+image_out+'.dat'

; The matrix for the new cropped image is created
Cropped_Image_Array = INTARR(Ncol_delta *2,Nrow_delta)

; Define the byte length of a single line as the Header plus the image
content.
; The Header_bytes variable was defined above when computing the file size
(i.e. Header_bytes = 12).
Bytes_per_line = Header_bytes + (Ncol * 4)

; As an Integer is made of 2 bytes (i.e. 16-bits), it is necessary to divide
its content by 2.
; Define a line as an Array of Integers
Line_Array = INTARR(Bytes_per_line/2)

```

```

; Define an array (of width in bytes = Ncol_delta*2) that will be used to read
and
; temporary store the cropped image
Col_Array = INTARR(2*Ncol_delta)

; Define two arrays for the columns (in bytes) before and after the image to
be cropped (Col_Array)
Bytes_Before = (Header_bytes/2)+((First_col-1)*2)
Before_Array = INTARR(Bytes_Before)
Bytes_After = (Bytes_per_line/2) - (Header_bytes/2) - ((First_col-1)*2) -
(Ncol_delta*2)
After_Array = INTARR(Bytes_After)

#####
#####          CHECK          #####
#####
PRINT, ''
PRINT, 'CHECK'
PRINT, ''
PRINT, 'Line_Array', SIZE(Line_Array)
PRINT, 'Before_Array', SIZE(Before_Array)
PRINT, 'Col_Array', SIZE(Col_Array)
PRINT, 'After_Array', SIZE(After_Array)
READ, PAUSING, PROMPT='Pausing - Enter any number to continue: '
#####

; Read the data line by line without doing any processing,
; until the line before the First_row.
; The file pointer procedure could also be used. It may perform faster but
; it appears to be more cryptic, and it is not easy to test and validate.
FOR row_disregard=0,First_row-2 DO BEGIN ; the -2 is needed as the routine
starts counting from 0 and
    ; it has to stop one line before the one to read.
    READU, lun_in, Line_Array ; read the data line by line
    IF ((row_disregard MOD 100) EQ 0) THEN print, '...reading line
',row_disregard
ENDFOR

#####
#####          CHECK          #####
#####
PRINT, ''
PRINT, 'CHECK'
PRINT, ''
PRINT, 'Value of current line position (row_disregard): ',row_disregard
READ, PAUSING, PROMPT='Pausing - Enter any number to continue: '
#####

; Open (OPENW for input and output) the new file that will store the cropped
image
OPENW, lun_out, path_out, /GET_LUN

; Continue reading the data line by line, and store the columns of interest
FOR row_regard=0,Nrow_delta-1 DO BEGIN
    READU, lun_in, Before_Array, Col_Array, After_Array

```

```

        Cropped_Image_Array[0:((Ncol_delta*2)-1), row_regard]=Col_Array
        IF ((row_regard MOD 100) EQ 0) THEN print, '...storing line ',row_regard
    ENDFOR

;#####
;#####          CHECK          #####
;#####
PRINT, ''
PRINT, 'CHECK'
PRINT, ''
PRINT, 'Value of row_regard is ',row_regard
READ, PAUSING, PROMPT='Pausing - Enter any number to continue: '
;#####

; Swapping the bytes from BIG ENDIAN to SMALL ENDIAN
Cropped_Image_Array = SWAP_ENDIAN (Cropped_Image_Array)

; The cropped image is written and saved
WRITEU, lun_out, Cropped_Image_Array

; Define the path of the output file compatible with DORIS (4B4B per pixel)
path_out_DORIS = image_location+image_out_doris+'.dat'

; Open (OPENW for input and output) the file that will store the DORIS
compatible cropped image
OPENW, lun_out_doris, path_out_DORIS, /GET_LUN

;#####
;#####          CHECK          #####
;#####
PRINT, ''
PRINT, 'CHECK'
PRINT, 'Size of Cropped_Image_Array', SIZE(Cropped_Image_Array)
PRINT, ''
READ, PAUSING, PROMPT='Pausing - Enter any number to continue: '
;#####

; Convert into FLOAT the Cropped_Image_Array
Cropped_Image_Array_DORIS = FLOAT(Cropped_Image_Array)

;#####
;#####          CHECK          #####
;#####
PRINT, ''
PRINT, 'Some values of what is being read without swapping the bytes'
PRINT, ''
PRINT, '[0,201] of Cropped_Image_Array is', Cropped_Image_Array[0,201]
PRINT, '[0,201] of Cropped_Image_Array_DORIS is', Cropped_Image_Array_DORIS
[0,201]
PRINT, '[1,201] of Cropped_Image_Array is', Cropped_Image_Array[1,201]
PRINT, '[1,201] of Cropped_Image_Array_DORIS is', Cropped_Image_Array_DORIS
[1,201]
PRINT, ''

```

```

PRINT, 'Size of Cropped_Image_Array', SIZE(Cropped_Image_Array)
PRINT, 'Size of Cropped_Image_Array_DORIS', SIZE(Cropped_Image_Array_DORIS)
PRINT, ''
READ, PAUSING, PROMPT='Pausing - Enter any number to continue: '
;#####

; The DORIS compatible cropped image is written and saved
WRITEU, lun_out_doris, Cropped_Image_Array_DORIS

; The three i/o files are closed.
FREE_LUN, lun_in
FREE_LUN, lun_out
FREE_LUN, lun_out_doris

;-----
;-----
;-----
; The program ceates a TXT file ; - Creates a TXT file with the
; cropping parameters used, and the Doris cropping text required.

; Define the path of the txt file
txt_out = image_location+image_out+'.txt'

; OPENW (OPEN Write) opens a new file for input and output.
; If the file exists, it is truncated and its old contents are destroyed
OPENW, lun_txt, txt_out, /GET_LUN

current_date = SYSTIME()
PRINTF, lun_txt, current_date
PRINTF, lun_txt, ' '
PRINTF, lun_txt, ' '
PRINTF, lun_txt, 'ORIGINAL IMAGE:           ', image_name, '.DAT'
PRINTF, lun_txt, ' '
PRINTF, lun_txt, 'Pixels (columns):           ', Ncol
PRINTF, lun_txt, 'Lines (rows):              ', Nrow
PRINTF, lun_txt, 'Total bytes (with 12 header): ', Image_size
PRINTF, lun_txt, ' '
PRINTF, lun_txt, ' '
PRINTF, lun_txt, 'CROPPED SUBSCENE:         ', image_out, '.dat'
PRINTF, lun_txt, 'Central Pixel:             ', Ncol_crop
PRINTF, lun_txt, 'Central Line:              ', Nrow_crop
PRINTF, lun_txt, 'Number of Pixels:          ', Ncol_delta
PRINTF, lun_txt, 'Number of Lines:           ', Nrow_delta

sz = SIZE(Cropped_Image_Array)
n = N_ELEMENTS(sz)
type = sz[n-2] ; -2 is needed because IDL starts counting from 0.
; type = 2 --> INT Integer
; type = 4 --> FLOAT Floating point

total_elements_cropped = N_ELEMENTS(Cropped_Image_Array)
cropped_size = type * total_elements_cropped

PRINTF, lun_txt, 'Number of bytes:           ', cropped_size
PRINTF, lun_txt, ' '
PRINTF, lun_txt, ' '

```

```

PRINTF, lun_txt, ' '
PRINTF, lun_txt, ' '
PRINTF, lun_txt, ' '
PRINTF, lun_txt, 'OUTPUT for DORIS'
PRINTF, lun_txt, ' '
PRINTF, lun_txt, ' '
PRINTF, lun_txt, ' '
PRINTF, lun_txt, '*****'
PRINTF, lun_txt, '*_Start_crop:      master step01'
PRINTF, lun_txt, '*****'
PRINTF, lun_txt, 'Data_output_file:      Outdata/',image_out,'.dat'
PRINTF, lun_txt, 'Data_output_format:      complex_short'
PRINTF, lun_txt, 'First_line (w.r.t. original_image):      ',First_row
PRINTF, lun_txt, 'Last_line      (w.r.t.      original_image):
', (First_row+Nrow_delta-1)
PRINTF, lun_txt, 'First_pixel (w.r.t. original_image):      ',First_col
PRINTF, lun_txt, 'Last_pixel      (w.r.t.      original_image):
', (First_col+Ncol_delta-1)
PRINTF, lun_txt, '*****'
PRINTF, lun_txt, '* End_crop:_NORMAL'
PRINTF, lun_txt, '*****'
PRINTF, lun_txt, ' '
PRINTF, lun_txt, ' '
PRINTF, lun_txt, ' '

FREE_LUN, lun_txt

;-----
;-----
;-----
; The image is now opened for a quick visualisation and saved as a JPG.
; Averaging over the rows occurs.

f_line = INTARR(2*Ncol_delta)
Ival = FLTARR(Nrow_delta,Ncol_delta)
Qval = FLTARR(Nrow_delta,Ncol_delta)
mag_avg = FLTARR(Ncol_delta,Nrow_delta/Navg)

OPENR, lun_show, path_out, /GET_LUN

FOR row=0,Nrow_delta-1 DO BEGIN

  READU, lun_show, f_line      ; read the data line by line (the file
  pointer procedure could also be used)

  IF ((row MOD 100) EQ 0) THEN print, '...loading line ',row

  FOR col=0,Ncol_delta-1 DO BEGIN ; then load the in-phase and quadrature
  values into separate arrays
    ; note that INTARR become FLTARR
    Ival[row,Ncol_delta-1-col] = f_line[col*2]
    Qval[row,Ncol_delta-1-col] = f_line[col*2+1]

```

```

;#####
;##### CHECK #####
;#####
IF (col EQ 0) AND (row EQ 201) THEN BEGIN
    PRINT, ''
    PRINT, 'CHECK'
    PRINT, ''
    PRINT, '[0,201] - f_line is', f_line[col*2]
    PRINT, '[1,201] - f_line is', f_line[col*2+1]
    PRINT, '[0,201] - Ival is', Ival[row,Ncol_delta-1-col]
    PRINT, '[1,201] - Qval is', Qval[row,Ncol_delta-1-col]
    READ, PAUSING, PROMPT='Pausing - Enter any number to continue: '
ENDIF
;#####

ENDFOR

ENDFOR

FREE_LUN, lun_show

;#####
;##### CHECK #####
;#####
PRINT, ''
PRINT, 'CHECK'
PRINT, ''
PRINT, 'Averaging over the rows'
READ, PAUSING, PROMPT='Pausing - Enter any number to continue: '
;#####

FOR i=0, ((Nrow_delta/Navg)-1) DO BEGIN ; average over the Navg rows
    row = i*Navg
    Isum = Ival[row,*]
    Qsum = Qval[row,*]

    FOR j=row+1,row+Navg-1 DO BEGIN
        Isum = Isum+Ival[j,*]
        Qsum = Qsum+Qval[j,*]
    ENDFOR

    Isum = Isum/Navg ; devide by 5
    Qsum = Qsum/Navg

    mag_avg[*, (Nrow_delta/Navg)-1-i] = SQRT(Isum[*]*Isum[*]+Qsum[*]*Qsum[*])
ENDFOR

; The cropped image is saved as a JPEG

; Path of JPG image to be saved
image_out_jpg = image_location+image_out+'.jpg'

```

```

#####
#####          CHECK          #####
#####
PRINT, ''
PRINT, 'The JPG image: ',image_out_jpg,' has been created.'
READ, PAUSING, PROMPT='Pausing - Enter any number to continue: '
#####

scaled = BYTSCL(mag_avg,MIN=0, MAX=150)
WRITE_JPEG, image_out_jpg, scaled, QUALITY=100

; The cropped image is shown

PRINT,'Value range = ',MIN(mag_avg),' to ',MAX(mag_avg)

WINDOW,0, XSIZE=Ncol_delta, YSIZE=Nrow_delta/Navg, TITLE='Magnitude, File
'+path_out

; scaled = mag_avg
scaled = BYTSCL(mag_avg,MIN=0, MAX=150)
; scaled = BYTSCL(mag_avg,MIN=50,MAX=200)
; scaled = BYTSCL(mag_avg)
TV, scaled

; END ; comment this out to allow program to proceed beyond initial display

SET_PLOT, 'PS'
DEVICE, Bits_Per_Pixel=8, FILENAME='mag'+image_name+'.eps', /Encapsulated
TVScl, scaled
DEVICE, /CLOSE
SET_PLOT, 'WIN'

;-----
;-----
;-----
; End of "SARcrop.pro" program
END

```


A.5 SARmodify.pro

This IDL routine modifies an area of interest of an ERS SLC data file.

SCRIPT:

```
; PROGRAM IN BRIEF
;
; - Opens the selected ERS1/2 subscene file (Small Endian with 4B per pixel)
; - Asks user what part to modify
; - Applied modification (i.e. division by 2). Anything else can be
;   programmed
; - Saves the modified image in a 2B real 2B imaginary format (Small Endian)
; - Creates a TXT file with the parameters used.
; - Creates a jpg image for a quick look
; - Show immediately the image in IDL

;#####
;#####          CHECK          #####
;#####
; In the script you will find sections headed with the above 3 'check' lines.
; These sections are used to make cross validations on the data while the
; program is running. If you want you can delete these section or simply
; make them comments by adding semicolons at the beginning of the line.

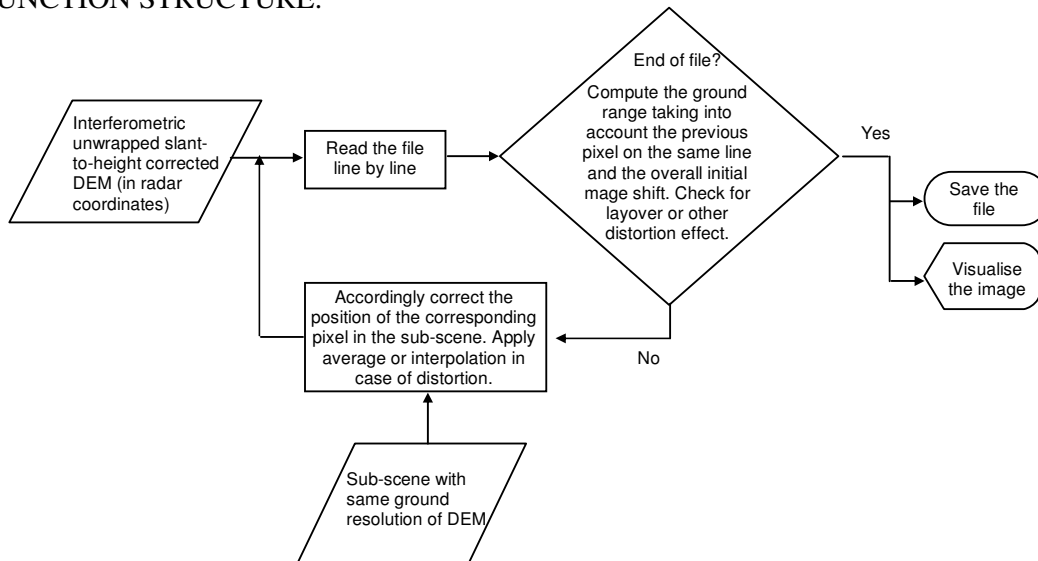
; PROGRAM DESCRIPTION
;
; This program crops ERS1/2 SLC SAR files and quickly views them in order to
; make sure the cropping has been carried out correctly.
;
; The programme runs interectively and requests inputs from the user to be
; specified on the IDL terminal.
;
; The number of rows and columns of these files must be known.
; This information can be found in the Crop *.txt file produced during the
; crop procedure.
;
; The program supports both 2 bytes (2B) and 4 bytes (4B) per value.
; i.e. one pixel defined by 2B for the real and 2B for the imaginary part or
; defined by 4B for the real and 4B for the imaginary part
;
;
; IMAGE - STRUCTURE of 1 ROW
;
; Pixel no.           : | 1 | 2 | 3 | 4 | 5 | ...
; Image structure     : | Re Im | Re Im | Re Im | Re Im | Re Im | ...
;
; 2-Byte content      : | 2B 2B | 2B 2B | 2B 2B | 2B 2B | 2B 2B | ...
;
; 4-Byte content (Doris) : | 4B 4B | 4B 4B | 4B 4B | 4B 4B | 4B 4B | ...
;
;
```

```
;
; It is important to notice that even if the number of lines (rows) is
; not exactly divisible by 5 (i.e. for the azimuth averaging), the image
; immediately showed by IDL and the IPG image might have have 1 to 4 lines
; missing at the bottom.
; Even so, the modified image is fine and fully compatible with Doris.
;
;
; When providing the coordinates of the area to be modified, do NOT consider
; the 12 byte header that was present in the Original files.
;
; The modified images is saved in Small Endians for compatibility with Linux
; and Windows systems.
;
;
; PROGRAM HISTORY
;
; Developed by G. Ottavianelli (July 2005)
; g.ottavianelli@tiscali.it
;
; V0.0 :
;   - The procedure is based on the Cropping routine.
;
;
; COMPILE AND RUN from IDL "Run" menu
```

A.6 terrain_correction.m

This Matlab routine applies the slant to ground terrain correction (Equation 4-5).

FUNCTION STRUCTURE:



SCRIPT:

```

function elements = terrain_correction(dem, filename, dimension, precision);

% ;+
% ; NAME:
% ;     terrain_correction
% ;
% ; PURPOSE:
% ;     The purpose of this program is to apply a terrain correction on the
% ;     SAR backscatter amplitude image or the Coherence magnitude
% ;     by using the DEM computed with Doris.
% ;
% ; INPUT PARAMETERS:
% ;     dem           Dem file generated by Doris
% ;     filename      SAR backscatter amplitude or Coherence
% ;     magnitude
% ;     dimension     Dimension of the file
% ;     precision     file precision
% ;
% ; OUTPUTS:
% ;     The new image is saved with the suffix _terrcorr
% ;
% ;
% ;
% ;

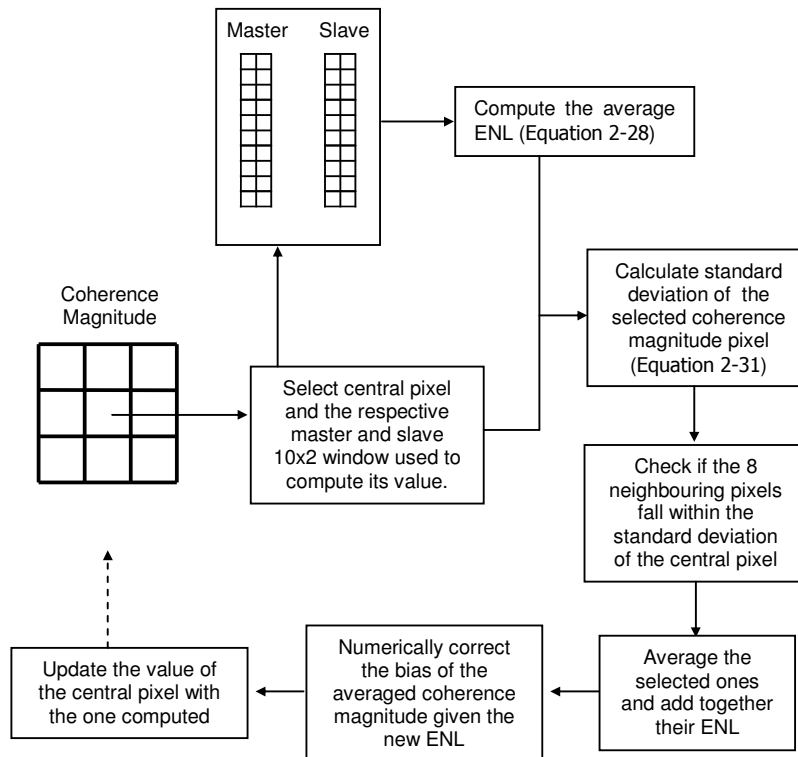
```

```
% ;
% ; CALLING SEQUENCE EXAMPLE:
% ;           elements = terrain_correction('s2h_heights_19950626_25',
'coherence_real_19950626_25', [600,600], 'float32') %Floating-point; 32 bits
% ;           elements = terrain_correction('s2h_heights_19950626_25',
'master19950625_afilt_rfilt_magni_avey01x01', [600,600], 'float32')
% ;
% ; MODIFICATION HISTORY:
% ;           Written by: Giuseppe Ottavianelli, 13/03/2006
% ;
```

A.7 coherence_correction.m

This Matlab routine corrects the coherence magnitude bias. It calls coherence_sd.m and genHyper.m. Full script is provi

FUNCTION STRUCTURE:



SCRIPT:

```

function elements = coherence_correction(amplitude_master, amplitude_slave,
dimension, MN, coh_mag, SubScene, precision)

% ;+
% ; NAME:
% ; coherence_correction
% ;
% ; PURPOSE:
% ; The purpose of this program is to correct the biased computed
% ; coherence of an area of interest.
% ; It first computes the overall average Equivalent Number
% ; of Look (ENL). Oliver and Quegan (1998, page 106).
% ; It then applies the coherence estimation optimisation suggested
% ; by Touzi et al. (1999, page 140, section III.B).
% ; Last, if the NewENL is This process is done numerically

```

```

% ;      using Eq. 4.3.4 in Hanssen (2001).
% ;
% ;      The multilook number is fixed to 20.
% ;
% ; INPUT PARAMETERS:
% ;      amplitude_master      Master scene amplitude file
% ;      amplitude_slave      Slave scene amplitude file
% ;      dimension            Dimension of the amplitude files
% ;      MN                   Processing window used in the Coherence
% ;                          estimation step in Doris
% ;      coh_mag              Coherence Magnitude file
% ;      SubScene             Area of interest in the Coherence image before
% ;                          being flipped. Row and column of top-left
% ;                          pixel and row and column of bottom-right pixel
% ;      precision            file precision
% ;
% ; OUTPUTS:
% ;      The new image is saved with the suffix _cohcorrL(multilooknumber)
% ;
% ; CALLING SEQUENCE EXAMPLE:
% ;      elements = coherence_correction('master19960216_afilt_rfilt_ampli',
% ;      'slave19960217_afilt_res_rfilt_ampli',      [1200,      6000],      [2,      10],
% ;      'coherence_real_19960217_16',      [300,220,370,260],      'float32')      %
% ; [300,220,370,260] is usually the AOI for DESCENDING ORBITS
% ; float32 = Floating-point 32 bits

% ;      elements = coherence_correction('master19960216_afilt_rfilt_ampli',
% ;      'slave19960217_afilt_res_rfilt_ampli',      [1200,      6000],      [2,      10],
% ;      'coherence_real_19960217_16',      [190,320,290,390],      'float32')      %
% ; [190,320,290,390] is usually the AOI for ASCENDING ORBITS
% ; float32 = Floating-point 32 bits
% ;
% ; MODIFICATION HISTORY:
% ;      Written by: Giuseppe Ottavianelli, 13/05/2006
% ;

% Load Images
format long

% ;#####
% ;##### CHECK #####
% ;#####
% Some lines used while testing the program
% dimension=[1200, 6000] ;
% amplitude_master='master19950625_afilt_rfilt_magni';
% amplitude_slave='slave19950626_afilt_res_rfilt_magni';
% MN=[2, 10] ;
% coh_mag='coherence_real_19950626_25';
% precision='float32';
% SubScene = [300,220,370,260] ;
% ;#####

Start_total = clock;
disp(' ')
disp(' ')
disp('XXXXXXXXXXXXXXXXXXXXXXXXXXXXXXXXXXXXXXXXXXXXXXXXXXXXXXXXXXXXXXXXXXXX')
disp('BIAS CORRECTION ROUTINE STARTED')

```

```

disp('---')
disp('Loading images into Matlab.')

fid = fopen (amplitude_master,'r','l'); %Open file, in read-only mode, IEEE
floating point with little-endian byte ordering
%read the Master Amplitude file
Master_Ampli = fread (fid, [dimension(1), dimension(2)], precision);
Master_Ampli = Master_Ampli' ; % This is required otherwise the columns are
inverted with the rows
fclose(fid);

fid = fopen (amplitude_slave,'r','l'); %Open file, in read-only mode, IEEE
floating point with little-endian byte ordering
%read the Slave Amplitude file
Slave_Ampli = fread (fid, [dimension(1), dimension(2)], precision);
Slave_Ampli = Slave_Ampli' ; % Transpose. This is required otherwise the
columns are inverted with the rows
fclose(fid);

%Calculate the coherence magnitude dimation
coh_dimension = dimension./MN;

fid = fopen (coh_mag,'r','l'); %Open file, in read-only mode, IEEE floating
point with little-endian byte ordering
%read the Slave Amplitude file
Coherence_Magnitude = fread (fid, [coh_dimension(1), coh_dimension(2)],
precision);
Coherence_Magnitude = Coherence_Magnitude' ; % This is required otherwise the
columns are inverted with the rows
fclose(fid);

%;#####
%;##### CHECK #####
%;#####
%figure
%imshow(Coherence_Magnitude)
% figure
% image (Master_Ampli)
%;#####

disp('---')
disp('Images loaded into Matlab.')

%%%%%%%%%%%%%%%%%%%%%%%%%%%%%%%%%%%%%%%%%%%%%%%%%%%%%%%%%%%%%%%%%%%%%%%%
% Computer the local Equivalent Number of Looks based on the formula by Oliver
and Quegan (1998, page 106).
pause(1)
Start = clock ;
disp(' ')
disp(' ')
disp(' ')
disp('XXXXXXXXXXXXXXXXXXXXXXXXXXXXXXXXXXXXXXXXXXXXXXXXXXXXXXXXXXXXXXXXXXXX')
disp('Estimation of ENL started.')
disp('---')

% The Intensity images have to be computed:
Master_Intensity = Master_Ampli.^2 ;

```

```

Slave_Intensity = Slave_Ampli.^2 ;

% create 4 vectors that will contain the columns and rows of the moving
processing window.
Master_Range = zeros(1,MN(1));
Master_Azimu = zeros(1,MN(2));
Slave_Range = zeros(1,MN(1));
Slave_Azimu = zeros(1,MN(2));

% Initialise 4 variables that are used in the following routine and that will
temporarily store the correlation coefficients.
Master_R_xcorr_TEMP = zeros (1,((MN(1) * 2) - 1)) ;
Master_A_xcorr_TEMP = zeros (1,((MN(2) * 2) - 1)) ;
Slave_R_xcorr_TEMP = zeros (1,((MN(1) * 2) - 1)) ;
Slave_A_xcorr_TEMP = zeros (1,((MN(2) * 2) - 1)) ;

% create a matrix with the dimensions of the Coherence image that will store
the values of the local ENL.
Local_ENL = zeros(coh_dimension(1), coh_dimension(2)) ;

% MOVING WINDOW LOOP. Start a for loop that makes the processing window move
pixel by pixel for every row over the whole image.
for Image_row = ((SubScene(1)*MN(2))-(MN(2)-1)) : MN(2) :
((SubScene(3)*MN(2))-(MN(2)-1) )
    disp('...local ENL estimation, processing row...')
    disp(Image_row)
    for Image_column = ((SubScene(2)*MN(1))-(MN(1)-1)) :MN(1):
((SubScene(4)*MN(1))-(MN(1)-1))
        % MASTER_RANGE: Calculate the correlation coefficient line by line
within the moving processing window.
        Master_R_xcorr_TEMP(:,:)=0;
        for row = 1 : MN(2)
            Master_Range = Master_Intensity ((Image_row + row -1),
Image_column:(Image_column+MN(1)-1)) ; % Select all pixels of the row
            [Master_R_xcorr,lags] = xcorr(Master_Range, (MN(1)-1),'coeff'); %
calculate the correlation coefficients for a lag equal to the MN matrix. from
-MN to +MN. The total number of lags will be [(MN * 2) - 1]
            Master_R_xcorr_TEMP = Master_R_xcorr_TEMP + Master_R_xcorr; %
store the values in the variable Master_R_xcorr_TEMP.
        end
        Master_R_xcorr = Master_R_xcorr_TEMP ./MN(2) ; % Average over the
number of rows.
        % Store the coeff.
        Master_R_coeff = zeros (1, MN(1)) ;
        Master_R_coeff (1, :) = Master_R_xcorr(1, (MN(1)):((MN(1) * 2) - 1)) ;

        % MASTER_AZIMUTH: Calculate the correlation coefficient column by
column.
        Master_A_xcorr_TEMP(:,:)=0;
        for col = 1 : MN(1) % it refers to dimension(1) because the matrix has
been transposed.
            Master_Azimu = Master_Intensity ((Image_row :(Image_row+MN(2)-1))
, (Image_column + col -1)) ; % Select all lines of the col
            Master_Azimu = Master_Azimu' ; % transpose to make it a one
            [Master_A_xcorr,lags] = xcorr(Master_Azimu, (MN(2)-1),'coeff'); %
calculate the correlation coefficients for a lag equal to the MN matrix. from
-MN to +MN. The total number of lags will be [(MN * 2) - 1]
            Master_A_xcorr_TEMP = Master_A_xcorr_TEMP + Master_A_xcorr; %
store the values in the variable Master_R_xcorr_TEMP.
        end
    end
end

```



```

end
Master_A_xcorr = Master_A_xcorr_TEMP ./MN(1) ; % Average over the
number of columns.
% Store the coeff.
Master_A_coeff = zeros (1, MN(2)) ;
Master_A_coeff (1, :) = Master_A_xcorr(1, (MN(2)):(MN(2) * 2) - 1) ;

% MASTER_OLIVER&QUEGAN formula
% Selectge the window of intensity
Window_Intensity= Master_Intensity((Image_row : (Image_row+MN(2)-1)),
Image_column:(Image_column+MN(1)-1)) ;
% Find the mean of the intensity window
Mean_Master = mean(Window_Intensity);
Mean_Master = mean(Mean_Master);
%find the Variance of the intensity window
Var_Master = var(Window_Intensity);
Var_Master = mean(Var_Master);
% computer the Summation_Coeff_Factor_Master
% initialize the variable
Summation_Coeff_Factor_Master = 0;
for X = 1 : MN(1)
    for Y = 1 : MN(2)
        Summation_Coeff_Factor_Master = Summation_Coeff_Factor_Master +
((1-((X-1)/MN(1)))*(1-((Y-
1)/MN(2)))*(Master_R_coeff(1,X))*(Master_A_coeff(1,Y))) ;
    end
end
end
% Calculate the Average Number of looks
ENL_Master = MN(1)*MN(2)* (Mean_Master^2) / Var_Master ;
ENL_Master = ENL_Master / Summation_Coeff_Factor_Master ;

Local_ENL(((Image_row+(MN(2)-1))/MN(2)), ((Image_column + (MN(1)-
1))/MN(1))) = ENL_Master;

%;#####
%;##### CHECK #####
%;#####
% ENL_Master
% pause
%;#####

% SLAVE_RANGE: Calculate the correlation coefficient line by line
within the moving processing window.
Slave_R_xcorr_TEMP(:,:)=0;
for row = 1 : MN(2)
    Slave_Range = Slave_Intensity ((Image_row + row -1),
Image_column:(Image_column+MN(1)-1)) ; % Select all pixels of the row
    [Slave_R_xcorr,lags] = xcorr(Slave_Range, (MN(1)-1),'coeff'); %
calculate the correlation coefficients for a lag equal to the MN matrix. from
-MN to +MN. The total number of lags will be [(MN * 2) - 1]
    Slave_R_xcorr_TEMP = Slave_R_xcorr_TEMP + Slave_R_xcorr; % store
the values in the variable Master_R_xcorr_TEMP.
end
Slave_R_xcorr = Slave_R_xcorr_TEMP ./MN(2) ; % Average over the number
of rows.
% Store the coeff.
Slave_R_coeff = zeros (1, MN(1)) ;
Slave_R_coeff (1, :) = Slave_R_xcorr(1, (MN(1)):(MN(1) * 2) - 1));

```

```

% SLAVE_AZIMUTH: Calculate the correlation coefficient column by
column.
Slave_A_xcorr_TEMP(:,:)=0 ;
for col = 1 : MN(1) % it refers to dimension(1) because the matrix has
been transposed.
    Slave_Azimu = Slave_Intensity ((Image_row :(Image_row+MN(2)-1)) ,
(Image_column + col -1)) ; % Select all lines of the col
    Slave_Azimu = Slave_Azimu' ; % transpose to make it a one
    [Slave_A_xcorr,lags] = xcorr(Slave_Azimu, (MN(2)-1),'coeff'); %
calculate the correlation coefficients for a lag equal to the MN matrix. from
-MN to +MN. The total number of lags will be [(MN * 2) - 1]
    Slave_A_xcorr_TEMP = Slave_A_xcorr_TEMP + Slave_A_xcorr; % store
the values in the variable Master_R_xcorr_TEMP.
end
Slave_A_xcorr = Slave_A_xcorr_TEMP ./MN(1) ; % Average over the number
of columns.
% Store the coeff.
Slave_A_coeff = zeros (1, MN(2)) ;
Slave_A_coeff (1, :) = Slave_A_xcorr(1, (MN(2)):(MN(2) * 2) - 1) ;

% SLAVE_OLIVER&QUEGAN formula
% Selectge the window of intensity
Window_Intensity= Slave_Intensity((Image_row :(Image_row+MN(2)-1)),
Image_column:(Image_column+MN(1)-1)) ;
% Find the mean of the intensity window
Mean_Slave = mean(Window_Intensity);
Mean_Slave = mean(Mean_Slave);
%find the Variance of the intensity window
Var_Slave = var(Window_Intensity);
Var_Slave = mean(Var_Slave);
% computer the Summation_Coeff_Factor_Master
% initialize the variable
Summation_Coeff_Factor_Slave = 0;
for X = 1 : MN(1)
    for Y = 1 : MN(2)
        Summation_Coeff_Factor_Slave = Summation_Coeff_Factor_Slave +
((1-((X-1)/MN(1)))*(1-((Y-
1)/MN(2)))*(Slave_R_coeff(1,X))*(Slave_A_coeff(1,Y))) ;
    end
end
% Calculate the Average Number of looks
ENL_Slave = MN(1)*MN(2)* (Mean_Slave^2) / Var_Slave ;
ENL_Slave = ENL_Slave / Summation_Coeff_Factor_Slave ;

%;#####
%;##### CHECK #####
%;#####
% ENL_Slave
% pause
%;#####

Local_ENL(((Image_row+(MN(2)-1)/MN(2)), ((Image_column + (MN(1)-
1))/MN(1))) = (Local_ENL(((Image_row+(MN(2)-1)/MN(2)), ((Image_column
+(MN(1)-1))/MN(1))) + ENL_Slave )./2 ;

% Local_ENL(((Image_row+(MN(2)-1)/MN(2)), ((Image_column + (MN(1)-
1))/MN(1)))
end

```

```

end

% ;#####
% ;##### CHECK #####
% ;#####
% Local_ENL((SubScene(1)-1):(SubScene(3)+1), (SubScene(2)-1):(SubScene(4)+1))
% pause
% ;#####

disp('ENL estimation terminated.')
Finish = clock;
Elapsed_time = Finish - Start;
disp('Computing time')
disp(Elapsed_time(1,4:6))

% delete all variables apart from: the 3 loaded images, the 2 intensity images
% and the ENL image
clear Mean_Master Mean_Slave Var_Master Var_Slave Slave_R_coeff Slave_A_coeff
Master_R_coeff Master_A_coeff
clear Master_Azimu Master_A_xcorr_TEMP Master_A_xcorr Master_Range
Master_R_xcorr_TEMP Master_R_xcorr Window_Intensity
clear Slave_Azimu Slave_A_xcorr_TEMP Slave_A_xcorr Slave_Range
Slave_R_xcorr_TEMP Slave_R_xcorr
clear Counter Image_row Image_column Master_A_xcorr_TEMP Master_R_xcorr_TEMP
Slave_A_xcorr_TEMP Slave_R_xcorr_TEMP
clear ENL_Slave Summation_Coeff_Factor_Slave ENL_Master
clear X Y Elapsed_time Finish Start counter elements col row lags
Summation_Coeff_Factor_Master

%%%%%%%%%%%%%%%%%%%%%%%%%%%%%%%%%%%%%%%%%%%%%%%%%%%%%%%%%%%%%%%%%%%%%%%%
% Compute the averaged sample coherence magnitude routine suggested by Touzi et
% al. (1999, page 140, section III.B).
pause(2)
Start = clock ;
disp(' ')
disp(' ')
disp(' ')
disp('XXXXXXXXXXXXXXXXXXXXXXXXXXXXXXXXXXXXXXXXXXXXXXXXXXXXXXXXXXXXXXXXXXXX')
disp('Averaged sample coherence magnitude estimation initiated.')
disp('---')
% create three matrices with the same dimension of the Coherence Magnitude
% image
% the first stores the New averaged sample coherence
New_Sample_Coh = zeros( coh_dimension(1), coh_dimension(2)) ;
% fill all values with the coherence value in case they will not be processes
New_Sample_Coh(:, :) = Coherence_Magnitude(:, :) ;
% the second stores the respective ENL based on the number of sampled pixels
% used
New_ENL = zeros(coh_dimension(1), coh_dimension(2)) ;

% the third stores the standard deviation of the New Sample Coherence
%New_SD_Sample_Coh =zeros(coh_dimension(1), coh_dimension(2)) ;

% Initialise the moving processing window. the dimensions must be odd numbers
window_dimensions = [3,3];

% Start the process pixel by pixel, one row after the other.

```

```

for Coh_row = SubScene(1) : SubScene(3)
    disp('...averaged sample coherence estimation, processing row:')
    disp(Coh_row)
    for Coh_column = SubScene(2) : SubScene(4)
        % compute the standard deviation of the coherence magnitude for the
        given ENL
        Local_ENL(Coh_row,Coh_column) = fix(Local_ENL(Coh_row,Coh_column)) ;
        elements = coherence_sd(Local_ENL(Coh_row,Coh_column),
        (Coherence_Magnitude(Coh_row,Coh_column))) ;
        % initialise a counter to store the number of selected coherence
        pixels
        counter = 0 ;
        Coherence_of_Selected_pixel = New_Sample_Coh(Coh_row,Coh_column) ;

        for Y = (-(window_dimensions(1)-1)/2) : 1 : ((window_dimensions(1)-
        1)/2)
            for X = (-(window_dimensions(1)-1)/2) : 1 :
            ((window_dimensions(1)-1)/2)
                if (Coherence_Magnitude((Coh_row+Y), (Coh_column+X)) >
                ((Coherence_Magnitude(Coh_row,Coh_column))-elements) &
                (Coherence_Magnitude((Coh_row+Y), (Coh_column+X)) <
                ((Coherence_Magnitude(Coh_row,Coh_column))+ elements))
                    New_Sample_Coh(Coh_row,Coh_column) =
                    New_Sample_Coh(Coh_row,Coh_column) +
                    (Coherence_Magnitude((Coh_row+Y), (Coh_column+X))) ;
                    counter = counter +1 ;
                end
            end
        end

        %;#####
        %;##### CHECK #####
        %;#####
        % counter
        % pause
        %;#####

        % average the summed Coherence values and store this value in the
        New_Sample_Coh matrix
        New_Sample_Coh(Coh_row,Coh_column) =
        ((New_Sample_Coh(Coh_row,Coh_column))-Coherence_of_Selected_pixel) / counter ;

        %;#####
        %;##### CHECK #####
        %;#####
        % Coherence_Magnitude(Coh_row,Coh_column)
        % New_Sample_Coh(Coh_row,Coh_column)
        % pause
        %;#####

        % store the new value of the ENL
        New_ENL(Coh_row,Coh_column) = Local_ENL(Coh_row,Coh_column) * counter
        ;

        %;#####
        %;##### CHECK #####
        %;#####

```



```

disp(' ')
disp('XXXXXXXXXXXXXXXXXXXXXXXXXXXXXXXXXXXXXXXXXXXXXXXXXXXXXXXXXXXXXXXXXXXX')
disp('Coherence bias correction initiated.')
disp('---')

% create a matrix with the same dimension of the Coherence Magnitude image
% this stores the bias corrected averaged sample coherence
New_Sample_Coh_Bias(:, :) = New_Sample_Coh(:, :);

for Coh_row = SubScene(1) : SubScene(3)
    disp('...coherence bias correction, processing row:')
    disp(Coh_row)
    for Coh_column = SubScene(2) : SubScene(4)

%#####
%#####          CHECK          #####
%#####
%           New_ENL(Coh_row,Coh_column)
%           pause
%#####

        if New_ENL(Coh_row,Coh_column) > 30

            Limit_Zero_Coh    =    coherence_bias((New_ENL(Coh_row,Coh_column)),
0.001) ;

%#####
%#####          CHECK          #####
%#####
%           pause
%#####

            if    New_Sample_Coh(Coh_row,Coh_column)    >    Limit_Zero_Coh    &
New_Sample_Coh(Coh_row,Coh_column) < 0.5
                % initialise the true coherence to the mid value of 0.25. This
will be increased or decreased accordingly
                coh_true = 0.25;

%#####
%#####          CHECK          #####
%#####
%           pause
%#####

                % re-initialise the counter used to stop the routine after 10
iterations
                counter = 1 ;
                Approx_coh    =    coherence_bias((New_ENL(Coh_row,Coh_column)),
coh_true) ;

                % if the counter has not reach the final iteration or the
difference between the Expected_coherence and Biased coherence is bigger than
0.01

                % then start the correction routine
                while    (counter    <    10)    &    ((abs(Approx_coh-
(New_Sample_Coh(Coh_row,Coh_column)))) > 0.0001)
                    counter = counter + 1 ;

```

```

        % increase or decrease the value of the true coherence to
reduce the difference between the Expected_coherence and Biased coherence
        if Approx_coh < (New_Sample_Coh(Coh_row,Coh_column))
            addition_value = (0.25)/(2^(counter-1));
            coh_true = coh_true + addition_value;
        else
            addition_value = (0.25)/(2^(counter-1));
            coh_true = coh_true - addition_value;
        end
        % recompute the required values
        Approx_coh = coherence_bias((New_ENL(Coh_row,Coh_column)),
coh_true);
        end
        % store the corrected coherence in the matrix
        New_Sample_Coh_Bias(Coh_row,Coh_column)= coh_true;
    end
else
    New_Sample_Coh_Bias(Coh_row,Coh_column) =
New_Sample_Coh(Coh_row,Coh_column) ;
end
end
end

disp('---')
disp('Coherence bias correction terminated.')
disp('---')
disp('Saving file into:')
Outputfilename = strcat(coh_mag,'_BiasCorr')
fid = fopen (Outputfilename,'w');
New_Sample_Coh_Bias = New_Sample_Coh_Bias' ; % This is required before it is
reimported into IDL
elements = fwrite(fid, New_Sample_Coh_Bias , precision) ;
fclose(fid);
New_Sample_Coh_Bias = New_Sample_Coh_Bias' ;

disp('---')
disp('Output processed files saved.')
Finish = clock;
Elapsed_time = Finish - Start;
disp('---')
disp('Computing time')
disp(Elapsed_time(1,4:6))
Elapsed_time = Finish - Start_total;
disp('---')
disp('TOTAL Computing time')
disp(Elapsed_time(1,4:6))

disp('')
disp('')
disp('')
disp('')
disp('END OF ROUTINE')
disp('XXXXXXXXXXXXXXXXXXXXXXXXXXXXXXXXXXXXXXXXXXXXXXXXXXXXXXXXXXXXXXXXXXXX')
disp('XXXXXXXXXXXXXXXXXXXXXXXXXXXXXXXXXXXXXXXXXXXXXXXXXXXXXXXXXXXXXXXXXXXX')

```

A.8 coherence_sd.m

This Matlab routine computes the coherence magnitude standard deviation.

SCRIPT:

```
function elements = coherence_sd(ENL, coh);

% ;+
% ; NAME:
% ;     coherence_sd
% ;
% ; PURPOSE:
% ;     The purpose of this program is to compute the standard deviation of
% ;     the estimated coherence.
% ;     This process is done numerically using Eq. 4.3.4 and 4.3.5 in
% ;     Hanssen (2001).
% ;
% ; INPUT PARAMETERS:
% ;     ENL     Equivalent Number of Looks
% ;     gamma   Coherence
% ;
% ; OUTPUTS:
% ;     Coherence standard deviation.
% ;
% ; CALLING SEQUENCE EXAMPLE:
% ;     ;                               elements = coherence_sd(Average_ENL,
% ;     (Coherence_Magnitude(Coh_row,Coh_column)));
% ;
% ; MODIFICATION HISTORY:
% ;     Written by: Giuseppe Ottavianelli, 07/5/2006
% ;
```


A.9 GBSAR_min_RCS.m

This Matlab routine computes the minimum radar cross section (Equation 4-6) of the GB-SAR system given the distance entered by the user.

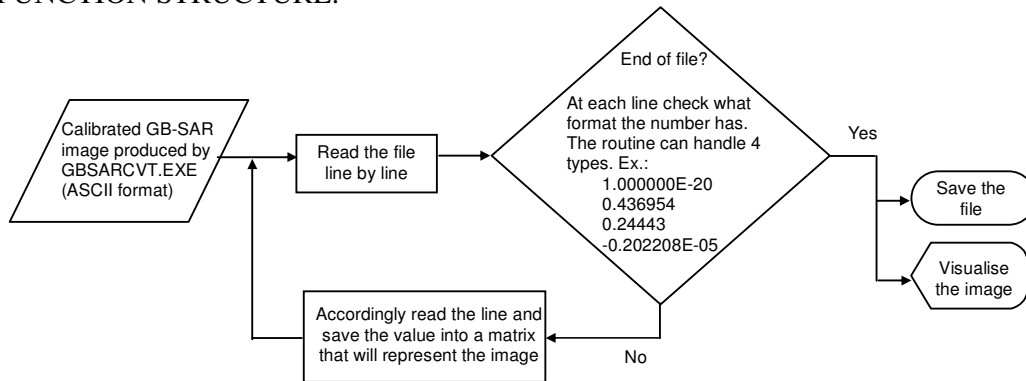
SCRIPT:

```
% ;+
% ; NAME:
% ;     GBSAR_min_RCS
% ;
% ; PURPOSE:
% ;     The purpose of this program is to compute the minimum radar cross
% ;     section for the GBSAR at different distance.
% ;
% ; INPUT PARAMETERS:
% ;     Distance entered by the user.
% ;
% ; OUTPUTS:
% ;     The min RCS
% ;
% ; CALLING SEQUENCE EXAMPLE:
% ;     Highlight the whole routine, right click and then select
% ;     'Evaluate Selection'
% ;
% ; MODIFICATION HISTORY:
% ;     Written by: Keith Morrison and Giuseppe Ottavianelli, 13/10/2005
% ;
```

A.10 GBSAR_read.pro

This IDL routine imports the fully polarisation calibrated data into ENVI.

FUNCTION STRUCTURE:



SCRIPT:

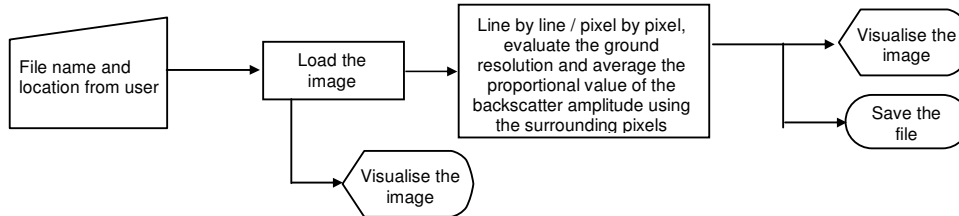
```

; GBSAR_read.pro
;
; PROGRAM IN BRIEF
;
; - Opens the selected GBSAR file. The number of
; columns (ftt) and rows (nrow) of the image can be found in the header.
; The header must be eliminated from the original file (or a copy of it)
; which is selected in the procedure. The file must not contain
; any additional row after the last digit.
; - Rearranges the single long list of numbers into a matrix of the given
; dimensions of Floating numbers.
; - The program can handle the four types of number structure.
; Examples follow:
; 1.000000E-20
; 0.436954
; 0.24443
; 0.202208E-05
;
;#####
;##### CHECK #####
;#####
; In the script you will find sections headed with the above 3 'check' lines.
; These sections are used to make cross validations on the data while the
; program is running. If you want you can delete these section or simply
; make them comments by adding semicolons at the beginning of the line.
;
; PROGRAM HISTORY
; Developed by G. Ottavianelli (August 2005)
; g.ottavianelli@tiscali.it
;
; COMPILE AND RUN from IDL "Run" menu
  
```

A.11 GBSAR_proportional.pro

This IDL routine computes a 4x4 cm pixel GB-SAR image that contains the correct proportional values of backscatter amplitude which depend on the system ground resolution at a given position in range and azimuth

FUNCTION STRUCTURE:



SCRIPT:

```

; PROGRAM IN BRIEF
;
; - Opens the selected GBSAR file that was previously processed
;   with GBSAR_read. The number of columns and rows is fixed.
; - It processes the Area of Interest in order to obtain a 4*4 cm
;   pixel image which contain the proportional values of backscatter
;   depending on the actual system resolution.
; - The output image can then be opened with ENVI:
;   col 1000 x row 500 (Floating Point) [BSQ]
;
;
;#####
;#####          CHECK          #####
;#####
; In the script you will find sections headed with the above 3 'check' lines.
; These sections are used to make cross validations on the data while the
; program is running. If you want you can delete these section or simply
; make them comments by adding semicolons at the beginning of the line.
;
;
; PROGRAM HISTORY
; Developed by G. Ottavianelli (May 2006)
;
;
; COMPILE AND RUN from IDL "Run" menu

```

A.12 GBSAR_sigma0.pro

This IDL routine transforms the GB-SAR amplitude data into backscatter coefficient values. This program is meant to be launched using the ENVI BASIC TOOLS/BAND MATHS on the main ENVI menu within ENVI.

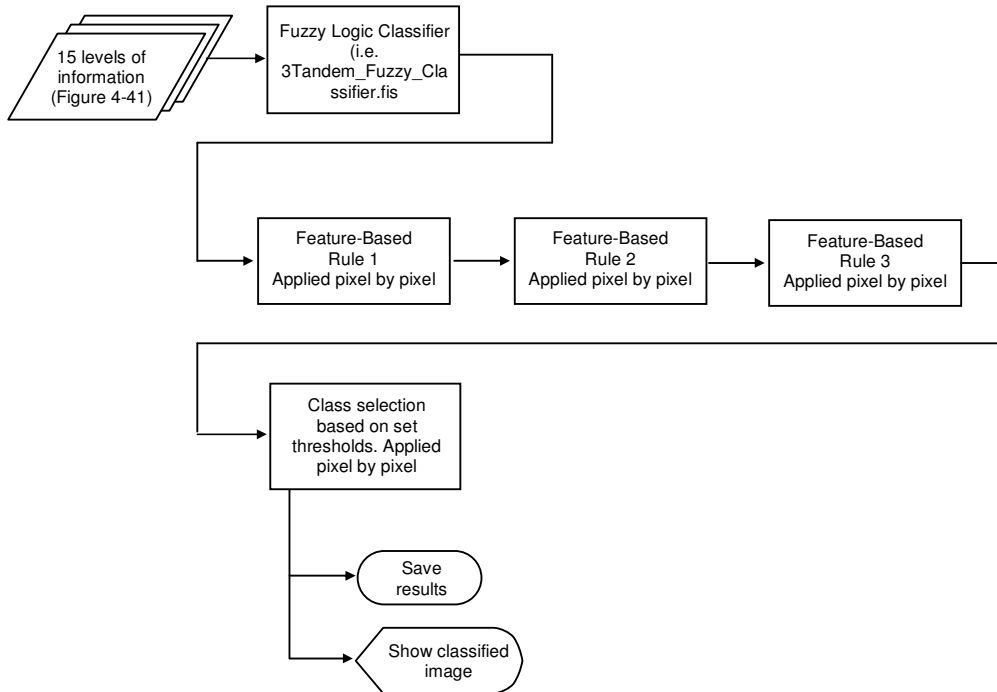
SCRIPT:

```
;+
; NAME:
;     GBSAR_sigma0
;
; PURPOSE:
;     The purpose of this program is to compute sigma 0 from the GBSAR
;     amplitude values.
;     This program is meant to be launched using
;     the ENVI BASIC TOOLS/BAND MATHS on the main ENVI menu within ENVI.
;     The recommended way to use this program is to place this
;     source code file (or save it to a *.sav file for ENVI Runtime)
;     in the save_add/ subfolder of the ENVI installation.
;     No editing of the "display.men" ASCII text file is required.
;
;     Please consult the ENVI documentation on "Band Maths" in the ENVI
;     Programmer's Guide for further information.
;
; CATEGORY:
;     ENVI Band Maths Function
;
; CALLING SEQUENCE:
;     GBSAR_sigma0(B1)
;
; USAGE:
;     After compiling, this program must be called directly from an
;     interactive session of ENVI as a Band function from
;     the BASIC TOOLS/BAND MATHS menu.
;
; INPUT PARAMETERS:
;     One band should be already opened.
;
; KEYWORD PARAMETERS:
;     None.
;
; OUTPUTS:
;     The new image can be saved into a file or into the FID memory.
;
; MODIFICATION HISTORY:
;     Written by: Giuseppe Ottavianelli, 25/08/2005
;-
```

A.13 land_use_classification.m

This Matlab function carries out the land-use classification procedure described in Section 4.9. The Fuzzy Rules can be found in Appendix C.

FUNCTION STRUCTURE:



SCRIPT:

```

function elements = land_use_classification (folder_files,
degree_of_ownership, degree_of_class_success, dimension, precision)

% ;+
% ; NAME:
% ; land_use_classification
% ;
% ; PURPOSE:
% ; The purpose of this program is to carry out the land-use
% ; classification. It interactively asks the user the files to import.
% ; These files must be prepared in advance by the user (i.e. cropping,
% ; the terrain correction and coregistration must be
% ; done before calling this routine).
% ;
% ;

```

```
% ;
% ; INPUT PARAMETERS:
% ;     folder_files           Folder containing all the necessary files
% ;     degree_of_ownership   As defined in Section 4.9.4 of the thesis
% ;     degree_of_class_success As defined in Section 4.9.4 of the thesis
% ;     dimension             Dimension of the files
% ;     precision             file precision
% ;
% ; The routine calles the FL classifier: 3_SAR_Tandem_Fuzzy_Classifier.fis
% ;
% ;
% ; OUTPUTS:
% ;     The classified image is saved with the suffix:
% ;     "_3tandemclassified"
% ;
% ; CALLING SEQUENCE EXAMPLE:
% ;     elements = land_use_classification (S:\Classification\26_26_02_1996,
0.6, 0.18, [40, 70], 'float32')
% ;
% ; MODIFICATION HISTORY:
% ;     Written by: Giuseppe Ottavianelli, 13/05/2006
% ;
```

Appendix B - Access to DORIS and DORIS Card Examples

B.1 How to access and use DORIS from Windows

DORIS 3.16 (Delft, 2005) has been installed on the Cranfield University Linux system. Currently (June 2006) Cranfield University is using the "CentOS" distribution of Red Hat Enterprise Linux 3, also known as RHEL3. This is functionally equivalent to Red Hat Linux 9 but is more robust.

DORIS is therefore accessible from any Linux machine or via a Linux emulator running on a Windows OS.

The additional supporting packages SNAPHU (unwrapper with statistical costs) and GETORB (DEOS precise orbits) have also been installed.

STEP 1 – Putty

- Log in a computer running Windows
- Go to the P drive (DFSRoot on 'Cnt')
- In the P drive, go to the "Terminal Emulators" folder and copy the 'Putty' executable file on your system (e.g. Z drive or desktop of your PC). Putty allows you to access a Linux system while on a Windows machine. Putty can also be easily found on the net.
- Run Putty. In the configuration window enter 'grid-fe-a' as the Host Name (or grid-fe-a.central.cranfield.ac.uk if you are not on campus). Always in Putty, look down the tree of categories & locate "SSH" - under that enable compression if coming from broadband (improves performance). Below that is "X11", in that section click the box for X11 forwarding but leave the "X Display location" box blank. Save the session with any name you want (this allows you to load it in the future without entering these settings again). Then click on Open. Enter your University Login and Password. You will be logged into your Linux drive as shown below.

```

CRANFIELD
login as: er052576
#####
Linux/UNIX Mailing List
#####

All users of campus Linux or UNIX services (Desktop Linux/Cluster Grid/Sun
Supercomputer) are strongly advised to subscribe to the Cranfield
"HPC-Users" mailing list. This is the main channel used by the HPC team
for alerting its users to service changes etc. All previous messages are
viewable in a message archive accessible via the "MailMan" web-link below.

Subscribing could not be easier - simply visit
http://mailman.cranfield.ac.uk & follow the on-screen instructions. Users
who were subscribed to the previous mailing list via "majordomo" do not
have to re-subscribe as they have already been migrated to the new
"MailMan" service.

#####
er052576@grid-fe-a.central.cranfield.ac.uk's password:
er052576@grid-fe-a [101] [12:10pm] [~] █

```

STEP 2 – Linux format: Exceed, PFE or dos2unix

- As you might already know, DORIS works by reading ASCII files that you create, which have the necessary information to tell DORIS which process to run (e.g. obtain the precise orbits, crop the files, coregister the two scenes etc). It is critical that all these files you create are in Linux format (i.e. with the correct End Of Line character). The figure below shows that in a Putty screen the files appear in different colours depending whether they are Windows (green) or Linux (white) formatted. There are three different options in order to make sure you files have the Linux format before calling DORIS.

```

CRANFIELD
login as: er052576
#####
Linux/UNIX Mailing List
#####

All users of campus Linux or UNIX services (Desktop Linux/Cluster Grid/Sun
Supercomputer) are strongly advised to subscribe to the Cranfield
"HPC-Users" mailing list. This is the main channel used by the HPC team
for alerting its users to service changes etc. All previous messages are
viewable in a message archive accessible via the "MailMan" web-link below.

Subscribing could not be easier - simply visit
http://mailman.cranfield.ac.uk & follow the on-screen instructions. Users
who were subscribed to the previous mailing list via "majordomo" do not
have to re-subscribe as they have already been migrated to the new
"MailMan" service.

#####
er052576@grid-fe-a.central.cranfield.ac.uk's password:
er052576@grid-fe-a [101] [12:10pm] [~] cd COHERENCE/19950625/
er052576@grid-fe-a [102] [12:13pm] [19950625] ls
01input.m_porbits          06input.filtazi          outdata/
02input.s_porbits          07input.fine             coherence.ras
03crop.txt                 08input.coregpm         coherence.ras.sh
04input.coregistration     09input.resample        slave_rs_mag.ras
05input.coarsecorr        10input.coherence       slave_rs_mag.ras.sh
06ainput_filtorange.txt    CPM_Data
er052576@grid-fe-a [103] [12:13pm] [19950625] █

```


- The first option is to use the standard Linux command `nedit`. If you are operating from a Windows OS, in order to visualise the Graphical User Interface of this Linux tool on your Windows screen, you have to first execute a software called Exceed. This software runs in the background and once started, you don't have to run it again. Exceed is part of a larger package provided by "Hummingbird Connectivity V7.1". In order to install it you have to contact the Computer Centre or directly Ramish on 07771531605.
- It is also possible to create the Doris files by using the Programmer's File Editor (PFE32.exe) in Windows and saving them in Unix format. The PFE is available in the P drive.
- The last option is to create them with Notepad and convert these Dos formatted files with the `dos2unix` command when working in Linux with Putty. Sometimes `dos2unix` does not have any effect on the selected files. In order to force the action, use the command with the `-n` option as below:

```
dos2unix -n 01input.m_readfiles 01input.m_readfiles
```

STEP 3 – Getting the data you want: Network or DVDs.

- Some original ERS 1/2 SAR data is available on the Linux system. These data have been read from tapes and digitally stored. All you need is for the Systems Group of the Computer Centre to make you a member of the "SARdata" group through which access to the data is controlled.
- The location of the data is: `/rh/u09b/SharedDrives/SARdata/`
- Once you are a member of the group, you can create a "soft link" to this directory thereby making it appear as if it is in your home directory. To achieve this, go to your home directory and type the following command:

```
ln -s /rh/u09b/SharedDrives/SARdata ./SARdata
```

- So you can refer to SAR data directories & files as being under the directory `~/SARdata/` rather than the full path above. Choice is yours but always remember that the data is read-only so you cannot write to the SARdata tree, but only open the files there and subsequently write results elsewhere that you have write permission.
- If you want to copy a file from these folders, you can use the following command as an example:

```
cp -R /rh/u09b/SharedDrives/SARdata/26061995 MyFolder
```

Where "MyFolder" is the folder in your Linux drive where you should be when typing the command.

- DVDs of the same ERS1/2 scenes, more recent ones, and of additional ENVISAT ASAR have also been obtained from ESA. Please ask Dr Hobbs for details.

STEP 4 – Use DORIS

- To call DORIS commands you can either call `doris` (for version 3.14) or `doris316` (for version 3.16).
- Below you can find examples of DORIS files used to run certain processes.
- It is important to keep in mind that the ODR files used by Getorb are also in the SARdata folder. The structure is the following:

```
/rh/u09b/SharedDrives/SARdata/ODR/ERS1  
/rh/u09b/SharedDrives/SARdata/ODR/ERS2  
/rh/u09b/SharedDrives/SARdata/ODR/ERS2int  
/rh/u09b/SharedDrives/SARdata/ODR/ENVISAT
```

- Using the commands

<code>cd ..</code>	To go one folder up
<code>cd directory_name</code>	To enter the folder
<code>ls</code>	To list the files and directories in a folder
<code>pwd</code>	To know what the current path is
- go to the directory where the DORIS files are stored in your Linux drive.
- After carefully reading the DORIS user manual (Kampes, 2005) you can start using the software.
- Once finished the session, close Putty by typing Logout or Exit.

For additional info contact:

Dr Les Oswald R.L.Oswald@cranfield.ac.uk ext. 2824

B.2 DORIS Card Examples

m_readfiles

```

#          _____          //
#          _____GENERAL OPTIONS_____          //
#          _____          //
SCREEN          debug          // level of output to
standard out
BEEP          warning          // level of beeping
BATCH          ON          // non-interactive
OVERWRITE          ON          // overwrite existing
files
PREVIEW          off          // SUNraster files with
cpxfiddle
MEMORY          20          // MB
LISTINPUT          ON          // copy this file to log
#          //
#          //
#          //
#          _____          //
#          _____CARDS TO BE USED_____          //
#          //
PROCESS          m_readfiles          // Read Master File
#          //
#          //
#          _____          //
#          _____OUTPUT FILES_____          //
#          //
LOGFILE          log19950626_25.out          //
M_RESFILE          master19950625.out          // parameter file
S_RESFILE          slave19950626.out          // parameter file
I_RESFILE          interferogram19950626_25.out          // parameter file
#          //
#          //
#          //
#          _____          //
#          _____READFILES_____          //
#          //
M_IN_METHOD          ERS          // Selected
ERS method to read header
M_IN_VOL          ../19950625/SCENE1/VDF_DAT.001          // name of
volumefile
M_IN_LEA          ../19950625/SCENE1/LEA_01.001          // name of
leaderfile
M_IN_NULL dummy          // name of nullfile
M_IN_DAT          ../19950625/SCENE1/DAT_01.001          // name of
datafile
#          //
#          //
#          //
#          //
STOP          // mandatory

```

m_crop

```

#          _____          //
#          _____GENERAL OPTIONS_____          //
#          _____          //
SCREEN          debug          // level of output to
standard out
BEEP          warning          // level of beeping
BATCH          ON          // non-interactive
OVERWRITE          ON          // overwrite existing
files
PREVIEW          off          // SUNraster files with
cpxfiddle
MEMORY          20          // MB
LISTINPUT          ON          // copy this file to log
#          //
#          //
#          //
#          _____CARDS TO BE USED_____          //
#          //
PROCESS          m_crop          // get precise orbits
#          //
#          //
#          _____          //
#          _____OUTPUT FILES_____          //
#          //
LOGFILE          log19950626_25.out          //
M_RESFILE          master19950625.out          // parameter
file
S_RESFILE          slave19950626.out          // parameter
file
I_RESFILE          interferogram19950626_25.out          //
parameter file
#          //
#          //
#          //
#          _____CROP_____          //
#          //
M_CROP_IN          ../19950625/SCENE1/DAT_01.001          // name of
file to be cropped
M_CROP_OUT          master19950625.raw          // name of the
output cropped file
M_DBOW          19294 25293 250 1449          //          CROPPED
PIXELS:
#          //          linelow  linehi  pixellow
pixelhi
#          //
#          //
#          //
#          //
STOP          // mandatory

```

m_porbits

```

#          _____          //
#          _____GENERAL OPTIONS_____          //
#          _____          //
SCREEN          debug          // level of output to
standard out
BEEP          warning          // level of beeping
BATCH          ON          // non-interactive
OVERWRITE          ON          // overwrite existing
files
PREVIEW          off          // SUNraster files with
cpxfiddle
MEMORY          20          // MB
LISTINPUT          ON          // copy this file to log
#          //
#          //
#          //
#          _____CARDS TO BE USED_____          //
#          //
PROCESS          m_porbits          // get precise orbits
#          //
#          //
#          _____          //
#          _____OUTPUT FILES_____          //
#          //
LOGFILE          log19950626_25.out          //
M_RESFILE          master19950625.out          //
parameter file
S_RESFILE          slave19950626.out          //
parameter file
I_RESFILE          interferogram19950626_25.out          //
parameter file
#          //
#          //
#          //
#          _____PORBITS_____          //
#          //
M_ORBDIR          /rh/u09b/cc/SARdata/ODR/ERS1          // Directory
containing the files
M_ORB_EXTRATIME 210          // Time
before first line
M_ORB_INTERVAL 15          // Time
between data
#          //
#          //
#          //
#          //
STOP          // mandatory

```

coarseorb

```
#          _____          //
#          _____GENERAL OPTIONS_____ //
#          _____          //
SCREEN          debug          // level of output to
standard out
BEEP          warning          // level of beeping
BATCH          ON          // non-interactive
MEMORY          50          // MB
OVERWRITE          OFF          // overwrite existing
files
LISTINPUT          ON          // copy this file to log
#          //
#          //
#          _____          //
#          _____CARDS TO BE USED_____ //
#          //
PROCESS          coarseorb          // Coregistration of the images
#          // No cards required
#          //
#          _____          //
#          _____OUTPUT FILES_____ //
#          //
LOGFILE          log19950626_25.out          //
M_RESFILE          master19950625.out          // parameter
file
S_RESFILE          slave19950626.out          // parameter
file
I_RESFILE          interferogram19950626_25.out          //
parameter file
#          //
#          //
#          //
STOP          // mandatory
```

coarsecorr

```

#           _____           //
#           _____GENERAL OPTIONS_____           //
#           _____           //
SCREEN          debug                // level of output to
standard out
BEEP            warning              // level of beeping
BATCH           ON                   // non-interactive
MEMORY          50                   // MB
OVERWRITE       OFF                  // overwrite existing
files
LISTINPUT       ON                   // copy this file to log
#               //
#               //
#           _____           //
#           _____CARDS TO BE USED_____           //
#           _____           //
PROCESS         coarsecorr           // Coregistration of the images
#               // based on correlation.
#               //
#           _____           //
#           _____OUTPUT FILES_____           //
#           _____           //
LOGFILE         log19950626_25.out   //
M_RESFILE       master19950625.out   // parameter
file
S_RESFILE       slave19950626.out    // parameter
file
I_RESFILE       interferogram19950626_25.out //
parameter file
#               //
#               //
#           _____           //
#           _____COARSE CORR_____           //
#           _____           //
CC_METHOD       magfft               // default
CC_NWIN         60                   // number of windows
CC_WINSIZE      64 64                // size of windows
CC_INITOFF      orbit                // use result of orbits
#               //
#               //
#               //
STOP            // mandatory

```

m_filtazi

```

#          _____          //
#          _____GENERAL OPTIONS_____          //
#          _____          //
SCREEN          debug          // level of output to
standard out
BEEP          warning          // level of beeping
BATCH          ON          // non-interactive
MEMORY          250          // MB
OVERWRITE          ON          // overwrite existing
files
LISTINPUT          ON          // copy this file to log
#          //
#          //
#          _____          //
#          _____CARDS TO BE USED_____          //
#          //
PROCESS          m_filtazi          // Master Azimuth Filter
PROCESS          s_filtazi          // Master Azimuth Filter
#          //
#          //
#          _____          //
#          _____OUTPUT FILES_____          //
#          //
LOGFILE          log19950626_25.out          //
M_RESFILE          master19950625.out          // parameter
file
S_RESFILE          slave19950626.out          // parameter
file
I_RESFILE          interferogram19950626_25.out          //
parameter file
#          //
#          //
#          _____          //
#          _____AZIMUTH FILTERING_____          //
#          //
AF_BLOCKSIZE          1024          //
fftlenth each column
AF_OVERLAP          64          // hbs
AF_HAMMING          0.75          // de- and
re-weighted
AF_OUT_MASTER          master19950625_afilt          //
AF_OUT_SLAVE          slave19950626_afilt          //
AF_OUT_FORMAT          cr4          //
#          //
#          //
#          //
STOP          // mandatory

```


fine

```

#          _____          //
#          _____GENERAL OPTIONS_____          //
#          //
SCREEN          debug          // level of output to
standard out
BEEP          warning          // level of beeping
BATCH          ON          // non-interactive
MEMORY          50          // MB
OVERWRITE          OFF          // overwrite existing
files
LISTINPUT          ON          // copy this file to log
#          //
#          //
#          _____          //
#          _____CARDS TO BE USED_____          //
#          //
PROCESS          fine          // fine coregistration
#          //
#          //
#          _____          //
#          _____OUTPUT FILES_____          //
#          //
LOGFILE          log19950626_25.out          //
M_RESFILE          master19950625.out          // parameter
file
S_RESFILE          slave19950626.out          // parameter
file
I_RESFILE          interferogram19950626_25.out          //
parameter file
#          //
#          //
#          _____          //
#          _____FINE COREGISTRATION_____          //
#          //
FC_METHOD          magfft          //
FC_NWIN          500          // number of
windows
FC_WINSIZE          32 32          // size of
windows
FC_ACC          4 4          // search
window, 2^n
FC_INITOFF          COARSECORR          // use result
of coarse to compute first
FC_OSFACTOR          16          // oversampling
factor
#          //
#          //
#          //
STOP          // mandatory

```

coregpm

```

#           _____ //
#           _____GENERAL OPTIONS_____ //
#           //
SCREEN      debug          // level of output to
standard out
BEEP        warning       // level of beeping
BATCH       ON            // non-interactive
MEMORY      50            // MB
OVERWRITE   OFF          // overwrite existing
files
LISTINPUT   ON           // copy this file to log
#           //
#           //
#           _____ //
#           _____CARDS TO BE USED_____ //
#           //
PROCESS     coregpm       // Estimate coregistration
parameters
#           //
#           //
#           _____ //
#           _____OUTPUT FILES_____ //
#           //
LOGFILE     log19950626_25.out           //
M_RESFILE   master19950625.out          // parameter
file
S_RESFILE   slave19950626.out           // parameter
file
I_RESFILE   interferogram19950626_25.out //
parameter file
#           //
#           //
#           _____ //
#           _____COMPUTE COREGISTRATION PARAMETERS_____ //
#           //
CPM_THRESHOLD 0.8          //
CPM_DEGREE    1           //
CPM_MAXITER   20          //
#           //
#           //
#           //
STOP          // mandatory

```

resample

```

#           _____ //
#           _____GENERAL OPTIONS_____ //
#           //
SCREEN          debug           // level of output to
standard out
BEEP            warning         // level of beeping
BATCH           ON              // non-interactive
MEMORY          50              // MB
OVERWRITE       OFF            // overwrite existing
files
LISTINPUT       ON              // copy this file to log
#              //
#              //
#              //
#           _____CARDS TO BE USED_____ //
#           //
PROCESS          resample       // Estimate   coregistration
parameters
#              //
#              //
#           _____OUTPUT FILES_____ //
#           //
LOGFILE          log19950626_25.out           //
M_RESFILE        master19950625.out           // parameter
file
S_RESFILE        slave19950626.out           // parameter
file
I_RESFILE        interferogram19950626_25.out //
parameter file
#              //
#              //
#           _____RESAMPLING SLAVE_____ //
#           //
RS_METHOD        cc6p           //
RS_OUT_FILE      slave19950626_afilt_res
RS_OUT_FORMAT    cr4
RS_DBOW          19294 25293 250 1449 //   linelow   linehigh
pexellow pixelhigh
#              //
#              //
#              //
STOP             // mandatory

```

filrange

```

#          _____          //
#          _____GENERAL OPTIONS_____          //
#          _____          //
SCREEN          debug          // level of output to
standard out
BEEP          warning          // level of beeping
BATCH          ON          // non-interactive
MEMORY          50          // MB
OVERWRITE          OFF          // overwrite existing
files
LISTINPUT          ON          // copy this file to log
#          //
#          //
#          _____          //
#          _____CARDS TO BE USED_____          //
#          //
PROCESS          filrange          // Estimate      coregistration
parameters
#          //
#          //
#          _____          //
#          _____OUTPUT FILES_____          //
#          //
LOGFILE          log19950626_25.out          //
M_RESFILE          master19950625.out          // parameter
file
S_RESFILE          slave19950626.out          // parameter
file
I_RESFILE          interferogram19950626_25.out          //
parameter file
#          //
#          //
#          //
#          _____RESAMPLING SLAVE_____ //
#          //
RF_METHOD          adaptive          //
RF_FFLENGTH          128
RF_NLMEAN          15
RF_THRESHOLD          5          //
RF_HAMMING          0.75          //
RF_OVERSAMPLE          4
RF_WEIGHTCORR          OFF
RF_OUT_MASTER          master19950625_afilt_rfilt
RF_OUT_SLAVE          slave19950626_afilt_res_rfilt
RF_OUT_FORMAT          cr4
#          //
#          //
#          //
STOP          // mandatory

```

interfero

```

#          ___          ___          //
#          ___GENERAL OPTIONS___    //
#          //
SCREEN          debug                // level of output to
standard out
BEEP           warning               // level of beeping
BATCH          ON                    // non-interactive
MEMORY         50                    // MB
OVERWRITE      OFF                   // overwrite existing
files
LISTINPUT      ON                    // copy this file to log
#          //
#          //
#          ___          ___          //
#          ___CARDS TO BE USED___    //
#          //
PROCESS        interfero             //
#          //
#          //
#          ___          ___          //
#          ___OUTPUT FILES___       //
#          //
LOGFILE        log19950626_25.out     //
M_RESFILE      master19950625.out     // parameter
file
S_RESFILE      slave19950626.out      // parameter
file
I_RESFILE      interferogram19950626_25.out //
parameter file
#          //
#          //
#          ___          ___          //
#          ___INTERFERO___          //
#          //
INT_OUT_CINT   int_complex_19950626_25 // optional complex
interferemogram
INT_OUT_INT    int_real_19950626_25   // optional real
interferemogram
INT_MULTILOOK  10 2                   // factor lines,pixels
#          //
#          //
#          //
STOP           // mandatory

```

comprefpha

```

#          _____          //
#          _____GENERAL OPTIONS_____          //
#          //
SCREEN          debug          // level of output to
standard out
BEEP          warning          // level of beeping
BATCH          ON          // non-interactive
MEMORY          50          // MB
OVERWRITE          OFF          // overwrite existing
files
LISTINPUT          ON          // copy this file to log
#          //
#          //
#          _____          //
#          _____CARDS TO BE USED_____          //
#          //
PROCESS          comprefpha          //
#          //
#          //
#          _____          //
#          _____OUTPUT FILES_____          //
#          //
LOGFILE          log19950626_25.out          //
M_RESFILE          master19950625.out          // parameter
file
S_RESFILE          slave19950626.out          // parameter
file
I_RESFILE          interferogram19950626_25.out          //
parameter file
#          //
#          //
#          //
#          _____          //
#          _____COMPREFPHA_____          //
#          //
FE_METHOD          porbits          //
FE_DEGREE          5          //
FE_NPOINTS          501          //
#          //
#          //
#          //
STOP          // mandatory

```

subtrefpha

```

#          _____          //
#          _____GENERAL OPTIONS_____          //
#          //
SCREEN          debug          // level of output to
standard out
BEEP          warning          // level of beeping
BATCH          ON          // non-interactive
MEMORY          50          // MB
OVERWRITE          OFF          // overwrite existing
files
LISTINPUT          ON          // copy this file to log
#          //
#          //
#          //
#          _____          //
#          _____CARDS TO BE USED_____          //
#          //
PROCESS          subtrefpha          //
#          //
#          //
#          _____          //
#          _____OUTPUT FILES_____          //
#          //
LOGFILE          log19950626_25.out          //
M_RESFILE          master19950625.out          // parameter
file
S_RESFILE          slave19950626.out          // parameter
file
I_RESFILE          interferogram19950626_25.out          //
parameter file
#          //
#          //
#          //
#          _____          //
#          _____SUBTREFPHA_____          //
#          //
SRP_METHOD          polynomial          //
SRP_OUT_CINT          int_complex_srp_19950626_25          //
SRP_MULTILOOK          1 1          //
#          //
#          //
#          //
STOP          // mandatory

```

coherence

```

#           _____           //
#           _____GENERAL OPTIONS_____           //
#           //
SCREEN          debug           // level of output to
standard out
BEEP            warning         // level of beeping
BATCH           ON              // non-interactive
MEMORY          50              // MB
OVERWRITE       OFF             // overwrite existing
files
LISTINPUT       ON              // copy this file to log
#               //
#               //
#               //
#           _____           //
#           _____CARDS TO BE USED_____           //
#           //
PROCESS         coherence       //
#               //
#               //
#           _____           //
#           _____OUTPUT FILES_____           //
#           //
LOGFILE         log19950626_25.out           //
M_RESFILE       master19950625.out           // parameter
file
S_RESFILE       slave19950626.out           // parameter
file
I_RESFILE       interferogram19950626_25.out           //
parameter file
#               //
#               //
#               //
#           _____           //
#           _____COHERENCE_____           //
#           //
COH_OUT_CCOH    coherence_complex_19950626_25           //
COH_OUT_COH     coherence_real_19950626_25           //
COH_MULTILOOK  10 2           // multilooking
COH_WINSIZE    10 2           // window size
#               //
#               //
#               //
STOP            // mandatory

```


filtphase

```

#          _____          //
#          _____GENERAL OPTIONS_____          //
#          _____          //
SCREEN          debug          // level of output to
standard out
BEEP          warning          // level of beeping
BATCH          ON          // non-interactive
MEMORY          50          // MB
OVERWRITE          OFF          // overwrite existing
files
LISTINPUT          ON          // copy this file to log
#          //
#          //
#          _____          //
#          _____CARDS TO BE USED_____          //
#          //
PROCESS          filtphase          //
#          //
#          //
#          _____          //
#          _____OUTPUT FILES_____          //
#          //
LOGFILE          log19950626_25.out          //
M_RESFILE          master19950625.out          // parameter
file
S_RESFILE          slave19950626.out          // parameter
file
I_RESFILE          interferogram19950626_25.out          //
parameter file
#          //
#          //
#          _____          //
#          _____FILTER PHASE_____          //
#          //
PF_IN_FILE          int_complex_srp_19950626_25          600
//
PF_OUT_FILE          int_complex_srp_19950626_25_gold08win32          //
PF_METHOD          goldstein          //
PF_ALPHA          0.8
//
PF_OVERLAP          15          //
PF_BLOCKSIZE          32          //
#          //
c PF_KERNEL          3 1 1 1
#          //
#          //
#          //
#          //
STOP          // mandatory

```

unwrap

```

#          _____          //
#          _____GENERAL OPTIONS_____          //
#          _____          //
SCREEN          debug          // level of output to
standard out
BEEP          warning          // level of beeping
BATCH          ON          // non-interactive
MEMORY          50          // MB
OVERWRITE          OFF          // overwrite existing
files
LISTINPUT          ON          // copy this file to log
#          //
#          //
#          //
#          _____          //
#          _____CARDS TO BE USED_____          //
#          //
PROCESS          unwrap          //
#          //
#          //
#          _____          //
#          _____OUTPUT FILES_____          //
#          //
LOGFILE          log19950626_25.out          //
M_RESFILE          master19950625.out          // parameter
file
S_RESFILE          slave19950626.out          // parameter
file
I_RESFILE          interferogram19950626_25.out          //
parameter file
#          //
#          //
#          //
#          _____          //
#          _____UNWRAP_____          //
#          //
UW_METHOD          SNAPHU
UW_OUT_FILE          unwrapped_19950626_25
UW_OUT_FORMAT          HGT
UW_SNAPHU_MODE          TOPO
UW_SNAPHU_COH          coherence_real_19950626_25_BiasCorr
UW_SNAPHU_INIT          MST
UW_SNAPHU_VERBOSE ON
#          //
#          //
#          //
STOP          // mandatory

```

slant2h

```

#          _____          //
#          _____GENERAL OPTIONS_____          //
#          _____          //
SCREEN          debug          // level of output to
standard out
BEEP          warning          // level of beeping
BATCH          ON          // non-interactive
MEMORY          50          // MB
OVERWRITE          OFF          // overwrite existing
files
LISTINPUT          ON          // copy this file to log
#          //
#          //
#          //
#          _____          //
#          _____CARDS TO BE USED_____          //
#          //
PROCESS          slant2h          //
#          //
#          //
#          //
#          _____          //
#          _____OUTPUT FILES_____          //
#          //
LOGFILE          log19950626_25.out          //
M_RESFILE          master19950625.out          // parameter
file
S_RESFILE          slave19950626.out          // parameter
file
I_RESFILE          interferogram19950626_25.out          //
parameter file
#          //
#          //
#          //
#          _____          //
#          _____S2H CONVERSION_____          //
#          //
S2H_METHOD          ambiguity          //
S2H_OUT_HEI          s2h_heights_19950626_25          //
S2H_OUT_LAM          s2h_lambda_19950626_25          //
S2H_OUT_PHI          s2h_phi_19950626_25          //

#          //
#          //
#          //
STOP          // mandatory

```

geocode

```

#           ___GENERAL OPTIONS___           //
#           ___GENERAL OPTIONS___           //
#           //                               //
SCREEN      debug                          // level of output to
standard out
BEEP        warning                        // level of beeping
BATCH       ON                             // non-interactive
MEMORY      50                             // MB
OVERWRITE   OFF                            // overwrite existing
files
LISTINPUT   ON                             // copy this file to log
#           //                               //
#           //                               //
#           //                               //
#           ___CARDS TO BE USED___         //
#           //                               //
PROCESS     geocode                         //
#           //                               //
#           //                               //
#           //                               //
#           ___OUTPUT FILES___            //
#           //                               //
LOGFILE     log19950626_25.out              //
M_RESFILE   master19950625.out             // parameter
file
S_RESFILE   slave19950626.out              // parameter
file
I_RESFILE   interferogram19950626_25.out   //
parameter file
#           //                               //
#           //                               //
#           //                               //
#           ___GEOCODE___                 //
#           //                               //
GEO_OUT_PHI geo_phi25061995                //
GEO_OUT_LAM geo_lambda25061995            //
#           //                               //
#           //                               //
#           //                               //
STOP        // mandatory

```

Appendix C - Fuzzy Logic Classifier Rules

C.1 Fuzzy Rules

1. If (1_DCCoinMag is Low) and (BCCoinMag is Low) then (Laggon is YES/Building is NOT/Trading phase is NOT/Ccy_operations is NOT/Capped is NOT/Restored_LowMag is NOT/Restored_HighMag is NOT) (1)
2. If (1_DCCoinMag is High) and (BCCoinMag is Low) then (Laggon is NO/Building is YES/Trading phase is NOT/Ccy_operations is NOT/Capped is NOT/Restored_LowMag is NOT/Restored_HighMag is NOT) (1)
3. If (1_DCCoinMag is High) and (BCCoinMag is Low) and (BSCoinMag is not Low) and (MASTERBACKINT is Low) and (BACKRATIO is High) and (SLAVEBACKINT is Low) then (Laggon is NO/Building is NOT/Trading phase is NOT/Ccy_operations is NOT/Capped is NOT/Restored_LowMag is NOT/Restored_HighMag is NOT) (1)
4. If (1_DCCoinMag is Low) and (BCCoinMag is not Medium) and (BSCoinMag is Low) and (MASTERBACKINT is not Low) and (BACKRATIO is High) and (SLAVEBACKINT is not Low) then (Trading phase is YES) (1)
5. If (1_DCCoinMag is Low) and (BCCoinMag is not Medium) and (BSCoinMag is Low) and (MASTERBACKINT is Low) and (BACKRATIO is High) and (SLAVEBACKINT is Low) then (Trading phase is YES) (1)
6. If (1_DCCoinMag is not Low) and (BCCoinMag is not High) and (BSCoinMag is Low) then (Restored_LowMag is YES) (1)
7. If (1_DCCoinMag is Low) and (BCCoinMag is Low) and (BSCoinMag is Low) then (Restored_LowMag is YES) (1)
8. If (1_DCCoinMag is Low) and (BCCoinMag is Low) and (BSCoinMag is Low) and (MASTERBACKINT is not Low) and (BACKRATIO is High) and (SLAVEBACKINT is not Low) then (Ccy_operations is YES) (1)
9. If (1_DCCoinMag is High) then (Laggon is YES/Building is NOT/Trading phase is YES/Ccy_operations is YES/Capped is NOT/Restored_LowMag is NOT/Restored_HighMag is YES) (1)
10. If (1_DCCoinMag is Medium) then (Laggon is NO/Building is NOT/Trading phase is YES/Ccy_operations is NOT/Capped is YES/Restored_LowMag is YES/Restored_HighMag is NO) (0.7)
11. If (1_DCCoinMag is High) then (Laggon is YES/Building is YES/Trading phase is NOT/Ccy_operations is NOT/Capped is YES/Restored_LowMag is YES/Restored_HighMag is NO) (0.7)
12. If (1_DCCoinMag is High) then (Laggon is YES/Building is YES/Trading phase is NOT/Ccy_operations is NOT/Capped is YES/Restored_LowMag is YES/Restored_HighMag is NO) (0.7)
13. If (BCCoinMag is Medium) then (Laggon is NO/Building is NOT/Trading phase is NOT/Ccy_operations is YES/Ccy_operations is YES/Capped is NOT/Restored_LowMag is YES/Restored_HighMag is NO) (0.7)
14. If (BCCoinMag is High) then (Laggon is YES/Building is YES/Trading phase is YES/Ccy_operations is YES/Capped is YES/Restored_LowMag is YES/Restored_HighMag is NO) (0.7)
15. If (BCCoinMag is Low) then (Laggon is YES/Building is NOT/Trading phase is YES/Ccy_operations is YES/Capped is YES/Restored_LowMag is YES/Restored_HighMag is NO) (0.7)
16. If (BCCoinMag is High) then (Laggon is YES/Building is YES/Trading phase is NOT/Ccy_operations is NOT/Capped is YES/Restored_LowMag is NOT/Restored_HighMag is NO) (0.9)
17. If (BSCoinMag is Low) and (SLAVEBACKINT is Low) then (Laggon is YES/Building is NOT/Trading phase is NOT/Ccy_operations is NOT/Capped is NOT/Restored_LowMag is NOT/Restored_HighMag is NO) (0.4)
18. If (BSCoinMag is Low) and (SLAVEBACKINT is Low) then (Laggon is YES/Building is NOT/Trading phase is NOT/Ccy_operations is NOT/Capped is NOT/Restored_LowMag is NOT/Restored_HighMag is NO) (1)
19. If (MASTERBACKINT is Low) and (SLAVEBACKINT is Low) then (Laggon is YES/Building is NOT/Trading phase is NOT/Ccy_operations is NOT/Capped is NOT/Restored_LowMag is NOT/Restored_HighMag is NO) (1)
20. If (1_DCCoinMag is Low) and (BCCoinMag is Low) and (BSCoinMag is Low) and (MASTERBACKINT is Low) then (Laggon is YES/Building is NOT/Trading phase is NOT/Ccy_operations is NOT/Capped is NOT/Restored_LowMag is NOT/Restored_HighMag is NO) (1)
21. If (1_DCCoinMag is Low) and (BCCoinMag is Low) and (BSCoinMag is Low) and (SLAVEBACKINT is Low) then (Laggon is YES/Building is NOT/Trading phase is NOT/Ccy_operations is NOT/Capped is NOT/Restored_LowMag is NOT/Restored_HighMag is NO) (1)
22. If (1_DCCoinMag is Low) and (BCCoinMag is Low) and (BSCoinMag is Low) and (MASTERBACKINT is Low) and (SLAVEBACKINT is Low) then (Laggon is YES/Building is NOT/Trading phase is NOT/Ccy_operations is NOT/Capped is NOT/Restored_LowMag is NOT/Restored_HighMag is NO) (1)
23. If (1_DCCoinMag is Low) and (BCCoinMag is Low) and (BSCoinMag is Low) and (MASTERBACKINT is Low) and (SLAVEBACKINT is Low) and (BACKRATIO is High) and (SLAVEBACKINT is Low) then (Laggon is YES/Building is NOT/Trading phase is NOT/Ccy_operations is NOT/Capped is NOT/Restored_LowMag is NOT/Restored_HighMag is NO) (1)
24. If (1_DCCoinMag is Low) and (BCCoinMag is Low) and (BSCoinMag is Low) and (MASTERBACKINT is Low) and (SLAVEBACKINT is Low) and (BACKRATIO is High) and (SLAVEBACKINT is Low) then (Laggon is YES/Building is NOT/Trading phase is NOT/Ccy_operations is NOT/Capped is NOT/Restored_LowMag is NOT/Restored_HighMag is NO) (1)
25. If (1_DCCoinMag is Low) and (BCCoinMag is Low) and (BSCoinMag is Low) and (BACKRATIO is High) and (SLAVEBACKINT is Low) then (Laggon is YES/Building is NOT/Trading phase is NOT/Ccy_operations is NOT/Capped is NOT/Restored_LowMag is NOT/Restored_HighMag is NO) (1)
26. If (1_DCCoinMag is High) and (BCCoinMag is not High) and (BSCoinMag is Medium) and (BACKRATIO is High) and (SLAVEBACKINT is High) and (BSCoinMag is Low) then (Laggon is NO/Building is NOT/Trading phase is YES/Ccy_operations is YES/Capped is NOT/Restored_LowMag is NOT/Restored_HighMag is NO) (0.7)
27. If (BCCoinMag is not Low) then (Laggon is NO/Building is NOT/Trading phase is YES/Ccy_operations is YES/Capped is NOT/Restored_LowMag is NOT/Restored_HighMag is NO) (0.7)

Appendix D - L-band SAR Mission Analysis and Design

D.1 Mission Analysis and Design

The mission analysis and design developed in this section is based on space system engineering and radar systems material provided respectively in Wertz and Larson (1999) and Elachi (1988) and knowledge acquired during the Master of Science in Astronautics and Space Engineering course, read by the author at Cranfield University. The author also acknowledges the support of Dr Helmut Rott and Dr Peter Schrotter for the analysis of the L band resolution calculations. The analysis focuses only on the orbit parameters and the spatial and temporal resolutions. All other spacecraft subsystems are not considered.

The mission requirements are listed in Section 7.2.6, with the additional specification of achieving full coverage. In order to reduce the spacecraft mass, the baseline system design envisages the utilisation of a low-weight radar payload similar to the Israeli TecSAR satellite previously presented. As explained by Blumberg (2007), such a radar antenna system has been extensively validated with an airborne predecessor flown on a Boeing 737 which achieved a 1 m ground resolution with full polarisation.

The satellite payload therefore consists of a deployable Cassegrain type antenna with a parabolic reflector. As for the TecSAR satellite, this antenna does not allow the beam to be electronically steered. As a solution, the system will have three L-band feeders with a dual-polarised SAR electronic module. The multi-feeder configuration, which is common in telecommunication satellites and it has been presented by Heer and Shutie (2005), can achieve a flexible imaging capability and a larger potential imaging swath. In practice, each single beam illuminates a specific sub-swath of the total SAR image. Specific technical details on the antenna design and sub-systems (e.g. deployable structure, electronic sub-system) are beyond the scope of this research.

The satellite is envisaged to be 3-axis stabilized and with a tilting capability to increase the incidence angle from 18° up to 44°. Redundancy of momentum wheels and attitude thrusters would be one of the main system needs.

Taking into account orbit mechanics constraints, swath requirements for complete coverage, ground resolution requirements, PRF constraints, SNR, a trade-off analysis led to the selection of an orbit with an altitude of 843 km, an inclination of 98.62° and a right ascension of the ascending node of 359.21°. The orbit trade-off is presented in Section D-2. The visualisation in these figures is obtained with the Satellite Tool Kit

(STK), a flexible commercial-off-the-shelf analysis software developed by Analytical Graphics, Inc.

The achieved SAR antenna parameters are presented in Table D-1 and the computed values for these specifications are listed in Table D-2. Three acquisitions modes can be envisaged. The achieved resolutions in range and azimuth with signal and dual polarisation for both the minimum and maximum incidence angles are presented above in Table D-3.

Table D-1. Antenna Parameters

Frequency	1.41 GHz
Wavelength	21.3 cm
Antenna Diameter	5.5 m
Antenna type	Cassegrain
Feeders type	Square horns
Number of feeders	3
Antenna Efficiency	50 %
Transmitting Power	4 kW
Power Transmitting Efficiency	50 %
Bandwidth	85 MHz
Receiver Noise Temperature	600° K
Minimum incidence angle	18 °
Maximum incidence angle	44 °

Table D-3. Signal parameters and swath capabilities.

Antenna Gain	36 dB
Receive Power	7.49 pW
Noise Power	0.704 pW
Signal To Noise Ratio	10.3 dB
Beam Width	2.71 °
Swath Width with 1 feeder	44.9 km
Total swath width with 3 feeders	135.2 Km
Potential swath by steering the satellite	514.7 Km
PRF (with 1.1 margin) at a 22.5° incidence angle	2800

Table D-3. Acquisition modes: range and azimuth resolution.

Mode	No. of Feeders	18° Inc. Angle		44° Inc. Angle	
		Single polarization	Dual polarization	Single polarization	Dual polarization
StripMode	1 feeder	5.69 m x 2.75 m	11.39 m x 5.5 m	2.53 m x 2.75 m	5.07 m x 5.5 m
ScanMode1	2 feeders	5.69 m x 5.5 m	11.39 m x 11 m	2.53 m x 5.5 m	5.07 m x 11 m
ScanMode2	3 feeders	5.69 m x 8.25 m	11.39 m x 16.50 m	2.53 m x 8.25 m	5.07 m x 16.50 m

D.2 Orbit Selection

Due to the advantage of having almost constant sunlight illumination, a dusk-dawn sun-synchronous orbit is selected. Figure D-1 shows the trade-off between the orbit altitude and the full coverage requirement. For each altitude a different instantaneous access area is obtained. By comparing this image swath with the ground track separation for the different orbits, it is found that the optimal solution is the 4-day repeat pass orbit with 57 cycles per repeat pass at an altitude of 843 km. At this altitude the image swath is 514 km, achievable by the tilting capabilities of the satellite.

In order to achieve the 24 hour repeat pass for interferometric acquisitions a 4-satellite scenario can be developed with each satellite on the same orbit with a true anomaly separation of 90° from each other (e.g. like the COSMO-SkyMed constellation). The computed interferometric critical baseline is circa of 850 m. Figure D-2 shows the various achievable swaths and an example of the ground track and coverage of the satellite.

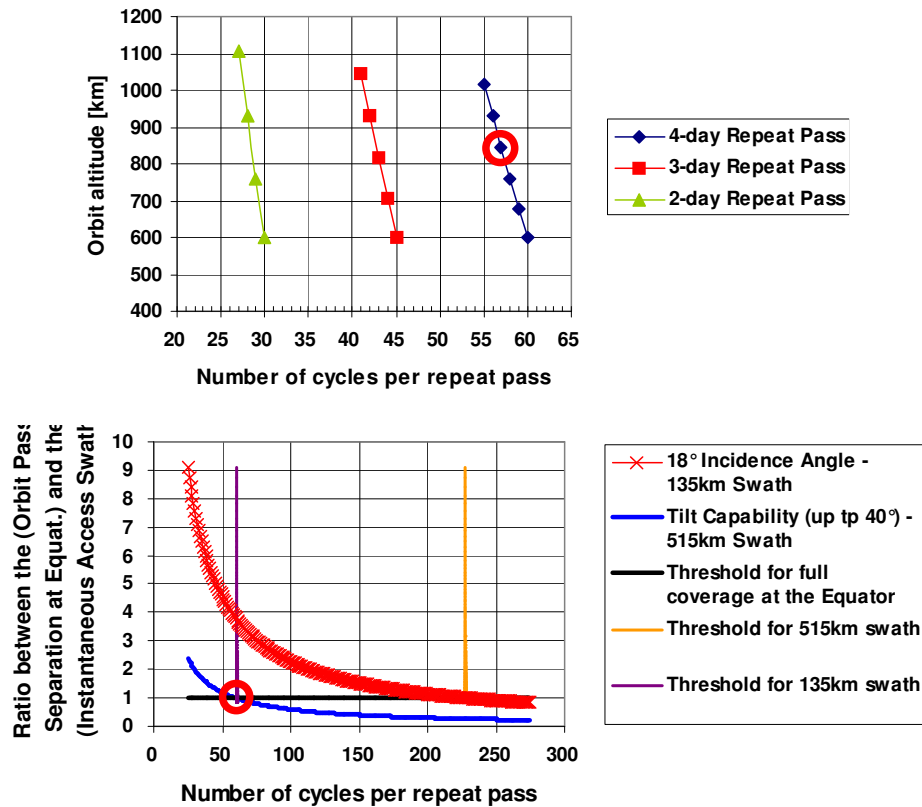


Figure D-1. Trade-off between Number of cycles per repeat pass and Orbit altitude and between the Number of cycles per repeat pass and the Pass Separation. The red circle identifies the selected orbit altitude.

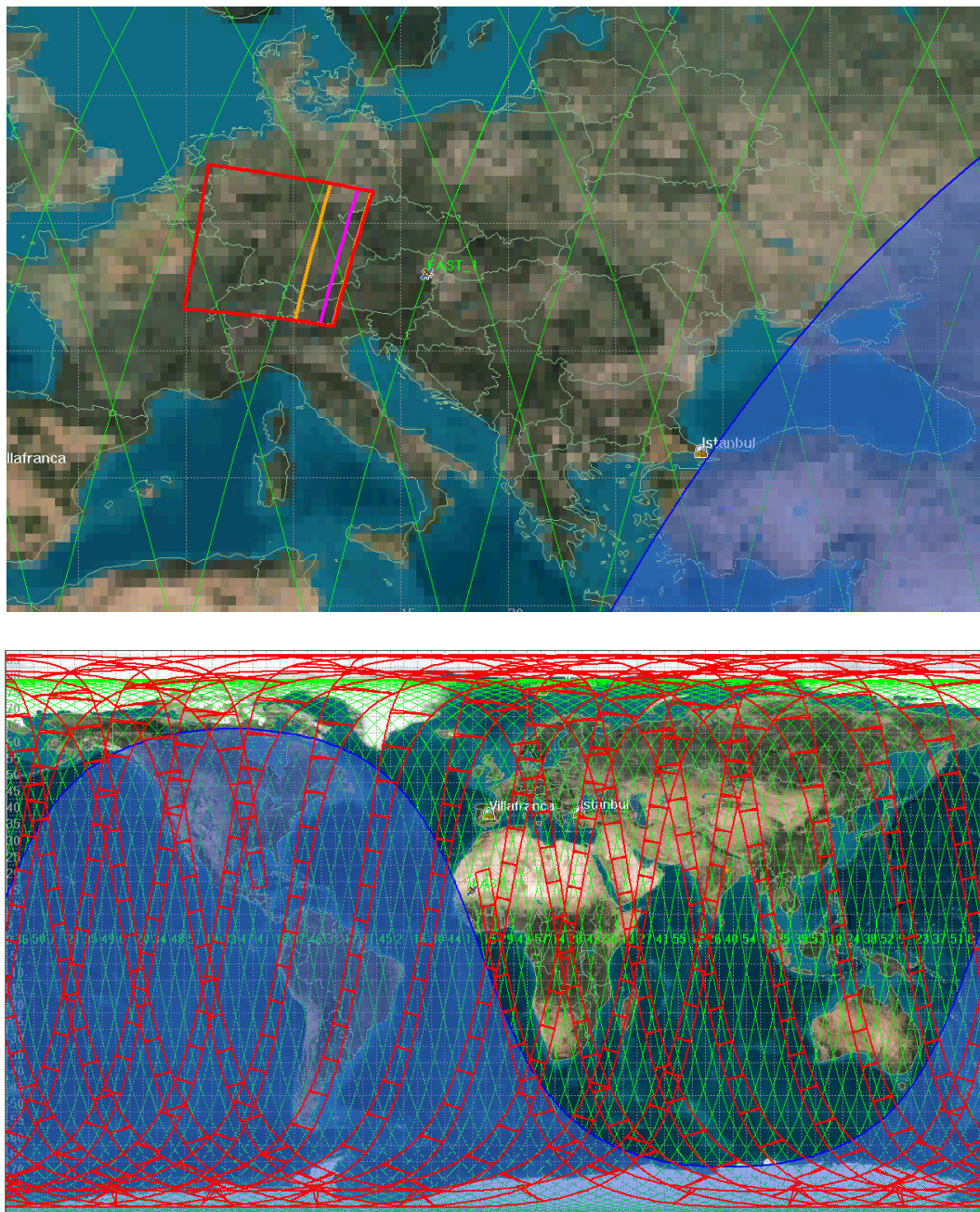


Figure D-2. Top: in pink the swath achievable with one feeder (44.9 km); in orange the swath achievable with 3 feeders (135.2 km) and in red the one potentially achievable with 3 feeders and by steering the satellite. Bottom: example of the satellite ground track and coverage over a number of satellite orbits.

D.3 SAR Scene Dimensions

Considering 8 bits per pixel per channel and 2 channels per polarisation (i.e. real and imaginary parts), the data handling calculations are presented in Table D-4. They assume an on-board storage capability of 600 Gb and a duty cycle of 2%.

Table D-4. Acquisition modes: range and azimuth resolution.

	Single polarization, 1 feeder, 18° incidence angle	Dual polarization, 3 feeders, 44° incidence angle
Image width (cross track)	45 km	135 km
Image width (cross track)	9783 pixels	26627 pixels
Maximum image height (along track)	658 km	658 km
Maximum image height (along track)	115641 pixels	39878 pixels
Square meters per pixel	15.64 m ²	83.65 m ²
Bits per pixel	16 bits	32 bits
SAR Image dimensions	~ 2.1 Gb	~ 4 Gb